UNIVERSITÉ DE STRASBOURG

ÉCOLE DOCTORALE DE PHYSIQUE ET CHIMIE PHYSIQUE (ED 182)
Institut Charles Sadron (ICS) – CNRS-UPR22

THÈSE présentée par :

Quentin WEINBACH

soutenue le : **14 Décembre 2022**

pour obtenir le grade de : **Docteur de l'Université de Strasbourg**
Discipline/ Spécialité : **Physique et Chimie-Physique**

Elaboration and Characterization of Porous Conducting Polymers: Application to Thermoelectricity

Elaboration et Caractérisation de Polymères Conducteurs Poreux : Application à la Thermoélectricité

THÈSE dirigée par :

Mme. BINIEK Laure	Chargée de Recherches, HDR, CNRS-ICS, Université de Strasbourg

RAPPORTEURS :

M. KEMERINK Martijn	Professeur des Universités, CAM, Universität Heidelberg
M. PLESSE Cédric	Maître de Conférences, HDR, LPPI, Cergy Paris Université

EXAMINATEUR :

M. LECLERC Nicolas	Directeur de Recherches, HDR, ICPEES, Université de Strasbourg

MEMBRES INVITES :

M. COLLIN Dominique	Chargé de Recherches, HDR, CNRS-ICS, Université de Strasbourg
M. STEIN Nicolas	Maître de Conférences, HDR, IJL, Université de Lorraine

ACKNOWLEDGMENT

Je tiens tout d’abord à remercier du fond du cœur **Laure**, ma directrice de thèse qui m'a encadré pendant ces 3 années. Merci pour ta disponibilité, ton soutien indéfectible et tous tes précieux conseils ! J'ai beaucoup aimé ta façon de m’encadrer, le fait que notre relation ne soit pas trop hiérarchique et que tu m'impliques dans tous les aspects de ce travail. Nous avons eu des discussions passionnantes, fait de belles découvertes et même eu quelques débats scientifiques animés ! Je suis profondément reconnaissant pour toutes les expériences et les enseignements que j'ai pu tirer de ces trois années grâce à toi. Initialement je n’avais pas vraiment prévu de faire une thèse mais tu m’as convaincu et je ne regrette absolument pas cette décision. Tout n’a pas toujours été facile mais j’ai beaucoup appris, tant scientifiquement, que sur le plan personnel. Pour tout cela je te remercie sincèrement.

Je tiens également à remercier **Dominique**, pour ton temps, ton aide, et ton soutien tout au long de cette aventure. En particulier, merci pour nos discussions et toutes les anecdotes que tu as pu me raconter.

Je tiens à remercier tous les membres de mon jury, **Dr. Nicolas Leclerc**, **Prof. Martijn Kemerink** et **Dr. Cédric Plesse**, pour leur précieux temps et leur contribution à la qualité de ma thèse. Leurs remarques et suggestions ont été précieuses pour améliorer mon travail et j’ai beaucoup apprécié nos échanges pendant la soutenance. Je voudrais remercier en particulier **Nicolas Stein** pour sa présence dans mon jury de thèse mais surtout pour notre longue collaboration tout au long de ma thèse. Merci pour tes conseils, pour ton aide et pour l’accueil, toujours chaleureux, à Metz.

Je tiens à remercier tous les membres de l’équipe SYCOMMOR, en particulier **Jean-Phillipe** et **Laurent** pour leur aide quasi quotidienne au labo, j’aurais souvent été bien bloqué sans vous ! Je voudrais aussi remercier particulièrement **Martin** pour nos discussions et pour son aide. Merci également à **Phillipe** et **Amparo**, cela a toujours été un plaisir de discuter.

Evidemment je voudrais remercier les stagiaires avec qui j’ai pu travaillé pour leur aide et leur contribution à ce travail, merci à **Naoures** et **Mohamed**, j’ai apprécié travailler avec vous ! Je veux remercier un peu plus spécifiquement **Emma**, cela a été un plaisir de t’encadrer (presque tout seul), d’essayer de te transmettre ce que j’ai appris, ravi que tu ai passé un peu de temps dans l’équipe !

Un grand merci aux membres des plateformes Plamics et Differix ! Je l’ai déjà dit mais sans vous, une bonne moitié de ma thèse n’aurait pas été possible. Merci en particulier à **Doru** pour tout le temps que tu as passé à m’aider et a essayer de me faire comprendre les bases de la diffusion des rayons X (bien que ce ne fut pas simple !). Je voudrais grandement remercier **Alain** et **Marc**, en premier lieu pour leur aide et leur expertise en microscopie mais aussi pour tous les autres moments que nous avons pu passer, autour d'un repas ou d'un verre.

Evidemment je remercie tous les membres de l'ICS qui m'ont aidé à accomplir ce travail, je pense notamment à **Patrick**, **Christophe**, **Damien**, **Mélanie**, **François**, **Thibaud**, merci beaucoup pour votre contribution.

Je voudrais également remercier les non-permanents, collègues puis amis avec qui j'ai partagé ces trois dernières années. Merci à **Duncan**, **Ricardo** et **Marion** pour tous ces moments, ces discussions, repas sorties… J'ai beaucoup apprécié passer autant de temps avec vous. Spéciale dédicace à **Duncan** avec qui j'ai partagé presque tous les moments importants, drôles ou moins drôles de cette thèse, ravi d'avoir partagé cela avec toi, je te souhaite plein de bonheur dans le futur. Merci à ceux qui ont rejoint en cours de route **Swapneel**, **Adèle**, **Eulalie**, **Alexandre**, **Thibault** j'ai vraiment apprécié passer du tout avec vous ! **Souhail**, je suis content d'avoir pu te rencontrer même si notre temps en commun au labo aura été court, bon courage pour la suite !

Je tiens également à remercier toutes les personnes externes au laboratoire avec qui j'ai pu collaborer **Sadiara**, **Thomas**, **Vaso**, **Laurent**, **Gérald**, **Bertrand** et **Soufiane**, merci à tous pour votre aide et pour votre accueil.

Enfin, je tiens à remercier ma famille pour leur soutien et leur amour, merci à mes amis pour avoir su garder mon mental dans un bon état pendant cette thèse, merci en particulier à **Koko**, **Charlotte**, **Alexis**, **Clara**, **Flo**, **Marine**, **Ni** et **Antoine** qui ont dû me supporter très (trop ?) souvent pendant ces trois années, je suis vraiment heureux d'avoir pu être à Strasbourg pour cette thèse et vous avoir à mes côtés. Pour finir je voudrais remercier **Barbara** pour avoir cru en moi, tu avais raison, j'ai bien fait d'avoir fait cette thèse ! Merci d'être là, de me soutenir, j'ai hâte de partager cette nouvelle vie à Colmar avec toi.

TABLE OF CONTENTS

LIST OF ABBREVIATIONS

BC	Bacterial Cellulose
BET	Brunauer-Emmett-Teller
CMP	Conjugated Microporous Polymer
CO_{2S}	Dry ice
COF	Covalent Organic Framework
DCB	Dichlorobenzene
DFT	Density Functional Theory
DLS	Dynamic Light Scattering
DMSO	Dimethyl Sulfoxide
DOS	Density of State
EG	Ethylene Glycol
EtOH	Ethanol
F4TCNQ	tetrafluoro tetracyano-quinodimethane
FTIR	Fourier Transformed Infrared
FTS	(tridecafluoro-1,1,2,2- tetrahydrooctyl)trichlorosilane
FWHM	Full Width at Half Maximum
G'	Storage modulus
G''	Loss modulus
GISAXS	Grazing Incidence Small Angle X-ray Scattering
GIWAXS	Grazing Incidence Wide Angle X-ray Scattering
GOPS	glycidoxypropyl trimethoxysilane
HOMO	Highest Occupied Molecular Orbital
HCP	Hypercrosslinked Polymer
HWHM	Half-Width at Half Maximum
IoT	Internet of Things
IPA	Isopropanol
IPCC	Intergovernemental Planel on Climate Change
κ_{elec}	Electronic contribution to the thermal conductivity
κ_{gas}	Gas contribution to the thermal conductivity
$\kappa_{lattice}$	Lattice contribution to the thermal conductivity
κ_{solid}	Solid contribution to the thermal conductivity
LD	Lyophilized Dispersion
LUMO	Lowest Unoccupied Molecular Orbital
MOF	Metal Organic Framework
MWCNT	Multi-Wall Carbon Nanotube
N_{2L}	Liquid nitrogen
NFC	Nanofibrillated cellulose
NIR	Near Infrared
NMP	N-methyl pyrrolidone
PANI	Polyaniline
PBTTT	Poly(2,5-bis(3-amkylthiophen-2-yl)thieno[3,2-b]thiophene)
PCP	Porous Conducting Polymer

PEDOT	poly(3,4-ethylenedioxythiophene)
PF	Power Factor
PGEC	Phonon-Glass Electron-Crystal
PH1000	Commercial PEDOT: PSS dispersion
PIM	Polymer of Intrisic Microporosity
PPy	Polypyrrole
PSS	Poly(styrene sulfonate)
PTFE	Polytetrafluoroethylene
PVA	Polyvinyl alcohol
PVDF	Polyvinylidene fluoride
q	Wavevector
S	Seebeck coefficient
SANS	Small Angle Neutron Scattering
SAXS	Small Angle X-ray Scattering
SEM	Scanning Electron Microscopy
SWCNT	Single-Wall Carbon Nanotube
TA	Tannic Acid
TATHCP	Triazatruxene based hypercrosslinked polymers
TDAE	Tetrakis(dimethylamino)ethylene
TDTR	Time-Domain Thermoreflectance
TE	Thermoelectric
TEG	Thermoelectric generator
TEM	Transmission Electron Microscopy
TFMSA	Trifluoromethanesulfonic acid
TFSI	Bis(trifluoromethane sulfonyl) imide
TPS	Transient Plane Source
USANS	Ultra-Small Angle Neutron Scattering
UV-vis	Ultraviolet-Visible
VT	Vapor Treatment
WAXS	Wide Angle X-ray Scattering
WFL	Wiedemann Franz Law
XPS	X-ray photoelectron spectroscopy
XRD	X-Ray Diffraction
ZT	Figure of merit

GENERAL INTRODUCTION

GENERAL INTRODUCTION

The energy consumption of the world population has been drastically increasing in the past decades and is expected to reach up to 26 TW in 2050.[1,2] In the context of global warming and the alarming climate changes, it is mandatory to develop means to produce enough energy while decreasing our carbon emissions. Renewable energy sources are of great interest for such goal. Today, these energy sources are mostly the sunlight, wind and tidal. Although the conversion of heat into electricity is well known and has been used for decades (combustion engines), its use as a source of renewable energy is relatively poor. Indeed, heat is one of the most present energy sources on earth. Naturally, it is found mainly from the sun, geothermal energy, human activities, and body heat. For example, the sun alone provides (by infrared waves) more than enough energy to meet the world's energy demand. The problem is that, although this source of energy is abundant, it is present on earth in a very diffuse way resulting in temperature differences of a maximum of a few dozen degrees. The same is true for geothermal heat. On the other hand, about 60 % of the world's energy consumption is transformed into heat. Recovering and converting part of this heat into electricity seems to be an interesting way to increase the global energy efficiency. In particular, the latest IPCC report shows that limiting energy losses is of great importance in order to meet future global energy needs while limiting our impact on the environment. Waste heat can be found from both domestic households (low temperature waste heat) and industrial waste/processes (medium to high temperature waste heat). This heat is usually quite localized which makes it easier to convert than heat from the sun or geothermal energy. Finally, the heat released by the human body (up to 80 mW/cm² for a moving individual)[3,4] is an easily accessible source of low-grade waste heat. It is in this context that thermoelectric generators (which can convert heat into electricity) are of interest. From a temperature gradient, this kind of generator can produce up to a few W of electricity (depending on the temperature gradient and the efficiency of the generator). One can immediately think of applications, especially in the automotive sector (or for any equipment containing a thermal engine) to convert the heat released by placing a thermoelectric generator on the exhaust pipes.

It exists many different thermoelectric materials, mainly divided into two categories: inorganic and organic materials. To convert heat at gradients above 800 K, there are several types of promising technologies, using non-toxic and abundant inorganic materials.[5] For lower temperature gradients, the situation is different. There are also promising inorganic technologies but using scarcer and more toxic materials such as Pb, Bi or Te. Conversely, organic materials are generally less toxic, more abundant, light and mechanically flexible. These advantages are to be considered in a nuanced way because their generally petro-sourced origin risks, in the long run, to be problematic. The performances of these materials are weaker than their inorganic counterparts, but the advantages mentioned, and their low operating temperature (300-500 K) makes them good complements to inorganic materials. In this thesis we are interested in organic materials for thermoelectric applications. In view of their relatively low performance and low-grade waste heat harvesting, their optimal use is for body heat recovery to power small sensors or wearable low-consumption electronic devices for sports/medical use.

The field of organic thermoelectric received considerable attention after the pioneer work of Bubnova et al. in 2011.[6] By controlling the oxidation level of poly(3,4-ethylenedioxythiophene) (PEDOT), they reached ZT values (the figure of merit, a dimensionless number that reflects the quality of a thermoelectric material) of 0.25 at room temperature. After this work, the community focused mainly on increasing the charge transport properties[7] (i.e., the Seebeck coefficient and the electrical conductivity) until reaching electrical conductivities up to 10^5 S/cm and power factors ($PF = \sigma S^2$) of several mW/(m.K^2) for p-type doped polythiophenes derivatives.[8] Overall, the research work in the field of organic thermoelectric is mainly focused on the development of thin films with high power factors (mainly p-type materials, n-type materials being more challenging to produce).

This raises several issues. Although laboratory research is focused on the development of thin films, their final integration into thermoelectric generators is quite challenging. In addition, good charge transport properties are obviously required for efficient TE materials, but their thermal conductivity should not be neglected either. Finally, the air stability and the cost of these materials are important parameters if they are to be used in the future. In this PhD work, we decided to take a different approach to try to find solutions to these problems. To better understand this approach, we need to define ZT:

$$ZT = \frac{\sigma S^2}{\kappa_{elec} + \kappa_{lattice}}.T,$$

where σ is the electrical conductivity, S is the Seebeck coefficient, T is the temperature, and κ_{elec} and $\kappa_{lattice}$ are the electronic and lattice contribution to the thermal conductivity, respectively. Electrical conductivity, Seebeck coefficient and electronic thermal conductivity are interdependent parameters. The only isolated parameter is $\kappa_{lattice}$, which is a real lever to reduce the overall thermal conductivity without disturbing the other transport properties. Moreover, it has been shown by Scheunemann et al. that for energetically non-disordered organic TE materials to reach a ZT greater than or equal to unity, $\kappa_{lattice}$ must be lower than 0.2 W/(m.K) (which is not currently the case for doped organic TE materials).[9] Thus, phonon engineering is an interesting route for reducing $\kappa_{lattice}$. Inspired by the highly thermally insulating aerogels, we demonstrate in this thesis the interest of implementing porosity in organic p-type TE materials. In addition to reducing $\kappa_{lattice}$, producing porous materials allows their size to be significantly increased easily, enabling simple integration into vertical TEGs. Moreover, producing porous and low-density materials requires little amount of raw material, reducing their production cost. For this purpose, we develop in this thesis PEDOT: PSS gels, then by solvent drying techniques, a porous material can be obtained. By a combination of structural (SEM, TEM, WAXS/SAXS), spectroscopic (UV-vis, FTIR, XPS), and transport properties measurements (measurement of σ, S and κ) characterization methods, we demonstrate the interest of implementing porosity in TE materials and we study their structure-properties relationships.

Chapter I of this thesis focuses on the state of the art and the basic concepts relevant to this work. The first section defines some basic concepts of charge transport in organic materials, with a focus on p-type materials. Some state-of-the-art strategies to improve the TE properties of thin film organic TE materials are discussed, focusing then on the particular case of the PEDOT derivative. Finally, the interest of porosity to reduce the thermal conductivity is detailed and ideal material specifications are defined. The second part focuses on the state of the art of methods for the development of porous conducting materials. This section is divided by porosity ranges, focusing particularly on meso- and macro-porous materials. Conductive gels and solvent drying techniques are also discussed. Finally, the objectives of this PhD work are detailed.

In Chapter II, we first study the structure of the raw material used herein: the commercial dispersion of PEDOT: PSS. By a combination of cryo-TEM and X-ray scattering analysis, we demonstrate that this dispersion is composed of fibrils, contrary to what is announced by the supplier. From this dispersion, a gelation protocol via the addition of H_2SO_4 has been developed. The formation mechanism and the final structure of the fibrillar mesoporous gel were studied by a combination of spectroscopic (UV-vis, FTIR, XPS) and structural (cryo-TEM, SEM and X-ray scattering) analyses. The second section focuses on three different drying methods of the gels providing three different porous structures. The structural and physical properties of the xerogel (obtained by air drying under ambient conditions), the mesoporous sulf-aerogel (obtained by supercritical drying) and the macroporous quenched cryogel (obtained by freeze-drying) are discussed. Then, the structure-property relationships of these three different materials are studied, showing a clear influence of porosity on electrical and thermal conductivities. The implementation of porosity in the materials reduces their thermal conductivity but also their electrical conductivity. Finally, to further improve the charge transport properties of the sulf-aerogel and the quenched cryogel, a DMSO vapor treatment is applied.

In Chapter III, the freeze-drying technique is modified to tune the porous structure of the cryogels (ice-templating). Through careful control of the freezing conditions, we demonstrate the possibility to control the orientation and size of the pores in macroporous materials. Moreover, we demonstrate by X-ray scattering studies the anisotropy of pore walls. Finally, we study the influence of pore size on the electrical conductivity, Seebeck coefficient and thermal conductivity of templated cryogels. Preliminary results on the anisotropic electrical conductivity are also presented.

Chapter IV focuses on the development of a gel by another method. The alcogel, produced by the gelation of the dispersion of PEDOT: PSS with ethanol, exhibits a mesoporous fibrillar network. The alcogel is dried by the supercritical drying method and give rise to a robust alco-aerogel. Its structural and mechanical properties are studied by SEM, X-ray scattering,

N_2 physisorption and rheological studies. The material is well ordered at the molecular scale and exhibits the best charge transport properties among the porous conducting materials produced in this PhD work. In addition, its mesoporous network provides a low thermal conductivity. To demonstrate the promising interest of porous TE materials, the power output of the alco-aerogel is measured. Finally, the first results on the evolution of TE properties in the air of the porous materials are shown.

REFERENCES

[1] O. Bubnova, X. Crispin, *Energy Environ. Sci.* **2012**, *5*, 9345.

[2] M. Campoy-Quiles, *Philos. Trans. R. Soc. A* **2019**, *377*, 20180352.

[3] M. Thielen, L. Sigrist, M. Magno, C. Hierold, L. Benini, *Energy Convers. Manag.* **2017**, *131*, 44.

[4] V. Leonov, *IEEE Sens. J.* **2013**, *13*, 2284.

[5] D. Beretta, N. Neophytou, J. M. Hodges, M. G. Kanatzidis, D. Narducci, M. Martin-Gonzalez, M. Beekman, B. Balke, G. Cerretti, W. Tremel, A. Zevalkink, A. I. Hofmann, C. Müller, B. Dörling, M. Campoy-Quiles, M. Caironi, *Mater. Sci. Eng. R Reports* **2019**, *138*, 100501.

[6] O. Bubnova, Z. U. Khan, A. Malti, S. Braun, M. Fahlman, M. Berggren, X. Crispin, *Nat. Mater.* **2011**, *10*, 429.

[7] A. D. Scaccabarozzi, A. Basu, F. Aniés, J. Liu, O. Zapata-Arteaga, R. Warren, Y. Firdaus, M. I. Nugraha, Y. Lin, M. Campoy-Quiles, N. Koch, C. Müller, L. Tsetseris, M. Heeney, T. D. Anthopoulos, *Chem. Rev.* **2022**, *122*, 4420.

[8] V. Vijayakumar, Y. Zhong, V. Untilova, M. Bahri, L. Herrmann, L. Biniek, N. Leclerc, M. Brinkmann, *Adv. Energy Mater.* **2019**, *9*, 1900266.

[9] D. Scheunemann, M. Kemerink, *Phys. Rev. B* **2020**, *101*, 75206.

CHAPTER I. STATE OF THE ART AND FUNDAMENTALS

I. STATE OF THE ART AND FUNDAMENTALS

1. GENERAL CONCEPTS

1.1. ENERGY HARVESTING AND THERMOELECTRICITY

In a world where energy consumption must be monitored and new ways of powering electrical devices must be found, energy harvesting might be a means of achieving net zero emission in the near future.[1,2] Energy harvesting is the collection of small amounts of ambient energy to power low-consumption devices. Whilst their concept is identical to that of large-scale technologies such as wind turbines or hydroelectricity production, typically, only a few microwatts are produced by these technologies. Amongst them, the three main sources of potential energy harvesting are motion (piezoelectric), light (photoelectric), and heat (thermoelectric).[3–6] These technologies could be used to eliminate the need of batteries in many devices such as the Internet of Things (IoT).[7] Above all, thermoelectrics demonstrate promising results to be used as wearable electronics[8,9] using body heat to work. The thermoelectric (TE) effect is defined by any transport phenomenon implying a conversion from a temperature gradient to an electrical potential and vice versa. It arises originally from the Seebeck effect reported at the beginning of the 19th century[10,11] which stands on a simple principle: the application of a temperature gradient between the ends of a device composed of two electrically jointed dissimilar conductors results in the production of an electrical potential function of the temperature distribution.[12] The Seebeck coefficient (S) represents the change of voltage with respect to a temperature gradient and is defined as:[13]

$$S = -\frac{dV}{dT} \tag{I.1}$$

Where V is the electric potential and T the absolute temperature. By convention, the sign of the Seebeck coefficient is given by the potential of the cold side with respect to the hot side. Thus, it reflects the major charge carriers present in the conducting material: positive for holes (p-type material), and negative for electrons (n-type material). The intrinsic property S is not the only one necessary for good thermoelectric material. In order to determine the suitability of a TE material, Ioffe et al. introduced the dimensionless figure of merit ZT defined as follows:[14]

$$ZT = \frac{\sigma S^2}{\kappa} T \qquad (I.2)$$

with σ the electrical conductivity, S the Seebeck coefficient, κ the thermal conductivity, and T the absolute temperature. In the simplest case, κ can be divided into two contributions: κ_{elec} the electronic contribution, and $\kappa_{lattice}$ the phononic contribution to the lattice. Hence, an ideal TE material must combine metal-like electrical charge conductivity while being a thermal insulator. As thermal conductivity can be very challenging to measure, the power factor (PF) is often used to highlight the potential efficiency of a TE material. It is defined as:

$$PF = \sigma S^2 \qquad (I.3)$$

with σ the electrical conductivity and S the Seebeck coefficient.

Although the ZT is a very useful tool to estimate if a TE material can be of potential use, one must be careful as it does not represent its efficiency. The maximum thermoelectric efficiency of a TE generator (TEG), η_{max}, can be defined in terms of Carnot efficiency as:[15]

$$\eta_{max} = \eta_C \frac{\sqrt{1 + ZT_{av}} - 1}{\sqrt{1 + ZT_{av}} + \frac{T_c}{T_h}} \qquad (I.4)$$

with η_C the Carnot efficiency, T_h and T_c are the temperature at the hot and cold side of the TEG, respectively, and $T_{av} = (T_h + T_c)/2$. Hence, it is clear that the maximum efficiency depends on the Carnot efficiency and ZT. As an example, a TEG with ZT = 2 and T_h = 393 K and T_c = 293 K, the Carnot efficiency would be ~ 25 % and the maximum efficiency of the generator would only be of ~ 7.5 %. Even with materials with very high ZT, the maximum efficiency will always be limited by the Carnot efficiency.

The thermoelectric materials need to be integrated into generators for energy production. Several architectures exist to create thermoelectric generators (TEGs),[16] the simplest theoretical model is represented in Figure I.1.A. The vertical generator is made with two legs, one of p-type and the other of n-type TE materials (in real TEGs, the number of legs' pairs is optimized to reach the highest efficiency) which are connected electrically in series but thermally in parallel. The temperature gradient induces a charge accumulation at cold ends leading to the production of energy. This architecture can only be used with bulk-size materials (thickness>2-3 mm).

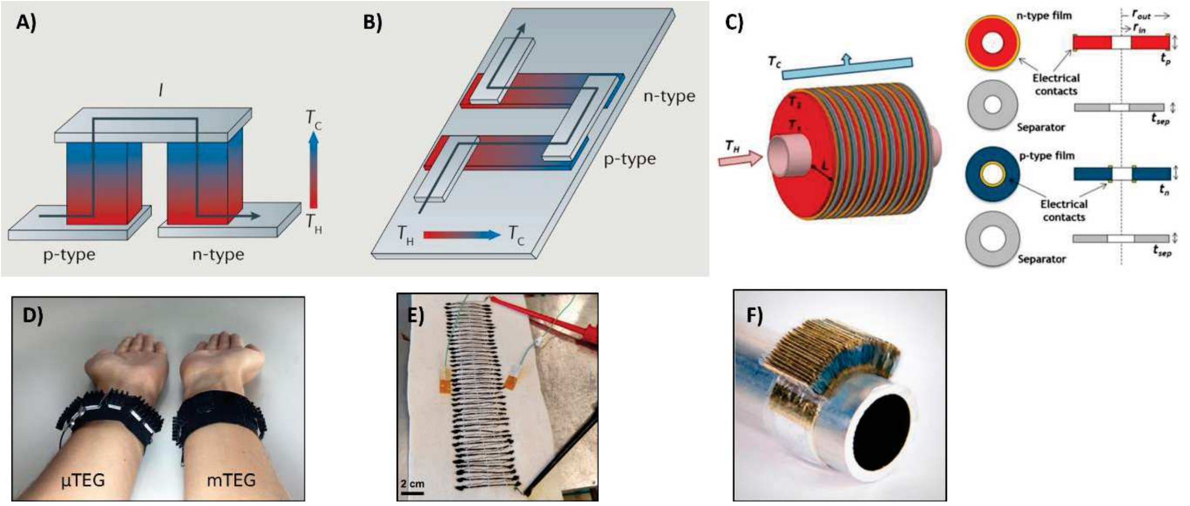

Figure I.1: A) Vertical and, B) Planar TEG reproduced from [5]; C) Radial TEG reproduced from [17]; D) Worn wristband TEG reproduced from [18]; E) In-plane embroidered textile TEG made with coated p-type and n-type yarns, reproduced from [19]; F) Concept of organic thin films TEG for round surfaces. Reproduced from [20].

The use of materials of different dimensions such as thin films results in the use of much more complex architectures as presented in Figure I.1.B, Figure I.1.C and Figure I.1.F.

In the past decades, thermoelectricity grew much interest in the scientific community and for commercial application. Indeed, the advantages of TEGs are numerous: direct energy conversion, no moving part or fluids, no scale effect, and a long lifetime. For now, the best TE materials are inorganic telluride and tin selenide-based alloys (with $ZT > 2$).[21–24]

1.1.1. INORGANIC TE MATERIALS

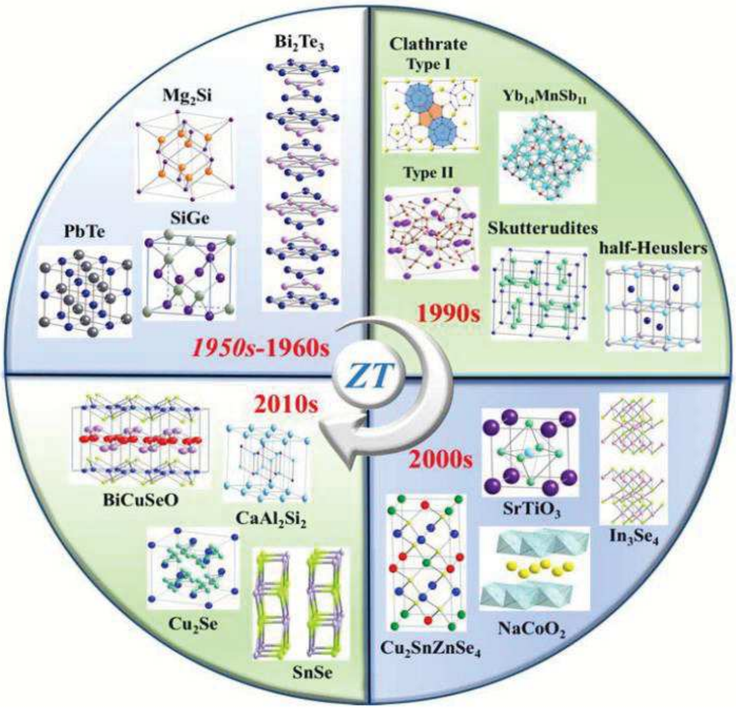

Figure I.2: Timeline of representative inorganic TE material from the 1960s to the present, the state-of-the-art materials have ZT between 1 and 2. Reproduced from [25].

Figure I.2 shows the past advances in material design and band gap engineering to achieve high ZT inorganic TE materials.[20,25] Even though they are made of rare and toxic raw materials, these materials are promising for heat harvesting at high temperatures such as electricity generation in extreme environments, and waste heat recovery in industrial plants or in aircraft engines.[26] Indeed, radioisotopes TEGs have been used since the beginning of space exploration due to their low mass, compact volume, and high-reliability source of energy for long distant missions.[27] More recently, for high operation temperatures above 800K, technologies using abundant raw materials such as silicides, Heusler compounds or skutterudites can be used with good performances.[28–31] Conversely, chalcogenides or tin selenide technologies that can operate well in the mild to low-temperature range use rare, often toxic, and heavy raw materials.[32,33] Organic materials such as conducting polymers could be a good complement for the low-temperature operation range using abundant, less toxic, and mechanically flexible materials. Moreover, their low intrinsic thermal conductivity (0.2-0.8 $W.m^{-1}.K^{-1}$), ease of processability via the liquid phase, and their large versatility through molecular engineering make them very good candidates for ambient temperature TE applications.[34]

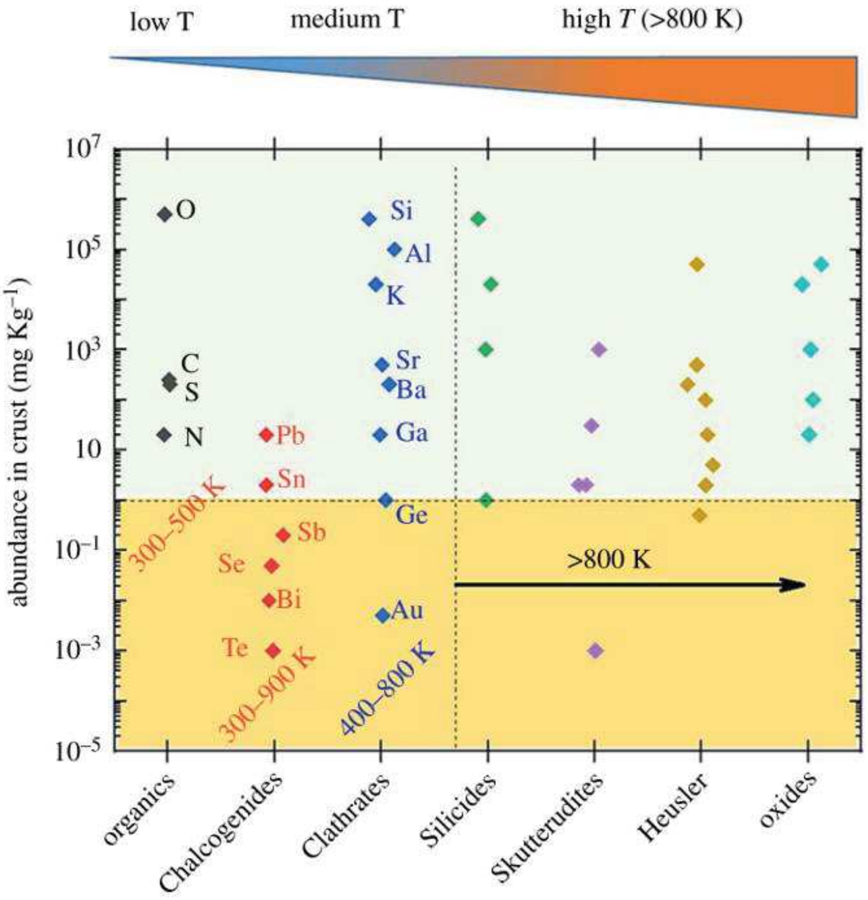

Figure I.3 Optimum temperature range and abundance in the earth's crust of different elements used in thermoelectric technologies. Reproduced from [34].

1.1.2. STATE-OF-THE-ART ORGANIC TE MATERIALS

On a general basis, polymer TE is a newly emerging field that has only developed since the pioneering work of Bubnova and coworkers in 2011.[35] They achieved a ZT of 0.25 at room temperature thanks to fine control of the oxidation level of poly(3,4-ethylenedioxythiophene)-tosylate (PEDOT-Tos). Despite their benefits, organic TE materials, limited by their low electrical conductivity and Seebeck coefficient struggle to match their inorganic counterparts. However, current efforts in the scientific community to increase the charge transport properties of semiconducting polymers led to achieving a high ZT value of 0.42 for p-type PEDOT: PSS[36] and above 0.3 for n-type doped fullerene derivatives.[37] As shown in Figure I.4 the community focused on increasing the power factor of organic TE materials. Hybrid organic-inorganic materials were also developed and some high power factors were reported.[38] Hybrid material is one of the ways to improve the ZT. However, very little is known in the literature concerning the mechanisms of PF improvement, and the "buff" effect due to the addition of inorganic materials is not always observed.

Often processed as thin films, these organic and hybrid materials are very challenging to integrate into generators and need specific architectures as demonstrated in Figure I.1.B, Figure I.1.C and Figure I.1.F.

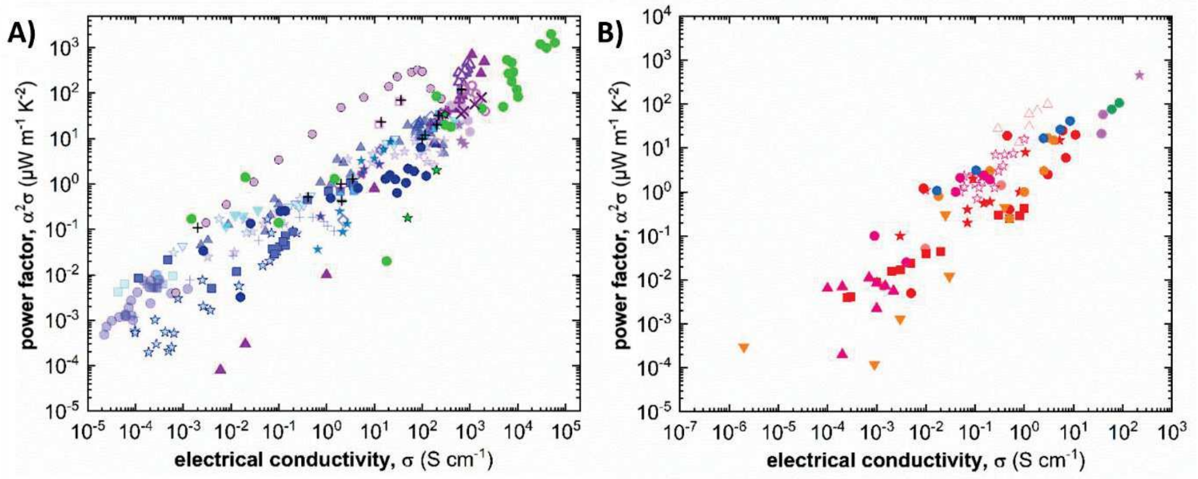

Figure I.4: Thermoelectric power factor of various organic materials extracted from the literature as a function of the electrical conductivity. A) p-type polymers, in blue : polythiophene derivatives, purple : PEDOT based blends, green : polyacetylene. B) n-type materials. Reproduced from [39].

After this general introduction, we will concentrate, in the next section, on our topic of interest and on the fundamental principles of conducting polymers.

1.2. SEMI-CONDUCTING POLYMERS FOR TE

1.2.1. BASICS AND FUNDAMENTALS ON π-CONJUGATED POLYMERS

Semi-conducting polymers are conjugated molecules that constitute a special class of organic materials able to conduct electrical charges thanks to their π-conjugation. These molecules have an alternating single-double bond on their backbones allowing semiconducting properties. Carbon atoms are sp^2 hybridized meaning that planar σ-bond arises from the hybridization of one s and two p orbitals. Consequently, the remaining 2p electrons of each carbon on the backbone are delocalized in π-orbitals, in which electronic density is predominant in the plane perpendicular to the σ-bond. Hence, p-electrons do no longer belong to a single bond but are delocalized over a group of atoms resulting in the formation of a fully occupied bonding π orbital and an empty π* orbital. Such bonding prevents chain bending and twisting resulting in a stiffer backbone than saturated polymers. Figure I.5 illustrates the p-orbital overlapping of a simple ethylene molecule.

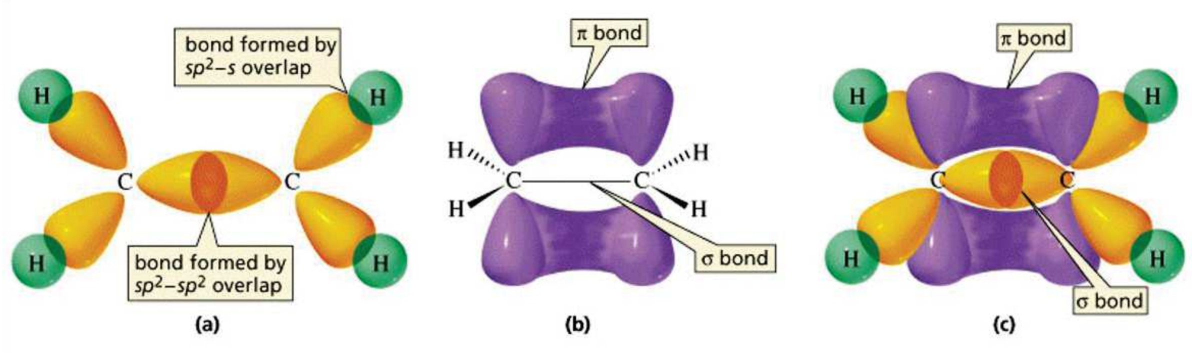

Figure I.5: Schematic of the sp^2 hybridization of an ethylene molecule. Reproduced from [40].

In a conjugated polymer, the repetition of several coupled conjugated monomer units leads to energy level splitting of the π and π* orbitals forming quasi-continuous energy bands as shown in the simplified schematic in Figure I.6. These energy levels correspond to the highest occupied molecular orbital (HOMO) for the π-bonding orbital and the lowest unoccupied molecular orbital (LUMO) for the π*-antibonding orbital. Such energy levels can be compared to conduction and valence band in inorganic semiconductors, respectively. They are separated by a band gap of energy E_g[41] typically between 1 eV and 3 eV, smaller than in transparent and insulating saturated polymers. This low band gap allows the injection of charge carriers (extra electron or extra hole) that can be easily transported along the conjugated backbone while the chain structure is maintained by the σ-bonding skeleton.

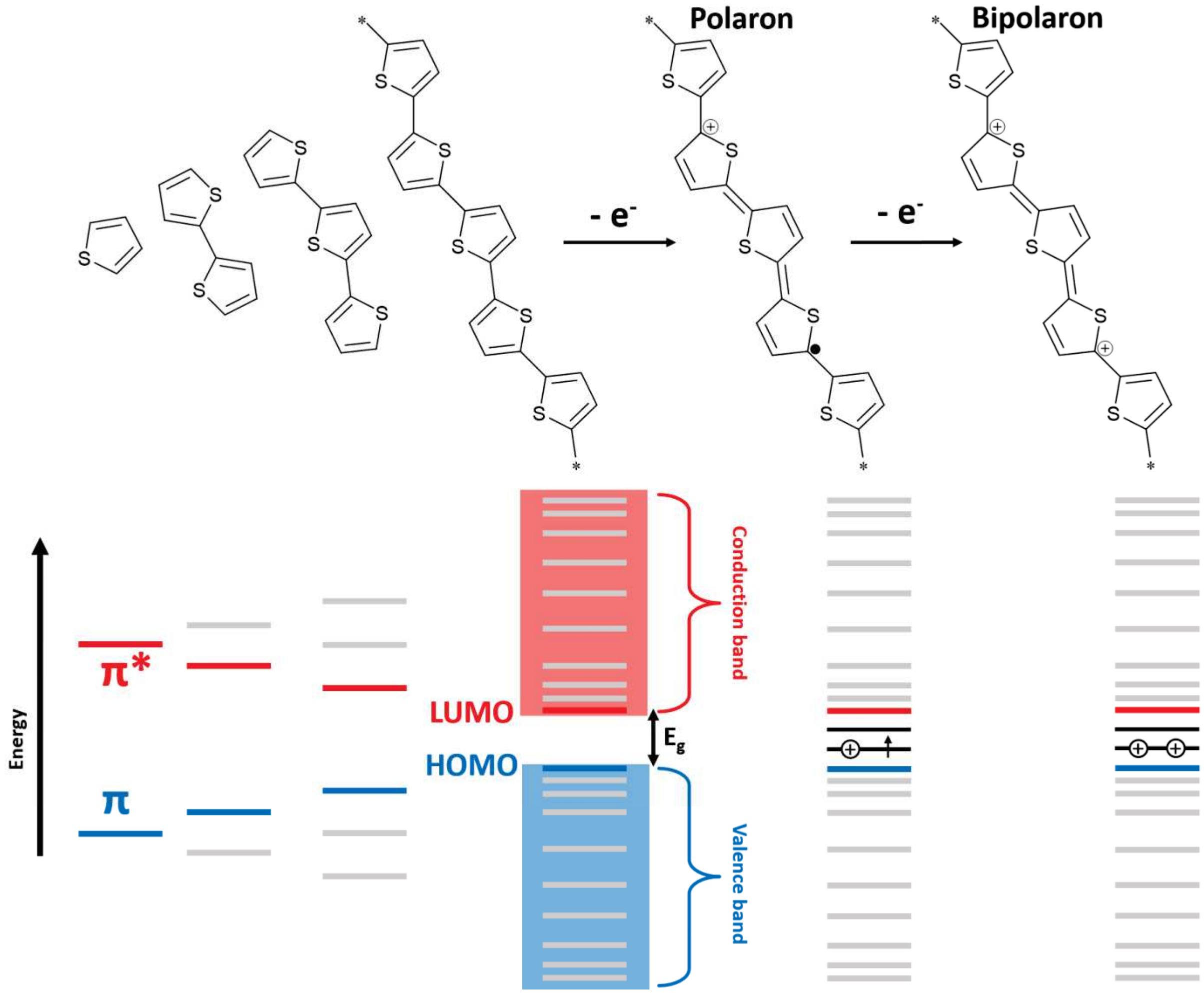

Figure I.6: Evolution of HOMO, LUMO levels, and band gap E_g upon increasing conjugation length and formation of polaron and bipolaron after p-type doping of polythiophene.

By analogy to inorganic semiconductors, the electrical conductivity of such materials depends on the charge carrier density and mobility. The electrical conductivity can be described as follows:

$$\sigma = en\mu \tag{I.5}$$

Where e is the electric charge of a charge carrier, n is the charge carrier density and μ is the charge carrier mobility. Hence, the electrical conductivity of a semi-conducting polymer is governed by its doping level (affecting n), and its nanostructure (affecting μ). To increase the charge carrier density, semiconducting polymers can be tuned via doping. Doping introduces new electronic states in the band gap allowing new optical transitions that can be observed as a broad infrared absorption band. These intermediate states are represented by the so-called polarons and bipolarons presented in Figure I.6.A. Polaron is a single charge excitation that can be either positive (i.e., radical cation as presented in Figure I.6) or negative (i.e., radical anion) in case an electron is added to or extracted from the polymer chain. At high doping concentrations, bipolarons are created when electrons are added to or removed from polarons. In other words, di-cations (or di-anions) with strong local distortions are formed.

There are different possible ways to dope a conjugated polymer, either by electrochemical doping or by chemical reaction. In the case of electrochemical doping, the extra charge carrier is provided by a metal electrode in contact with the semi-conducting polymer. Counterions from an electrolyte can penetrate the polymer to maintain a neutral global state. The oxidation or reduction of the polymer takes place when the electrochemical potential of the metal in contact reaches the ionization potential of the polymer via an externally applied potential.[42,43] The other way to dope a semi-conducting polymer would be to exchange an electron or ion between a dopant and the conjugated polymer via an oxydo-reduction reaction. In that case, the polymer is exposed to a gas or a solution containing a molecule of high electron or proton affinity. Oxidizing agents of high electron affinity are the so-called p-type dopants presented in Figure I.7.A, conversely, reducing agents of high proton affinity are the so-called n-type dopants in Figure I.7.C. In the case of p-type doping, the reduced dopant transforms into an anion, neutralizing the positive charge introduced in the HOMO level of the conjugated polymer. One of the driving forces for efficient doping is the energy levels compatibility. In the case of p-type doping, electron transfer can occur favorably if the dopant has a higher electron affinity than the ionization energy of the semiconducting polymer. Therefore, for efficient charge transfer, the LUMO of the dopant must be deeper than the HOMO of the conducting polymer for p-type doping and the HOMO of the dopant must be shallower than the LUMO of the conducting polymer for n-type doping.[44]

1.2.2. POLYMERS STRUCTURES AND CHARGE TRANSPORT MECHANISMS

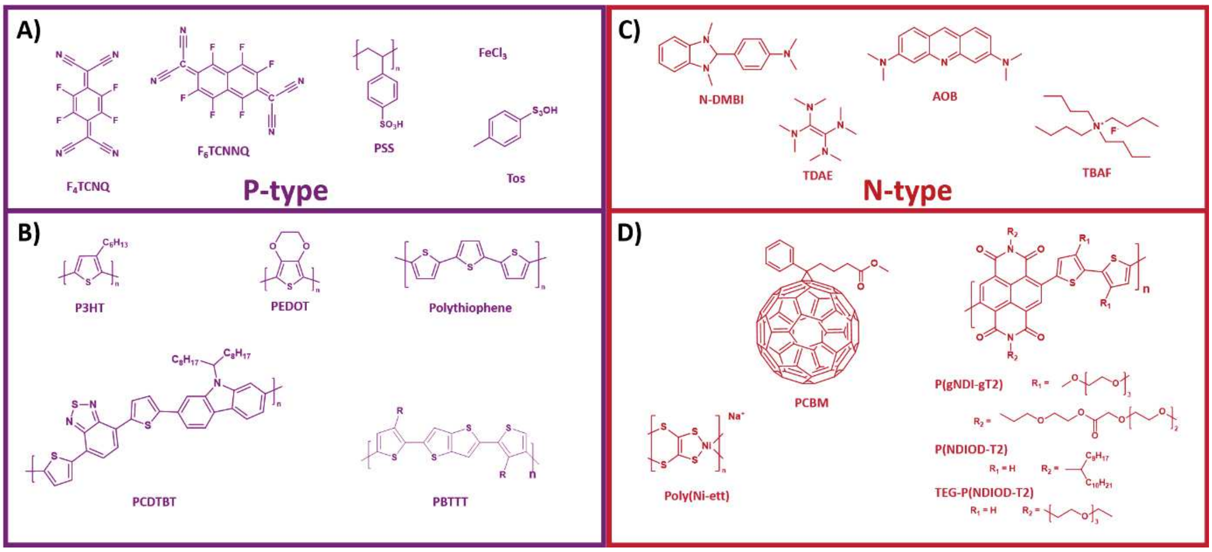

Figure I.7: Chemical structures of A) p-type dopants, B) p-type semiconducting polymers, C) n-type dopants, and D) n-type semiconducting molecules/polymers.

Such molecular engineering led to the development of a great variety of structures as shown in Figure I.7.B and Figure I.7.D. Concerning p-type polymers, the current research is mainly focused on polythiophene derivatives for their great versatility. Even though such polymers are often rather short (in general fewer than 50 repetition units), they are subject to a great disorder and chains intertwining. Consequently, semiconducting polymers are usually amorphous with a small degree of crystallinity. Morphology plays a great role in the charge transport properties of the conjugated polymer. Due to the high degree of disorder of the material, charges tend to localize resulting in poor charge carrier mobility and electrical conductivity (several orders of magnitude lower than their inorganic counterparts).[45,46] Even though fully crystalline semiconducting polymers cannot be obtained, long-range crystallites with high connectivity between ordered regions play a major role in the charge transport (see Figure I.8 A-C). By analogy with the transport mechanism in inorganic semiconductors, the interchain order, crystal domain size, and connectivity allowing charge carrier delocalization along the conjugated molecules must be important. In conducting polymers, charge transport can occur by intrachain propagation of the charge carrier along the polymer backbone, by interchain propagation across polymer chains via hopping, or by tunneling between conducting domains separated by amorphous regions (see Figure I.8.C and Figure I.8.D). Although intrachain propagation is the fastest, interchain coupling is essential to ensure a good charge transport along the whole material.

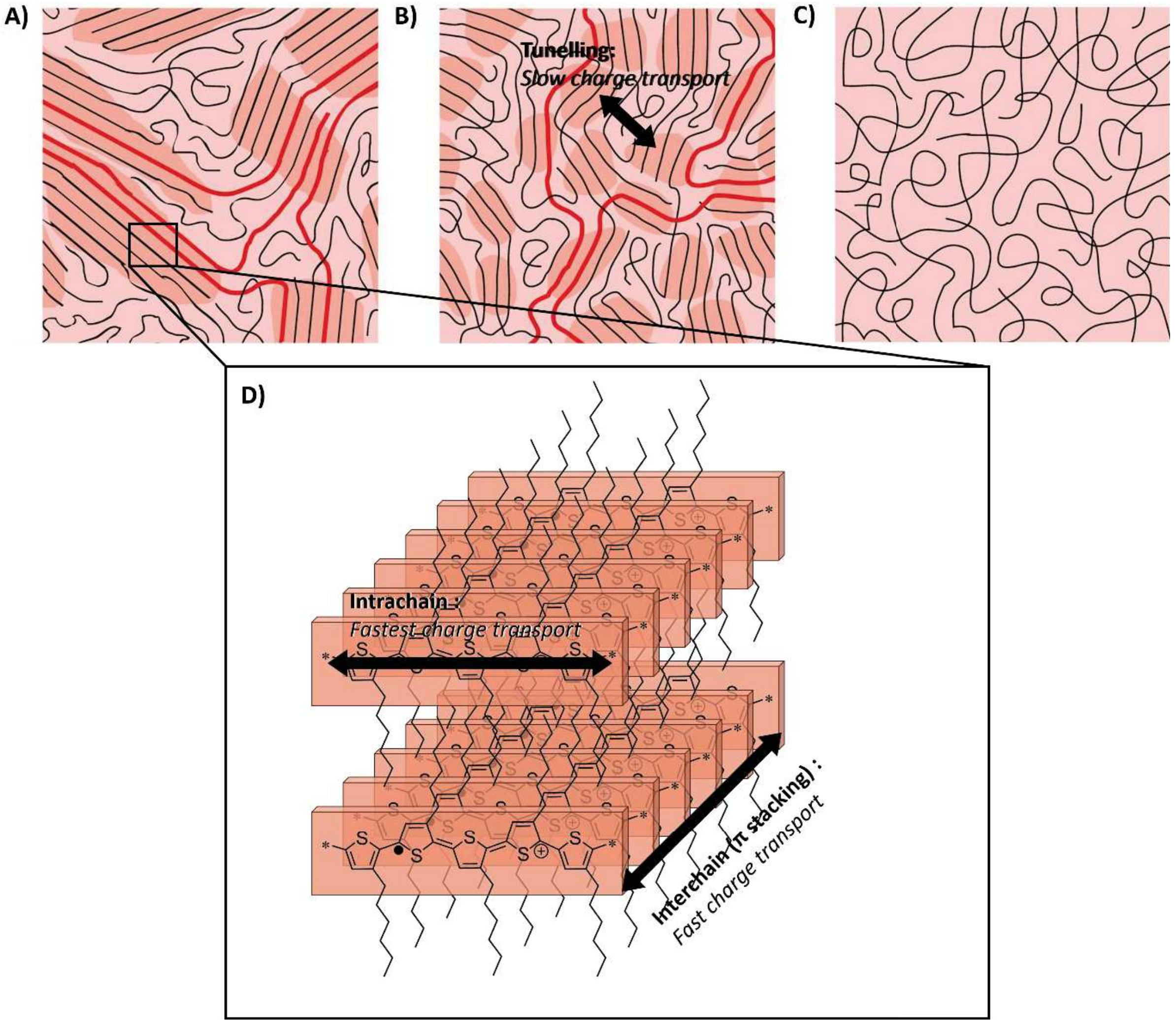

Figure I.8: A-C) Schematic microstructure of a P3HT conjugated polymer film. A) semi-crystalline film, B) disordered aggregates, and C) completely disordered film. The darker shadowed area represents ordered regions, surrounded by spaghetti-like amorphous regions. The red lines represent long polymer chains that can connect several grains of ordered regions, increasing the charge transport of the film. D) Schematic of the lamellar arrangement of P3HT chains and the different charge transport mechanisms. Adapted from [47].

Thus, due to the high degree of disorder in conjugated polymers, the mechanism of charge transport is different from that in classical semiconducting materials. Based on the theory of Anderson predicting localization and absence of charge diffusion due to high disorder,[45,46] Mott's variable range hopping (VRH) theory was established to describe charge transport mechanisms in conjugated polymers.[48] According to this theory, charge transport is a function of the distance between two localized sites and their associated energies. Hence, for charges with sufficient activation energy, if the energy barrier between two sites cannot be neglected, the charge will hop to a further site with a lower energy barrier. In other words, polaron or bipolaron present on the polymer chain hops from one site to another only if the arrival site is free and a counterion is present, as described schematically in Figure I.9. The fact that hopping depends on both energy barriers and distance results in VRH rather than nearest-neighboring hopping (NNH) occurring when the energy barrier between sites can be neglected. With the development of novel architectures of semiconducting polymers, more ordered morphologies were achieved and observed behaviors could not be explained by VRH. The model has therefore been revisited by Sheng et al. into the fluctuation-induced tunneling.[49,50] Conversely to VRH, it stands on NNH and states that hopping is thermally activated, and when so, a charge from the arrival site is transferred to the nearest neutral neighboring one. Thus, transport is dominated by charge transfers between large conducting segments separated by disordered domains. Generally, progresses in the field of organic semiconductors allowed a better understanding of the charge transport mechanisms, highlighting the importance of both crystalline domains and disordered areas.

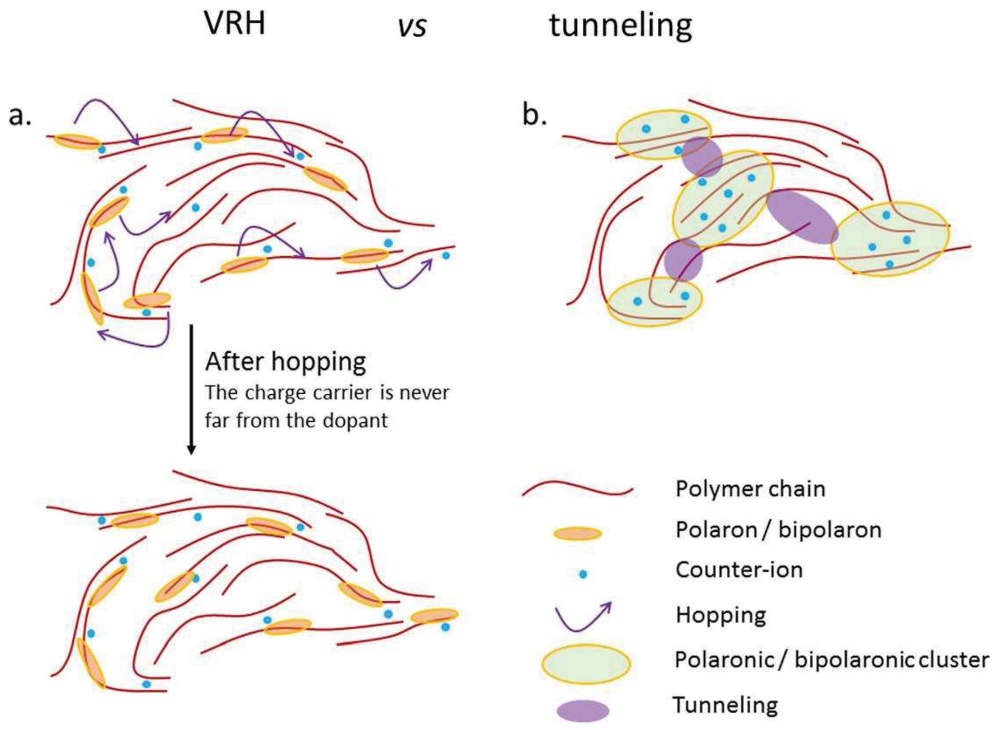

Figure I.9: Schematic representation of Mott's VRH model and Sheng's tunneling models. Reproduced from [51].

1.3. SOME STRATEGIES TO IMPROVE THE TE PROPERTIES

The strategies for improving the TE properties of organic semiconductor materials are numerous. This section does not aim to give an exhaustive account of the different methods and mechanisms of TE properties improvement, there are many excellent reviews on the subject.[39,52–56] However, I have chosen to discuss some key approaches for improving the electrical conductivity of polymers in thin films (such as the effects of the nature of the dopant, the doping process, and the structural changes). This part will focus on p-type semiconducting polymers since it is the main subject of this thesis.

1.3.1. EFFECT OF THE NATURE OF THE DOPANT ON THE ELECTRICAL CONDUCTIVITY

As discussed earlier, an ion pair composed of the donor and the acceptor molecule is formed when chemical doping is performed. The transfer of an electron from the HOMO of the conjugated polymer to the LUMO of the acceptor results in p-type doping. To facilitate p-type doping efficiency, the LUMO of dopant molecules should have a lower energetic value than the HOMO of the semiconducting polymer. Moreover, a slight difference between the HOMO and LUMO levels involved is required to enhance the charge transfer. Consequently, the choice of both dopant and hosting molecule should be chosen accordingly. Following the historical doping of polyacetylene, p-type doping of conjugated polymers (such as polycarbazoles, polyfluorenes, and polythiophenes) has been performed with a number of oxidizing agents, including $FeCl_3$, $NOPF_6$, and F_4TCNQ.

The first evidence of a significant increase in electrical conductivity was obtained by Yim and colleagues.[57] They investigated the influence of the HOMO level on the doping strength when treating the conjugated polymer and the dopant from the same solution. As discussed earlier, doping efficiency is directly related to the compatibility of the energy levels of the polymer and the dopant. Amongst the polymers studied, the highest conductivity of 10^{-1} S/cm was obtained with poly(3-hexylthiophene) (P3HT) doped with tetrafluoro tetracyano-quinodimethane (F_4TCNQ) due to a suitable mismatch between the HOMO and LUMO of P3HT and F_4TCNT, respectively. Then, a wide range of polymer/dopant couples were reported in the literature. Using a ferric salt of triflimide anions ($TFSI^-$) as an oxidizing agent, Zhang et al. demonstrated obtaining of high electrical conductivity of almost 100 S/cm correlating with a high carrier concentration of around $1.6.10^{21}$ cm^{-3} upon doping of P3HT films.[58] More recently, Glaudell et al. investigated the solution doping of several polythiophenes with F4TCNQ and (tridecafluoro-1,1,2,2- tetrahydrooctyl)trichlorosilane (FTS).[59] Promising values at 3 S/cm were obtained by doping poly(2,5-bis(3-tetradecylthiophen-2-yl)thieno[3,2-b]thiophene) (PBTTT), which exhibits slightly lower HOMO with F4TCNQ. More recently, high charge transport properties were reached by the use of innovative dopants such as magic blue[60] or molybdenum derivatives.[61]

1.3.2. EFFECT OF DOPING PROCESS ON ELECTRICAL CONDUCTIVITY

The method of incorporating the dopants into the hosting polymer plays an important role in determining the effectiveness of charge transfer doping. The simplest and most commonly used method is the solution-mixed doping, in which the dopant in the appropriate ratio is poured in a polymer solution before producing a doped polymer film. Despite its simplicity, this method leads to critical defects in the film homogeneity. Aggregates are often formed in solution as the doping concentration increases. The charge transfer between the polymer and the dopant forms charge transfer complexes and since the solubility of the charge species differs from that of the neutral polymer, and dopant, they tend to precipitate. This ultimately leads to a reduction in film quality or phase separation. Therefore, films prepared by solution doping with high concentrations of dopants often take the form of mixed film morphology with low carrier mobility. One solution to avoid aggregates and poor film morphology is the use of modified polythiophene such as $p(g_42T\text{-}T)$ reported by Kroon et al.[62] The glycol side chains of the polymer allow a better solubility of the polymer and the use of a wider range of solvent. Hence, they achieved solution-mixed doping up to 10%mol F_4TCNQ without the formation of precipitates allowing the preparation of thin films. Overall, they succeeded in increasing the charge carriers' density leading to high electrical conductivity up to 100 S/cm. In a more general way, a common solution to avoid the issues mentioned above is the sequential post film doping. The polymer film is realized before doping. Then, contact between the precast layer and the dopant is typically established by dipping, solution casting or vapor phase doping. One of the first examples was demonstrated by Crispin and coworkers. The sequential dipping of P3HT film into a $NOPF_6^-$ solution led to the improvement of the film's electrical conductivity from 10^{-6} S/cm to 1 S/cm.[63] Recently, the common method that has emerged is vapor phase doping (or solid-state diffusion doping). In this case, the polymer is pre-casted on a substrate, then the film is sequentially exposed to vapors of the dopant. Although, the question to which extent the dopant would be able to penetrate a bulk material still remains. This method led to high electrical conductivity of 250 S/cm for F_4TCNQ vapor-doped PBTTT films reported by Kang et al.[64] An electrical conductivity of 1000 S/cm was achieved via FTS vapor exposition of PBTTT thin films.[65] As a comparison the same thin films were immersed in 4-ethyl-benzene sulfonic acid (EBSA). They showed that solution-mixed doping with EBSA induced more crystalline disorder in the polymer structure. Patel et al.[65,66] and other reports[67,68] attribute the higher electrical conductivities obtained by vapor-phase doping to the maintained crystalline order of the film after doping. As discussed before, the macro- and microstructure of conjugated polymers are of high importance for efficient charge transfer.

1.3.3. EFFECT OF STRUCTURAL ENHANCEMENT ON ELECTRICAL CONDUCTIVITY

As mentioned in section I.1.2, morphology is a major aspect to consider when searching for strategies to enhance the electrical conductivity of semiconducting polymers. Macromolecular engineering allowed the design of several high-performance p-type materials of highly crystalline order. For example, PBTTT was widely used in the literature due to its highly ordered morphology, comparable to liquid-crystal arrangement.[69] More recently, Park et al. reported a five-times enhanced charge carriers' mobility with polypyrroles (PPy) modified films as compared to regular PPy. The films were ionically interconnected by various diacid linkers resulting in a decreased π-stacking distance and enhanced crystalline morphology exhibiting an electrical conductivity up to ~ 78 S/cm (as compared with ~ 6 S/cm for the regular PPy films).[70]

As discussed above, doping has been reported to induce morphological modifications of polymer films. For organic semiconductors, the optimal doping concentration can be up to several tens of mole percent. Insertion of such a large dopant fraction often goes together with a change in the microstructure of the polymer film when the dopant molecule is inserted between the host molecules.[59] By comparing the doping efficiency of PBTTT by F_nTCNQ (n=2 or 4) in the vapor or solution phase, Patel et al. showed the key role of morphology modifications on the charge transport properties.[66] Both doping methods yield roughly the same increase in charge carrier concentration, and local order is almost not impacted. However, in the case of vapor-doped PBTTT films, the long-range correlation lengths of conjugated backbones tend to be maintained, favoring charge transport. Lim et al. showed the contribution of form factor, long-range, and connectivity of conjugated polymer crystallites in thin films through the vapor-phase doping of P3HT with F_4TCNQ.[71] Upon doping, distance along the side chains and π-π stacking distance decrease suggesting the insertion of the dopant into the side chains of the polymer as the thiophene rings get closer. Moreover, they demonstrated by Resonant Soft X-ray Scattering that vapor-doped films have long fibrils of crystalline P3HT with great connectivity. Overall, the increase in both carrier density and mobility led to the high electrical conductivity of around 100 S/cm.

A combination of precise macromolecular engineering, doping, and polymer chain alignment can exhibit even higher charge transport properties. Durand et al. achieved very high electrical conductivity of 5.10^4 S/cm through “incremental concentration doping”[72] of a modified C_{12}-PBTTT by hexafluoro-tetracyanonaphthoquinodimethane (F_6TCNNQ).[73] The semiconducting polymer’s alkyl side chains were replaced by n-C_7OC_4 side chains. This modification improves the structural order of the PBTTT backbones and its thermo-mechanical stability, allowing the use of high-temperature rubbing to further align the polymer chains. Consequently, the modified PBTTT doped films exhibit an electrical conductivity improved by more than one order of magnitude when compared to regular C_{12}-PBTTT films. Using the same strategy of precise doping and chain alignment, the historical electrical conductivity record of 10^5 S/cm for I_2 doped polyacetylene demonstrated by Nogami et al.[74] was even reached by Vijayakumar and coworkers.[75] The very high electrical conductivity beyond 10^5 S/cm was achieved via high-temperature rubbing orientation of PBTTT films doped by $FeCl_3$. As discussed earlier, large domains of a high order can increase charge carrier mobility and ease dopants’ introduction. Here, the doping process improved the crystallinity of PBTTT chains by reducing the π-stacking distance as the dopant intercalates between the alkyl side chains of the polymer. The liquid-crystal-like morphology of the ordered PBTTT chains was highlighted and highly ordered domains of π-stacked backbones separated by amorphous alkyl side chains domains were observed. Such orientation induces anisotropic charge carrier transport with an anisotropic ratio of parallel over perpendicular electrical conductivity of almost 100. This work also discusses the differences in charge transport mechanisms, highlighting better TE properties along the chain direction. Overall, metal-like electrical charge transport properties can be achieved via precise doping and crystallinity control. However, such an increase in electrical conductivity must induce modifications in the thermal transport which is rarely discussed in the literature

1.3.4. INCREASING THE SEEBECK COEFFICIENT

Despite great advances in the understanding and control of electrical conductivity, increasing the power factor is not straightforward. The low Seebeck coefficient of semiconducting polymers is still a limiting factor in reaching ZT values close to inorganic records. From an energetic point of view, the Seebeck coefficient can be defined as the average entropy per charge carrier weighted by the contribution of the carrier to conduction. That means that the Seebeck coefficient is very sensitive to any disorder in the system and that only carriers of sufficient energy (i.e., carriers of energy close to the Fermi level E_F) contribute to the conduction. To go further in detail, because of the energetic disorder and charge localization in semiconducting polymers the HOMO and LUMO levels should be considered as delocalized states band described by the density of states (DOS).[76] The distribution of these states is assumed to be a Gaussian in most semiconducting polymers.[77] Even though electrical conductivity and Seebeck coefficient have different coupling behavior due to their complex dependence on charge carriers, they are directly related. Actually, a power law dependence of the Seebeck coefficient on the electrical conductivity was shown by Glaudell et al. for several polythiophenes derivatives/p-type dopants couples.[59] As measuring carrier concentration in semiconducting polymer films can be quite challenging, they compared the evolution of the Seebeck coefficient and power factor to the electrical conductivity in the range 10^{-5} S/cm to 10^{3} S/cm upon doping. Vapor-phase doping of several polythiophenes derivatives (P3HT, PBTTT and P2TDC$_{17}$-FT4) with F_4TCNQ and FTS highlighted the empirical power law of $S \sim \sigma^{-1/4}$. Apart from being a great tool to predict the potential high PF of a polymer, these results (correlated with other data from the literature) demonstrate the limits of the improvement of the charge transport properties of such polymer for TE application. However, other strategies using inorganic dopants such as Molybdenum derivative exhibited higher Seebeck with P3HT films.[78]

Recent progress in the manipulation of DOS demonstrated promising results of very high Seebeck coefficients above 1000 µV/K. Typically, various p-type polymers with different HOMO and LUMO levels are blended in order to shift the so-called transport energy E_{tr} to maximize charge and energy transport via hopping.[79–81] This new material engineering is a very promising tool to overcome the interdependency of S and σ and achieve high Seebeck coefficient while maintaining electrical conductivity in the range of ~1 S/cm leading to high power factors.

Even though Glaudell et al. demonstrated this empirical power law for a large number of polythiophene derivatives/p-type dopants, PEDOT derivatives do not follow this trend, demonstrating atypical charge transport properties,[51] very promising for TE applications.

1.4. CASE OF PEDOT DERIVATIVES

Being the most extensively studied conducting polymer, poly(3,4-ethylenedioxythiophene) (PEDOT) has been used in thin and thick films for the past decade in fields such as organic and perovskite solar cells,[82,83] sensors,[84,85] actuators,[86] supercapacitors,[87] or thermoelectrics.[88,89] Although this polymer can be prepared with different counter anions (such as tosylate), we will focus on its more common form doped with poly(styrene sulfonate) (PSS). In this case, PEDOT is a p-type polymer obtained by oxidative polymerization of ethylenedioxythiophene (EDOT) monomer in presence of PSS polyanions, its molecular structure is depicted in Figure I.10.A.[90] Thanks to this counterion, PEDOT: PSS is water processable and quite stable in air. More interestingly, depending on the processing conditions and batch grade, electrical conductivity of at least 1000 S/cm in thin films can be obtained with current records above 6000 S/cm.[91–93] Several commercial aqueous dispersion grades are available and their properties show batch-to-batch variation.[94] Along all this thesis, only one grade of PEDOT: PSS commercial dispersion has been used (Clevios PH1000 from Heraeus).[94] The aqueous dispersion is composed of the two charged polymers. PEDOT is a semi-conducting polymer while PSS is an insulator. However, it has a major role in this blend as a counterion for PEDOT and also a surfactant allowing dispersion of PEDOT in water. Several models report that PEDOT: PSS arranges in a micellar-like structure with the hydrophobic PEDOT-rich core at the center and the hydrophilic PSS-rich shell on the external part.[95–99] In commercial blends, PSS is present in excess (1:2.5 weight ratio PEDOT: PSS for PH1000). The excess of isolating chains can be detrimental to the transport properties of PEDOT: PSS and several studies showed the influence of the PEDOT: PSS ratio on its charge transport properties. Treatment by several polar solvents, acidic or reducing agents have been used to increase PEDOT: PSS's electrical conductivity in thin films.[92] As discussed by Ouyang et al. for another PEDOT: PSS grade, several mechanisms can induce this increase in charge transport properties: removal of the insulating PSS in excess, change in PEDOT conformation and PEDOT chain increased orientation and order.[100] The following section will focus on PEDOT: PSS films and the different strategies used to optimize their TE properties.

1.4.1. TUNING THE PEDOT: PSS RATIO TO OPTIMIZE ITS TE PERFORMANCES

Polar solvent treatment such as methanol exposition of PEDOT: PSS thin film can be used to improve its conductivity from 0.3 S/cm to over 1300 S/cm.[96] Thanks to X-ray photoelectron spectroscopy (XPS), Alemu et al. were able to reveal the change of PEDOT: PSS ratio after methanol treatment in the commercial dispersion PH1000. The S (2p) peaks of the sulfur atom in the thiophene ring of PEDOT (163-165 eV) and the sulfur atom from the sulfonate group of PSS (168 eV) can be discriminated due to their different chemical environment as shown in Figure I.10.B. Estimated from the calculation of the integral of the corresponding peaks, the molar PEDOT: PSS ratio decreased from 1:2.71 before treatment to 1:1.76 after treatment. The excess PSS chains on the external shell of the micelle are weakly interacting with PEDOT and can easily form hydrogen bonds (or be protonated in the case of acid treatment[101]) with the polar solvent favoring their solubility. Moreover, according to Alemu and coworkers, methanol induces a screening effect between the two polymers, reducing the coulombic interaction assuring integrity of the polyelectrolyte system. Thus, a phase separation is induced and the hydrophilic methanol washes part of the PSS reducing the PEDOT: PSS ratio. Likewise, Kim et al. demonstrated that other polar treatment with DMSO or ethylene glycol (EG) dipping exposition of PEDOT: PSS film led to the successful washing of the PSS layer resulting in a high electrical conductivity of around 1000 S/cm.

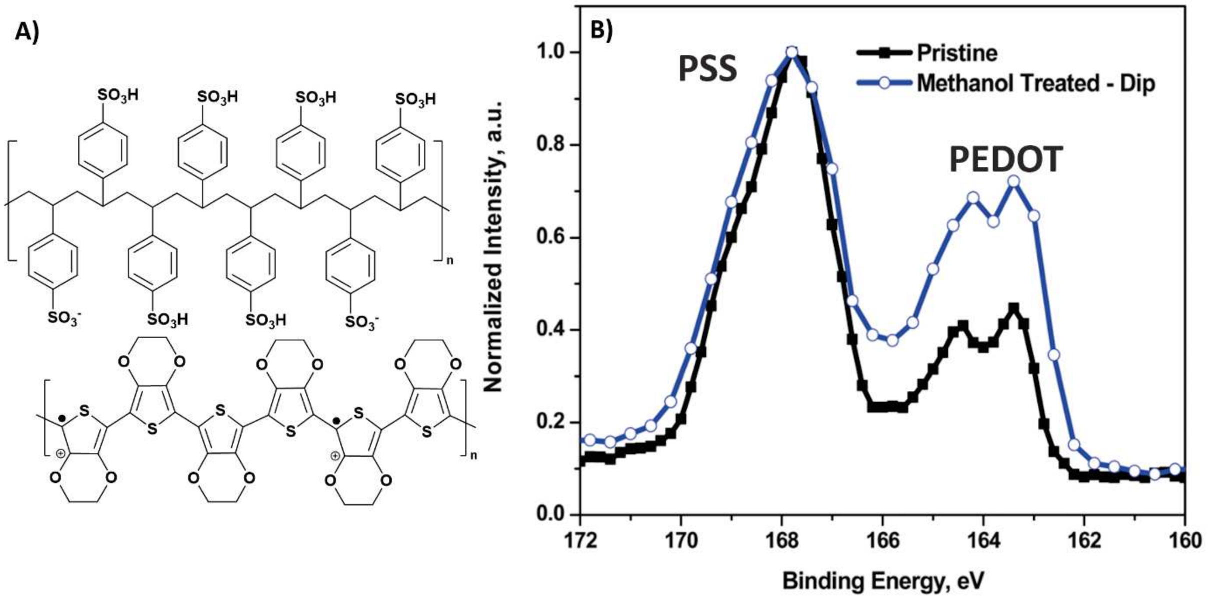

Figure I.10 A): Molecular structure of PEDOT: PSS, B) S(2P) XPS spectra of PH1000 thin film treated (in blue) and untreated (in black). PSS signature is around 168 eV and PEDOT signature is around 163 and 164 eV. Reproduced from [96].

1.4.2. CHANGING THE POLYMER CHAIN CONFORMATION TO OPTIMIZE PEDOT:PSS TE PERFORMANCES

Several types of so-called secondary doping of PEDOT were realized with strong acids such as sulfuric acid (H_2SO_4), trifluoromethanesulfonic acid (TFMSA) or tannic acid (TA). In such cases, conformational modifications of PEDOT have been observed induced by the PEDOT: PSS molecular rearrangement.[102–104] Treatment with such acid was realized either by direct mixing with the PH1000 dispersion or by immersion of thin films. In all cases, evidences of PSS removal, as discussed in the section I.1.4.1, were presented and resulted from the weakening of coulombic interaction between PEDOT and PSS in addition to the protonation of PSS into PSSH. In addition, PEDOT chain conformation changes were observed. It is well known that conjugated polymers are usually distributed in a random coil conformation favored by the benzoid conformation as shown in Figure I.11. Upon doping, polarons and bipolarons can be formed resulting in the delocalization of π-bonds. This delocalization induces more rigidity to the backbone which tends to be more linear, this is the so-called quinoid conformation. The change of chain conformation can be at the origin of a more rod-like structure. In pristine PEDOT:PSS, PEDOT is already doped, but its close arrangement with the excess of PSS prevents it from being too linear. After the removal of this excess of PSS (by acid treatment), it can be observed via Raman spectroscopy or Fourier-Transform Infrared spectroscopy (FTIR) that more quinoidal PEDOT form is present. Ali et al. and Yi et al. demonstrated important Raman shifts of the C=C and C_{α}-C_{β} symmetric and stretching characteristic bands upon acid treatment.[103,104] These shifts, also observed by FTIR,[102] are associated to the increase of the π-bond length upon conformational changes. This conformational change yields to an extended length of conjugation and can further improve the general order of PEDOT chains. Overall, a more linear and extended chain conformation, favored by the quinoid conformation of PEDOT, is beneficial for achieving high electrical conductivity.

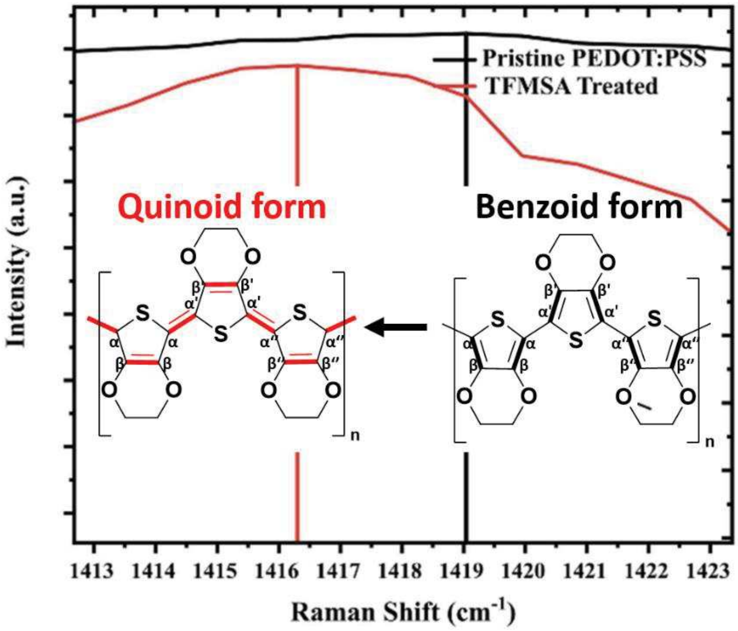

Figure I.11: Raman spectra of red shifting bands of a PEDOT: PSS film untreated (black) and treated (red) with TFMSA to illustrate change from benzoid to quinoid. Adapted from [103].

1.4.3. STRUCTURAL MODIFICATIONS TO OPTIMIZE PEDOT:PSS TE PERFORMANCES

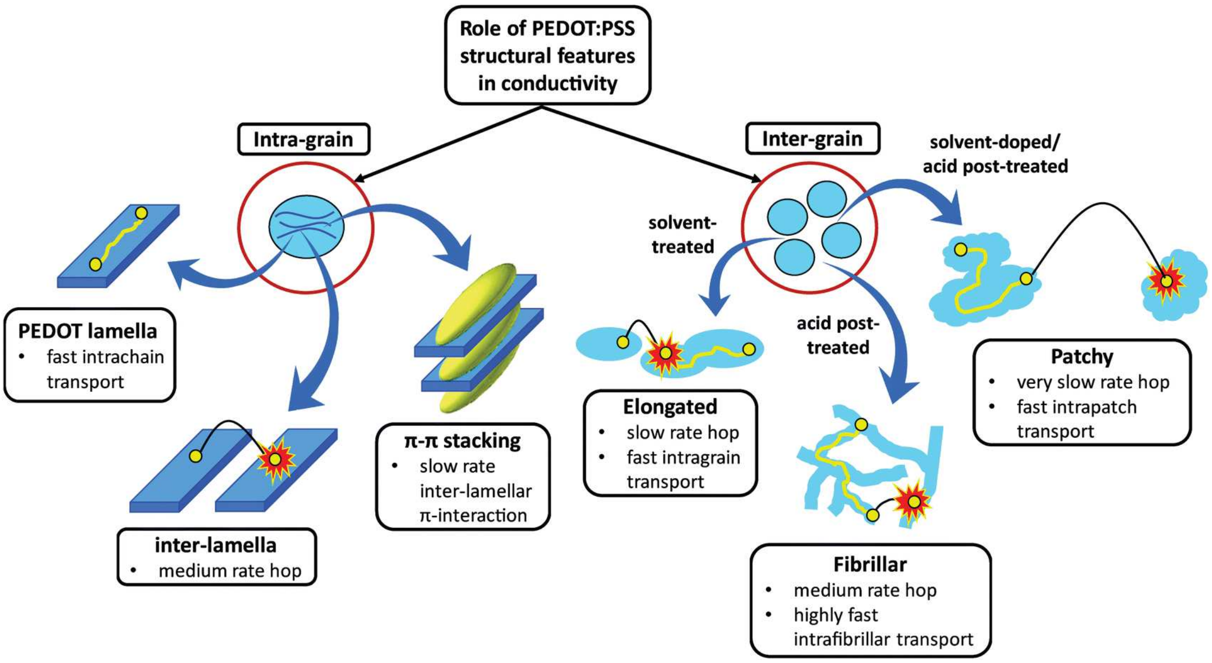

Figure I.12: Schematic of post-treatment influence on PEDOT: PSS morphology and associated inter and intra-grain charge transport mechanisms. Reproduced from [102].

As discussed earlier, one of the main factors in electrical conductivity increase upon secondary doping is the improved chain order and crystallinity. PEDOT: PSS undergoes several structural modifications at different scales upon exposition to various post-treatment agents as depicted in Figure I.12. Wei et al. exposed PEDOT: PSS films to ethylene glycol (EG), achieving high conductivity increase from 1.2 S/cm to 830 S/cm.[105] The authors attributed this charge transport improvement to the increased ordered domains' size of PEDOT: PSS upon solvent exposition. GIWAXS (Grazing-Incidence Wide Angle X-ray Diffraction) and GISAXS (Grazing-Incidence Small-Angle X-ray Scattering) patterns illustrate the improved crystallinity of the film after EG treatment. The diffraction peak at 1.85 Å^{-1} (3.4 Å) characteristic of the π-π stacking distance is sharper after EG exposure indicating an increase of the crystallite size. Moreover, on a mesoscopic scale, GISAXS patterns highlight the increased order of PEDOT: PSS nanocrystals forming a layered structure. PEDOT: PSS films processed with sulfuric acid were also reported to have an overall increased order of the crystalline.[106] Through sulfuric acid exposition of PEDOT: PSS films, Kim et al. achieved high electrical conductivity values above 3000 S/cm. The sharpness of the π-stacking characteristic diffraction peak after H_2SO_4 treatment indicates a high order in the molecular packing of PEDOT chains comparable to vapor phase deposited PEDOT. The compact structure depicted by High-Angle Annular Dark-Field Scanning Transmission Electron Microscope (HAADF-STEM) indicates the restructuring of PEDOT: PSS system into a fibrillar structure. Morphology modification induced by the use of an acid was confirmed by the work of Ali et al.[103] TFMSA was used as a superacid in order to remove more PSS than with inorganic acids. The greater PSS removal illustrated by XPS led to a strong morphology enhancement of the PEDOT: PSS system. The sharp π-stacking peak was shifted from 25.6° (3.5 Å) to 26.1° (3.4 Å) suggesting better molecular packing. Moreover, the diffraction peak attributed to the lamella stacking of PEDOT: PSS with alternate ordering chains of PEDOT and PSS is greatly reduced from 25.2 Å to 23.8 Å after TFMSA treatment. This denser packing is highlighted by High Resolution Transmission Electron Microscopy (HRTEM) showing visible crystalline regions. The high mobility induced by the crystalline order was measured by Hall effect increasing from 0.89 $cm^2/(V.s)$ to 4.72 $cm^2/(V.s)$ leading to the high electrical conductivity of 1685 S/cm. Similar results were obtained by Wang et al. using a combination of TFMSA and methanol.[107] Despite many studies on the structural arrangement of PEDOT: PSS and XRD peak attribution, no consensus has been reached to elucidate a clear structural model. PEDOT and PSS backbones were reported to be either perpendicular[106,107] or parallel[102] to each other. Yildrim et al. showed that planes of PEDOT interacting could bend over the PSS chain orthogonally to minimize their thermodynamic energy.[108] The characteristic peak at 23 Å has often been attributed differently between reports. Molecular dynamics simulations determined PEDOT and PSS planes' sizes to be ~7.5 Å and ~ 15.5 Å, respectively. Hence, Kim et al. attributed the characteristic distance of 23 Å to the alternate lamella stacking distance d_{100} of PEDOT and PSS arranging in a comb-tooth conformation.[109] Conversely, Hosseini et al. attribute this d_{100} spacing to the alternate inter-lamella stacking distance of PEDOT to PEDOT molecules.[102] Amongst the different models discussed above, the π-stacking distance attributed to around 3.4-3.6 Å is the only consistent value. Overall, many structural rearrangements have been proposed after PEDOT: PSS post-treatment as depicted in Figure I.12.

Hosseini and coworkers attempt to propose a structural model through XRD analysis of several post-treated films along with molecular dynamics simulations (see Figure I.13).[102] Hereafter, we will use this structural model as a reference for discussion. The most common characteristic distances (corresponding to XRD peaks at 4.1°, 8,1°, 11.2°, 13.8°, 18.2° and 25.5°) discussed in the literature are attributed on the structural model in Figure I.13. As suggested in other reports, PEDOT stacked along the π-π axis are distributed along the PSS chain. The distances of 22 Å (4.1°) and 11 Å (8.1°) are attributed to the first and second order of d_{100} and d_{200} spacing of the alternate inter-lamella stacking distance of PEDOT to PEDOT. PSS to PSS lamellae and PSS to PSS neighboring distances are reported to be 7.9 Å (11.2°) and 6.4 Å (13.8°) respectively. The ionic interactions of PSS and PEDOT are responsible for the rotation of PSS styrene rings toward thiophene PEDOT resulting in the d_{001} spacing of π-stacking of PSS benzene rings at 4.9 Å (18.2°). The π-π stacking of PEDOT rings is represented by the d_{010} reflection with the spacing of 3.6 Å (25.2°). Such morphology is susceptible to modification through the so-called secondary doping.

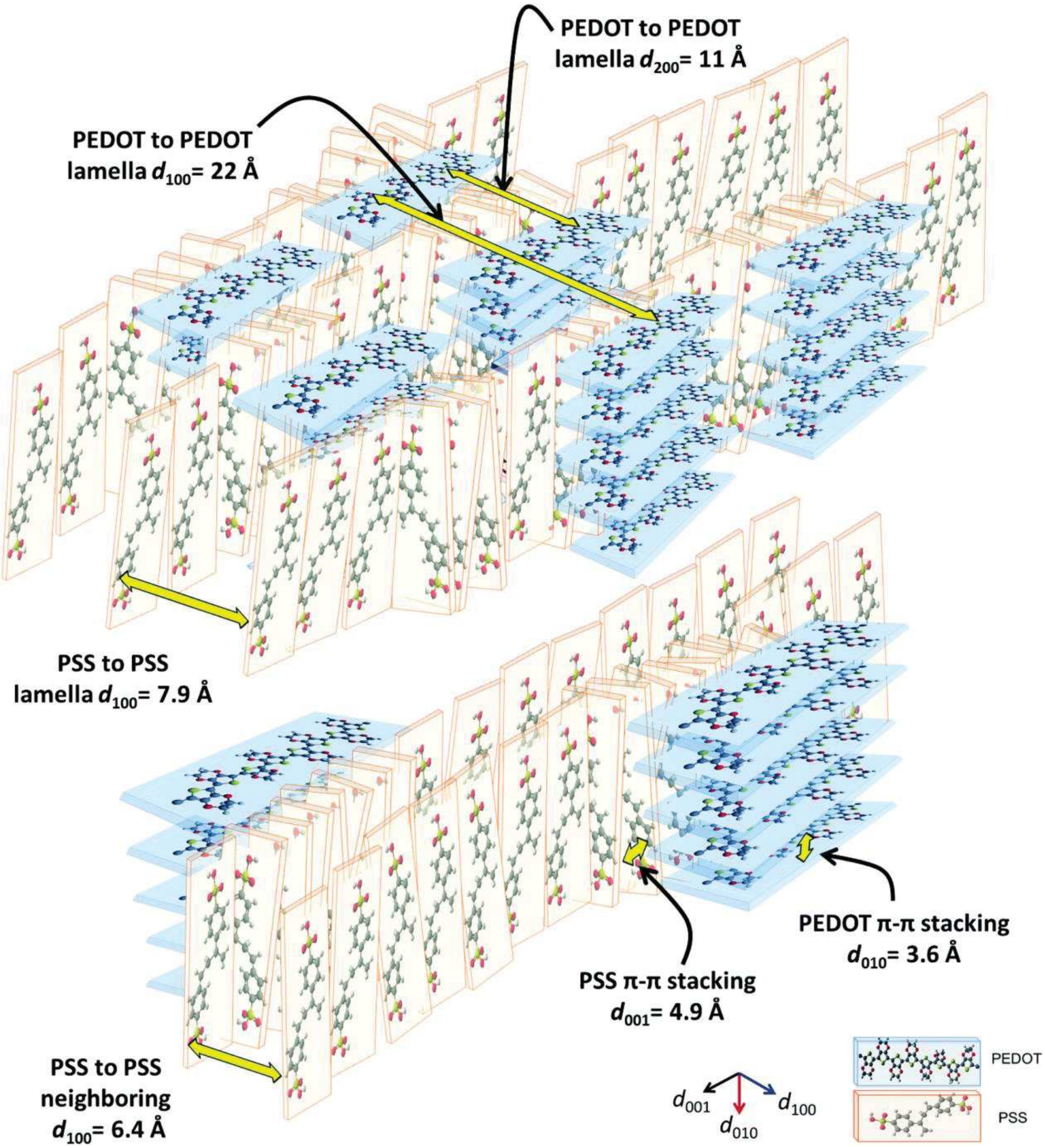

Figure I.13: Structural model schematic of semi-crystalline PEDOT: PSS. Reproduced from [102].

1.4.4. PEDOT: PSS AND THERMAL CONDUCTIVITY

The scientific community has been able to demonstrate very high power factors of a few hundreds of µW/(m.K²) for PEDOT: PSS thin films.[89,92] However, the ZT is generally only estimated and the thermal conductivity rarely discussed. Yet, thermal conductivity plays a great role in the global performances of a TE material and is surely influenced by the post-treatments discussed above. Several values of thermal conductivity were reported in the

]

literature and seem to depend on the doping state and processing of the PEDOT: PSS films. Moreover, the observation of an anisotropic thermal conductivity between in-plane and through-plane measurement is redundant. Liu et al. prepared drop-casted films of PEDOT: PSS with added DMSO to increase the electrical conductivity (ranging from 1 to around 500 S/cm depending on the DMSO concentration).[110] The thermal conductivity of such films was measured by Time-Domain Thermoreflectance (TDTR) in the in-plane and through-plane directions. For the most electrically conducting sample, thermal conductivity was highly anisotropic (with $\kappa_{\text{in-plane}}$ = 1 W/(m.K) > $\kappa_{\text{through-plane}}$ = 0.3 W/(m.K)). This difference between in- and through-plane directions was attributed to a difference in the electronic contribution to the thermal conductivity κ_{elec} (in-plane electrical conductivity happened to be larger). Similar results of anisotropic thermal conductivity were reported by Wei et al.[111] They measured in-plane and through-plane electrical conductivity and thermal diffusivity (and calculated thermal conductivity) of PEDOT: PSS EG treated films. A huge anisotropy was observed with $\kappa_{\text{in-plane}}$ = 0.84 W/(m.K) (and σ= 820 S/cm) for the in-plane measurements and $\kappa_{\text{through-plane}}$ = 0.15 W/(m.K) (and σ= 36 S/cm) for the through-plane measurements. This anisotropy was attributed to the lamellar ordering of PEDOT chains and to, the in-plane orientation of polymer chains. These results show limitations in the use of thin films for TEG. Indeed, as shown in Figure I.1.B, in-plane configuration would lead to TE properties governed by the highest in-plane thermal and electrical conductivity.

Overall it is crucial to understand the influence of each TE properties on the others to design the best material. It is pretty clear from the discussion above that σ, S and κ are interdependent. Figure I.14.A illustrates the interdependence of the TE properties. As discussed earlier, improving the power factor is delicate as σ and S are inversely related. Moreover, the thermal conductivity being proportional to σ, becomes very detrimental for the ZT value at high charge carrier concentration. Thermoelectric materials need to possess metal-like electrical charge transport properties as well as glass-like thermal insulation ability. Arises from this statement the concept of phonon-glass electron-crystal material. “Electron-crystal” comes from the fact that crystalline organic semiconductors have shown the most promising results as being able to achieve a high power factor. “Phonon glass” comes from the need to lower κ_{lattice} as much as possible. Figure I.14.B, proposed by Snyder and coworkers, illustrates the impact of reducing the lattice component to the thermal conductivity to an electron-crystal system with high power factor.[112] Liu et al. demonstrated that the lattice component to the thermal conductivity seems to be independent from the electrical conductivity.[110] In other reports, is it typically assumed that $\kappa_{lattice}$ is around 0.2 W/(m.K) for dense organic semiconductors.[113] Hence, achieving high ZT above current records will need a precise design, keeping high power factor while reducing $\kappa_{lattice}$ below 0.2 W/(m.K). This being known, there is room for improvement of TE properties and particularly by phonon engineering, rarely discussed in the organic thermoelectric literature.

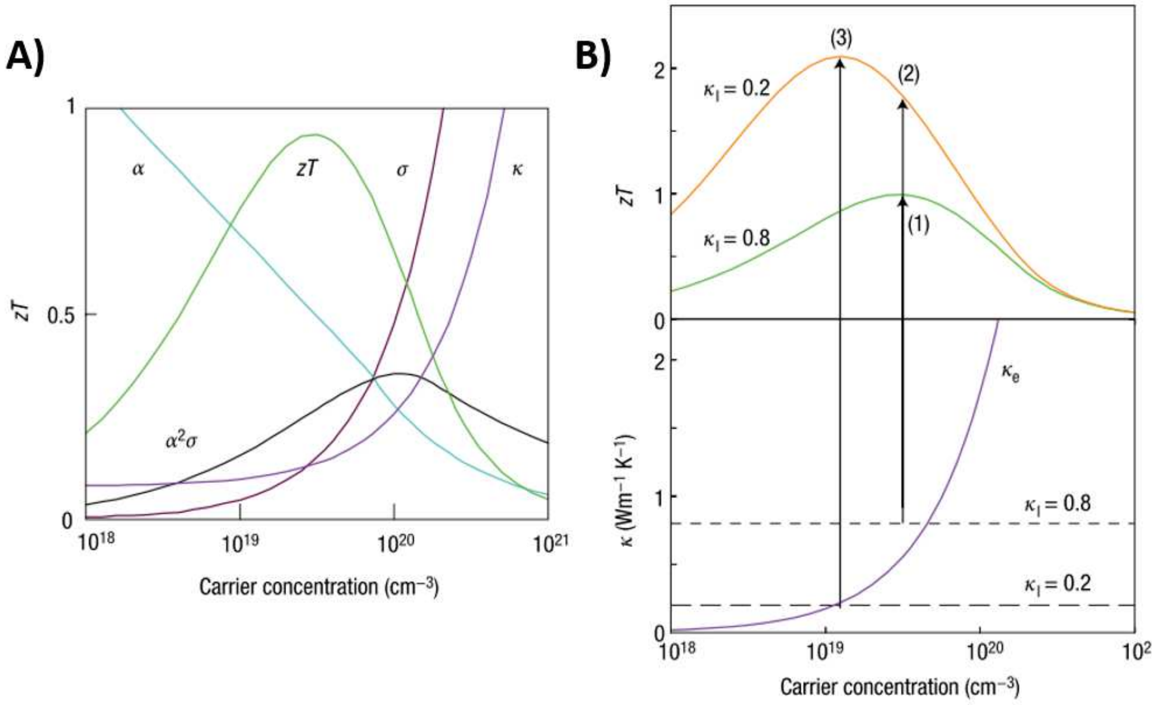

Figure I.14: A) Interdependence of σ, S and κ on the carrier concentration, B) Influence of $\kappa_{lattice}$ on an optimized ZT. Reproduced from [112].

1.5. INTEREST OF POROSITY TO REDUCE THE THERMAL CONDUCTIVITY

Inspired by the highly efficient silicon aerogels,[114] nanostructured porous polymers[115] make excellent candidates as best thermally insulating materials (κ < 0.03 W/(m.K)) with unique characteristics, such as fine internal void spaces, open-pore geometry and trapped air in the meso-/ micro-porous structure. To take the most benefit out of PCPs, one needs to understand the breakthroughs related to the thermal conductivity in porous media.

Heat transfer through an electrically insulating porous medium is carried by phonons in the material lattice. It has been conventionally considered as a combination of thermal conduction along its solid matrix (κ_s), thermal radiation across internal pores (κ_{rad}), and either thermal convection (κ_{conv}) by or conduction through gases (κ_g) filling the pores as depicted in Figure I.15.A. Thus, the total thermal conductivity ($\kappa_{lattice}$) of an electrically insulating medium is calculated by:[116]

$$\kappa_{lattice} = \kappa_s + \kappa_g + \kappa_{rad} + \kappa_{conv} \qquad (I.6)$$

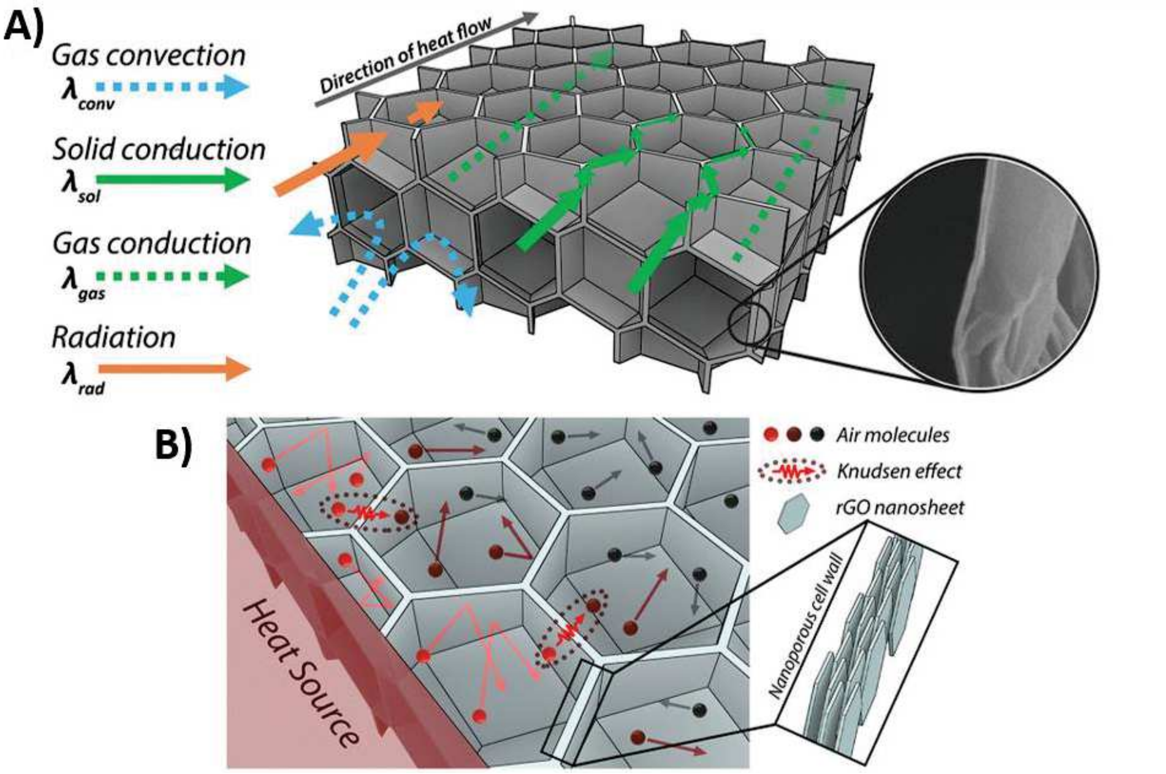

Figure I.15: A. Schematic representation of heat transfer mechanism in a porous media, B) Gas conduction mechanisms in macropores and meso/micropores (porous walls). Reproduced from [117].

Convective heat transfer requires that gas be transported across the full temperature gradient within the material. In bulk (thick) material, the contribution from convection can be disregarded when the pore sizes are sufficiently small (<1 mm).[116] The radiative thermal conductivity rises with an increase in pore size and most importantly shows a power law temperature dependence (T^3).[118] Therefore, at ambient temperature and pressure conditions, the radiation contribution is also negligible. The last two components (gas and solid thermal conductivity) are highly dependent on the porous structure.

The gas thermal conductivity as a function of the pore-size can be described as follows:

$$\kappa_g = \frac{\kappa_g^0}{1 + 2\beta Kn} \tag{I.7}$$

$$Kn = \frac{\Lambda_g}{D} \tag{I.8}$$

Where κ_g^0 is the thermal conductivity of the gas in free space, β is a coefficient depending on accommodation and adiabatic coefficients of the gas (typically β = 2 for air)[119] and Kn is the Knudsen number defined as the ratio between the mean free path of the gas molecules Λ_g (typically 70 nm for air at ambient pressure and temperature conditions) to the mean pore diameter D.[115,120] Thus, in order to minimize the gas thermal conductivity, below the one of air (25 mW/(m.K)), one must reduce the size of the pore below 70 nm. When the pore diameter is inferior to the mean free path of air (e.g., Kn > 1), the transport mode of the gas molecule is known as Knudsen diffusion.[121] In this regime, the molecule-wall interactions dominate over molecule-molecule interactions conversely with normal diffusion. Thus, scattering of phonons trapped in pores as schematized in Figure I.15.B drastically reduces the gaseous thermal conductivity component.

It has been recently demonstrated that gas-solid coupling effects can also have a significant impact of heat transfer and contribute to the total thermal conductivity. The coupling component depends on the solid phase structure and the pore size.[122] The theoretical models are based on the assumption of spherical particles in the solid backbone which cannot fit with the structure of most porous conducting polymers. Too little is known at the moment to consider the contribution of this coupling effect, although it should not be ignored.

Finally, the solid thermal conductivity (κ_s) can be calculated as follows:

$$\kappa_s = \kappa_0 \frac{\rho\nu}{\rho_0\nu_0} \tag{I.9}$$

where κ_0 is the thermal conductivity of the solid backbone, ρ and ρ_0 are respectively the density of the bulk porous material and of the solid backbone, ν and ν_0, respectively the sound velocity in the bulk porous material and in the solid backbone. According to the kinetic theory, κ_0, in its simplest form, is given by the Debye formula:

$$\kappa_0 = \frac{1}{3} C_v v \Lambda_{phonons} \qquad (I.10)$$

where C_v is the lattice-specific heat at constant volume, v is the group velocity of phonons (the velocity of sound) and $\Lambda_{phonons}$ the phonons mean free path. As seen from equations 9 and 10, the solid contribution to the thermal conductivity can be reduced by minimizing the density of the bulk porous material and the phonon transport. A low bulk density is necessary to maintain a low solid thermal conductivity.[123] The propagation of phonons on the polymer chains can be hindered by scattering events such as those at boundaries (chain ends), interfaces (amorphous-crystalline domain boundaries, pores), or between two adjacent chains (intermolecular scattering).[124] As such, micro-/meso-porosity constitutes a major impediment for phonon transport as holes/pores can scatter phonons, in particular at solid-gas interfaces. The scattering and loss in energy are even greater if the pore dimension is of the order of magnitude of the mean free path of a phonon.

In the case of electrically conducting material, one also needs to consider an electronic contribution (κ_{el}) to the total thermal conductivity according to:

$$\kappa = \kappa_{elec} + \kappa_{lattice} \qquad (I.11)$$

The electronic contribution corresponds to the heat carried by the electrical charges when they delocalize and can be described, in general, by the Wiedemann-Franz law (WFL):

$$\kappa_{elec} = \sigma L T \qquad (I.12)$$

where T is the temperature in Kelvin, σ is the electrical conductivity in S/m and L is the Lorenz number. The Lorenz value is often taken at the Sommerfeld value.[125] Although it has been demonstrated by Scheuenemann et al. that various values of L can be found depending on the energetic disorder and DOS of the material, one can still consider that $\kappa_{elec} \propto \sigma$.[126] Since the electronic contribution κ_{el} is proportional to σ, it cannot be tuned to optimize ZT. However, as discussed previously, decreasing the lattice contribution can be of interest to reach low total κ values independently of electrical conductivity. Actually, Scheuenemann et al.[126] demonstrated that reaching ZT value beyond 1 with energetically ordered organic thermoelectrics would require to decrease $\kappa_{lattice}$ below 0.2 W/(m.K). Thus, one strategy would be to induce porosity in conducting polymers to reduce the lattice component to the thermal conductivity. According to the previous discussion, the ideal PCP structure to reach higher ZT values would be a very low-density material with pore size below the mean free path of air.

Measuring thermal conductivity of organic materials is not straightforward. Many different experimental techniques can give access to the thermal properties of a material. They are distinguished according to the heat conduction conditions which are considered (i.e., at steady state or transient state). One can also use time-domain or frequency-domain methods such as the laser flash, transient plane source or 3ω-methods. However special attention should be paid when applying one or the other technique since the measurement accuracy and reliability are significantly affected by the sample characteristics (e.g., size, morphology, mechanical, thermal and optical properties). A suitable method should also be selected according to the temperature range of the measurements and the range of thermal conductivity of the materials. An excellent review by Wang et al. reports on the operating principles, merits and limitation of the different techniques available to measure the thermal conductivity of organic TE materials.[127] Only a few of them can be applied to porous materials characterizations, the most popular being the transient plane source method despite the fact that it does not allow directional measurement of the thermal conductivity.

Because of the inherent experimental limitations and the lack of theoretical models on heat transport in porous conducting organic materials, the absolute values of thermal conductivity found in the literature for PCP must be taken with precautions. Crosschecking the results by different techniques is highly desirable for ensuring credibility.

1.6. IDEAL MATERIAL SPECIFICATIONS

Overall, the design of a novel architecture for TE materials has precise specifications. As mentioned earlier, the ideal TE material is a phonon-glass electron-crystal (PGEC), meaning that it should have thermal insulation glass-like properties as well as very high charge transport properties. Thus, one needs to focus on increasing the power factor via a precise control of the doping level and charge mobility of the organic TE material. Moreover, chain orientation and crystalline order must be enhanced to facilitate charge carriers transport. On the other hand, the thermal conductivity of such material increases due to the higher electrical conductivity, being detrimental for the ZT. Yet, decreasing the lattice contribution to the thermal conductivity without changing the electrical transport properties is theoretically feasible leading to potentially higher ZT than reported before in the literature.

As discussed by Yee et al.,[128] the “bigger picture” should be considered concerning such materials for practical applications. Indeed, optimizing ZT is a primary concern but other parameters should be respected to define a TE material’s interest. In the model described by Yee and coworkers, the overall TEG cost over power generation is discussed. In a thermoelectric generator, some component’s costs such as ceramic plate or heat exchangers cannot be reduced. Thus, the only parameters one can play with are the TE efficiency (ZT) and the material’s cost. Leblanc et al. estimated the $/W of several materials, providing evidence on the importance of the material’s volumetric cost and manufacturing cost on its interest in practical applications.[129] Hence, porous materials are very promising candidates to reach low-cost production with a small amount of material. Moreover, their bulk size makes possible the fabrication of simple vertical TEGs.

This strategy has already been applied for TE applications and we will discuss hereafter the state-of-the-art on porous organic TE materials.

2. ELABORATION OF CONDUCTING POROUS MATERIALS

The use of bulk porous conducting polymers (PCPs) is particularly appealing for both the possible tailoring of thermal conductivity via phonon engineering and the material integration into a vertical TEG. We published a review article on this topic aiming to discuss the interest of PCPs in particular for thermoelectricity, the following part is adapted from this article.[130] The concept of assembling nanostructures into macroscopic 3D polymer architectures has been previously developed for applications such as separating membranes,[131] thermal insulators,[115] or support for catalysis.[132,133] Such technologies have consequently begun to attract attention over recent years in the context of energy harvesting. Using conducting polymers to make such porous 3D architectures is therefore of interest to reach low κ while maintaining a reasonably high PF for TE application. In this part, we will only focus on porous materials for which the matrix is conducting.

2.1. DIFFERENT RANGES OF POROSITIES

Many types of PCPs exist in the literature with various pore sizes or network specificities. Unfortunately, various terminologies have been used and could lead to ambiguous understanding of the material's features. First, we will briefly introduce the different classes of PCPs and their IUPAC recommended nomenclature.[134]

As depicted in Figure I.16, porous materials can be described according to their pore's sizes. Polymeric material with pore sizes not exceeding 2 nm should be classified as microporous polymers. Mesoporous polymers have intermediate pore sizes in the range of 2-50 nm. Macroporous polymers have pore sizes larger than 50 nm. Within those classes of porous polymers, the main types of PCPs used for organic electronic applications are presented below.[135]

In order to maintain inner cavities, rigid polymer networks must be built up to prevent the collapse of polymer chains into a nonporous dense state. One of the key strategies for this purpose is the use of rigid building units (conjugated units) fixed either with strong covalent bonds (for microporous polymers) or with coordination bonds (for covalent organic framework). Another strategy is to form a coherent network of connected polymer objects (fibers/ aggregates/colloids/…) through a liquid-solid phase transition, providing, after solvent evaporation, dried porous material.

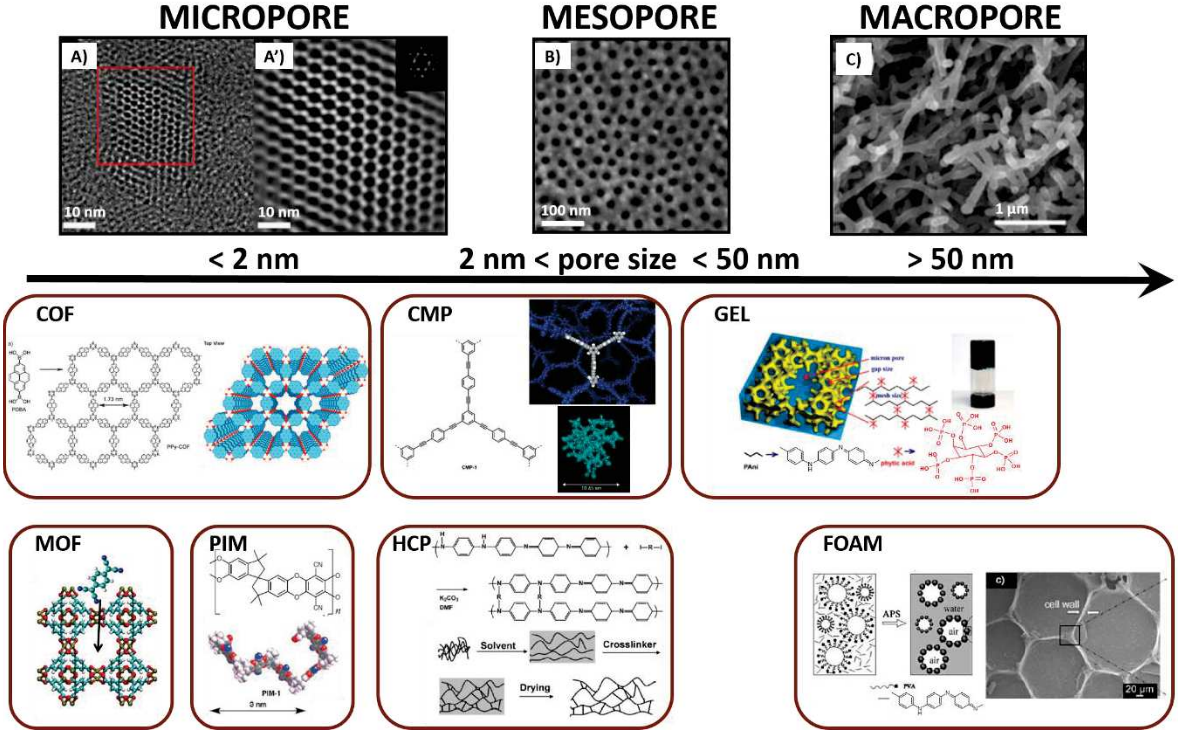

Figure I.16: Illustration of the diverse range of pore sizes that can be found in PCPs: A-A') High Resolution and Fourier-filtered images of COF1, respectively (reproduced from [136]) ; B) SEM image of 2D Graphene Oxide based mesoporous polypyrrole nanosheets (reproduced from [137]) ; C) SEM image of nanostructured polypyrrole hydrogel with CuPcTs as dopant (reproduced from [138]); and illustrations of the structure of different types of porous materials such as covalent organic framework (COF);[139] conjugated microporous polymer (CMP);[140] gel;[141] metal-organic framework (MOF);[142] polymers of intrinsic microporosity (PIM);[131] hypercrosslinked polymer (HCP);[143] and foam.[144]

2.2. MICROPOROUS STRUCTURES

2.2.1. COVALENT ORGANIC FRAMEWORKS (COFS) AND METAL ORGANIC FRAMEWORKS (MOFS)

Covalent Organic Frameworks (COFs) are purely organic coordination polymers with an open framework extending in two or three dimensions. COFs are synthesized using dynamic covalent chemistry, taking advantage of reversible bond formations. Due to the richness of the organic chemistry toolbox, an endless number of vertices and linkers can be used to construct a plethora of frameworks with different pore shapes (hexagonal, tetragonal, rhombic, and trigonal) and different pore sizes (typically 1-5 nm) as illustrated for a hexagonal structure in Figure I.16. Unlike the other PCPs described hereafter, this synthesis strategy allows a rational pore size engineering at a molecular level and a fine-tuned control over the topology of the structure, providing crystalline frameworks. Bulk COF synthesis produces insoluble powders that are difficult to process due to the highly crystalline nature of the framework. However, different synthetic protocols such as liquid-liquid interface synthesis and solvent-mediated exfoliation are being developed,[145–147] which provide means for thin film formation and a better control of the microstructure over different length scales. COFs are emerging as an important class of porous organic materials with interesting and tunable properties for a variety of applications such as gas separation and catalysis.[145] Semiconducting COFs have been reported as early as 2008, but the implementation into organic electronic devices is still in its infancy.[148,149]

COFs should not be confused with **Metal Organic Frameworks** (MOFs). MOFs are inorganic–organic hybrid materials comprised of single metal ions or polynuclear metal clusters linked by organic ligands principally through coordination bonds (see Figure I.17). Due to the strength of these coordination bonds, MOFs are geometrically and crystallographically well-defined framework structures. MOFs are also known as porous coordination polymers.

The encouraging thermoelectric performances of framework materials result from a high electrical conductivity combined with a very low thermal conductivity. The latter characteristic is mostly linked with a very low lattice thermal conductivity contribution: the phonons are unable to propagate across the vacant pores and there is a high degree of phonon scattering.[150]

Various approaches have been used to increase the low electrical conductivity of MOFs, often due to their low π-orbital overlap in the organic linker groups. Charge transport can be improved by designing MOFs with specific metal ions and linkers to promote the metal-ligand charge transfer. Covalent interaction of aromatic groups with the metal ions can improve charge delocalization along a specific direction in the network and enhanced electrical conductivity. Thiophenoxide linkages,[151] redox-active linkers,[152] and Fe-triazolate frameworks[153] demonstrated promising results and these strategies led to MOFs breakthrough electrical conductivity of 10^1 S/cm.[154] Sun et al. took advantage of the low thermal conductivity of MOFs to design a new type of n-type TE material with $Ni_3(HITP)_2$ (see Figure I.17.D).[150] The graphite-like material with a honeycomb porous structure was processed as pellets with a hydraulic press. Moreover, it exhibited high electrical conductivity of around 60 S/cm at ambient temperature. Its low thermal conductivity of 0.2 W/(m.K) is attributed to phonon scattering due to the small (1.5 nm) pores. Overall, the material demonstrated promising result with ZT of 1.19 x 10^{-3} at 298 K under vacuum.

By analogy with semi-conducting polymers, another strategy to improve the electrical conductivity of MOFs is the introduction of guest molecules into the framework. Redox-active molecules can bridge metal centers, creating a new conducting path for charge carriers. TCNQ introduction to the $Cu_3(BTC)_2$ framework has shown an improved electrical conductivity up to 0.07 S/cm.[142] Moreover, TCNQ@$Cu_3(BTC)_2$ (see Figure I.17.E films were processed and their TE properties were measured by Erickson and coworkers.[155] Electrical conductivity up to 5.10^{-3} S/cm and large positive Seebeck coefficient >300µV/K were reported upon TCNQ infiltration and were attributed to the Fermi level in $Cu_3(BTC)_2$ getting closer to the valence band. The thermal conductivity of 0.27 W/(m.K) was determined by TDTR measurements and is ascribed to the phonon scattering and grain boundaries in the MOF pellets. Finally, they obtained a ZT of ~ 8 x 10^{-5} at 298K, validating the potential use of such material for TE application.

Overall, much work has been devoted to the thermoelectric properties of metal-organic frameworks (MOFs). By contrast, their purely organic counterparts, covalent organic frameworks (COFs), have only recently reached similar promising results as active materials for energy harvesting.[156,157] Electrical charge transport properties of COFs are often excellent (mobility exceeding 1 $cm^2 V^{-1} s^{-1}$), but these values are generally derived from time-resolved microwave conductivity (TRMC) measurements.[158,159] Actually, this technique measures the mobility within the nanometer regime and thus tends to overestimate the macroscopic mobility by disregarding domain boundary and electrode contact effects. This ambiguity highlights the challenge of transferring the microscopic transport properties to the macroscopic regime. It also explains why investigations of COFs for thermoelectric applications have so far mainly been based on theoretical studies.

The low electrical conductivity of organic semiconductors necessitates doping as a means to significantly increase the charge carrier concentration and thus the conductivity. By analogy to MOFs, a few studies have outlined similar scenarios for semiconducting organic frameworks. Jiang and coworkers used the fully π-conjugated framework sp^{2}c-COF (see Figure I.17.A constructed from all sp^2-hybridised carbons to investigate the impact of doping on electrical properties.[160] For a so-called AA-stacking structure with tightly stacked layers (3.58 Å interlayer spacing) of ordered pyrene columnar arrays and 1D pores, the electrical conductivity increased by twelve orders of magnitude upon exposure to iodine vapor. The doped sample had ohmic conduction and a conductivity of 7.1×10^{-4} S/cm, compared to the much lower conductivity of 6.1×10^{-16} S/cm reported for the pristine sample. Further computational studies of this system support a p-type doping mechanism. Triiodides are formed and occupy the 1D pores. They contribute to a relatively high anion conductivity, on par with the measured electrical conductivity.[161] The pristine sp^{2}c-COF is predicted to have low electron and hole mobility owing to flat electronic bands near the Fermi level, but p-doping leads to a much enhanced predicted hole mobility of 86 cm^2 V^{-1} s^{-1}. Using a similar doping protocol with iodine vapor, a ZnPc-based COF (see Figure I.17.B) showed 1000-fold conductivity enhancement upon doping ($\sigma = 10^{-4}$ S/cm).[162] Interestingly, Hall effect measurements revealed an increased hole mobility of 22 cm^2 V^{-1} s^{-1} which was ascribed to a reduction of detrimental scattering processes upon doping.

Bein and coworkers took a slightly different approach. They created frameworks with a high electron-rich and thus easily oxidizable Wurster-type compound as vertices and employed not only iodine as p-type dopants but also antimony pentachloride and F$_4$TCNQ.[163] F$_4$TCNQ-doped material afforded superior electrical conductivity. Remarkably, with the use of an optimized benzodithiophene linker, the electrical conductivity approached 4×10^{-2} S/cm.

In 2017, Wang and colleagues used a fluorene-based imine-linked COF (FL-COF1, see Figure I.17.C to carry out the first thermoelectric characterization of a purely organic framework material.[164] Limited by a moderate electrical conductivity upon doping with iodine ($\approx 10^{-4}$ S/cm), a power factor of 0.063 µW m^{-1} K^{-2} at room temperature was obtained due to a high Seebeck coefficient of 2450 µV K^{-1}. The stability and robustness of the framework was evidenced by retained thermoelectric properties after one-month storage under ambient conditions. The framework also withstands de-doping and subsequent re-doping without a significant drop in thermoelectric performance. With the quite low electrical conductivity reported for COFs compared to other PCPs described hereafter, there is clearly significant room for improvement as more organic framework materials will be brought forward for detailed thermoelectric studies. Moreover, the potential interest of COFs and MOFs for low thermal conductivity is almost never discussed in the literature due to the lack of adapted method to measure it.

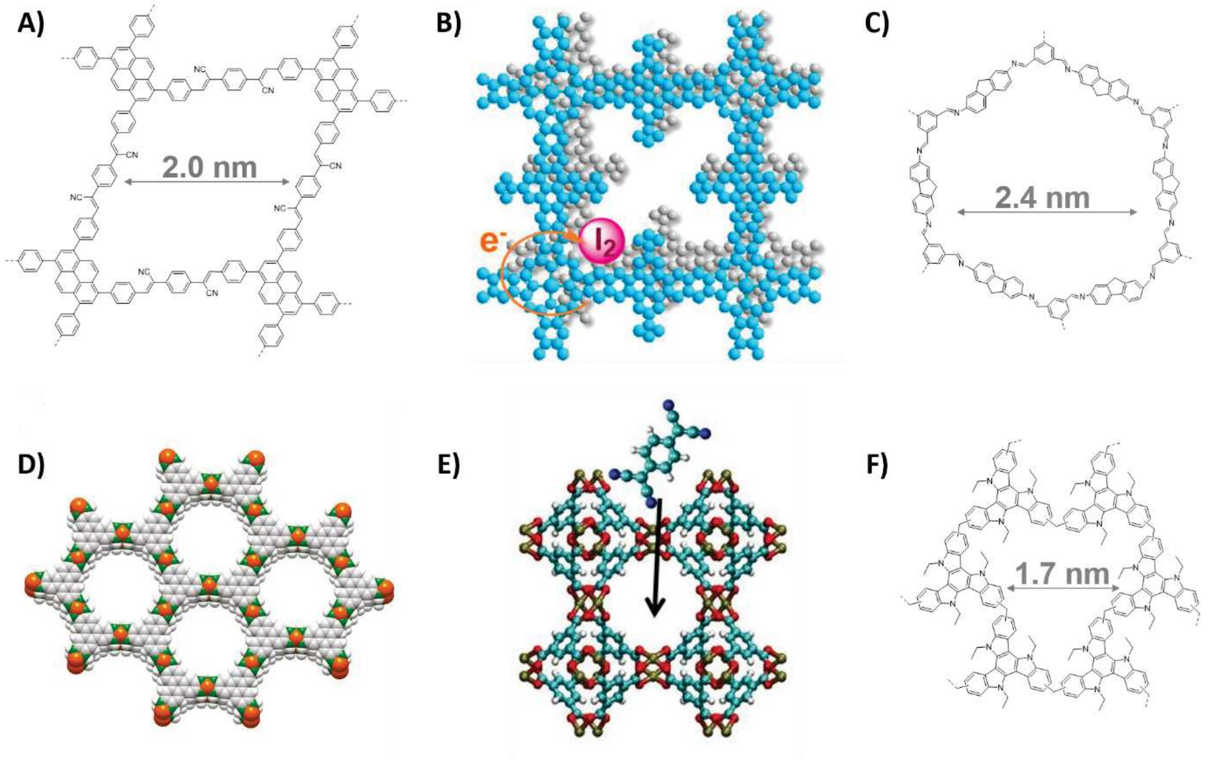

Figure I.17 Several chemical structures of COFs, MOFs and HCP. A) sp^{2}c-COF, B) ZnPc-based COF doped with I_2, reproduced from [162]*, C) FL-COF1, D) $Ni_3(HITP)_2$ reproduced from* [150]*, E) $Cu_3(BTC)_2$ doped with F_4TCNQ reproduced from* [142]*, F) TATHCP.*

2.2.2. CONJUGATED MICROPOROUS POLYMERS (CMPS), POLYMERS OF INTRINSIC MICROPOROSITY (PIMS) AND HYPERCROSSLINKED POLYMERS (HCPS)

Unlike COFs, which are synthesized under thermodynamic control, 3D networks of **Conjugated Microporous Polymers** (CMPs) are formed by irreversible covalent bonds and the polymerization proceeds via a kinetic route. Consequently, nearly all CMPs are amorphous (there are a few exceptions). CMP networks can be formed through the reaction of two or more different monomers or, in some cases, by homocoupling of a single monomer. Extended π-conjugated microporous networks are obtained when conjugated units are linked together, either directly, or via double or triple bonds through C-C cross coupling reactions.[165] The development of CMPs started in 2007 with the synthesis of poly(aryleneethylene) network.[140] Since then, the field of CMPs materials has grown considerably, given their wide range of potential applications exploiting both the optoelectronic properties and the presence of permanent voids within their structure. As for COFs, the pore structure can be tuned by varying the monomer geometry and length or by the use of co-monomers. Their average pore diameter is generally less than 2-5 nm.

The most common approach to synthesize CMPs is the combination of a conjugated core of C3 symmetry (e.g., 1,3,5-triethynylbenzene) with a linker with C2 symmetry (e.g., 1,4-diiodobenzene, as illustrated in Figure I.16).

Depending on their synthesis routes or their chemical structures, other subclasses of CMPs have been reported. For the potential purpose of TE application, we will briefly describe hypercrosslinked polymers (HCPs) and polymers of intrinsic microporosity (PIMs).

Hyper-crosslinking of preformed linear conjugated polymers such as polyaniline or polypyrrole provides another approach to produce CMPs. They are known as **Hypercrosslinked Polymers** (HCPs) (see Figure I.16). The reaction method, choice of solvent, and choice of cross-linker greatly affected the porosity.[165] However a high number of crosslinking bonds limit the solubility and processability of HCPs. From a synthetic perspective, HCPs are predominantly prepared by the following three approaches: (1) post-crosslinking polymer precursors, (2) direct one-step polycondensation of functional monomers, and (3) knitting rigid aromatic building blocks with external crosslinkers.

A first example of a thermoelectric HCP has been reported in 2020 by Sadak and coworkers. It consists in a highly porous triazatruxene (TAT) based hypercrosslinked polymers (TATHCP, see Figure I.17.F.[166] The polymer network has been synthesized by the knitting method through Friedel-Crafts crosslinking of TAT (a fully aromatic molecule with a planar C3 symmetry) with methylal as an external crosslinker. The obtained TATHCP ordered in stacks separated by 4.13 Å and showed a microporous structure (calculated pore size 1.7 nm). Inspired by the work on fluorene-based COFs,[167] DFT and Boltzmann transport were applied to estimate the TE transport coefficients and the band structure of TATHCP. Theoretical values of Seebeck and *ZT* have been found at 70-80 μV/K and 0.3, respectively, at 300K along the x- and y-axes (in-plane directions).

Polymers of Intrinsic Microporosity (PIMs) refer to a specific class of rigid chain-contorted microporous polymers (ladder-like structure). Intrinsic microporosity is defined as a continuous network of intermolecular microcavities of less than 2 nm, which is formed as a consequence of the inefficient packing of the rigid and twisted polymer backbone (see Figure I.16). The contortion site (often a tetrahedral carbon atom) causes the polymer to fill the space ineffectively. In the archetypal soluble PIM1, a spirobisindane function acts as a center of contortions. When the solvent is removed, the free volume between polymer chains leads to an open pore structure. Even though such structure should be promising, they have not yet been investigated in the context of thermoelectrics. One possible limiting factor is their low electrical conductivity (because of the not fully conjugated backbone and the twisted structure that hamper efficient chains packing). However, their microporous structure (of high interest for thermal conductivity) could also host conducting fillers such as graphene or carbon nanotubes. We therefore anticipate that PIMs can become part of the field and develop alongside COFs, CMPs and HCPs as promising candidates for micro- and mesoporous organic thermoelectric materials.

To summarize, the large body of work on MOFs and COFs clearly illustrates how porosity can be precisely engineered through chemical control.[145,168] As such, microporous structures can be designed easily to host a chemical dopant without affecting the polymer matrix structure. Given the volatility of many chemical dopants, however, attention must be paid to ensure the doping stability at elevated temperatures.[169] Combined with the excellent charge carrier mobility reported for microporous systems (often from measurements across short length scales), there is a significant potential for thermoelectric applications with these materials. Nonetheless, at present too few detailed investigations into thermoelectric properties make it difficult to draw general trends, but several theoretical studies confirm the significant potential of both COFs and HCPs.

Moving from microporous COFs and HCPs to systems with significantly larger pore sizes opens up a wide range of new challenges and opportunities within the meso- and macro-porous structures.

2.3. MESO- AND MACROPOROUS CPS STRUCTURES

2.3.1. CONDUCTING POLYMER FOAMS

Even though many porous gels have pore geometries which resemble those of polymer foams, they commonly form two separate sub-classes in the wider class of macro-porous polymers. This separation is given by the method of production combined with the physical mechanisms which control the pore geometries. Unlike porous gels, polymer foams are obtained by creating closely packed gas bubbles in an initial liquid or viscoelastic medium which is then solidified through polymerization/crosslinking/drying. These gas bubbles can be created by many different means (physical or chemical blowing, mechanical agitation, etc.). They are commonly (but not necessarily) larger than 10 micrometers and separated by thin pore walls of characteristic thicknesses of 0.1-1 micrometer in "closed-cell foams". These pore walls can break during the solidification stage, leading to "open-cell foams" (or sponges). In either case, the recognizable characteristic pore shapes of the resulting polymer foam are controlled by the mechanical stresses arising from the minimization of the interfacial energies of the gas/liquid interfaces in the liquid state. To the best of our knowledge, only a few pure organic conducting polymer-based foams have been obtained, all of them being composites. An example of PANI/PVA foams and their porous structure is given in Figure I.16. Heng and coworkers[144] proposed that PVA foams are firstly formed by mechanical frothing and then enwrapped by PANI molecules. Their uses in optoelectronic applications are limited by the foam stability (drainage or creaming effect leading to a heterogeneous porous structure) and the low mechanical properties of the dried films. Even though it should not be defined strictly as a foam due to its formation process, Kroon et al. reported the fabrication of porous P3HT "foams" for TE application.[170] They used a thermally induced phase separation between P3HT and *ortho*-dichlorobenzene (o-DCB) upon cooling combined with a smart salt leaching approach. Small NaCl crystals (<20 μm) were used as porogens. The amount of salt directly impacts the final porosity of the sample. After liquid-liquid phase separation and solidification of the polymer sample, both *o*-DCB and NaCl salts were leached out by immersing the sample into methanol for some time. After drying in air, a P3HT "foam" was obtained with macropores of 14± 6 μm interconnected by mesopores of around 63 nm size, resulting in an estimated porosity of 66%. The authors further demonstrated that such a 3D porous structure facilitates the diffusion of dopant molecules (F_4TCNQ in their specific case). Maximum values of 0.22 S/cm for the electrical conductivity and 68.4 µV/K for the Seebeck coefficient were obtained after doping the meso-/macro-porous structure (see Table I.1). Although the electrical conductivity has been decreased by an order of magnitude compared to the solid sample (σ= 3.24 S/cm), the Seebeck coefficient remains high in both doped structures (58.1 µV/K). The average thermal conductivity (in-plane and out-of-plane) for such 66% porous and 4 mm-thick sample was measured via the transient plane source method providing a value of 0.14 W/(m.K) (to be compared with the solid doped P3HT film: 0.32 W/(m·K)). The porous structure is beneficial in that it decreases the thermal conductivity and improves the doping efficiency (faster and more homogeneous through the entire thickness), but the decrease in electrical conductivity results in a lower ZT (2.3 x 10^{-4} for the foam, 1.0 x 10^{-3} for the thick solid sample). However, this study is a rare example that fully describes the structure and the TE properties of a new PCP. This process helps reach a controlled porous structure with pore size down to 63 nm. Further optimizations can be foreseen, such as the increase of charge carrier density (e.g., vapor phase doping of stronger oxidizing agent) and may lead to a higher electrical conductivity and enhanced performances.

2.3.2. CONDUCTING GELS

Gels constitute a vast class of materials that can be subdivided into two categories: chemical gels and physical gels, the latter being also referred as thermo-reversible gels if the regions of local order are thermally reversible. According to IUPAC, gels are defined as non-fluid colloidal networks or polymer networks that are expanded throughout their whole volume by a fluid. The networks are composed of connected objects. For the chemical gels, the connectedness is achieved by covalent bonds (via crosslinking or non-linear polymerization). For physical gels, the co-operative bonds are less energetic (e.g., hydrogen-bonds or Van der Waals interactions).[171] Such material can provide either mesoporous or macroporous materials depending on the type of bonding and the morphology of the building block unit constituting the network.

According to those definitions, we will consider the so-called “crosslinked polymer network” or “crosslinked conductive polymer gels”[141] as chemical gels. As an example, the research works of Pan[141], Shi[172] and coworkers illustrate well a dopant crosslinking method to synthesize conductive polyaniline hydrogels. Multifunctional dopant molecules such as phytic acid or copper phthalocyanine-3,4′,4″,4‴-tetrasulfonic acid tetrasodium salt (CuPcTs) interact with more than one polymer chain (by protonation) to form an interconnected porous network (see Figure I.16). Another method to produce chemical gels consists in in-situ polymerization of the conductive gel precursors through chemical oxidation coupling. PEDOT (poly(3,4-ethylenedioxythiophene)), polypyrrole or polyaniline hydrogels can be synthesized with the presence of a series of oxidants such as $FeCl_3$, $Fe(NO_3)_3$ or $(NH_4)S_2O_8$ with a controlled oxidation rate.[173] In both crosslinking and in-situ polymerization methods, the coherent network formed during the gel formation influences the final microstructure strongly.

In contrast to chemical gels, the polymer physical gel network can be formed through the physical aggregation of polymer chains (caused by hydrogen bonds, crystallization or complexation) or through glassy junction points. Some gel structures can also be formed via lamellar mesophases.[173] Polymer physical gels are mostly formed by cooling a mixture of miscible components (i.e., polymer and solvent). The polymer undergoes a liquid-solid transition below a so-called gelation threshold while the solvent remains liquid. The polymer chains create therefore a framework within which the solvent is confined. In the case of water, such structures are called hydrogels.

Gels can be used as such or dried by removing the solvent. Several techniques have been developed.[174] Depending on the drying method, the polymer dried gels are named **xerogels** (ambient in air drying), **aerogels** (supercritical drying), or **cryogels** (freeze-drying) (see Figure I.18). It is clear that the drying process is a key step as it plays a major role in the final internal structure of the porous network. For instance, the polymer network may collapse during drying because of capillary stress changes through the direct liquid –gas transition (case of xerogels). To avoid this ‘fatal’ issue, it is preferred to go through the solid-gas barrier (removing the solvent by freezing followed by sublimation, case of freeze-drying) or to dry the gel beyond the critical point, at high temperature and pressure (supercritical drying). Conversely, freeze-drying technique is easier and less aggressive for sensitive samples. The gel is firstly frozen (with liquid N_2) to prevent structure collapsing, then the solvent is removed by sublimation of the crystals (ice in the case of hydrogels) providing cryogels. This technique allows preparing robust cryogels but the pore size is determined by the size of ice crystals and the native gel network is modified during drying. At the end, dried 3D architectures are extremely porous: up to 99.8% of their volume is air.[173]

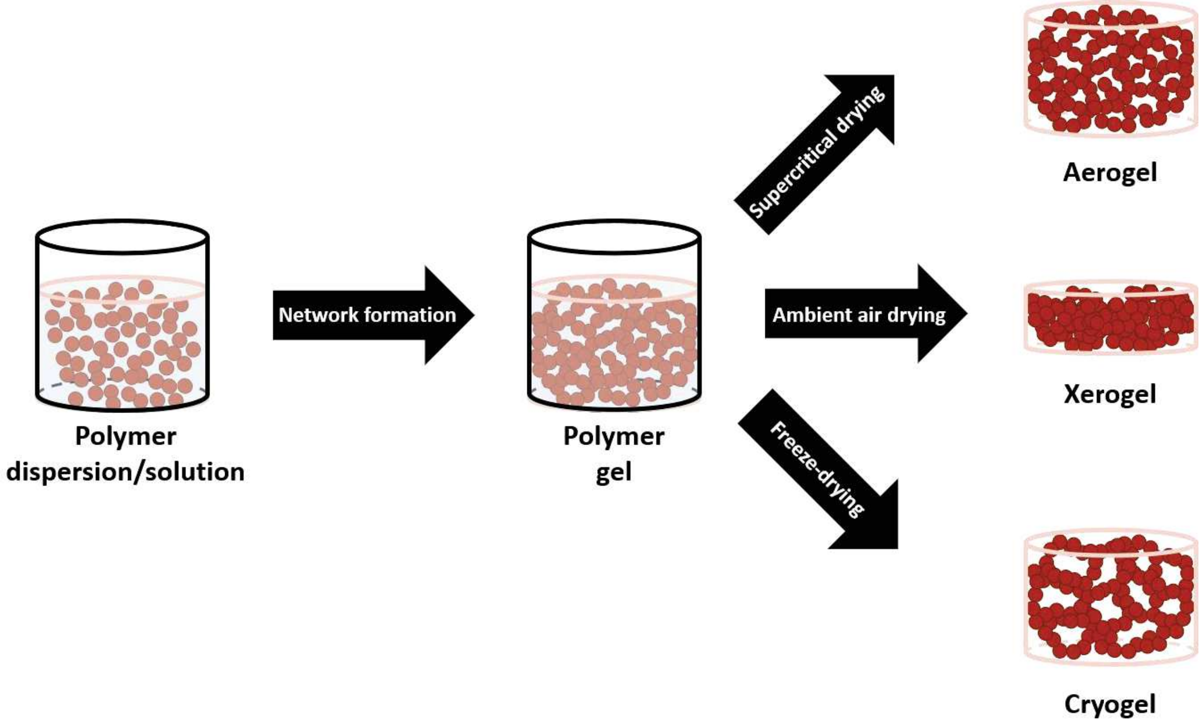

Figure I.18: Schematic representation of a polymer gel formation and solvent drying leading to three different structures: xerogel, aerogel and cryogel. For convenience spheres have been chosen to represent the building block of the polymer network but its morphology can take various forms such as fibers, rods or sheets, for example.

Mesoporous structures based on PEDOT

Mesoporous structures possess pores in the range between 2 nm and 50 nm. To the best of our knowledge, there are only few reports concerning mesoporous CPs, and even fewer for thermoelectric applications.[175,176] However, this range of porosity can be of great interest as the pore size is inferior to the phonons mean free path (in air). The strategy consists in producing gel phase with a meso-structure and then drying it. As discussed above, removing the solvent from a structure without modification is not straightforward. Supercritical drying is an interesting path because it can conserve the native structure of the gel after drying. Typically, in the supercritical state, the surface tension of a fluid is considered null. Then, removing the solvent from a network in this condition prevent the network from capillary stresses that could lead the structure to collapse.[175] Most organic solvents have very high pressure and temperature supercritical conditions, leading to important cost and possible destruction of the sample, especially for sensitive organic materials. However, drying at mild conditions is possible with the use of supercritical CO_2. In that case, one needs to replace the gel's solvent with CO_2 and then dry it under supercritical conditions. Importantly, the solvent of the gel must be fully miscible in liquid CO_2 (i.e., ethanol, acetone).[177] After several solvent exchange steps in the liquid state, the solvent is fully replaced with CO_2. Then, the autoclave is brought to a sufficiently high temperature and pressure (typically, above 31°C and 7.5 MPa which corresponds to the critical point of pure CO_2) to reach the supercritical state of the fluid. At this point, the supercritical fluid continuously flows through the sample's pores by depressurizing the autoclave. Then, pressure is slowly released, until the supercritical CO_2 reverts to its gas form. Theoretically, this drying allows the production of aerogels with the exact same network as the native gel. However, for pressure/temperature sensitive samples such as organic materials, supercritical drying parameters have to be finely controlled to avoid any shrinkage.

Zhang et al. succeeded in producing mesoporous PEDOT: PSS aerogels via supercritical drying (see Figure I.19 H-J). They synthesized PEDOT: PSS via the oxidative polymerization of EDOT in presence of NaPSS. Different ratio of PEDOT: PSS were obtained and hydrogels were formed after purification in HCl. Then, the solvent was exchanged with ethanol which is highly soluble with CO_2 conversely to water. The so-called alcogels were then dried firstly by replacing ethanol with liquid CO_2 and then by flowing supercritical CO_2. The obtained mesoporous aerogels have an average pore size around 15 nm as well as a low density (0.138-0.232 g/cm^3) and high Brunauer-Emmett-Teller (BET) area (178-370 m^2/g). However, this material exhibits a low electrical conductivity of 10^{-1} S/cm, probably limited by the synthesis conditions and doping efficiency.

Macroporous conducting dried gels

Conducting macroporous materials can be produced by different methods such as gelation and solvent removal. Actually, macroporous CPs have been obtained via different processes: rehydration of thin films, ionic or dopant crosslinking, or in situ oxidative polymerization.[178–

184] Only a few reports mention the use of those macroporous gels for TE applications, the mainly used material being PEDOT: PSS. Interestingly, none of them apply the same process to fabricate the porous bulk materials. Hereafter, we report the various processes found in the literature.

Table I.1 Best reported thermoelectric properties of several PCPs discussed herein. A reference thick free-standing PEDOT: PSS film is also included for comparison. The ZT value has been calculated at 298K. BET stands for Brunauer-Emmett-Teller specific surface area, t stands for thickness.

Material	Material preparation	σ [S/cm]	S [μV/K]	PF [μW/(m.K²)]	κ [W/(m.K)]	ZT (298 K)	Porosity/ structural information	Ref
PEDOT: PSS film	Free-standing thick film treated with sulfuric acid	2500	20.6	107	In-plane: 0.64 Out-of-plane: 0.27	0.05 (in-plane)	• Layered like structure • Few μm thick	[185]
Lyophilized PEDOT: PSS	Direct lyophilization of the dispersion containing polar solvent followed by mechanical compression	35	18.8	1.24	In-plane : 0.14 (estima-ted)	2.6E^{-3}	• No defined porosity, • Density: 0.25 g cm^{-3} • t= 100 μm after compression	[182]
PEDOT: PSS cryogel	Ionic crosslinking of PEDOT: PSS with EG – freeze-drying and further EG soaking treatment	≈70	≈16	1.8	/	/	• Sheet like morphological arrays, 100 μm spaced and 20 μm thick walls. • t= 500 μm	[181]
PEDOT :PSS cryogel	Covalent crosslinking with GOPS and NFC	10^{-3}	≈20	4E^{-5}	/	/	• Randomly distributed thin flakes and fibers • ~50 μm pores dimension	[186]
Lyophilized PEDOT: PSS	Direct lyophilization of the dispersion	2.23	17.9	0.072	0.032 (estimati on based on	6.6E^{-4}	• Density= 0.052 g/cm^3 • Porosity 95.7 % • Sheet like	[187]

	and methanol post-treatment under 1h supercritical condition				porosity)		morphological arrays ~1-20 µm spaced • t= 3-6 mm thick	
Lyophilized PEDOT: PSS/ MWCNTS/Ag	Lyophilization of a hybrid organic/inorganic aq. dispersion (33.3w% Ag load)	6.7	61.3	2.5	0.11	6.7E^{-3}	• 3D macroporous network structure with MWCNTs wrapped in PEDOT: PSS • BET surface area =: 170 m² g • Pore size: 10 – 100 µm • t > mm thick	[188]
Lyophilized PEDOT: PSS/Te NWs (30w%)	Lyophilization of the hybrid dispersion containing polar solvent and TE NWs followed by mechanical compression	15	49.2	3.6	In-plane : 0.16 (estima-ted)	6.7E^{--3}	• Wrapped Te NWs in PEDOT: PSS • No well-defined porosity • Density: 0.25 g cm^{-3} • t= 100 µm after compression	[182]
Lyophilized PEDOT/SWCNT /Bacterial cellulose	Lyophilization of aq. dispersion of BC/SWCNT fibers coated with PEDOT. (best results given for 32wt % SWCNT.) Films further pressed at 10 MPa)	291	20.3	12	0.13	2.8E^{-2}	• SWCNT and BC 2D porous fiber network coated with PEDOT with coexistence of micro and mesopores (~ 20 nm) • Porosity ~ 70%. • BET surface area =28.04 m² g^{-1} • t= 169 µm (after compressing)	[189]
F4TCNQ doped P3HT "foam"	P3HT gelation by thermally induced phase separation followed by salt leaching and drying	0.22	68.4	0.1	0.14	2.3E^{-4}	• Porosity 66%. • pores size: ~ 14 µm interconnected with smaller ones~ 63 nm • few mm thick macroporous	[170]

							sample	
FL-COF1	Fluorene-based imine-linked COF doped with iodine	1E^{-4}	2450	0.063	/	/	• Pore size 2.1 nm • BET surface area= 1308 m² g^{-1} before doping and 22 m² g^{-1} after doping	[164]
$Cu_3(BTC)_2$	Thin film of copper based benzene tricarboxylate linked MOF doped with F4TCNQ	~ 0.42	~ 360	~ 0.06	0.27	8E^{-5}	• Micropores	[155]

Wang et al. used a direct lyophilization technique by freezing the PEDOT: PSS aqueous dispersion with liquid N_2 and sublimating the solvent, which resulted in what is called in Table I.1 “lyophilized PEDOT: PSS”.[182] Polar solvents (such as EG or N-methyl pyrrolidone (NMP)) were added to the polymer dispersion (5 %vol), prior to drying, promoting a structural change in PEDOT: PSS. As discussed earlier, these solvents can remove the excessive insulating PSS and enhance the PEDOT domains' crystallinity (decreased π-stacking distance and increase in crystalline domain size).[190,191] In this direct lyophilization technique, the π-stacking interactions in PEDOT: PSS are strong enough and seem to promote the direct formation of a polymer network during ice sublimation process. The obtained 1 mm-thick samples are light and flexible. However, only a couple of “voids” of 10-100 µm size can be observed within the polymer network by SEM (see Figure I.19 K-M).[182] The images do not really support a porous structure, unless the mean size of the pores is in the nanometer range, below the SEM resolution. Depending on the nature of the solvent (EG for instance), the electrical conductivity of such lyophilized samples was tuned up to 32 S/cm. The authors further applied mechanical compression to the sample (decrease of the thickness from 1 to 0.1 mm and densification of the structure), which resulted in an interesting power factor of 1.24 µW/(m.K²) (with σ= 35 S/cm and S = 18.8 µV/K for NMP treated samples, see Table I.1). Despite the uncontrolled porosity, the in-plane thermal conductivity of 0.14 W/(m.K) (estimated by transient hot wire technique) is below the one of dense PEDOT: PSS films (see Table I.1). This decrease of κ for the lyophilized sample (accepting that the reported values are correct) highlights the positive effect of porosity on thermal insulation properties. Wang et al. further showed that such bulk thick samples can be integrated into TE generators made of six pairs of p-type PEDOT: PSS porous samples and n-type carbon nanotube fibers. The output performances are modest (maximum output power Pmax = 0.6 µW at ΔT = 68K), but it represents the first demonstration of PCPs integrated into a thermoelectric generator.

In a somewhat similar study, Maeda et al. prepared a porous PEDOT: PSS 3D network without using any crosslinker. In this study, gels were formed prior drying at ambient temperature and pressure.[183] The PEDOT: PSS dispersion was deposited slowly at the bottom of a beaker filled by ethanol and then heated at 80°C for 20-150 min. Ethanol removed the excess of PSS from the PEDOT domains. The 3D network is believed to be formed by the PEDOT: PSS micelles interacting by Van der Waals interactions or hydrogen-bonds. Once physical gels were formed, they were left to dry at ambient air resulting in free-standing films with thicknesses ranging from 1 to 30 µm (which we considered as xerogels). High electrical conductivity (300 to 1070 S/cm) were obtained depending on the sample thickness (21 µm to 1 µm, respectively). Interestingly, the Seebeck coefficient (16 -21 µV/K) is in the same range as for the lyophilized dried samples, reported by Wang et al.[182] and for the typical value of PEDOT: PSS in thin films. No description of the microstructure is provided in this study. Drying the gel in air may result in some porosity. Here, the porosity depends directly of the PEDOT: PSS gel native morphology (although drying in air may lead to a dense film). A thinner and denser sample could explain the much higher electrical conductivity reported in Maeda’s study as compared to the more porous sample designed by Wang and coworkers.[182]

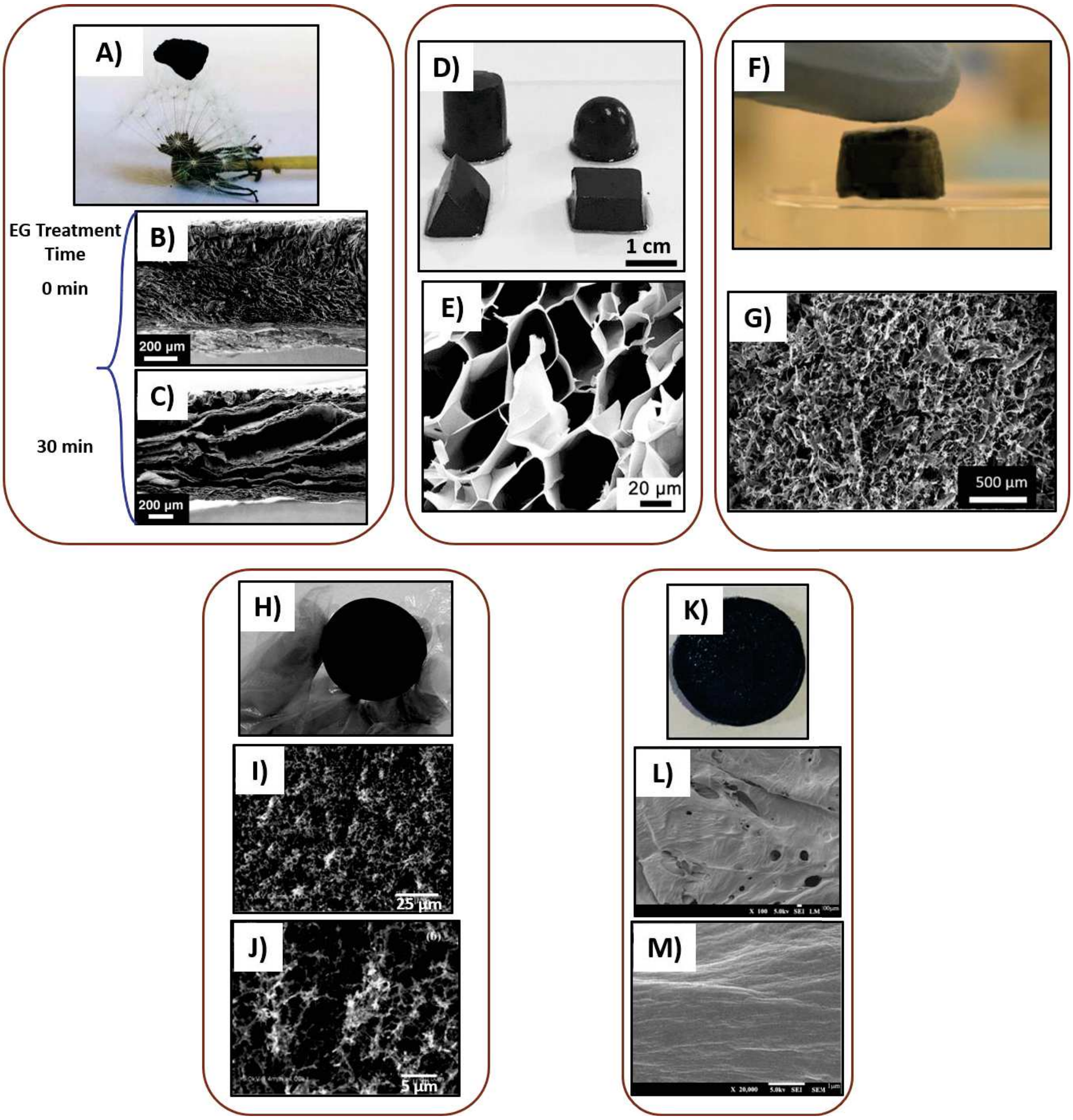

Figure I.19: Different PCP states and their porous structure observed by SEM. A - C) ultra-low-density PEDOT: PSS cryogel placed on top of a dandelion and SEM characterizations of the gel before and after treatment with EG;[181] *D – E) Digital pictures of PEDOT: PSS hydrogels with different geometric shapes and cross-section SEM image of a freeze-dried PEDOT: PSS hydrogel and after the treatment with concentrated H_2SO_4;*[178] *F - G) PEDOT: PSS, GOPS, and NFC PCP composite and SEM image of the internal structure;*[186] *H - J) PEDOT: PSS mesoporous aerogel;*[175] *K - M) Direct lyophilization of PEDOT: PSS dispersion containing polar solvent before mechanical compression.*[182]

It should be noted that the PEDOT: PSS porous structure produced via lyophilization technique without crosslinking agents is likely to be fragile, as mentioned by Khan et al.[192] To overcome this possible weakness, Gordon and coworkers proposed to resort on ionic crosslinking to better control the network structure and elasticity of both PEDOT: PSS hydrogels and cryogels.[181] In their approach, a dried free-standing thick film of PEDOT: PSS was first rehydrated. The resulting hydrogels were frozen in liquid N_2 and vacuum-pumped overnight. The method produced ultralight (d= 0.21- 0.25 mg cm^{-3}), robust, flexible and macroporous PEDOT: PSS cryogels. Gordon and coworkers consider the formation of this 3D structure to be related to the ionically crosslinked polymeric hydrogel network formed when the thick PEDOT: PSS film is rehydrated. The pores of the dried matrix (thick film) are filled with water due to the hydrophilicity of the excess PSS. Their formation was induced both by ionic interactions between PEDOT and PSS, and by hydrophilic/hydrophobic interactions between water and the polymer chains. This method provides a bulk porous structure with a pore size in the range of 50-100 µm according to reference SEM images.[181] However, the porous network exhibits large-scale heterogeneity in its arrangement. In some regions, the pores in the PCP network appear to align preferentially in the same direction; the structure is denser at the interfaces, which may be due to local stronger capillary forces or structure collapse. These porous samples show limited electrical conductivity of only a few S/cm. To further improve their performance, the cryogel samples were soaked in ethylene glycol for varying time (2-30 min). As mentioned previously, PSS excess removal and the use of a polar solvent induce a structural rearrangement of the polymer and an increased crystallinity. When soaking is long enough, the treated EG cryogels undergo a morphological change, with thicker walls and a more layered-like structure (see Figure I.19 B-C). This structural change increases σ to ~70 S/cm. The Seebeck coefficient is slightly lower in the porous samples: on average around 15 µV/K. The power factor is thus ~1.8 µW/(m.K^2) for 500 µm thick cryogels (see Table I.1). The thermal conductivity properties were not studied in this work.

The three pure PEDOT: PSS systems discussed above are amongst the few reports in the field of thermoelectricity. It is interesting to note that hydrogels of commercial PEDOT: PSS suspension can be easily produced in spite of their very low solid content (< 1.5 w% for PH1000). This polymer has indeed an extremely low critical concentration of gelation (CCG), about one order of magnitude lower than for more "conventional" polymers such as poly(vinyl alcohol) (about 6 wt%).[193] Overall, the performances of the porous structures are lower than the films ones (see the values in Table I.1 for PEDOT: PSS free-standing film as comparison). However, as anticipated, porosity can minimize the thermal conduction and the Seebeck coefficient is marginally affected by the voids.

A better control over both the polymer chains order and the porous structure (during the gel formation and/or the gel drying process) should lead to higher charges conductivity. As a matter of fact, acid (or polar solvent) treatments of PEDOT: PSS hydrogels and dried scaffolds can lead to an increase of the pore wall thickness and a narrowing of pore sizes which can enhance the electrical conductivity. Yao et al.[178] have observed an increase in σ by a factor of twenty (from 0.46 to 8.8 S/cm) with a decrease of pore size by a factor two (80 down to 40 µm) after sulfuric acid post treatment of their PEDOT: PSS cryogels (see the porous structure in Figure I.19 D-E). To limit a possible structure shrinkage during this post-drying step (secondary doping / solvent annealing) aiming at boosting the electrical conductivity, Yanagishima et al.[187] investigated a secondary doping of a PEDOT: PSS cryogel with methanol under supercritical condition ($ScCO_2$). Secondary doping by $ScCO_2$ methanol treatment or by dipping in DMSO leads to a remarkable enhancement of electrical conductivity (from 2×10^{-4} S/cm to 2 S/cm) due to the promotion of PEDOT crystallization. Note that the $ScCO_2$ treatment induces a more limited shrinkage than the dipping method. Other drying techniques such as ice-templating[179,194,195] (similar to freeze-drying but with a control over the ice crystal growth) or microwave drying[196] could also be investigated to control the final porous structure. For instance, both the size and the unidirectional growth of the ice crystals during the freezing process of the hydrogels could leave behind highly ordered structures with potentially anisotropic TE properties.

Another strategy to overcome the apparent brittleness of macroporous PEDOT: PSS xero- and cryogels is the use of *polymer blends* in which PEDOT: PSS still plays the dual role of scaffolding and conducting material. Han,[186] and coworkers proposed to reinforce PEDOT: PSS dried gels by adding elastomeric cross-linkers such as glycidoxypropyl trimethoxysilane (GOPS) and a mechanical strengthener like nanofibrillated cellulose (NFC). The chemical gel was formed by crosslinking the epoxy group of GOPS molecules onto the hydroxyl groups of PSS and NFC. After freeze-drying, the resulting cryogel is more elastic and mechanically robust than lyophilized stock PEDOT: PSS dispersion. The obtained PEDOT: PSS/GOPS/NFC cryogels are flexible and compressible (homogeneous porous structure of ~50 µm pore dimensions (see Figure I.19 F-G). However, their electrical conductivity is limited to 10^{-3} S/cm because of the high amount of insulating part (NFC framework) in the sample.

In addition to improving mechanical resistance, hybrid structures (porous conductive polymer matrix blended with inorganic particles) could enhance the TE properties. As an example, Sun et al.[188] designed porous PEDOT: PSS blended with multi walls carbon nanotubes (MWCNT) and silver flakes (Ag) by lyophilization. The resulting PEDOT: PSS/MWCNTS/Ag material has a macroporous structure (pore size range: 10-100 µm according to SEM pictures) with interconnected inorganic particles. The dense porous network is made of MWCNTs wrapped in PEDOT: PSS, showing a strong interaction between both the polymer matrix and the nanotubes, and Ag flakes that tend to agglomerate. The introduction of Ag flakes helps to reach higher electrical conductivity and Seebeck coefficient than for pure PEDOT: PSS cryogels (σ changing from 0.38 S/cm to 6.71 S/cm and S from 20 to 61.3 µV/K for 33.3 wt% of Ag). The real impact of the MWCNTs on the electrical conductivity could not be properly determined but wrapping of the MWCNTs with PEDOT: PSS allows a good phonon scattering and keeps a low thermal conductivity of the material between 0.06 to 0.11 W/(m.K) measured by transient plane source method. *ZT* values reaching a maximum of 7.56 x 10^{-3} have been obtained. Thanks to the addition of SWCNTs to a PEDOT: PSS dispersion, other porous structures were reported after ambient air drying by Liu et al. and Wei et al.[197,198] It is clear that the porosity is due to the presence of nanotubes in the blend, although it shows promising results for possible thin, flexible and porous films. Moreover, the added SWCNTs boost the Seebeck coefficient of the composite leading to high power factors of 20.68 µW/(m.K²) for Wei and coworkers. However, the thermal conductivity of such high PF materials is not discussed and is expected to be in the range 0.2-0.7 W/(m.K) as measured in other reports.[199,200] Another example of composite has been described by Wang et al.[182] These authors fabricated PEDOT: PSS/Tellurium nanowires (Te-NWs) porous sample (following the previously described process at the beginning of section) to increase the Seebeck coefficient of their porous materials. Typically, for inorganic materials such as Bi_2Te_3, the Seebeck coefficient is comprised between 150 and 200 µV/K for p-type materials[201] whereas for PEDOT: PSS it is around 15 to 20 µV/K. At high contents of Te-NWs, the Seebeck coefficient increased drastically (from 18.8 to 682 µV/K) but the electrical conductivity decreased from 35 to 0.002 S/cm. The optimal power factor value was found at 30 wt% of Te-NWs and reaches 3.6 µW/(m.K^2), three times higher than pure lyophilized PEDOT: PSS. This improvement of the Seebeck coefficient may be explained by a potential energy barrier formed at the interface of PEDOT: PSS and Te-NWs filtering, which would allow only high-energy charge carriers to pass through. This hypothesis rests on intimate contact between the two phases, the formation of an energy barrier at the interface of PEDOT: PSS and Te-NWs, and finally a low nanomaterial content. A very promising *ZT* value of 2 x 10^{-2} has been reached within such composites after DMSO vapor treatment, demonstrating the importance of structure control. Finally, Jia et al. combined the structural benefit of bacterial cellulose (BC) fibers (low thermal conductivity in dried gel states due to a mesoporous network formation), with the high charge conductivity of single-walled carbon nanotubes (SWCNTs) and PEDOT.[189] In situ polymerization allowed PEDOT to be uniformly coated on BC nanofibers and SWCNTs. Lyophilization of the dispersion provided ultralight porous conducting polymers with porosity up to 70%. The optimization of the structure, via mechanical pressing, together with an optimization of the SWCNTs loading afforded a record PF of 12 µW/(m.K^2) in the porous bulk structure. A thermal conductivity (calculated from the heat capacity and the bulk density of the sample) of 0.13 W/(m.K) was obtained. A TE prototype (assembled with 8 single legs of the porous composite) provided a maximum output power of 169 nW at $\Delta T = 65.6$ K. This result reinforces the promising interest of PCP for TE application, especially for the heat conversion of small thermal gradients (in the microwatt to milliwatts power range) for which the conventional systems are inefficient.[202]

Due to the lack of proper structural control, we believe that there is still significant room for improvement for macroporous samples. Mesoporous samples have not been studied in detail in the literature although their porosity range seems to be very interesting for reducing thermal conductivity. Other microporous samples (COFs, MOFs, HCPs, ...) are, to our knowledge, difficult to elaborate in bulk.

3. THESIS OBJECTIVES

To conclude, this project takes place in a context where the search for new ways to produce energy is essential. Conducting polymers are very promising for thermoelectric applications aiming to transform the low-grade waste heat in the ambient range (20 - 100°C) into electrical energy. The scientific community has mainly focused on developing these materials as thin films (<100 nm) while optimizing mainly the power factor. In contrast, few studies are devoted to optimizing the thermal conductivity of the material. Yet, recent work by Scheunemann et al. suggests that for energetically ordered organic TE materials to reach a ZT = 1, the lattice contribution to the thermal conductivity would have to reach values < 0.2 W/(m.K). It is therefore in this context that this thesis project is situated. To decrease the thermal conductivity of organic semiconductor materials, we aim to implement porosity into them while maintaining good charge transport properties. In addition, we pursue the production of large samples (>1 cm) by reducing the amount of raw material, and facilitating the production of vertical thermoelectric generators. Self-supporting, mechanically robust and with a dimension greater than a millimeter are the ideal targeted materials properties. Although microporosity could be of interest for TE properties, such structures can only be reached thanks to complex chemical synthesis and often lead to non-soluble materials that are difficult to process in bulk. Meso- or macroporous structures better match our specifications. For comparison purposes with the literature and ease of bulk processing, PEDOT:PSS looks as an ideal candidate. We aim to produce meso- / macro-porous materials made of pure PEDOT: PSS, without crosslinking agent or other external loading while keeping good charge transport properties.

Our main goal is to reveal the structure-properties relationships of porous PEDOT:PSS and investigate their relevance for TE application. PCPs reported in the literature show poor control of the drying process and the final porous structure. There is also a lack of understanding and characterization of the pore formation (and gelation mechanism). In this thesis, we strive to develop and adapt comprehensive experimental methods to measure all properties of interest in porous conducting materials. The main interest of implementing porosity in TE materials is to reduce the thermal conductivity. However, the impact of the porous structure on the thermal conductivity of the material is often difficult to monitor.

Here we intend to i) set up a robust method to measure the thermal conduction properties of PCPs, ii) evaluate the three thermoelectric parameters (σ, S and κ). In addition to their ZT, the power output of the most promising materials will be studied in order to quantify their potential interest in TE generators. Finally, the ultimate goal would be to produce a prototype generator with the material showing the best TE properties.

4. REFERENCES

[1] M. E. Kiziroglou, E. M. Yeatman, in *Funct. Mater. Sustain. Energy Appl.*, Woodhead Publishing, **2012**, pp. 541–572.

[2] M. Chetto, A. Queudet, in *Energy Auton. Real-Time Syst.*, Elsevier, **2016**, pp. 57–83.

[3] N. Sezer, M. Koç, *Nano Energy* **2021**, *80*, 1055.

[4] L. Xie, W. Song, J. Ge, B. Tang, X. Zhang, T. Wu, Z. Ge, *Nano Energy* **2021**, *82*, 105770.

[5] B. Russ, A. Glaudell, J. J. Urban, M. L. Chabinyc, R. A. Segalman, *Nat. Rev. Mater.* **2016**, *1*, 1.

[6] D. Ponnamma, G. J. Ogunleye, P. Sharma, M. A. AlMaadeed, in *Biopolym. Compos. Electron.*, Elsevier, **2017**, pp. 333–352.

[7] T. Sanislav, G. D. Mois, S. Zeadally, S. C. Folea, *IEEE Access* **2021**, *9*, 39530.

[8] J. H. Bahk, H. Fang, K. Yazawa, A. Shakouri, *J. Mater. Chem. C* **2015**, *3*, 10362.

[9] V. Leonov, *IEEE Sens. J.* **2013**, *13*, 2284.

[10] T. J. Seebeck, *Ann. Phys.* **1826**, *82*, 253.

[11] Oersted, *Ann. Phys.* **1823**, *73*, 430.

[12] D. M. Rowe, in *CRC Handb. Thermoelectr.* (Ed.: D.M. Rowe), CRC Press, **1995**.

[13] P. Limelette, *Sci. Rep.* **2021**, *11*, 1.

[14] A. F. Ioffe, *Phys. Today* **1959**, *12*, 42.

[15] C. Goupil, W. Seifert, K. Zabrocki, E. Müller, G. J. Snyder, *Entropy* **2011**, *13*, 1481.

[16] R. He, G. Schierning, K. Nielsch, *Adv. Mater. Technol.* **2018**, *3*, 1700256.

[17] A. K. Menon, O. Meek, A. J. Eng, S. K. Yee, *J. Appl. Polym. Sci.* **2017**, *134*, DOI 10.1002/app.44060.

[18] M. Thielen, L. Sigrist, M. Magno, C. Hierold, L. Benini, *Energy Convers. Manag.* **2017**, *131*, 44.

[19] J. D. Ryan, A. Lund, A. I. Hofmann, R. Kroon, R. Sarabia-Riquelme, M. C. Weisenberger, C. Müller, *ACS Appl. Energy Mater.* **2018**, *1*, 2934.

[20] D. Beretta, N. Neophytou, J. M. Hodges, M. G. Kanatzidis, D. Narducci, M. Martin-Gonzalez, M. Beekman, B. Balke, G. Cerretti, W. Tremel, A. Zevalkink, A. I. Hofmann, C. Müller, B. Dörling, M. Campoy-Quiles, M. Caironi, *Mater. Sci. Eng. R Reports* **2019**, *138*, 100501.

[21] T. C. Harman, M. P. Walsh, B. E. Laforge, G. W. Turner, *J. Electron. Mater.* **2005**, *34*, L19.

[22] L. D. Zhao, S. H. Lo, Y. Zhang, H. Sun, G. Tan, C. Uher, C. Wolverton, V. P. Dravid, M. G. Kanatzidis, *Nature* **2014**, *508*, 373.

[23] M. R. Burton, T. Liu, J. McGettrick, S. Mehraban, J. Baker, A. Pockett, T. Watson, O. Fenwick, M. J. Carnie, *Adv. Mater.* **2018**, *30*, 1801357.

[24] J. Zhang, T. Zhang, H. Zhang, Z. Wang, C. Li, Z. Wang, K. Li, X. Huang, M. Chen, Z. Chen, Z. Tian, H. Chen, L. D. Zhao, L. Wei, *Adv. Mater.* **2020**, *32*, 2002702.

[25] P. Ren, Y. Liu, J. He, T. Lv, J. Gao, G. Xu, *Inorg. Chem. Front.* **2018**, *5*, 2380.

[26] D. Champier, *Energy Convers. Manag.* **2017**, *140*, 167.

[27] L. Shure, H. Schwartz, in *Nasa-Tm-X-52158*, **1965**, p. 39.

[28] W. Liu, K. Yin, Q. Zhang, C. Uher, X. Tang, *Natl. Sci. Rev.* **2017**, *4*, 611.

[29] A. Nozariasbmarz, A. Agarwal, Z. A. Coutant, M. J. Hall, J. Liu, R. Liu, A. Malhotra, P. Norouzzadeh, M. C. Öztürk, V. P. Ramesh, Y. Sargolzaeiaval, F. Suarez, D. Vashaee, *Jpn. J. Appl. Phys.* **2017**, *56*, 05DA04.

[30] S. Chen, Z. Ren, *Mater. Today* **2013**, *16*, 387.

[31] G. Rogl, A. Grytsiv, P. Heinrich, E. Bauer, P. Kumar, N. Peranio, O. Eibl, J. Horky, M. Zehetbauer, P. Rogl, *Acta Mater.* **2015**, *91*, 227.

[32] L. D. Zhao, C. Chang, G. Tan, M. G. Kanatzidis, *Energy Environ. Sci.* **2016**, *9*, 3044.

[33] C. Han, Q. Sun, Z. Li, S. Xue, C. Han, Q. Sun, Z. Li, S. X. Dou, *Adv. Energy Mater.* **2016**, *6*, 1600498.

[34] M. Campoy-Quiles, *Philos. Trans. R. Soc. A* **2019**, *377*, 20180352.

[35] O. Bubnova, Z. U. Khan, A. Malti, S. Braun, M. Fahlman, M. Berggren, X. Crispin, *Nat. Mater.* **2011**, *10*, 429.

[36] G. H. Kim, L. Shao, K. Zhang, K. P. Pipe, *Nat. Mater.* **2013**, *12*, 719.

[37] J. Liu, B. van der Zee, R. Alessandri, S. Sami, J. Dong, M. I. Nugraha, A. J. Barker, S. Rousseva, L. Qiu, X. Qiu, N. Klasen, R. C. Chiechi, D. Baran, M. Caironi, T. D. Anthopoulos, G. Portale, R. W. A. Havenith, S. J. Marrink, J. C. Hummelen, L. J. A. Koster, *Nat. Commun.* **2020**, *11*, 1.

[38] J. Li, A. B. Huckleby, M. Zhang, *J. Mater.* **2022**, *8*, 204.

[39] A. D. Scaccabarozzi, A. Basu, F. Aniés, J. Liu, O. Zapata-Arteaga, R. Warren, Y. Firdaus, M. I. Nugraha, Y. Lin, M. Campoy-Quiles, N. Koch, C. Müller, L. Tsetseris, M. Heeney, T. D. Anthopoulos, *Chem. Rev.* **2022**, *122*, 4420.

[40] S. A. Moiz, I. A. Khan, W. A. Younis, K. S. Karimov, in *Conduct. Polym.*, IntechOpen, **2016**, pp. 91–118.

[41] J. Ashkenazi, W. E. Pickett, H. Krakauer, C. S. Wang, B. M. Klein, S. R. Chubb, *Phys. Rev. Lett.* **1989**, *63*, 1539.

[42] I. R. Jeon, N. Noma, R. F. C. Claridge, Y. Shirota, *Polym. J.* **1992**, *24*, 273.

[43] M. J. Panzer, C. D. Frisbie, *Adv. Funct. Mater.* **2006**, *16*, 1051.

[44] W. Zhao, J. Ding, Y. Zou, C. A. Di, D. Zhu, *Chem. Soc. Rev.* **2020**, *49*, 7210.

[45] P. W. Anderson, *Phys. Rev.* **1958**, *109*, 1492.

[46] N. Tessler, Y. Preezant, N. Rappaport, Y. Roichman, *Adv. Mater.* **2009**, *21*, 2741.

[47] R. Noriega, J. Rivnay, K. Vandewal, F. P. V. Koch, N. Stingelin, P. Smith, M. F. Toney, A. Salleo, *Nat. Mater.* **2013**, *12*, 1038.

[48] N. F. Mott, *Philos. Mag.* **1969**, *19*, 835.

[49] P. Sheng, B. Abeles, Y. Arie, *Phys. Rev. Lett.* **1973**, *31*, 44.

[50] P. Sheng, *Phys. Rev. B* **1980**, *21*, 2180.

[51] M. N. Gueye, A. Carella, J. Faure-Vincent, R. Demadrille, J. P. Simonato, *Prog. Mater. Sci.* **2020**, *108*, 100616.

[52] I. Salzmann, G. Heimel, M. Oehzelt, S. Winkler, N. Koch, *Acc. Chem. Res.* **2016**, *49*, 370.

[53] R. Kroon, D. A. Mengistie, D. Kiefer, J. Hynynen, J. D. Ryan, L. Yu, C. Müller, *Chem. Soc. Rev.* **2016**, *45*, 6147.

[54] M. Bharti, A. Singh, S. Samanta, D. K. Aswal, *Prog. Mater. Sci.* **2018**, *93*, 270.

[55] S. Lee, S. Kim, A. Pathak, A. Tripathi, T. Qiao, Y. Lee, H. Lee, H. Y. Woo, *Macromol. Res.* **2020**, *28*, 531.

[56] D. Wang, L. Liu, X. Gao, C. A. Di, D. Zhu, *CCS Chem.* **2021**, *3*, 2212.

[57] K. H. Yim, G. L. Whiting, C. E. Murphy, J. J. M. Halls, J. H. Burroughes, R. H. Friend, J. S. Kim, *Adv. Mater.* **2008**, *20*, 3319.

[58] Q. Zhang, Y. Sun, W. Xu, D. Zhu, *Energy Environ. Sci.* **2012**, *5*, 9639.

[59] A. M. Glaudell, J. E. Cochran, S. N. Patel, M. L. Chabinyc, *Adv. Energy Mater.* **2015**, *5*, 1401072.

[60] V. Untilova, J. Hynynen, A. I. Hofmann, D. Scheunemann, Y. Zhang, S. Barlow, M. Kemerink, S. R. Marder, L. Biniek, C. Müller, M. Brinkmann, *Macromolecules* **2020**, *53*, 6314.

[61] E. Järsvall, T. Biskup, Y. Zhang, R. Kroon, S. Barlow, S. R. Marder, C. Müller, *Chem. Mater.* **2022**, *34*, 5673.

[62] R. Kroon, D. Kiefer, D. Stegerer, L. Yu, M. Sommer, C. Müller, *Adv. Mater.* **2017**, *29*, DOI 10.1002/adma.201700930.

[63] Y. Xuan, X. Liu, S. Desbief, P. Leclère, M. Fahlman, R. Lazzaroni, M. Berggren, J. Cornil, D. Emin, X. Crispin, *Phys. Rev. B* **2010**, *82*, 115454.

[64] K. Kang, S. Watanabe, K. Broch, A. Sepe, A. Brown, I. Nasrallah, M. Nikolka, Z. Fei, M. Heeney, D. Matsumoto, K. Marumoto, H. Tanaka, S. I. Kuroda, H. Sirringhaus, *Nat. Mater.* **2016**, *15*, 896.

[65] S. N. Patel, A. M. Glaudell, D. Kiefer, M. L. Chabinyc, *ACS Macro Lett.* **2016**, *5*, 268.

[66] S. N. Patel, A. M. Glaudell, K. A. Peterson, E. M. Thomas, K. A. O'Hara, E. Lim, M. L. Chabinyc, *Sci. Adv.* **2017**, *3*, 1700434.

[67] I. E. Jacobs, E. W. Aasen, J. L. Oliveira, T. N. Fonseca, J. D. Roehling, J. Li, G. Zhang, M. P. Augustine, M. Mascal, A. J. Moulé, *J. Mater. Chem. C* **2016**, *4*, 3454.

[68] A. R. Chew, R. Ghosh, Z. Shang, F. C. Spano, A. Salleo, *J. Phys. Chem. Lett.* **2017**, *8*, 4974.

[69] M. L. Chabinyc, M. F. Toney, R. J. Kline, I. McCulloch, M. Heeney, *J. Am. Chem. Soc.* **2007**, *129*, 3226.

[70] J. Park, Y. Lee, M. Kim, Y. Kim, A. Tripathi, Y. W. Kwon, J. Kwak, H. Y. Woo, *ACS Appl. Mater. Interfaces* **2020**, *12*, 1110.

[71] E. Lim, K. A. Peterson, G. M. Su, M. L. Chabinyc, *Chem. Mater.* **2018**, *30*, 998.

[72] V. Vijayakumar, P. Durand, H. Zeng, V. Untilova, L. Herrmann, P. Algayer, N. Leclerc, M. Brinkmann, *J. Mater. Chem. C* **2020**, *8*, 16470.

[73] P. Durand, H. Zeng, T. Biskup, V. Vijayakumar, V. Untilova, C. Kiefer, B. Heinrich, L. Herrmann, M. Brinkmann, N. Leclerc, *Adv. Energy Mater.* **2022**, *12*, 2103049.

[74] Y. Nogami, H. Kaneko, T. Ishiguro, A. Takahashi, J. Tsukamoto, N. Hosoito, *Solid State Commun.* **1990**, *76*, 583.

[75] V. Vijayakumar, Y. Zhong, V. Untilova, M. Bahri, L. Herrmann, L. Biniek, N. Leclerc, M. Brinkmann, *Adv. Energy Mater.* **2019**, *9*, 1900266.

[76] B. Kramer, A. MacKinnon, *Reports Prog. Phys.* **1993**, *56*, 1469.

[77] O. Bubnova, X. Crispin, *Energy Environ. Sci.* **2012**, *5*, 9345.

[78] J. Hynynen, E. Järsvall, R. Kroon, Y. Zhang, S. Barlow, S. R. Marder, M. Kemerink, A. Lund, C. Müller, *ACS Macro Lett.* **2019**, *8*, 70.

[79] G. Zuo, X. Liu, M. Fahlman, M. Kemerink, *Adv. Funct. Mater.* **2018**, *28*, 1703280.

[80] G. Zuo, X. Liu, M. Fahlman, M. Kemerink, *ACS Appl. Mater. Interfaces* **2018**, *10*, 9638.

[81] A. Abtahi, S. Johnson, S. M. Park, X. Luo, Z. Liang, J. Mei, K. R. Graham, *J. Mater. Chem. A* **2019**, *7*, 19774.

[82] I. Borazan, A. C. Bedeloğlu, A. Demir, *Polym. Polym. Compos.* **2020**, *28*, 66.

[83] Y. Xia, S. Dai, *J. Mater. Sci. Mater. Electron.* **2021**, *32*, 12746.

[84] J. Liao, H. Si, X. Zhang, S. Lin, *Sensors (Switzerland)* **2019**, *19*, 218.

[85] N. Gao, J. Yu, Q. Tian, J. Shi, M. Zhang, S. Chen, L. Zang, *Chemosensors* **2021**, *9*, 79.

[86] K. Rohtlaid, G. T. M. Nguyen, S. Ebrahimi-Takalloo, T. N. Nguyen, J. D. W. Madden, F. Vidal, C. Plesse, *Adv. Mater. Technol.* **2021**, *6*, 2001063.

[87] S. Khasim, A. Pasha, N. Badi, M. Lakshmi, Y. K. Mishra, *RSC Adv.* **2020**, *10*, 10526.

[88] I. Petsagkourakis, N. Kim, K. Tybrandt, I. Zozoulenko, X. Crispin, *Adv. Electron. Mater.* **2019**, *5*, 1.

[89] Z. Fan, J. Ouyang, *Adv. Electron. Mater.* **2019**, *5*, 1.

[90] S. Kirchmeyer, K. Reuter, *J. Mater. Chem.* **2005**, *15*, 2077.

[91] H. Shi, C. Liu, Q. Jiang, J. Xu, *Adv. Electron. Mater.* **2015**, *1*, 1500017.

[92] Z. Zhu, C. Liu, F. Jiang, J. Xu, E. Liu, *Synth. Met.* **2017**, *225*, 31.

[93] X. Wang, X. Zhang, L. Sun, D. Lee, S. Lee, M. Wang, J. Zhao, Y. Shao-Horn, M. Dincă, T. Palacios, K. K. Gleason, *Sci. Adv.* **2018**, *4*, eaat5780.

[94] Y. Xia, J. Ouyang, *ACS Appl. Mater. Interfaces* **2012**, *4*, 4131.

[95] U. Lang, E. Muller, N. Naujoks, J. Dual, *Adv. Funct. Mater.* **2009**, *19*, 1215.

[96] D. Alemu, H. Y. Wei, K. C. Ho, C. W. Chu, *Energy Environ. Sci.* **2012**, *5*, 9662.

[97] A. M. Nardes, M. Kemerink, R. A. J. Janssen, J. A. M. Bastiaansen, N. M. M. Kiggen, B. M. W. Langeveld, A. J. J. M. Van Breemen, M. M. De Kok, *Adv. Mater.* **2007**, *19*, 1196.

[98] J. Rivnay, S. Inal, B. A. Collins, M. Sessolo, E. Stavrinidou, X. Strakosas, C. Tassone, D. M. Delongchamp, G. G. Malliaras, *Nat. Commun.* **2016**, *7*, 7:11287.

[99] T. Takano, H. Masunaga, A. Fujiwara, H. Okuzaki, T. Sasaki, *Macromolecules* **2012**, *45*, 3859.

[100] J. Ouyang, Q. Xu, C. W. Chu, Y. Yang, G. Li, J. Shinar, *Polymer (Guildf).* **2004**, *45*, 8443.

[101] S. R. S. Kumar, N. Kurra, H. N. Alshareef, *J. Mater. Chem. C* **2015**, *4*, 215.

[102] E. Hosseini, V. Ozhukil Kollath, K. Karan, *J. Mater. Chem. C* **2020**, *8*, 3982.

[103] M. Z. Ali, K. M. K. Ishak, M. A. M. Zawawi, M. Jaafar, Z. Ahmad, *Synth. Met.* **2022**, *286*, 117037.

[104] Z. Yi, Y. Zhao, P. Li, K. Ho, N. Blozowski, G. Walker, S. Jaffer, J. Tjong, M. Sain, Z. Lu, *Appl. Surf. Sci.* **2018**, *448*, 583.

[105] Q. Wei, M. Mukaida, Y. Naitoh, T. Ishida, *Adv. Mater.* **2013**, *25*, 2831.

[106] N. Kim, S. Kee, S. H. Lee, B. H. Lee, Y. H. Kahng, Y. R. Jo, B. J. Kim, K. Lee, *Adv. Mater.* **2014**, *26*, 2268.

[107] X. Wang, A. K. K. Kyaw, C. Yin, F. Wang, Q. Zhu, T. Tang, P. I. Yee, J. Xu, *RSC Adv.* **2018**, *8*, 18334.

[108] E. Yildirim, G. Wu, X. Yong, T. L. Tan, Q. Zhu, J. Xu, J. Ouyang, J. S. Wang, S. W. Yang, *J. Mater. Chem. C* **2018**, *6*, 5122.

[109] N. Kim, B. H. Lee, D. Choi, G. Kim, H. Kim, J. R. Kim, J. Lee, Y. H. Kahng, K. Lee, *Phys. Rev. Lett.* **2012**, *109*, 106405.

[110] J. Liu, X. Wang, D. Li, N. E. Coates, R. A. Segalman, D. G. Cahill, *Macromolecules* **2015**, *48*, 585.

[111] Q. Wei, M. Mukaida, K. Kirihara, T. Ishida, *ACS Macro Lett.* **2014**, *3*, 948.

[112] G. J. Snyder, E. S. Toberer, *Nat. Mater.* **2008**, *7*, 105.

[113] S. Dongmin Kang, G. Jeffrey Snyder, *Nat. Mater.* **2017**, *16*, 252.

[114] N. Hüsing, U. Schubert, *Angew. Chemie - Int. Ed.* **1998**, *37*, 22.

[115] M. Noroozi, M. Panahi-Sarmad, M. Abrisham, A. Amirkiai, N. Asghari, H. Golbaten-Mofrad, N. Karimpour-Motlagh, V. Goodarzi, A. R. Bahramian, B. Zahiri, *ACS Appl. Energy Mater.* **2019**, *2*, 5319.

[116] V. Apostolopoulou-Kalkavoura, P. Munier, L. Bergström, *Adv. Mater.* **2020**, *2001839*, 1.

[117] M. J. Oh, J. H. Lee, P. J. Yoo, *Adv. Funct. Mater.* **2021**, *31*, 1.

[118] J. (Jochen) Fricke, in *Springer Proc. Phys.*, **1986**, pp. 94–103.

[119] X. Lu, R. Caps, J. Fricke, C. T. Alviso, R. W. Pekala, *J. Non. Cryst. Solids* **1995**, *188*, 226.

[120] C. Bi, G. H. Tang, W. Q. Tao, *J. Non. Cryst. Solids* **2012**, *358*, 3124.

[121] P. Levitz, *J. Phys. Chem.* **1993**, *97*, 3813.

[122] C. Bi, G. H. Tang, Z. J. Hu, H. L. Yang, J. N. Li, *Int. J. Heat Mass Transf.* **2014**, *79*, 126.

[123] C. Bi, G. H. Tang, *Int. J. Heat Mass Transf.* **2013**, *64*, 452.

[124] A. Henry, *Annu. Rev. Heat Transf.* **2013**, *17*, 485.

[125] A. Sommerfeld, *Naturwissenschaften* **1927**, *15*, 825.

[126] D. Scheunemann, M. Kemerink, *Phys. Rev. B* **2020**, *101*, 75206.

[127] H. Wang, W. Chu, G. Chen, H. Wang, W. Chu, G. Chen, *Adv. Electron. Mater.* **2019**, *5*, 1900167.

[128] S. K. Yee, S. Leblanc, K. E. Goodson, C. Dames, *Energy Environ. Sci.* **2013**, *6*, 2561.

[129] S. Leblanc, S. K. Yee, M. L. Scullin, C. Dames, K. E. Goodson, *Renew. Sustain. Energy Rev.* **2014**, *32*, 313.

[130] Q. Weinbach, C. B. Nielsen, L. Biniek, *J. Mater. Chem. C* **2021**, *9*, 10173.

[131] P. M. Budd, N. B. McKeown, *Polym. Chem.* **2010**, *1*, 63.

[132] Q. Sun, Z. Dai, X. Meng, F. S. Xiao, *Chem. Soc. Rev.* **2015**, *44*, 6018.

[133] J. R. Li, R. J. Kuppler, H. C. Zhou, *Chem. Soc. Rev.* **2009**, *38*, 1477.

[134] *IUPAC. Compendium of Chemical Terminology, 2nd Ed. (the "Gold Book"). Compiled by A. D. McNaught and A. Wilkinson. Blackwell Scientific Publications, Oxford*, **1997**.

[135] F. Vilela, K. Zhang, M. Antonietti, *Energy Environ. Sci.* **2012**, *5*, 7819.

[136] X. Li, C. Zhang, S. Cai, X. Lei, V. Altoe, F. Hong, J. J. Urban, J. Ciston, E. M. Chan, Y. Liu, *Nat. Commun.* **2018**, *9*, 1.

[137] S. Liu, P. Gordiichuk, Z. S. Wu, Z. Liu, W. Wei, M. Wagner, N. Mohamed-Noriega, D. Wu, Y. Mai, A. Herrmann, K. Müllen, X. Feng, *Nat. Commun.* **2015**, *6*, 1.

[138] Y. Wang, Y. Shi, L. Pan, Y. Ding, Y. Zhao, Y. Li, Y. Shi, G. Yu, *Nano Lett.* **2015**, *15*, 7736.

[139] S. Wan, J. Guo, J. Kim, H. Ihee, D. Jiang, *Angew. Chemie Int. Ed.* **2009**, *48*, 5439.

[140] J. X. Jiang, F. Su, A. Trewin, C. D. Wood, N. L. Campbell, H. Niu, C. Dickinson, A. Y. Ganin, M. J. Rosseinsky, Y. Z. Khimyak, A. I. Cooper, *Angew. Chemie - Int. Ed.* **2007**, *46*, 8574.

[141] L. Pan, G. Yu, D. Zhai, H. R. Lee, W. Zhao, N. Liu, H. Wang, B. C. K. Tee, Y. Shi, Y. Cui, Z. Bao, *Proc. Natl. Acad. Sci. U. S. A.* **2012**, *109*, 9287.

[142] A. A. Talin, A. Centrone, A. C. Ford, M. E. Foster, V. Stavila, P. Haney, R. A. Kinney, V. Szalai, F. El Gabaly, H. P. Yoon, F. Léonard, M. D. Allendorf, *Science (80-.).* **2014**, *343*, 66.

[143] J. Germain, J. M. J. Fréchet, F. Svec, *J. Mater. Chem.* **2007**, *17*, 4989.

[144] L. Heng, X. Wang, J. Zhai, Z. Sun, L. Jiang, *ChemPhysChem* **2008**, *9*, 1559.

[145] X. Chen, K. Geng, R. Liu, K. T. Tan, Y. Gong, Z. Li, S. Tao, Q. Jiang, D. Jiang, *Angew. Chemie Int. Ed.* **2020**, *59*, 5050.

[146] H. S. Sasmal, A. Halder, S. H. Kunjattu, K. Dey, A. Nadol, T. G. Ajithkumar, P. Ravindra Bedadur, R. Banerjee, *J. Am. Chem. Soc.* **2019**, *141*, 20371.

[147] D. W. Burke, C. Sun, I. Castano, N. C. Flanders, A. M. Evans, E. Vitaku, D. C. McLeod, R. H. Lambeth, L. X. Chen, N. C. Gianneschi, W. R. Dichtel, *Angew. Chemie Int. Ed.* **2020**, *59*, 5165.

[148] S. Wan, J. Guo, J. Kim, H. Ihee, D. Jiang, *Angew. Chemie - Int. Ed.* **2008**, *47*, 8826.

[149] X. Feng, X. Ding, D. Jiang, *Chem. Soc. Rev.* **2012**, *41*, 6010.

[150] L. Sun, B. Liao, D. Sheberla, D. Kraemer, J. Zhou, E. A. Stach, D. Zakharov, V. Stavila, A. A. Talin, Y. Ge, M. D. Allendorf, G. Chen, F. Léonard, M. Dincă, *Joule* **2017**, *1*, 168.

[151] L. Sun, T. Miyakai, S. Seki, M. Dincă, *J. Am. Chem. Soc.* **2013**, *135*, 8185.

[152] Y. Kobayashi, B. Jacobs, M. D. Allendorf, J. R. Long, *Chem. Mater.* **2010**, *22*, 4120.

[153] F. Gándara, F. J. Uribe-Romo, D. K. Britt, H. Furukawa, L. Lei, R. Cheng, X. Duan, M. O'Keeffe, O. M. Yaghi, *Chem. - A Eur. J.* **2012**, *18*, 10595.

[154] D. Sheberla, L. Sun, M. A. Blood-Forsythe, S. Er, C. R. Wade, C. K. Brozek, A. Aspuru-Guzik, M. Dincă, *J. Am. Chem. Soc.* **2014**, *136*, 8859.

[155] K. J. Erickson, F. Léonard, V. Stavila, M. E. Foster, C. D. Spataru, R. E. Jones, B. M. Foley, P. E. Hopkins, M. D. Allendorf, A. A. Talin, A. Alec Talin, K. J. Erickson, F. Léonard, V. Stavila, M. E.

Foster, C. D. Spataru, R. E. Jones, M. D. Allendorf, A. A. Talin, B. M. Foley, P. E. Hopkins, *Adv. Mater.* **2015**, *27*, 3453.

[156] M. Dogru, T. Bein, *Chem. Commun.* **2014**, *50*, 5531.

[157] Y. Yusran, Q. Fang, V. Valtchev, *Adv. Mater.* **2020**, *32*, 2002038.

[158] S. Wan, F. Gándara, A. Asano, H. Furukawa, A. Saeki, S. K. Dey, L. Liao, M. W. Ambrogio, Y. Y. Botros, X. Duan, S. Seki, J. F. Stoddart, O. M. Yaghi, *Chem. Mater.* **2011**, *23*, 4094.

[159] X. Ding, L. Chen, Y. Honsho, X. Feng, O. Saengsawang, J. Guo, A. Saeki, S. Seki, S. Irle, S. Nagase, V. Parasuk, D. Jiang, *J. Am. Chem. Soc.* **2011**, *133*, 14510.

[160] E. Jin, M. Asada, Q. Xu, S. Dalapati, M. A. Addicoat, M. A. Brady, H. Xu, T. Nakamura, T. Heine, Q. Chen, D. Jiang, *Science (80-.).* **2017**, *357*, 673.

[161] Q. Zhang, M. Dai, H. Shao, Z. Tian, Y. Lin, L. Chen, X. C. Zeng, *ACS Appl. Mater. Interfaces* **2018**, *10*, 43595.

[162] M. Wang, M. Wang, H. H. Lin, M. Ballabio, H. Zhong, M. Bonn, S. Zhou, T. Heine, E. Cánovas, R. Dong, X. Feng, *J. Am. Chem. Soc.* **2020**, *142*, 21622.

[163] J. M. Rotter, R. Guntermann, M. Auth, A. Mähringer, A. Sperlich, V. Dyakonov, D. D. Medina, T. Bein, *Chem. Sci.* **2020**, *11*, 12843.

[164] L. Wang, B. Dong, R. Ge, F. Jiang, J. Xu, *ACS Appl. Mater. Interfaces* **2017**, *9*, 7108.

[165] J. S. M. Lee, A. I. Cooper, *Chem. Rev.* **2020**, *120*, 2171.

[166] A. E. Sadak, E. Karakuş, Y. M. Chumakov, N. A. Dogan, C. T. Yavuz, *ACS Appl. Energy Mater.* **2020**, *3*, 4983.

[167] Y. Chumakov, F. Aksakal, A. Dimoglo, A. Ata, S. A. Palomares-Sánchez, *J. Electron. Mater.* **2016**, *45*, 3445.

[168] J. Yang, Y. W. Yang, *Small* **2020**, *16*, 1906846.

[169] K. Kang, S. Schott, D. Venkateshvaran, K. Broch, G. Schweicher, D. Harkin, C. Jellett, C. B. Nielsen, I. McCulloch, H. Sirringhaus, *Mater. Today Phys.* **2019**, *8*, 112.

[170] R. Kroon, J. D. Ryan, D. Kiefer, L. Yu, J. Hynynen, E. Olsson, C. Müller, *Adv. Funct. Mater.* **2017**, *27*, 1704183.

[171] C. Daniel, C. Dammer, J. M. Guenet, *Polymer (Guildf).* **1994**, *35*, 4243.

[172] Y. Shi, G. Yu, *Chem. Mater.* **2016**, *28*, 2466.

[173] W. He, X. Zhang, in *Conduct. Polym.* (Ed.: F. Yilmaz), InTech, **2016**, pp. 49–72.

[174] M. E. El-Naggar, S. I. Othman, A. A. Allam, O. M. Morsy, *Int. J. Biol. Macromol.* **2020**, *145*, 1115.

[175] X. Zhang, D. Chang, J. Liu, Y. Luo, *J. Mater. Chem.* **2010**, *20*, 5080.

[176] Q. Weinbach, S. V. Thakkar, A. Carvalho, G. Chaplais, J. Combet, D. Constantin, N. Stein, D. Collin, L. Biniek, *Front. Electron. Mater.* **2022**, *2*, 875856.

[177] A. W. Francis, *J. Phys. Chem.* **1954**, *58*, 1099.

[178] B. Yao, H. Wang, Q. Zhou, M. Wu, M. Zhang, C. Li, G. Shi, *Adv. Mater.* **2017**, *29*, 1700974.

[179] A. G. Guex, J. L. Puetzer, A. Armgarth, E. Littmann, E. Stavrinidou, E. P. Giannelis, G. G. Malliaras, M. M. Stevens, *Acta Biomater.* **2017**, *62*, 91.

[180] A. M. D. Wan, S. Inal, T. Williams, K. Wang, P. Leleux, L. Estevez, E. P. Giannelis, C. Fischbach, G. G. Malliaras, D. Gourdon, *J. Mater. Chem. B* **2015**, *3*, 5040.

[181] M. P. Gordon, E. W. Zaia, P. Zhou, B. Russ, N. E. Coates, A. Sahu, J. J. Urban, *J. Appl. Polym. Sci.* **2017**, *134*, 44070.

[182] X. Wang, P. Liu, Q. Jiang, W. Zhou, J. Xu, J. Liu, Y. Jia, X. Duan, Y. Liu, Y. Du, F. Jiang, *ACS Appl. Mater. Interfaces* **2019**, *11*, 2408.

[183] R. Maeda, H. Kawakami, Y. Shinohara, I. Kanazawa, M. Mitsuishi, *Mater. Lett.* **2019**, *251*, 169.

[184] R. Maeda, Y. Shinohara, H. Kawakami, Y. Isoda, I. Kanazawa, M. Mitsuishi, *Nanotechnology* **2020**, *32*, 135403.

[185] Z. Li, H. Sun, C. L. Hsiao, Y. Yao, Y. Xiao, M. Shahi, Y. Jin, A. Cruce, X. Liu, Y. Jiang, W. Meng, F. Qin, T. Ederth, S. Fabiano, W. M. Chen, X. Lu, J. Birch, J. W. Brill, Y. Zhou, X. Crispin, F. Zhang, *Adv. Electron. Mater.* **2018**, *4*, 1700496.

[186] S. Han, F. Jiao, Z. U. Khan, J. Edberg, S. Fabiano, X. Crispin, *Adv. Funct. Mater.* **2017**, *27*, 1703549.

[187] N. Yanagishima, S. Kanehashi, H. Saito, K. Ogino, T. Shimomura, *Polymer (Guildf).* **2020**, *206*, 122912.

[188] X. Sun, Y. Wei, J. Li, J. Zhao, L. Zhao, Q. Li, *Sci. China Mater.* **2017**, *60*, 159.

[189] F. Jia, R. Wu, C. Liu, J. Lan, Y. H. Lin, X. Yang, *ACS Sustain. Chem. Eng.* **2019**, *7*, 12591.

[190] J. Wang, K. Cai, S. Shen, *Org. Electron.* **2014**, *15*, 3087.

[191] C. M. Palumbiny, F. Liu, T. P. Russell, A. Hexemer, C. Wang, P. Müller-Buschbaum, C. Heller, C. J. Schaffer, V. Körstgens, G. Santoro, S. V Roth, P. Müller-Buschbaum, F. Liu, T. P. Russell, A. Hexemer, C. Wang, P. Müller-Buschbaum, *Adv. Mater.* **2015**, *27*, 3391.

[192] Z. U. Khan, J. Edberg, M. M. Hamedi, R. Gabrielsson, H. Granberg, L. Wågberg, I. Engquist, M. Berggren, X. Crispin, *Adv. Mater.* **2016**, *28*, 4556.

[193] M. Liu, R. Cheng, R. Qian, *J. Polym. Sci. Part B Polym. Phys.* **1995**, *33*, 1731.

[194] M. A. Shahbazi, M. Ghalkhani, H. Maleki, *Adv. Eng. Mater.* **2020**, *22*, 2000033.

[195] X. Zhang, C. Li, Y. Luo, *Langmuir* **2011**, *27*, 1915.

[196] N. Tonanon, Y. Wareenin, A. Siyasukh, W. Tanthapanichakoon, H. Nishihara, S. R. Mukai, H. Tamon, *J. Non. Cryst. Solids* **2006**, *352*, 5683.

[197] F. W. Liu, F. Zhong, S. C. Wang, W. H. Xie, X. Chen, Y. G. Hu, Y. Y. Ge, Y. Gao, L. Wang, Z. Q. Liang, *Chinese Phys. B* **2022**, *31*, 027303.

[198] S. Wei, X. Huang, L. Deng, Z. C. Yan, G. Chen, *Compos. Sci. Technol.* **2021**, *208*, 108759.

[199] C. Yu, K. Choi, L. Yin, J. C. Grunlan, *ACS Nano* **2011**, *5*, 7885.

[200] G. P. Moriarty, S. De, P. J. King, U. Khan, M. Via, J. A. King, J. N. Coleman, J. C. Grunlan, *J. Polym. Sci. Part B Polym. Phys.* **2013**, *51*, 119.

[201] H. J. Goldsmid, *Materials (Basel).* **2014**, *7*, 2577.

[202] M. Goel, M. Thelakkat, *Macromolecules* **2020**, *53*, 3632.

CHAPTER II. ELABORATION OF P-TYPE PEDOT:PSS POROUS MATERIALS WITH VARIOUS RANGE OF POROSITIES: EFFECT ON TE PROPERTIES

II. ELABORATION OF P-TYPE PEDOT: PSS POROUS MATERIALS WITH VARIOUS RANGE OF POROSITIES: EFFECT ON TE PROPERTIES

1. INTRODUCTION

Chapter I emphasized the interest of porosity in organic TE materials with a particular focus on the well-known p-type material PEDOT: PSS. Chapter II will discuss the method used to prepare porous materials that would ideally meet the "phonon glass electron crystal" concept. As discussed in the material design section in I.1.6., we seek fine control over the porous structure while maintaining high order of the conducting polymer.

Inducing and controlling porosity in PEDOT: PSS is not straightforward. As discussed in section I.2, porous PEDOT: PSS can be obtained by solvent drying techniques such as lyophilization,[1,2] freeze-drying,[3] ice-templating[4] or supercritical drying.[5] Interestingly, different porosity ranges (meso- or macroporosity) can be obtained depending on the drying method. But most of the processes have been applied to the commercial dispersion of PEDOT: PSS. There is a clear lack of control of the pore structure and no real understanding of the pore formation mechanism. As an example, lyophilization (= freeze-drying) of the commercial dispersion led to low porosity and uncontrolled pore structures.[1,2] During freeze-drying, ice crystals form when the sample is frozen, leaving cavities after solvent removal. It has been demonstrated that mastering the freezing of water is one of the keys for controlling porosity.[4,6–8] However, freezing is a complex process as it depends on many variables, a strained and random environment such as a polymer dispersion makes it even more complex. In the case of PEDOT:PSS, the final porous structures were not well defined and various types of morphologies such as lamellar or interconnected open pores were reported since they were produced from a randomly dispersed PEDOT: PSS dispersion in water.

To overcome this issue, another strategy to produce a porous PEDOT: PSS sample is to first form a gel network before drying the solvent. Another interest of the gelation step is to increase the polymer chain order in the final porous sample. As discussed in section I.2.3.2, PEDOT: PSS gels were obtained via the addition of H_2SO_4,[9] ethanol,[10,11] or re-swelling of dried PEDOT: PSS.[3,12] By analogy with the observed enhancement of the electrical conductivity of solvent-treated PEDOT: PSS thin films (attributed to structural modifications), similar behaviors can be expected when gels are formed with the same solvents or acids.[13–16] These results highlight the importance of forming a 3D network before drying but also the significance of controlling the drying step parameters. However, even when a gel network was obtained, none of the works discussed above demonstrated a fine control of the structure after drying. The main challenge reported in the literature is the control of both the pore structure during the drying step and the preservation of good charge transport properties.

In this chapter, we propose to combine the two steps described above: gelation of PEDOT: PSS followed by a controlled drying. We aim to elaborate porous materials of various structures from the same polymer gel network. First, we strive to understand the commercial PH1000 dispersion composition and structure. Then, a PEDOT: PSS hydrogel is formed, and the mechanism of gelation is discussed. Three drying methods leading to different porous structures are used to produce xerogels, aerogels, and cryogels. Finally, the thermoelectric properties of the different porous materials are studied, and the structure-properties relationships are discussed. For comparison, the dispersion (prior gelation) is also freeze-dried. For clarity purpose, we will use hereafter the term "lyophilization" when this drying technique is applied to the dispersion and "freeze-drying" when this method is applied to the gel.

2. FROM THE DISPERSION TO THE HYDROGEL

2.1. STRUCTURAL STUDY OF THE INITIAL DISPERSION

In order to shed some light on the gelation mechanism, we first studied the PEDOT: PSS dispersion. Please note that in this thesis, we only used the commercial aqueous dispersion CLEVIOS PH1000 provided by Heraeus.

Various reports in the literature attempt to describe PEDOT: PSS structure and arrangement in both dispersion and thin films. To date, no consensus has been reached amongst the different models. However, it should be noted that some major features are commonly reported. The dispersion contains the two charged polymers in a total weight percentage of 1.0-1.3%wt. PEDOT is a semi-conducting polymer while PSS is an insulator. In the commercial blends, PSS is present in excess (1:2.5 weight ratio PEDOT:PSS for PH1000) to allow dispersion in water and favor wet processability. Although there is no information provided by the supplier on the chains' lengths, it is commonly accepted in the literature that PSS chains are rather long while the PEDOT chains are only composed of a few repeat units.[17,18] The polymer blend is claimed by the supplier to be in the form of spherical micelles with a mean diameter of 30 nm. Only a few analyses on PEDOT: PSS structural model in dispersion are reported due to the difficulty to perform routine analysis (strong absorbance in visible spectra, aggregation). It should be noted that structural models built on films studies cannot be applied to the dispersion state due to the diverse drying effects and aggregation at the solid state. However, the granular structure of a PEDOT-rich core and a PSS-rich shell is often described in the literature.[18–21] It has also been reported that PEDOT crystallites tend to be constituted of several π-stacked PEDOT oligomers.[21–24] An overview of representative morphological models is displayed in Figure II.1. Clearly there are still interrogations in the scientific community, including on the global shape and size of PEDOT: PSS agglomerates. Spheres,[18] ellipsoids,[21] and less ordered grains[13,23–25] have been reported.

The synthesis process and nature of the commercial batch could be at the origin of the different observed structures. To shed some light on the stock PH1000 commercial dispersion, we have been using Transmission Electron Microscopy (TEM) and X-ray scattering means to understand gelation mechanisms, further explained in this chapter. Note that attempts on multi-angle DLS were done. However, problems of stability and reproducibility were encountered. Hence, the obtained results are too preliminary at this stage to be considered.

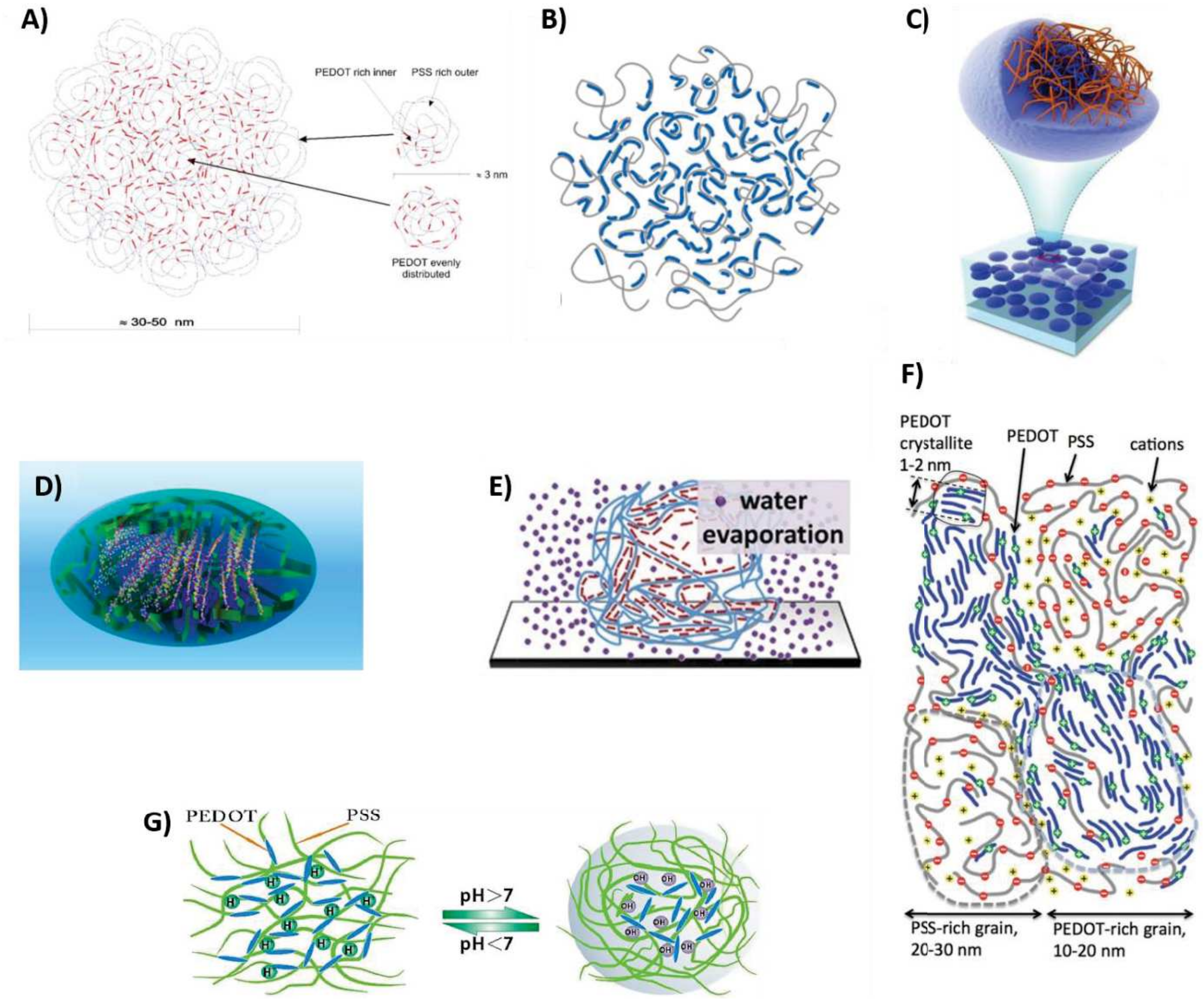

Figure II.1: Overview of several representative models of stock commercial PEDOT: PSS in solution state. A) CLEVIOS P spherical model reproduced from [18]*; B) CLEVIOS PH1000 model in dispersion reproduced from* [20]*; C) Amorphous CLEVIOS PH1000 grains model, PSS chains are in red and PEDOT oligomers are in blue, reproduced from* [13]*; D) Ellipsoidal model of CLEVIOS PH1000 with a PEDOT-rich core and PSS-rich shell, reproduced from* [21]*; E) Wet pristine CLEVIOS PH1000 deposited on a glass substrate, PSS chains are in blue and PEDOT oligomers are in red, reproduced from* [23]*; F) CLEVIOS PH1000 grain model composed of PEDOT-rich grains with crystalline domains due to PEDOT π-stacking, and PSS-rich domains, reproduced from* [24]*; G) Model of synthesized PEDOT: PSS representing self-assembly PEDOT: PSS system based on pH variations, reproduced from* [26]*.*

2.1.1. CRYO-TRANSMISSION ELECTRONIC MICROSCOPY OBSERVATIONS OF THE DISPERSION

Experimental details of the preparation of the dispersion for cryo-TEM experiments can be found in the Experimental section.

Cryo-TEM allows visualizing particles in their dispersion state by rapid vitrification in a thin layer of solvent (in this case, water). Although cryo-TEM requires complex sample preparation, it is the only technique able to image nanoparticles in their native form, without any drying effects. Figure II.2.A reveals that the dispersion is mainly composed of fibrils with a mean diameter of 5 ± 2 nm and a length of 110 ± 35 nm. In contrast with literature and Heraeus technical reports, no spherical particles were observed. The fibrils' dimensions were analyzed on TEM images by the ridge detection method on ImageJ software as depicted in Figure II.2.B. This plugin is based on Steger's algorithm for lines and ridges detection.[27] It was successfully used to analyze grayscale images in the literature.[28] It allows precise measurement of the fibrils' thickness, displayed in Figure II.2.C. Thanks to this plugin, the mean thickness of the fibrils was estimated on over 9000 measurements. The resulting histogram can be fitted with a Gaussian curve to calculate the mean diameter of the fibrils. Although it is a great tool, ridge detection was not well suited to estimate the fibrils' length due to the important lack of contrast between amorphous ice (background) and fibrils on the TEM images. Hence, their length was estimated by following the fibrils with the freehand line tool of the software and measuring their length as shown in Figure II.2.D (estimation of the length made on 100 measurements). However, this measurement is only an estimation as some parts of the fibrils may not be fully visible due to their orientation towards the beam.

This not-expected fibrillar morphology has also been reported by Yuk et al. (cryo-TEM images of PH1000 dispersion showing nanofibrils).[29] However the authors did not comment on the possible origin of these fibrils.

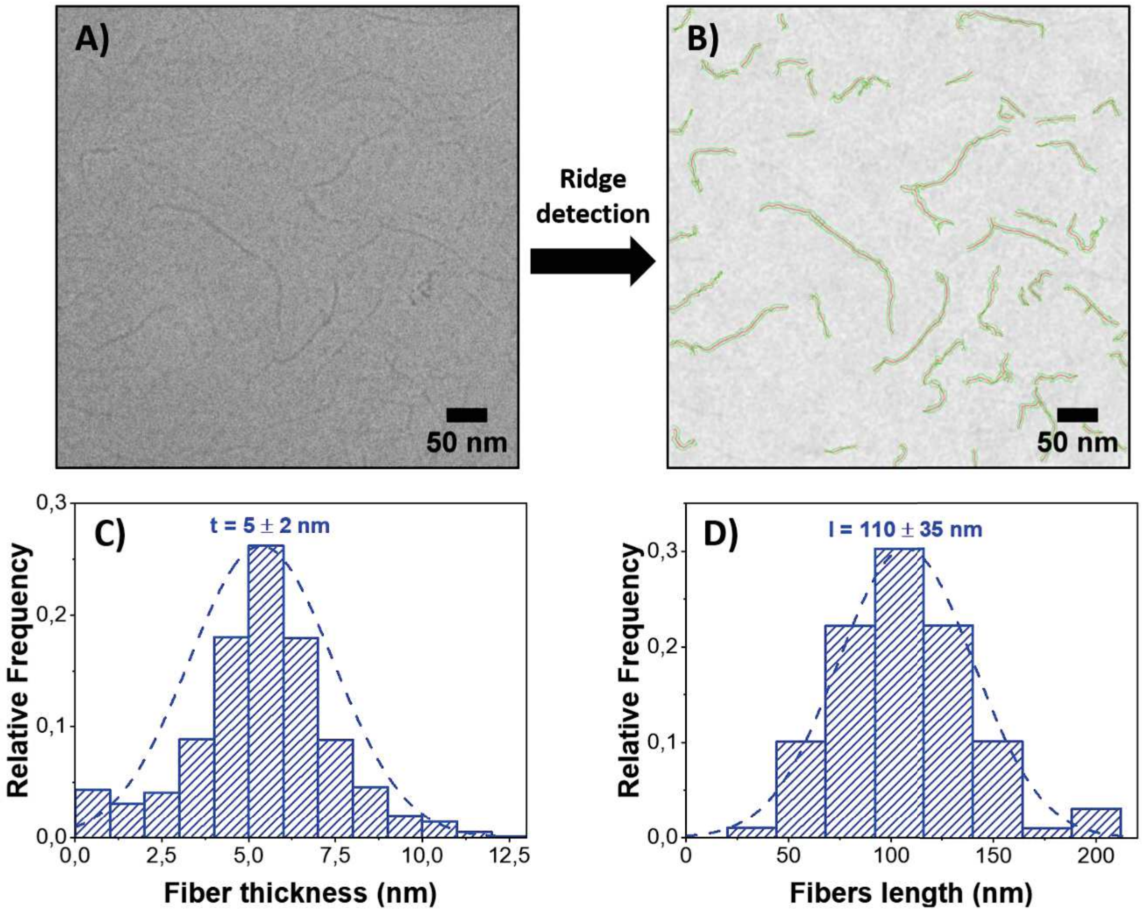

Figure II.2: A) cryo-TEM image of the PH1000 dispersion diluted eight times; B) Analyzed cryo-TEM image via the ridge detection, the red lines follow the fibrils' center, the green lines estimate the thickness; C) Fibrils' thickness histogram analysis made on over 9000 measures; D) Fibrils' length histogram analysis, the ridge detection is not suited for these images due to lack of contrast, the fibrils' length was estimated by measuring them with the freehand tool and measuring length on ImageJ software, 100 measurements were taken.

2.1.2. X-RAY SCATTERING OF THE PH1000 DISPERSION

To confirm the 1D shape of the objects, we performed Small-Angle X-ray Scattering (SAXS) measurements on the PH1000 dispersion at different concentrations. A monochromatic X-ray beam is passed through several apertures to control its angular divergence before reaching the sample. The low angle scattered intensity is then recovered by a 2D detector recording the number of scattered photons received in a given time. After an azimuthal average of the detected X-rays, one can plot the intensity against the wavevector q [Å^{-1}]. In a semi-dilute solution of identical particles, one can analyze the shape of a single particle and the positional correlation of the objects by analytical or numerical evaluation of the form and structure factors, respectively.[30,31] More information can be found in Experimental section.

The dispersion was vortexed and filtered through a PVDF 0.45µm filter. Then the dispersion was diluted twice (c/2), four times(c/4), and eight times (c/8) with deionized water. To increase the concentration of the dispersion, the vortexed and filtered dispersion was left in an open vial under an argon flow for 4h to produce cx1.75. SAXS measurements were performed on the SWING beamline of the SOLEIL synchrotron, other experimental details can be found in the Experimental section.

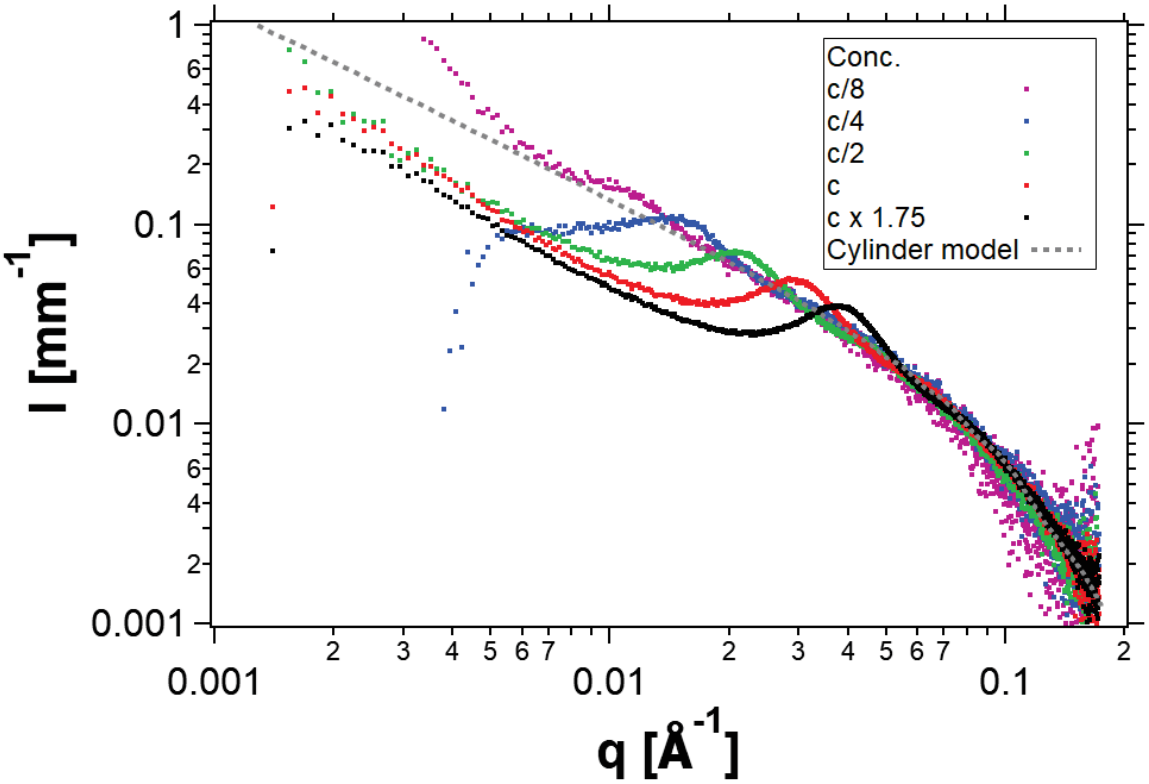

Figure II.3: Serial dilution of PH1000 SAXS intensity profiles as a function of the wavevector q, the gray data correspond to a fitted cylinder model.

As shown in Figure II.3, SAXS measurements were performed on the stock filtered PH1000 dispersion and dilutions. We observe one intensity peak situated in the $0.01\ \text{Å}^{-1} < q < 0.1\ \text{Å}^{-1}$ range whose position varies with the concentration. At low q, the intensity is noisy due to imprecision in subtracting the solvent scattering, and parasitic. For $q < 0.01\ \text{Å}^{-1}$, however, the same trend is observed for all the samples. Information on the shape of the particles can be determined by the Porod regime analysis. In the short-wavelength limit ($q < 0.01$ Å^{-1}), the SAXS intensity is proportional to the surface area of the object and inversely proportional to q power laws. The power law factor varies on the shape of the object. The form factor is directly related to the morphology of the particle. This numerical analysis can only be realized on a few types of shapes: spheres (3D), discs (2D), and rods (1D). It has been reported that in the Porod regime, the asymptotic q dependence of the form factor F(q) is such that $|F(q)|^2 \propto q^{-4}, q^{-2}$, and q^{-1} for objects of dimensionality = 3, 2, and 1, respectively. Such analysis provides useful information on the morphology of the observed particles.

In the Porod regime ($q < 0.01$ Å^{-1}), it is clear that the intensity follows a power law trend of q^{-1} suggesting one-dimensional objects. According to the TEM images, these results correlate with the morphology of PH1000 dispersion in the form of nanofibrils with a high aspect ratio. Moreover, performing Guinier's analysis in the long-wavelength limit allows us to determine the transversal radius of such objects. A cylinder model from the NIST SANS and USANS data analysis macro for Igor pro 7 was plotted to best fit the experimental data.[32] We considered rods of infinite length and finite thickness with a polydispersity in radius. The SAXS analysis shows a smaller fibril diameter (of around 1.6 ± 1.5 nm, with a relative polydispersity of 0.55) than the TEM images (of 5 ± 2 nm) but both these values are coherent within the experimental uncertainty.

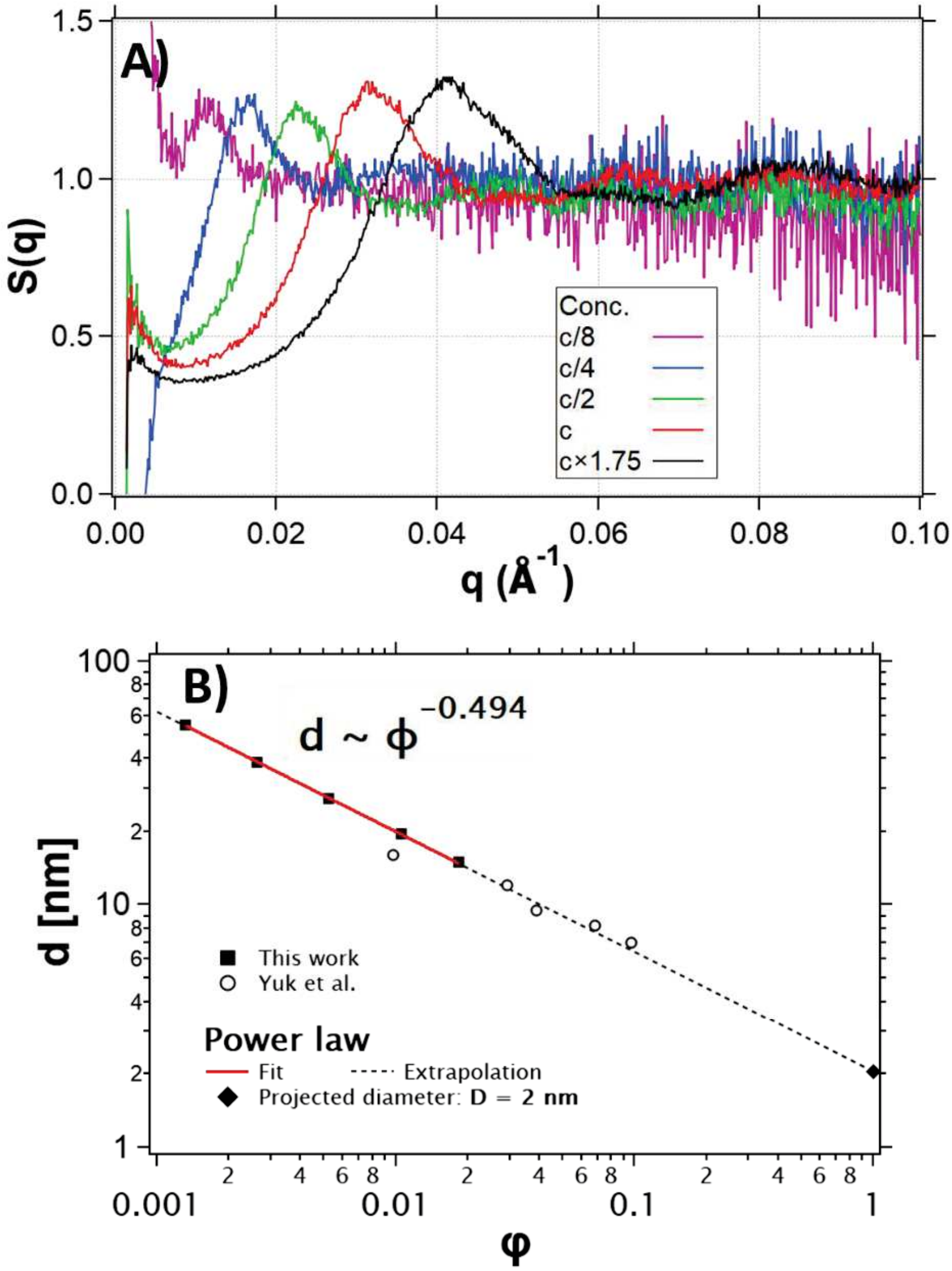

Figure II.4: A) Structure factor plotted as a function of the wavevector q; B) The characteristic distance d between two closest neighbors as a function of the volume fraction φ, the trends follow a $\varphi^{-1/2}$ power law.

To confirm the morphology of PEDOT: PSS particles, the structure factor S(q) (obtained by dividing the intensity curves with the model form factor) was also studied. S(q) was plotted against the scattering intensity as shown in Figure II.4.A. Clearly, q_{max} (at 0.037 Å^{-1} for c) is dependent on the concentration of the dispersion. The structure factor describes the spatial arrangement of particles with respect to each other. Here, we consider the system as parallel cylinders with d (corresponding to $2\pi/q_{max}$), the typical distance between neighbors. Hence, we can assume that the PEDOT: PSS volume fraction ϕ is proportional to $\sim \pi \frac{R^2}{d^2}$ meaning that the distance d varies like d $\sim \phi^{-\frac{1}{2}}$. The plot in Figure II.4.B shows the evolution of the volume fraction against d; the distance indeed follows a power law very close to $\phi^{-1/2}$. This behavior is typical of fiber-like object interaction when their concentration is increased. If we extrapolate this trend until $\phi \sim 1$ (i.e., the cylinders are in contact with each other), we can estimate d $\sim 2R$. This diameter of 2 nm correlates well with the estimated fibril thickness extracted from the form factor. Moreover, we can confirm these results with the data extracted from Yuk and coworkers, who realized different concentrations of PH1000 by lyophilization and redispersion.[29] They also analyzed the structure factor as a function of the dispersion concentration, and their points are very close to the dilution law we obtain although, it fitted separately, follow a power law $\phi^{-\frac{1}{2}}$.

Surprisingly, the diameter estimated by SAXS is smaller than the one observed by cryo-TEM. According to Takano et al. model, it is quite likely that a 3-4 nm loose PSS shell surrounds the PEDOT-rich core.[21] However, X-ray scattering length densities of the various moieties are proportional to their electron densities; hence we might not be able to detect the PSS shell (closer in electron density to water) with this technique. The difference in fibril diameter observed by SAXS and cryo-TEM supports the hypothesis of the core-shell structure of PEDOT: PSS. The two techniques confirm the presence of PEDOT: PSS nanofibrils of thicknesses below 5 nm in the stock PH1000 commercial dispersion.

So far, the PEDOT: PSS structure in the dispersion state was always considered as polyelectrolyte microgels[33] or micellar[13,21] structures. These structural models were proposed based on a low q intensity profile following a q^{-2} / q^{-3} behavior (unlike our findings), and a scaling behavior of $\phi^{-1/2}$ with concentration observed by SANS measurement (like our findings) for a similar PEDOT: PSS dispersion.[34] This striking difference in experimental data cannot be explained at the moment. But the clear demonstration of fibrils in our dispersion cannot correlate with the widely reported spherical micelles model or with the technical data given by the supplier.

2.2. FORMATION OF PEDOT: PSS HYDROGEL

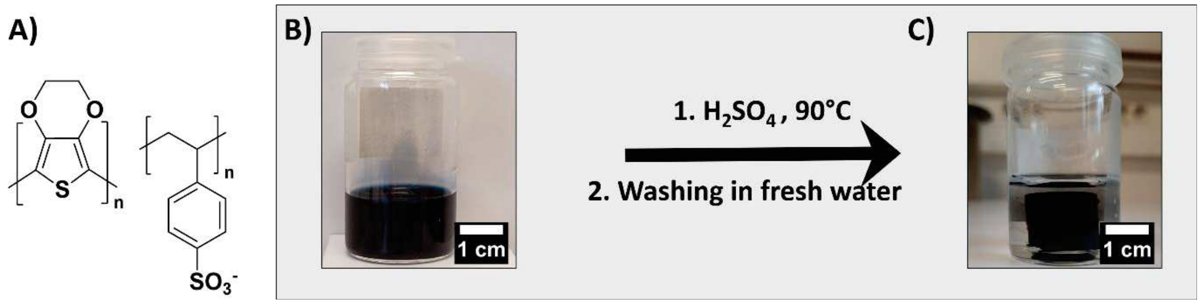

Figure II.5 Gelation setup. A) Chemical structure of PEDOT: PSS; B) Picture of the dark blue PH1000 dispersion; C) Picture of the gel floating in its supernatant

PEDOT: PSS hydrogels were prepared by treating the PH1000 dispersion in 0.1 mol.L^{-1} H_2SO_4 following the process described by Yao et al.[9] The chemical structure and gelation protocol are illustrated in Figure II.5. After heating at 90°C, a robust gel floating in a transparent supernatant was formed and then rinsed with fresh deionized water three times within 48h.

This method can be readily scaled to form PEDOT: PSS hydrogels in large dimensions (> 10 mm thick and > 10 mm in diameter). The samples can be easily manipulated with tweezers and are slightly elastic. The gel keeps the shape of the mold (in our case a flat-bottom vial) but decreases in volume. In the following, a combination of multiscale spectroscopy and microscopy techniques is used to understand better the mechanism of hydrogel formation.

2.2.1. STRUCTURAL MODIFICATIONS

First the change of structure upon acidification of the PEDOT: PSS dispersion was followed by cryo-TEM. As discussed above, this technique allows observing particles in dispersion in their native state. Cryo-TEM images of the acidified dispersion are presented in Figure II.6.A.

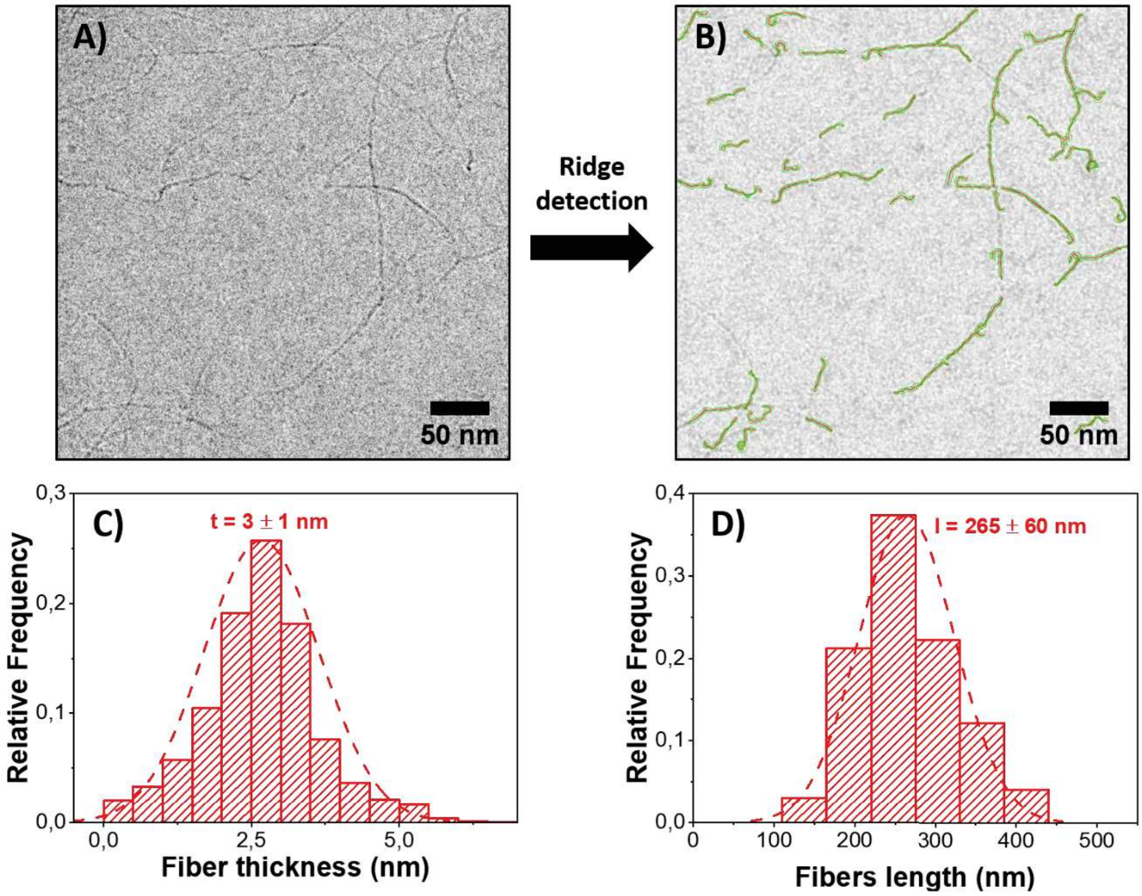

Figure II.6: A) cryo-TEM image of the diluted and acidified PH1000 dispersion; B) Analyzed cryo-TEM image via the ridge detection, the red lines follow the fibrils' center, the green lines estimate the thickness; C) Fibrils' thickness histogram analysis made on over 5000 measures; D) Fibrils' length histogram analysis, the ridge detection is not suited for these images due to lack of contrast, the fibrils' length was estimated by highlighting them with the freehand tool and measuring their length with the ImageJ software, 100 measurements were taken.

The dispersion was diluted 100 times for accurate observation of the objects. Moreover, only a very low concentration (4.8 x 10^{-3} mol/L) of H_2SO_4 was added to the dispersion to prevent complete gelation which would make impossible cryo-TEM observations. As for the dispersion, only fibrils could be observed in the acidified dispersion, they are slightly more contrasted and more in numbers. The observed fibrils are analyzed by the ridge detection method discussed above as depicted in Figure II.6.B. Surprisingly, these objects are thinner and longer than in the original dispersion. A mean thickness estimated over 5000 measurements of 3 ± 1 nm was obtained (see Figure II.6.C). Again, due to the low contrast, the fibrils' lengths of 265 ± 60 nm were estimated using the freehand line and measure tool.

The fibrils exhibit a higher persistence length (20-40 nm) than in the dispersion. The observations made with regular TEM show similar morphology of the objects (see Figure II.7.A-B). Upon blotting, the acidified PEDOT: PSS dispersion also shows fibril-like structures. Intertwined fibrils are observed, confirming the native structure observed by cryo-TEM. Entanglement is likely induced by the blotting process with an excess of fibril concentration. It can be anticipated that higher acid concentration can also lead to these entangled fibrils' formation. One explanation of the fibrils' thickness reduction would be the removal of the excess PSS shell. This has been suggested in previous reports[13,35] and will be confirmed in a later section by XPS.

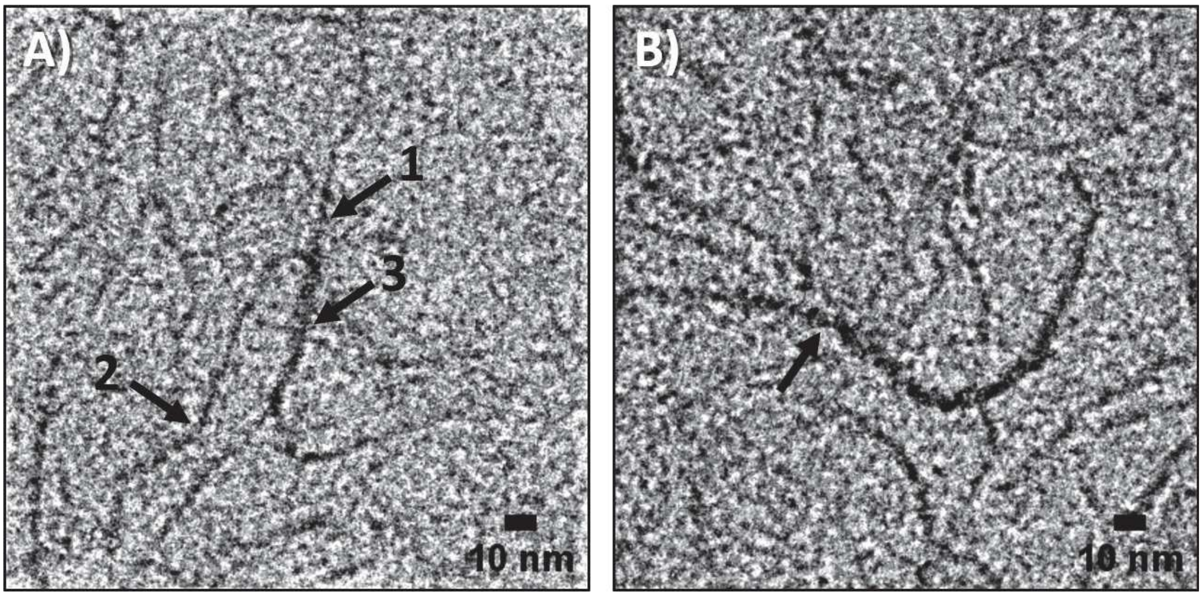

Figure II.7: TEM images of the acidified dispersion with positive stain at high magnification. A) The intertwinement of two fibrils can be clearly seen, fibril 2 entangles around fibril 1 to form a thicker fiber highlighted by arrow 3. B) A thicker fiber formed by the intertwinement of at least two fibrils is highlighted by the black arrow.

To reveal the inner structure of the final hydrogel, cryo-SEM was performed by quickly dipping the hydrogel in liquid ethane. This rapid freezing should avoid any ice crystal formation and preserve the native structure of the hydrogel. Figure II.8.A depicts the fibrillar morphology of the hydrogel, which structure is consistent with the fibril observed in the acidified dispersion. This 3D network is composed of an entanglement of thick fibers (13 ± 4 nm of mean diameter) and voids (10-50 nm wide). We suggest from the TEM analysis of the acidified dispersion that several fibrils tend to agglomerate into thicker ones (see Figure II.7.A) due to the strong π-π interactions between the PEDOT chains, resulting in a robust 3D network. The 3D fibrillar network of the hydrogel revealed by cryo-SEM (see Figure II.8.A) is in contradiction with previous reports. Yao et al.[9] claimed that the hydrogel structure is composed of micrometer-sized porous channels. In fact, the authors presented SEM images of the PEDOT: PSS gels after freeze-drying, not representative of the native hydrogel structure (revealed by our cryo-SEM experiment) but of its dried state. As we will discuss later, the drying process can strongly impact the network.

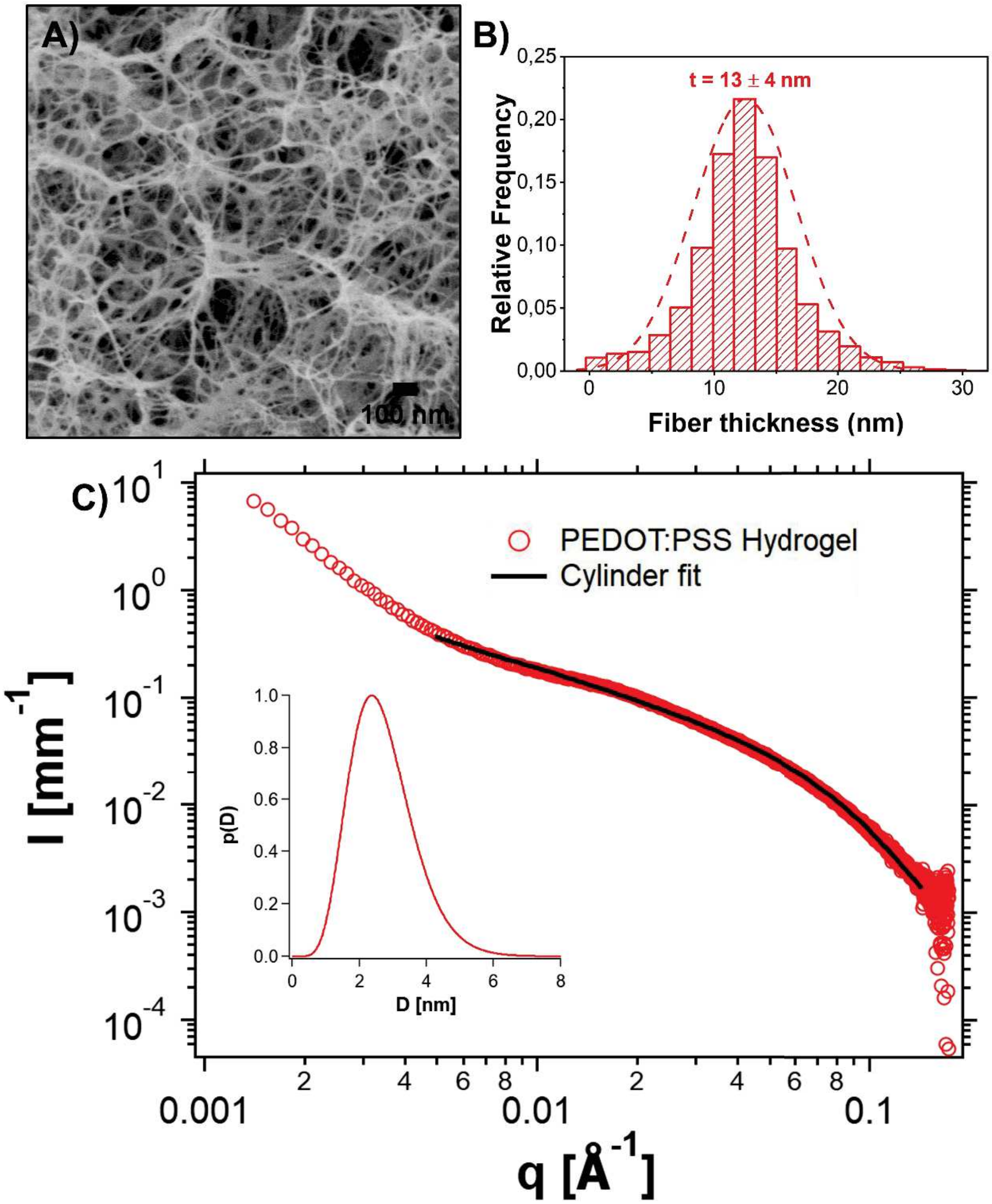

Figure II.8: A) Cryo-SEM image of the fibrillar morphology of the hydrogel; B) Fiber thickness distribution histogram made over 50000 measurements; the thickness was measured using the ridge detection plugin of ImageJ software. C) X-ray scattering intensity profile of a PEDOT: PSS hydrogel, the red dots correspond to the experimental data after subtraction of solvent's intensity profile, and the black line to a cylinder fit with radius polydispersity. The inset corresponds to the Schulz distribution of the cylinder fit diameter.

The hydrogel network was analyzed by SAXS and WAXS on the SOLEIL beamline. The intensity profile displayed in Figure II.8.C shows a similar trend to the dispersion (Figure II.3).

Indeed, in the Porod regime, the profile follows a q^{-1} power law, corresponding to a one-dimensional object. At very small angles ($q < 0.005$ Å^{-1}), the intensity profile rises and follows a slightly steeper power law between q^{-1} and q^{-2}. This rise means that the objects are no longer one-dimensional on large length scales, or that they interact. The intensity profile transcribes the average of the scattering of the objects on a large surface of the sample. The gel being made of fibers and nodes, it is possible that the presence of these nodes has an influence on the intensity profile at such wavelengths. It is difficult to assign a conclusive origin to this rise. However, by crossing the results obtained by cryo-TEM and cryo-SEM, we can still affirm that the network is made of 1D objects. Hence, the data were fitted with a cylinder model with uniform scattering length density and polydisperse radius from the NIST SANS and USANS data reduction macro for Igor pro 7.[32] The Schulz distribution in radius is plotted in the inset of Figure II.8.C. According to the cryo-TEM and cryo-SEM images, the fibers can be considered infinitely long compared to their diameter. The cylinder-fit yields a diameter of about 2.5 nm, confirming the cryo-TEM observations. These results well demonstrate the structural modification of the objects upon acidification of the dispersion. The acidified fibrils, of ≈ 2.5 nm in diameter, tend to entangle into thicker fibers composing the final 3D network. This suggests that the protective PSS shell layer was removed or somehow modified after the addition of H_2SO_4. Actually, modifications of the PEDOT: PSS ratio were reported after acid treatment of PEDOT: PSS films (see section I.1.4.1).

2.2.2. RATIO MODIFICATION

As mentioned above (see Figure II.5.C), the obtained hydrogels are contracted compared to their molds suggesting a syneresis effect (expulsion of liquid from the pores). This implies a modification of the polymer chains packing (confirmed by microscopy and X-ray scattering) and/or a rearrangement between PEDOT and PSS upon acid treatment. PEDOT vs. PSS ratio before and after acid treatment can be followed by X-ray Photoelectron Spectroscopy (XPS), in the S 2P XPS spectra of the dried dispersion and the dried gel (see Figure II.9.A-B). Both PEDOT and PSS contain one sulfur atom per repeat unit: within the thiophene ring for PEDOT and in the sulfonate moiety for PSS. Due to their different chemical environment, their binding energies are different and it is possible to discriminate their XPS signature peaks.[36,37]

The peak at 168.5 eV is related to the sulfur atoms of the sulfonate moiety of the PSS while the doublet at 164 and 165 eV is related to the sulfur atoms of the thiophene ring in PEDOT.[36,37] This asymmetric peak is due to the positive charges that accumulate along the doped PEDOT chain and are partially located on the sulfur atoms.[37,38] The difference of contribution of the $2p_{1/2}$ (165 eV) and $2p_{3/2}$ (164 eV) suggests a modification of the doping state of PEDOT. The intensity ratio between the peaks of PEDOT and PSS gives the sulfonate/thiophene unit ratio ($R_{S/T}$). This molar ratio drops from 2.33 for PH1000 dried dispersion to 1.43 for dried gels indicating partial protonation and removal of PSS during gelation (i.e., acid treatment and rinsing processes). Actually, during acid treatment, some PSS chains of the outside shell of the fibers are neutralized, after rinsing the gel, the PSSH can be washed away. Since pKa_1 of sulfuric acid is higher than the pKa of PSS, the reaction can be expressed as:[39]

$$H_2SO_4 + PSS^- \rightarrow HSO_4^- + PSSH \qquad (II.1)$$

XPS analysis was performed after the rinsing step on different parts and along the thickness of a dried gel sample to insure homogeneity of the composition. Finally, we observe that the gelation process (with the use of 0.1 M of H_2SO_4) reduces the PSS content from 70 mol% to 59 mol%.

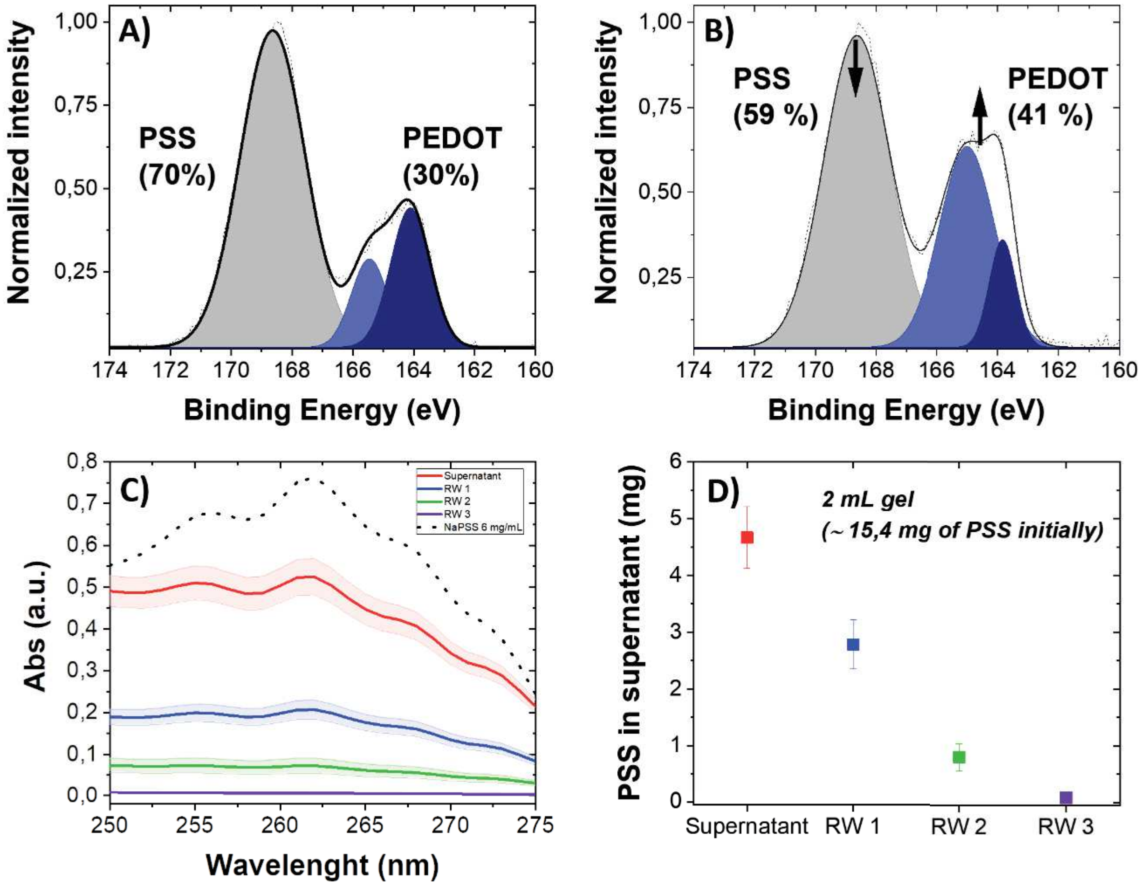

Figure II.9: A) S 2p XPS of the dried dispersion; B) S 2p XPS of the dried gel, the molar fraction of each component was estimated by integrating the peaks; C) UV-Vis absorbance spectra of the hydrogel supernatant and rinsing water as compared to a 5 mg/mL NaPSS solution; D) Mass of PSS estimated from the absorbance spectra in each supernatant and rinsing waters of 2 mL hydrogels (2 mL of PH1000 dispersion contains ≈ 15.4 mg of PSS according to the mass ratio provided by the supplier).

The gel aqueous supernatant was also investigated by UV-visible spectroscopy. A characteristic peak (max at 262 nm), attributed to the π-π* electron transition from the benzene ring of PSS[40] was observed (see Figure II.9.C). With the Beer-Lambert law, it is, therefore, possible to determine the mass of PSS which is solubilized in the supernatant during the gelation process (see Figure II.9.D). The molar extinction coefficient of PSS (1.45 x 10^6 $L.mol^{-1}.cm^{-1}$) was determined using a calibration curve of NaPSS in deionized water. The presence of PSS in the supernatant correlates with XPS measurement. An excessive amount of uncoupled PSS is partly released from the PEDOT: PSS complex and dissolved in the acidic medium. Hence, the PSS present in the supernatant is probably in its acidified form PSSH.

Interestingly, a certain quantity of PSS can be further washed out from the gel after two rinsing steps (RW1 and RW2) in deionized water. A third rinsing step (RW3) appears to be not necessary. Altogether, the PSS wt% decreases from ~71 wt% in the dispersion to 55 wt% in the rinsed gel. We observe some batch-to-batch variation in the PSS quantity detected in the supernatant or the rinsing water. However, the total weight % of PSS removed (after removal of the supernatant followed by two rinsing steps) is constant.

Overall, the PEDOT: PSS ratio was followed by two spectroscopy techniques. As we do not have any information on the molecular weight of the PSS chains, it is not possible to compare the results of both techniques quantitatively. However, both results indicate partial PSS removal during the gelation and rinsing steps. Furthermore, the decrease of the fibrils' thickness after acidification observed by cryo-TEM in section II.2.2.1 indicates a structural rearrangement of PEDOT and PSS. Hence, we suggest that the PSS-rich shell is somewhat modified or removed, inducing global rearrangement of the PEDOT: PSS system, leading to further conformation modification of the two polymers. Considering the change in PEDOT: PSS ratio, one could expect modification of the doping level of PEDOT as well. Unfortunately, despite our efforts, measuring the doping level of PEDOT by optical spectroscopy (reflectivity measurement with integration sphere) was not achievable.

2.2.3. CHAIN CONFORMATION MODIFICATIONS

To probe structural changes at a molecular scale, we followed the Fourier transform infrared (FTIR) spectra in the PEDOT: PSS before and after gelation (i.e., in the dried dispersion and the dried gel, blue and red spectra respectively). The entire FTIR spectrum is displayed in Figure II.10.A. The common characteristic bands of PEDOT: PSS associated with the C-S bond of the PSS moiety (682, 775 cm^{-1}), the PEDOT C_α-S bond (830, 925, and 970 cm^{-1}), the in-plane bending vibration of the benzene ring of PSS (1007 and 1036 cm^{-1}) or the C-O-C bond from the ethylenedioxy group of PEDOT (1077, 1130 and 1183 cm^{-1}) are present.[19,41–44] After gelation a weak peak at 1280 cm^{-1} appears and can be identified as the asymmetric S=O bond vibration of some remaining H_2SO_4 from gelation. Band shifts are also observed on the dried gel sample. Typically, the C-O-C vibration band shifts from 1077 to 1056 cm^{-1}. Any modification in the C_β- C_β-C_α bonds directly influences the vibrational band corresponding to the C-O-C ethylenedioxy group. It has been reported in the literature that such a shift can be attributed to the reduction of the PEDOT dipole moment when its morphology changes between quinoid and benzoid conformation (see Figure II.10.B).[41] In Figure II.10.C, the region 1300-1600 cm^{-1} shows characteristic band shifts after gelation.

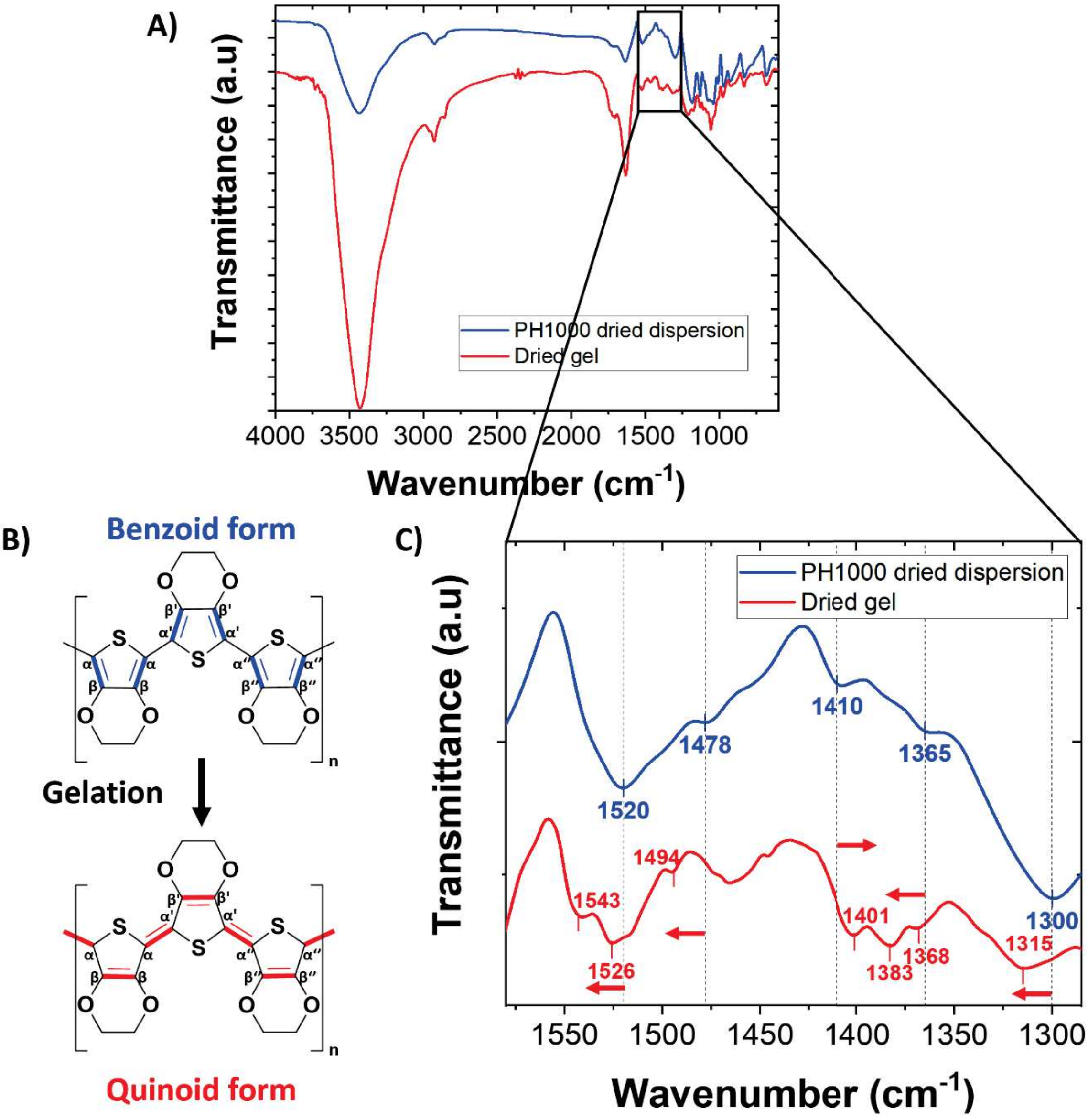

Figure II.10 A) FTIR spectra of the dried dispersion (blue curve) and the dried gel (red curve); B) Change of conformation from benzoid form to quinoid form upon gelation; C) Zoomed part of the spectra between 1300 and 1600 cm^{-1}. The red arrows represent the bands' shifts after gelation.

In the dried dispersion, the band at 1300 cm^{-1} is due to the symmetric C_α-$C_{\alpha'}$ stretching between the thiophene rings. After gelation, this vibrational band shifts to 1315 cm^{-1}. Similarly, C_β-$C_{\beta'}$ stretching vibration band shifts from 1365 cm^{-1} to 1368 cm^{-1} (with a doublet appearing at 1383 cm^{-1}). The C_α=C_β asymmetric band (and its shoulder) is located at 1520 cm^{-1} (1478 cm^{-1} for the shoulder) for the PH1000 dispersion sample and shifts after gelation to a higher wavenumber at 1526 cm^{-1} (1494 cm^{-1} for the shoulder). A new peak is also appearing at 1543 cm^{-1}. Conversely, the band corresponding to C=C symmetric stretching shifts to lower wavenumbers from 1410 cm^{-1} to 1401 cm^{-1}. These findings correlate well with the conformational changes observed by Raman spectroscopy after acidification of the PH1000 dispersion[9] and with the variation of FTIR peaks of PEDOT: Tos with pH.[42]

Doubling of the C_β-C_β stretching and C_α=C_β asymmetric stretching vibrational bands after gelation suggests that gels are not composed of a unique pure conformation but a mixture of both quinoid and benzoid forms. Hence, we suggest that during gelation the conformation of PEDOT changes from a dominant benzoid to a dominant quinoid structure. It has been reported that this linear conformation tends to improve the interactions between PEDOT oligomers.[45]

2.3. GELATION MECHANISM

According to IUPAC, a gel is a “non-fluid colloidal network or polymer network that is expanded through their whole volume by a fluid”.[46] Here, the obtained gel raises questions about its nature being both a colloidal network and a polymer network. A colloidal fibrillar dispersion such as PH1000 is subject to constant Brownian motion. This constant agitation induces particles to collide and interact between them. Moreover, London-Van der Waals (VdW) leads to attraction between two identical particles.[47] One solution to avoid aggregation despite attraction strengths is to modify the particle surface with a counter-force (VdW, electrostatic, steric). In this dispersion, PSS is present in excess, partly doping PEDOT and partly on the outer part of the particle, or free in the dispersion. Their very long chains prevent close contact between particles through steric hindrance. Moreover, electrostatic repulsions also occur as PSS chains from the external shell are not in direct contact with PEDOT and are thus negatively charged. Two particles of the same surface charge repel each other when in proximity, increasing the colloidal stability of the dispersion. Elucidating the mechanism of gelation from such a complicated dispersion by the addition of sulfuric acid is difficult. Nevertheless, with the information in our possession, we try in this section to describe the global process.

We demonstrated that gelation induces modifications of the PEDOT: PSS system at different scales. Thinner, entangled fibers were formed, composed of more ordered PEDOT stacks distributed along PSS chains. Moreover, we demonstrated that the acidification during gelation participates in the partial removal of PSS. From this information, we suggest the following gelation mechanism, illustrated in Figure II.11. In this complex system, several interactions participate in the formation of the network. We suggest that first, the addition of sulfuric acid induces an external stimulus that lowers the repulsive forces between the particles and destabilizes the dispersion. When acid is added, positively charged protons are attracted to the excess PSS chains. Protonation induces two major modifications in the dispersion. As PSS molecules are not charged anymore, the repulsion electrostatic forces are reduced. Although, neutralizing PSS chains weakens their coulombic interactions with PEDOT resulting in i) the solubilization of PSSH and ii) reconformation of freed PEDOT chains into their quinoidal and more linear form. The combination of losing repulsive electrostatic charges and steric hindrance destabilizes the dispersion while attraction forces at close contact become even stronger with higher potential π-π interactions. Thus, particles assemble mainly through π stacking and VdW interactions. The resulting fibrils tend to entangle as attraction forces are still stronger than repulsions ones. In the end, a 3D fibrillar network is formed.

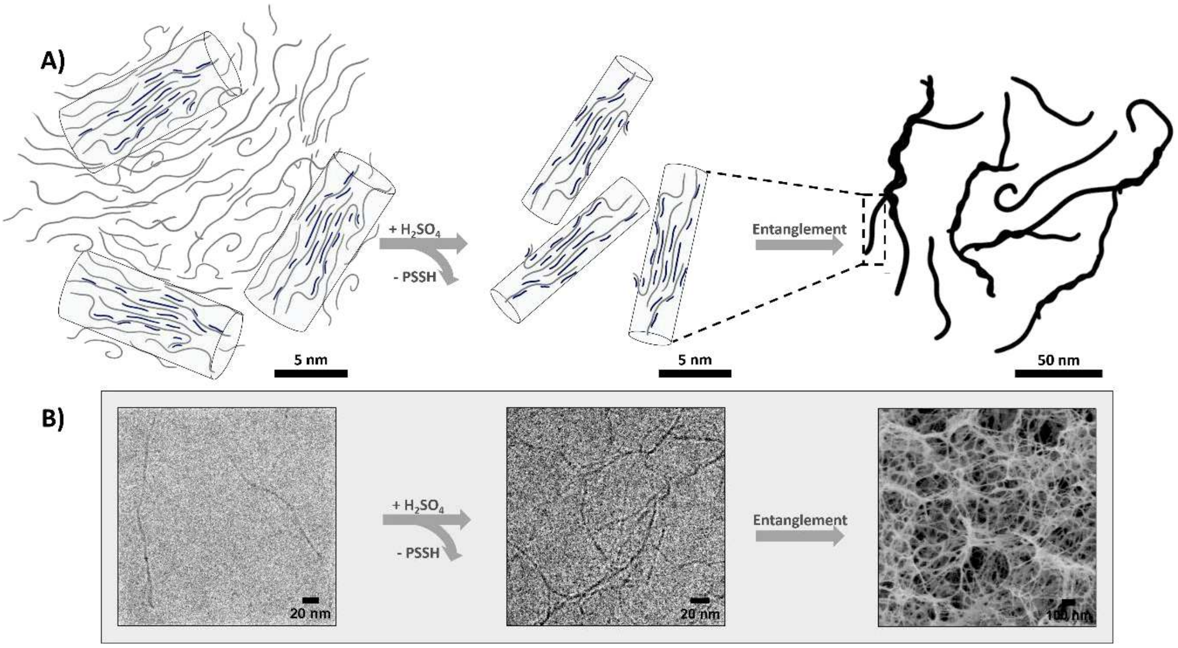

Figure II.11: A) Schematic of the proposed gelation mechanism with PEDOT stacks of oligomers in blue and PSS chains in gray, and B) TEM and SEM images associated with the different steps of the gelation. The initial dispersion is composed of PEDOT-rich core and PSS-rich shell fibrils of around 5 nm thickness, it is probable that some free PSS is present in the dispersion; after acidification, some PSS chains are protonated and removed during the washing of the gel. Hence, the dispersion is destabilized and the fibrils of around 3 nm thickness tend to assemble via VdW forces and π-stacking. Finally, after the entanglement of the assembled fibers, the mesoporous 3D network is formed.

No other experiments were conducted on the hydrogels to investigate the gelation mechanism. The gelation mechanism is very difficult to monitor and the discussion above is a suggestion according to the different characterizations performed. In the following section, we focus more on the drying techniques (i.e., ambient air, supercritical or freeze- dryings) used to obtain porous PEDOT: PSS materials from this wet gel.

3. ELABORATION OF POROUS CONDUCTING POLYMERS: EFFECT OF THE DRYING CONDITIONS ON THE POROUS STRUCTURE

3.1. XEROGEL

The simplest solvent-removal technique is drying in ambient air. When left at ambient pressure and temperature, a wet hydrogel will eventually dry to a **xerogel**. In our case, after gelling and rinsing, the PEDOT: PSS hydrogel was left to dry in the fume hood for a few hours to over 24 hours depending on the size of the hydrogel. A schematic of the ambient air drying is shown in Figure II.12.B. This drying technique is subject to many uncontrollable variables such as laboratory temperature or humidity. A representative photograph of the type of material obtained is shown in Figure II.12.A. Typically, the xerogels are very shrunken compared to the original hydrogel (see Figure II.5.C). The thickness of the xerogels is < 1.5 mm and the shrinkage occurs mainly in the vertical direction. Due to inhomogeneous drying, the xerogels are not uniform, as shown in Figure II.12.A. They are mechanically very strong and can be easily handled.

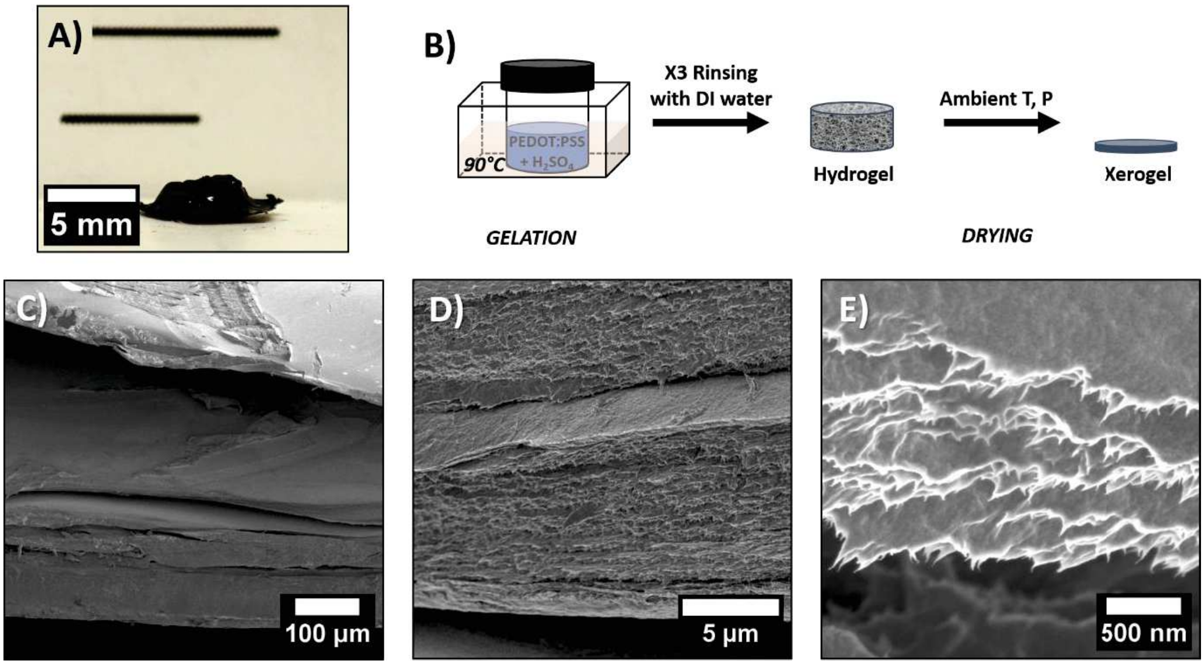

Figure II.12: A) Digital photo of a representative Xerogel, B) Schematic of the ambient air-drying steps, C-D) SEM images at magnifications of a PEDOT: PSS xerogel.

The internal structure of the xerogels was observed by SEM. The structure was very different from that of native hydrogels. The network is composed of densely stacked sheets (with a thickness > 100 nm) and large holes separating the sheet stacks. We do not know if these holes are present in the xerogel or if they are induced by the cutting method used to observe the inner part of the sample with SEM. Other than these holes, it is difficult to tell from the SEM images whether these PEDOT: PSS xerogels are porous or not. Since their density is lower than that of PEDOT: PSS (~0.6 g/cm^3 for the xerogels versus 1 g/cm^3 for dense PEDOT: PSS), we suggest that there is indeed some porosity in the material. It is even possible to reduce their density to even lower values by increasing the rate of solvent evaporation. Densities of ~ 0.5 g/cm^3 and ~ 0.3 g/cm^3 could be obtained when the gels were dried on a hot plate at 50 °C and 100 °C respectively. We would like to point out that the densities obtained are approximate due to the difficulty of accurately measuring the volume of such deformed materials.

The shrinkage of the polymer network results from the capillary forces exerted on the gel during drying at ambient pressure and temperature. Indeed, during the evaporation of the interstitial solvent, a liquid-vapor interface appears on the surface of the gel generating capillary constraints on the solid network. At the beginning of the drying process, a liquid-vapor meniscus forms on the surface of the gel. This causes a capillary migration of the solvent towards the surface where the capillary pressure is more important. The gel, being flexible, then undergoes a densification corresponding to the volume of solvent evaporated.

Overall, ambient air drying was not controllable, and the resulting materials were very difficult to characterize because of their shapes. Their small thickness does not correspond to the ideal design of the material mentioned in section I.1.6. Moreover, we cannot conclude on the type of porosity present in this material, either only macroporous due to the holes between the sheet stacks, or microporous between the PEDOT: PSS sheets. Nitrogen and mercury physisorption analyses could be good characterization techniques to determine the type of porosity present in these materials. Unfortunately, these techniques were not readily available and could not be performed on xerogels. Therefore, this type of drying was not studied further. The charge transport properties were still measured and are discussed in section II.4. Unfortunately, due to their sizes and shapes, the thermal conductivity could not be measured.

3.2. MESOPOROUS AEROGEL

3.2.1. THE SUPERCRITICAL DRYING TECHNIQUE

In the case of liquid-gas transition of the solvent, the capillary forces applied to the gel network induce a strong contraction. To avoid this discontinuous change of state from liquid to gas, a fluid can be subjected to high pressure and temperature conditions to enter the supercritical (SC) state. In fact, in the SC domain of the pressure-temperature diagram, the liquid phase, and the gaseous phase are no longer distinguishable and form a single phase. Hence, the liquid can be transformed into gas in the absence of surface tension and capillary stress. Only the density of the fluid is changed, so it can be changed from the liquid state to the gaseous state without phase transition.

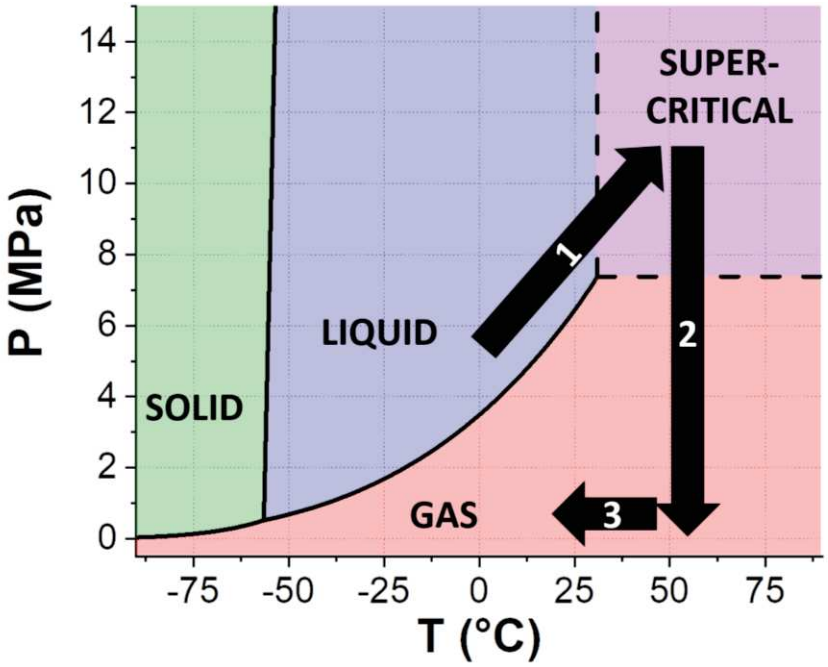

Figure II.13: Pressure-temperature diagram of CO_2, the arrows correspond to the different steps of SC drying: 1) After CO_2 liquid exchange, the pressure and temperature are increased to reach the SC state, 2) The pressure is decreased to reach the gas phase, 3) The temperature is decreased to the lab temperature.

Typically, the material of interest is placed in an autoclave where sufficient pressure and temperature are applied for the solvent to reach the supercritical state. Once all the solvent has gone to the SC state, the pressure is decreased until the fluid reaches the gaseous phase. In the end, when the supercritical fluid returns to the gaseous state, the network is theoretically not modified. In a more practical case such as ours, other steps need to be added to the process. Indeed, solvents such as water or alcohols have high SC conditions (water: P_{SC} = 22,1 MPa, T_{SC} = 647,1 K; ethanol : P_{SC} = 6.1 MPa, T_{SC} = 514 K) that could damage materials such as polymer gels. Instead, it is common to use supercritical CO_2 that requires mild conditions to reach its SC state (P_{SC} = 7.4 MPa, T_{SC} = 304.1 K). To do so, the gel's solvent needs to be replaced by liquid CO_2 before drying (e.g., the solvent has to be soluble with CO_2). In that case, the gel is placed in an autoclave at liquid CO_2 pressure and temperature conditions. By successive $CO_{2,L}$ baths, the solvent is gradually exchanged. Then, the supercritical conditions of CO_2 are reached, followed by a decrease in pressure to go to the gaseous phase. Figure II.13 shows the P, T diagram of CO_2 on which are represented the different drying steps for the supercritical drying of an aerogel.

As described in the schematic protocol in Figure II.14.B, before the supercritical drying, the solvent of the hydrogel (water) was exchanged with ethanol (which is fully CO_2-miscible), providing a so-called **"sulf-alcogel**". Once produced, the sulf-alcogels were placed in an autoclave to exchange the ethanol with $CO_{2,L}$. Finally, the alcogels were subjected to high pressure and temperature to reach the supercritical state of CO_2 before returning to the gas phase. More experimental details can be found in the Experimental section.

The resulting dried gels called **sulf-aerogels** are shown in Figure II.14.A. This technique required a great deal of optimization to successfully produce samples that were not too contracted. Clearly, the solvent exchange step with ethanol was crucial. If a significant fraction of water remains in the sulf-alcogel after ethanol exchange, the water was likely to pass to the gaseous state during the descent to ambient pressure inducing a contraction of the network. The same risk applies to the exchange step between ethanol and $CO_{2,L}$. In case of non-complete solvent exchange (with $CO_{2,L}$), the remaining ethanol would not go through the supercritical state to make its liquid-gas transition. Again, this would induce a significant contraction of the sample. Besides this, the apparatus used does not regulate the temperatures around the ambient. It is, however, essential to keep a stable temperature during the exchange with $CO_{2,L}$. Sometimes, the temperature of the room was too high and the CO_2 in the autoclave changed from liquid to the gaseous state inducing a strong contraction of the final sample.

Despite our efforts to optimize the drying technique, it was impossible to produce samples without any contraction. Besides the difficulties mentioned above, this contraction may be due to a too low weight percentage of the gels.

3.2.2. STRUCTURAL PROPERTIES OF THE SULF-AEROGELS

Dark blue sulf-aerogels were obtained after SC drying of sulf-alcogels. After drying, they were stored in an inert N_2 atmosphere to avoid any adsorption of the ambient moisture. Although the shrinkage of ~ 40 %vol was observed after drying, the sulf-aerogels kept a cylindrical form as shown in Figure II.14.A. They could be made in different sizes and shapes (depending on the dimensions of the initial gel) but typically they were more than 5 mm thick and had a diameter of around 10 mm. The sulf-aerogels exhibited a low density of 0.057 ± 0.01 g/cm^3 and a high porosity of 94 ± 1 %. These materials are very robust and can be manipulated very easily.

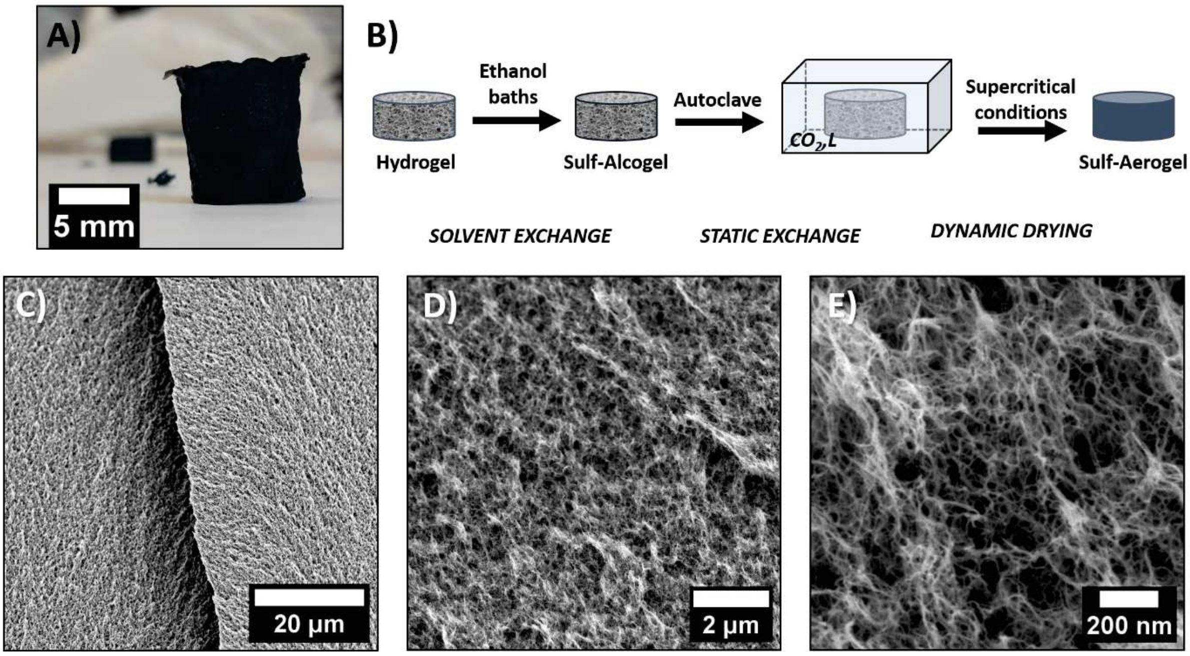

Figure II.14: A) Digital photo of a representative sulf-aerogel, B) Schematic of the supercritical drying steps, C-D) SEM images at different magnifications of a PEDOT: PSS sulf-aerogel.

The main interest of this drying technique is the conservation of the native fibrillar network observed in the gel state. SEM observations were performed on the sulf-aerogels and are presented in Figure II.14 C-E). To reveal their inner structure, the materials were cut with a razor blade, some deformation due to the shear stress induced can be observed in Figure II.14.C. The network, like the native one, was composed of entangled fibers of a thickness of 10 ± 3 nm (estimated by ridge detection of fibers) and voids with a width from 10 to 50 nm. A high magnification image is shown in Figure II.14.E. As a comparison, the native hydrogel structure described in section II.2.2.1 was composed of fibers with a thickness of 13 ± 4 nm. The slight difference in thickness between the hydrogel and the sulf-aerogel can be explained by the fact that in the hydrogel, the fibers are swollen by the solvent while the fibers are completely dried in the sulf-aerogel. As the difference is low, it could also be due to the difficulty to measure the fibers' thicknesses accurately. In the end, both values are in the error range.

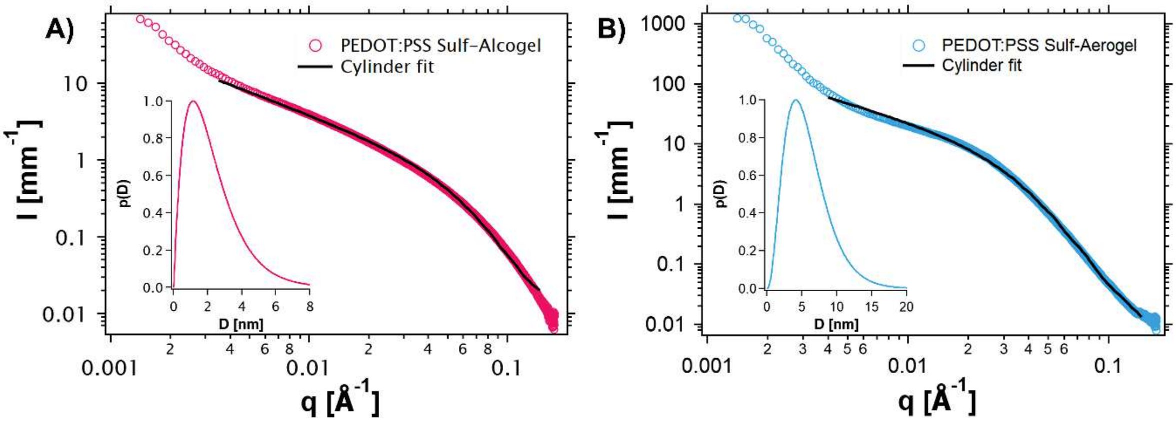

Figure II.15 X-ray scattering intensity profile of A) a PEDOT: PSS sulf-alcogel and B) a PEDOT: PSS sulf-aerogel. The colored dots (pink for the sulf-alcogel, light blue for the sulf-aerogel) correspond to the experimental data(after subtraction of the solvent's contribution for the sulf-alcogel), and the black line to a cylinder fit with radius polydispersity. The inset corresponds to the Schulz distribution of the cylinder fit radius.

SAXS measurements were also conducted on the sulf-alcogels and sulf-aerogels to confirm their mesoporous fibrillar network. The intensity profile of both sulf-alcogel and sulf-aerogel are displayed in Figure II.15. Like the hydrogel's intensity profile Figure II.8.C, for both sulf-alcogel and sulf-aerogel, the profile follows a q^{-1} power law in the Porod regime, corresponding to one-dimensional objects. It also exhibits a rise at very small angles ($q < 0.005$ Å^{-1}). The same cylinder poly-radius fit, and Schulz distribution used for the hydrogel were applied to the sulf-alcogel and sulf-aerogel data. Interestingly, the fitted diameter of ~ 2.5 nm for the sulf-alcogel is very similar to the one obtained for the hydrogel. This suggests that there are no network modifications induced by the solvent exchange with ethanol. Surprisingly, for the sulf-aerogel, the modeled diameter of the fibers is slightly higher ~ 5 nm. As the sample is slightly shrunk during drying, one could expect the fibers to be thinner. Another possibility is that we cannot detect a unique fibril in this case.

Interestingly, supercritical drying allows the preservation of the native fibrillar network, resulting in a dried mesoporous sulf-aerogel. The fibrillar structure of the sulf-aerogel agrees with the structure of PEDOT: PSS aerogels reported by Zhang et al.[5] Overall, this technique allows the design of reproducible mesoporous samples of PEDOT: PSS with very low density and high porosity. Although this route is interesting, we were unable to influence the final structure through the drying technique. Therefore, the production of other ranges of porosities implies the modification of the native gel structure or the use of another drying technique such as freeze-drying.

3.3. MACROPOROUS CRYOGEL

3.3.1. LYOPHILIZED PEDOT: PSS DISPERSION

As discussed in section I.2, porous PEDOT: PSS is often reported in the literature to be obtained by direct lyophilization of the commercial dispersion, with[48] or without[2] the addition of cross-linking agent or with additional solvent.[1] Before going further in our macroporous materials design, the structural properties of the lyophilized PEDOT: PSS dispersion are presented in the following section as a reference.

Prior to drying, the stock PH1000 dispersion was vortexed and filtered through a 0.45µm PTFE filter. Then, the PEDOT: PSS dispersion was frozen in liquid nitrogen (N_{2L}) for 10 min, and the ice was sublimated at -15°C. A schematic of the lyophilization steps is displayed in Figure II.16.B, more experimental details can be found in the Experimental section. The resulting sample is light blue and takes the shape of the vial it was frozen in (in that case a cylindrical vial) as shown in Figure II.16.A. The lyophilized dispersion (LD) is very brittle and can easily break when manipulated. The sample is very light and possesses a very low density (~ 0.02 g/cm^3) and a high porosity (~ 98%).

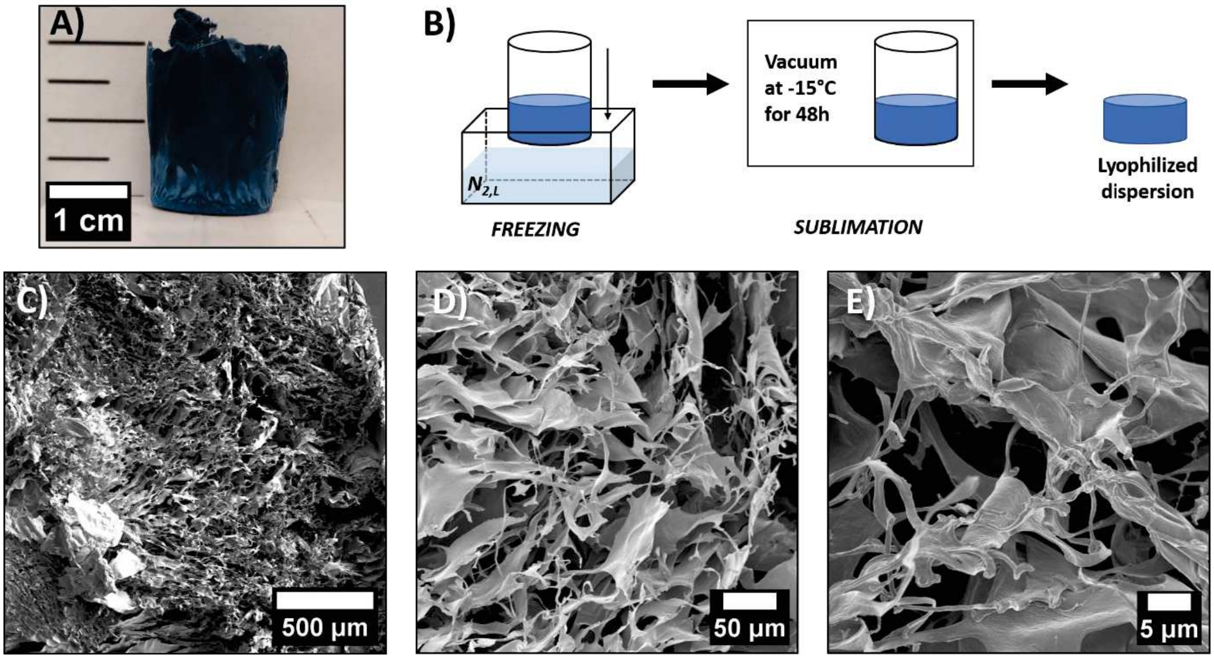

Figure II.16 A) Digital photo of the lyophilized dispersion, B) Schematic of the lyophilization steps, C-D) SEM images at different spots and magnifications of the lyophilized dispersion.

SEM was performed on the LD samples. Three SEM images at different locations and magnifications are shown in Figure II.16.C-D. Various porous morphologies consisting of thick fibers, sheets, and more disordered objects were observed. Clearly, the final structure of the porous LD does not resemble the initial gel network shown in Figure II.8.A.

Surprisingly, the dispersion spontaneously forms a random network. The random structural morphology can be attributed to the broad size distribution of ice crystals and the numerous ice nucleation sites. In a pure water solution, nuclei form until they reach a critical concentration where crystallization occurs. Therefore, all crystals are formed at the same time, resulting in homogeneous size distribution. In our case, the aqueous solution contains fibers that are perfect nucleation points for ice crystal growth. Consequently, nucleation can occur at different locations, triggering crystallization at different times, and in different directions, resulting in such a randomly distributed architecture. During the freezing step, the water in the dispersion crystallizes into ice. As they form, the ice crystals displace the PEDOT: PSS fibers, promoting contact between them, and triggering the formation of a 3D architecture.

This technique is indeed an effective and very simple way to produce porous PEDOT: PSS. However, it should be noted that these samples are too brittle to be handled correctly. The samples are so soft that tweezers instantly deform the structure. Additionally, the morphology of the porous structure is not reproducible and is very inhomogeneous within the same sample. As discussed in the introductory part of this chapter, to overcome these issues we first prepared gels before freeze-drying them.

3.3.2. PEDOT: PSS QUENCHED CRYOGELS

PEDOT: PSS hydrogels placed in glass vials were rapidly immersed in N_{2L} without specific control of the freezing process and allowed to cool for 10 minutes (see Figure II.17.B). The frozen hydrogels were then dried under vacuum for 48 h at low temperature to allow complete sublimation of the ice. Very light, handleable, dark blue cryogels (hereafter called **quenched cryogels**) were obtained (see Figure II.17.A). These PEDOT: PSS quenched cryogels have a very low density (0.03 ± 0.006 g/cm^3) and high porosity (97 ± 0.5%).

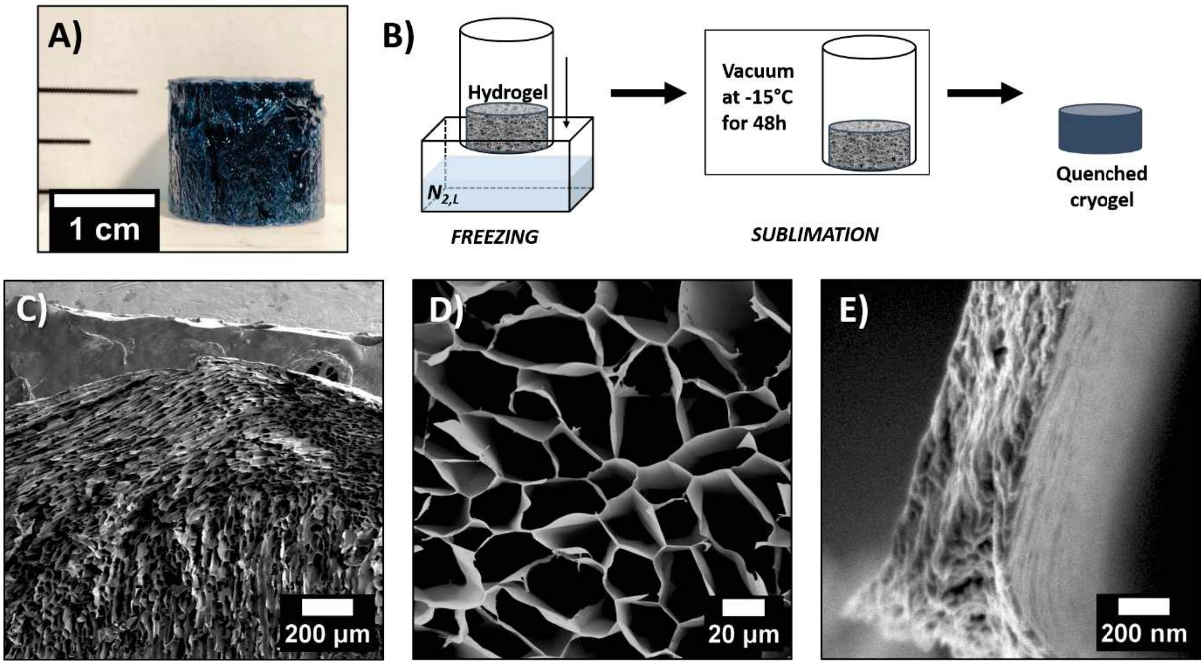

Figure II.17 A) Digital photo of the quenched cryogel, B) Schematic of the freeze-drying steps, C-D) SEM images at different spots and magnifications of the quenched cryogel: C) Low magnification of the channel-like porous structure, different grains of pores orientation can be observed, D) Honeycomb porous structure, E) High magnification of a pore wall.

SEM images reveal a macroporous structure. Interestingly, the porous structure is very different from the native one but resembles to the structure demonstrated by Yao et al. [Yao et al. 2017] It is composed of interconnected micrometer-wide channels. These channels are gathered to form a honeycomb-like structure composed of pore walls of ~ 300 - 400 nm in thickness and pores with a diameter of 24 ± 13 µm. Texturing of the pore walls can be observed at high SEM magnification as presented in Figure II.17.E. The pore walls are composed of densely stacked PEDOT: PSS fibers. Although the channels appear locally aligned as shown in Figure II.17.D, the samples are composed of multiple zones that are oriented by grains of several hundred micrometers as presented in Figure II.17.C. These different orientations are due to the uncontrolled ice crystal growth as the tube is plunged quickly into liquid nitrogen and the cold source is isotropic. Due to the Pyrex vial surrounding the sample, ice crystal formation begins on the container walls and bottom, directly in contact with liquid nitrogen. This "quenched freezing" method results in a low degree of supercooling but a high freezing rate.[49] Thus, the nucleation and solidification fronts are very close and move both in non-nucleated areas. This particular mechanism is known as local supercooling. Other defects such as hundreds of micrometers wide voids can be observed randomly. We suggest that these defects are due to the presence of air bubbles already trapped in the hydrogel before the freezing steps.

It was unclear to us how the structure of the gel varied from fibrillar to channel-like after drying. It is well known in the freeze-drying community (and highlighted in section II.3.3.1) that this drying process induces modifications to the network's structure. Indeed, the interstitial solvent retained in the gel crystallizes during the freezing step, serving as a template for the 3D polymer network. The frozen solvent is then sublimated, resulting in the so-called cryogel.[50] To investigate further the morphological modifications of the network from fibrillar to channel-like, induced by the freezing step, cryo-SEM was performed on a PEDOT: PSS hydrogel. The experiment allows us on a single sample, to investigate the change of morphology induced by the growth of solvent crystals. In normal cases, cryo-SEM allows the observation of wet samples such as gel in their native state as shown in Figure II.8.A. In the case of a hydrogel, the rapid freezing of the sample with liquid ethane[51,52] allows the formation of amorphous ice, which does not damage the native polymer network. However, if the sample is large enough, a temperature gradient can occur, between the outside part (that is in direct contact with the liquid ethane) and the inner part of the sample. Therefore, it is possible to observe a deformed network by different stages of ice crystallization on the same sample.

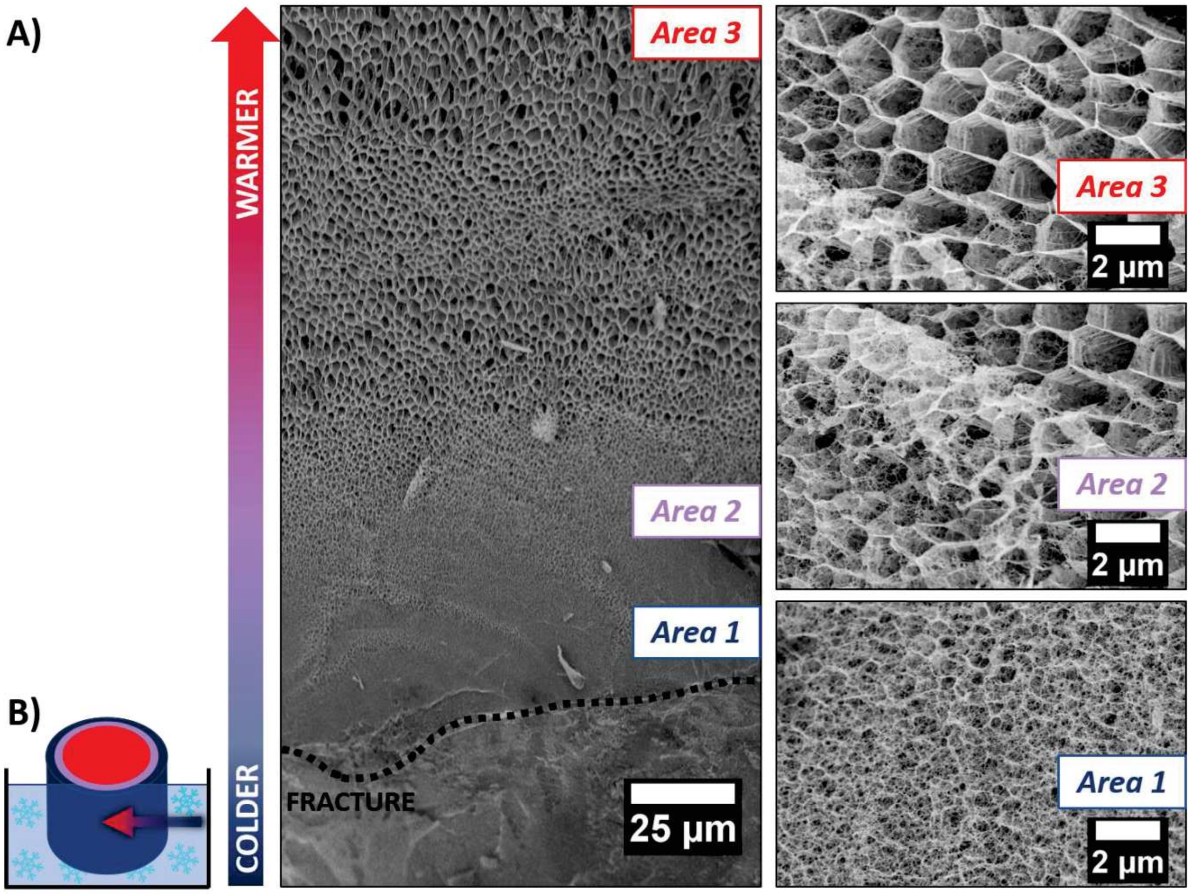

Figure II.18: A) cryo-SEM images of a unidirectional frozen piece of PEDOT: PSS hydrogel. Area 1 was in direct contact with liquid ethane; thus, the native gel structure was preserved. Areas 2 and 3 show the evolution of the structure as the freezing rate decrease in the inner part of the sample; B) Schematic of the gel piece dove in $C_2H_{6,\,L}$; the outer part in blue is in direct contact with the freezing solvent, resulting in the formation of amorphous ice. Deeper in the sample, the freezing rate decreases resulting in the formation of ice crystals.

Cryo-SEM images of the hydrogel dipped vertically into liquid ethane are shown in Figure II.18.A. The outer part of the frozen hydrogel (in close contact with the liquid ethane) is at the bottom part of Figure II.18.A whereas the inner part of the gel (at a slightly higher temperature) is at the top part of the image. The schematic in Figure II.18.B illustrates how the sample was frozen. As the piece of gel was about 2 mm thick, different areas can be observed. The dark blue outside part of the gel corresponds to Area 1. As it was in direct contact with liquid ethane, its freezing rate was extremely high. Thus, amorphous ice was formed, preserving the native fibrillar network of the gel, already discussed in section II.2.2.1. As we go deeper inside the gel, the freezing rate decreases, allowing ice crystals to form. Area 2 (represented in purple on schematic Figure II.18.B) shows the transition between two types of structures. At the bottom left of the SEM image, the fibrillar structure of the native gel is still present whereas porous hexagons are clearly defined at the top right corner of the image. This second channel-like structure is due to the crystallization of ice into the confined space of the network. The morphology of the pores is templated by the ice crystals. Their shape can vary depending on the solvent, environment, or freezing rate (see section III.2.1). In Area 3 (red part on the schematic Figure II.18.B), a honeycomb-like macroporous structure starts to develop. It is clear from these observations that ice crystals serve as a template for the porous structure. The pore walls are composed of densely stacked fibers of the native gel structure (see Figure II.17.E), pushed aside by the ice crystals during the freezing step while the pores’ sizes and shapes are defined by the ice crystals.

The pore walls do not seem porous on the SEM images. This was confirmed by nitrogen physisorption analysis on the cryogel, no micro- or mesoporosity was found in the material.

Overall, fast freeze-drying in liquid nitrogen of the hydrogels affords cm thick macroporous PEDOT: PSS samples (quenched cryogels). The macroporous honeycomb-like structure possesses homogeneous pore size distribution but their orientation is not controlled.

4. INFLUENCE OF POROSITY ON THE TE PROPERTIES

We successfully obtained different types of porosity and different porous structures from the same PEDOT: PSS hydrogel. In the following section, we investigate the structure-properties relationship of the materials presented above.

4.1. DESCRIPTION OF CHARACTERIZATION TECHNIQUES

In this PhD work, we had first to develop appropriate characterization techniques for our bulk and light samples. Our laboratory had the infrastructure to measure the electrical conductivity and the Seebeck coefficient of organic TE materials. However, the existing setups were designed for measurements on thin films deposited on substrates. We had to adapt the measurements to our samples (and vice versa) while ensuring the reliability of our measurements. For thermal conductivity measurements, a specific machine was purchased after comparison and testing of several different methods. Finally, it was necessary to take in hand this technique.

In the literature, porous conducting materials are often poorly characterized. Furthermore, the techniques used from one study to another can be very different and difficult to compare. There is a clear lack of consistency and the characteristic quantities to define such materials are generally partly missing. In this study, we systematically measured the electrical resistance, the Seebeck coefficient and the thermal conductivity of the PCPs. The characterization techniques were adapted to fit our bulk porous materials. Further details can be found in the Experimental section, but the characterization techniques are briefly presented in the following section.

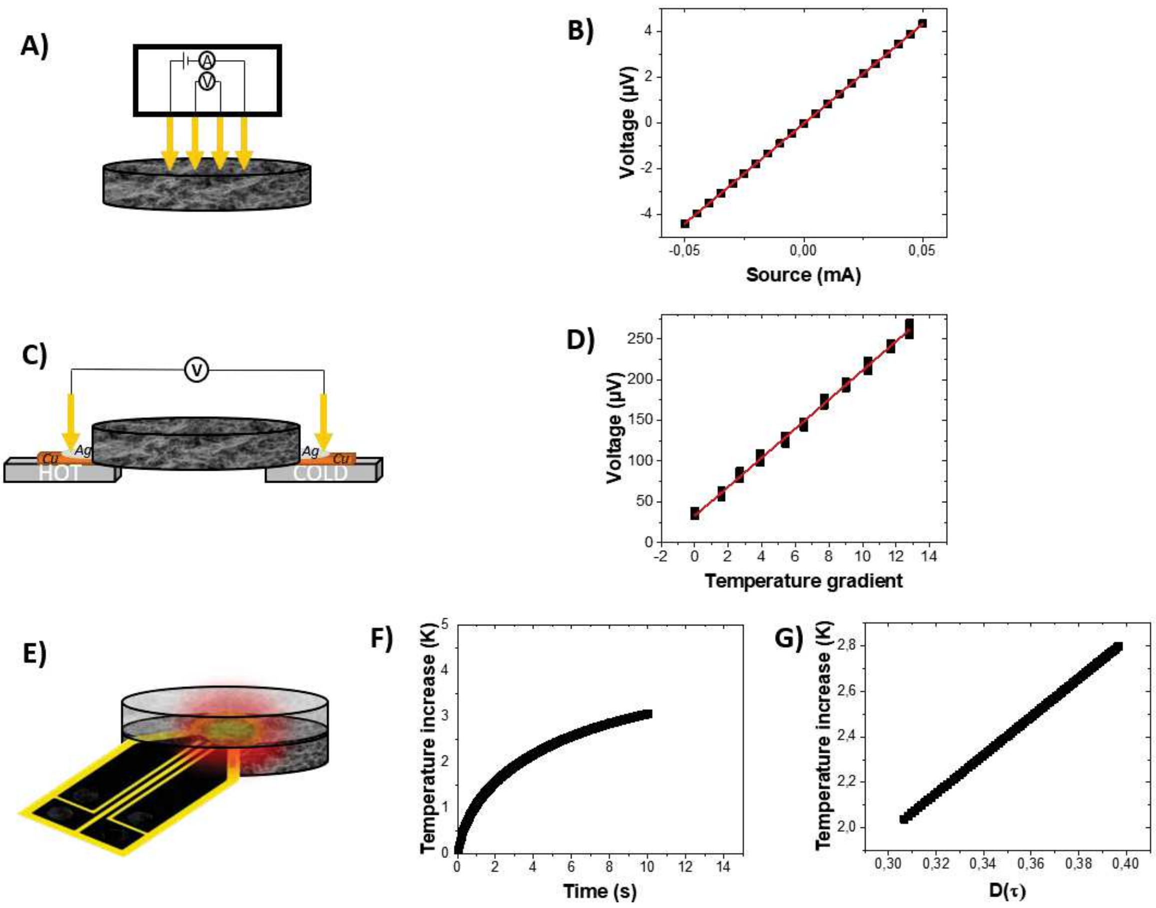

Figure II.19: Schematic and typical curves obtained during TE properties measurement. In the schematics, the sulf-aerogel is represented but the other PCPs were measured the same way. A) Schematic of the electrical resistance measurement using the four-point probe geometry on the aerogel; B) typical I/V curve of the electrical resistance measurement C) schematic of in-plane Seebeck coefficient measurement. To ensure good electrical contact with the probes and a good thermal contact with the Peltier elements, aerogel samples have been pasted on copper foil (Cu) with silver paste (Ag); D) typical curve for Seebeck measurement; E) sample configuration for isotropic thermal conductivity measurement, the sensor is sandwiched between two aerogels of fairly identical size. The samples were held in place using a lightweight aluminum pellet at the top of the upper sample, which ensured good contact between the sensor and the surface of the samples, F) typical transient curve of thermal conductivity measurements, G) Typical calculated graph (ΔT) as a function of D(τ).

Electrical resistance, Seebeck coefficient and thermal conductivity were measured on each sample to ensure a clear correlation between all TE properties. As a non-destructive method, thermal conductivity was first measured, then electrical resistance before the Seebeck coefficient that required the use of silver paste for a better electrical contact (for the 'in-plane' method). Figure II.19 shows how the samples have been characterized and a representative curve of each of the measurements is displayed. The method of sample preparation for these TE characterizations is described in the Experimental section.

4.1.1. ELECTRICAL CONDUCTIVITY

A four-probe resistivity station (see Figure II.19.A-B) was used to measure the electrical resistance (the electrical conductivity was then calculated from it). The measurements were performed under argon inert atmosphere. To validate the results, the measurements were realized on two setups described in the Experimental section. Moreover, both techniques were calibrated using a commercial indium tin oxide coated glass slide.

As the samples size and shape are not standard, geometrical correction factors were used to determine their electrical resistivity from the I-V curve obtained during measurement. Adapted from the Haldor Topsoe report of 1968,[53] Yilmaz reported geometrical corrective factors to calculate the electrical resistivity of cylindrical objects.[54] Generally, the electrical resistivity of a material can be defined as :

$$\rho = \frac{1}{\sigma} = \frac{V}{I} G \qquad (II.2)$$

Where ρ is the electrical resistivity, σ the electrical conductivity, V the voltage, I the current and G a geometric correction factor. For a semi-infinite sample measured by four-probe resistivity method with collinear probes, G can be as simple as 2πs with s the distance between two probes. In our case, the samples are considered as finite thick circular. Hence, G needs to consider the probes distance, but also the thickness and the diameter of the sample. In that case G becomes:

$$G = F_0(s) \,.\, F_1\left(\frac{t}{s}\right).\; F_2\left(\frac{d}{s}\right) \qquad (II.3)$$

Where t is the sample thickness and d the sample diameter. F_0, F_1 and F_2 are correction factors, more details can be found in the Experimental section.

Actually, for porous media, the measured resistance (and thus, the electrical conductivity) takes into account the great fraction of air contained in the material. Hereafter, we will consider this electrical conductivity as the "apparent electrical conductivity" σ_{app}. Thus, since the sulf-aerogels and quenched cryogels presented earlier contain more than 95% air, low electrical conductivity can be expected compared to a dense material. However, it is possible to estimate mathematically the electrical conductivity of the pure material if it were dense. Indeed, mathematical models have been reported in the literature for porous metals.[55–59] Although these models have not been developed for conductive polymers, we will use as an indication two mathematical models briefly presented below to estimate the "dense electrical conductivity" σ_{dense}. Further details about these models can be found in the Experimental section.

The honeycomb-like porous structure of quenched cryogels was considered to be a "closed-cell" material while the fibrillar structure of the sulf-aerogels was considered to be an "open cell". Hence, we have chosen two simple and rather general models. These models are not perfectly representative of the structures of our samples. The goal being to give an estimate of the dense electrical conductivity, we did not develop specific models for our porous structures.

The two models are described as a function of the porosity Θ. The porosity can be defined as $\Theta = \left[1 - \frac{\rho_{porous}}{\rho_{solid}}\right]$ where ρ_{porous} is the apparent density of the material and ρ_{solid} is the density of pure PEDOT: PSS.

The "closed-cell" model in equation II.4 chosen was experimentally determined on closed-cell aluminum-based foams from the more general model of Ashby et al.[55]

$$\frac{\sigma_{app}}{\sigma_{dense}} = (1 - \Theta)^{\frac{3}{2}} \tag{II.4}$$

The "open-cell" model in equation II.5 was determined by Ashby et al. for a three-dimensional network of struts with consideration of the effect of nodes.

$$\frac{\sigma_{app}}{\sigma_{dense}} = \frac{1}{3}\left[(1 - \Theta) + 2(1 - \Theta)^{\frac{3}{2}}\right] \tag{II.5}$$

4.1.2. SEEBECK COEFFICIENT

The Seebeck coefficient was measured in the in-plane configuration as presented in Figure II.19.C. To validate the accuracy of the measurement, a calibration with Constantan wire was realized and some samples were also measured in the cross-plane configuration with another setup described in the Experimental section. Although cross-plane measurements did not necessitate more sample preparation, it was not the case for the in-plane measurements. More details can be found in the Experimental section.

The in-plane measurement was realized on a home-made setup, consisting of two Peltier cells for controllable temperature gradient. The sample was suspended across the two Peltier cells, and the voltage was measured using a Keithley. This setup was initially designed to measure the Seebeck coefficient of films. In our case, because of the large size of the samples, it was impossible to apply a temperature gradient correctly. Thus, to ensure both a good thermal contact with the Peltier cells and a good electrical contact with the tips of the Keithley, two thin pieces of copper were glued on both sides of the sample with silver paste. Since the addition of metallic elements can induce leakage or slight short circuits, this method was calibrated with a Constantan wire to which the copper pieces were attached.

In both methods, the Seebeck coefficient was finally determined with the slope of the voltage versus the temperature difference (see Figure II.19.D).

4.1.3. THERMAL CONDUCTIVITY

As discussed in section I.1.5, various thermal conductivity measurement methods exist. In this study we only used the transient plane source method, derived from the hot wire method (see Figure II.19.E-G). The TPS 1000 apparatus is well suited to measure the low thermal conductivity of small samples.

One of the crucial parameters to measure the thermal conductivity properly with this method is the size of the sample. Minimum thickness and diameter should be reached to be able to measure thermal conductivity. The surface in contact with the sensor is also of importance, it should be as flat as possible, without defects. It was quite difficult to produce samples of good size and flatness. However, by carefully optimizing the gelation and drying processes, suitable samples were successfully produced. However, some samples remained either impossible to produce with the good requirements or happened to be damaged during any step of the process.

4.2. EFFECT OF THE POROUS STRUCTURE ON THE CHARGE TRANSPORT PROPERTIES

The TE properties of the xerogels, sulf-aerogels, lyophilized dispersion and quenched cryogels were measured by the methods discussed in section II.4.1. A free-standing film of a few µm thicknesses was realized as a reference, more details on its preparation method can be found in the Experimental section. Despite their porosity, all the samples were conducting enough to be measured. Table II.1 summarizes the average apparent and dense electrical conductivity and the Seebeck coefficient of the film reference, xerogel, sulf-aerogel, LD, and quenched cryogel.

*Table II.1: Electrical conductivity, Seebeck coefficient and thermal conductivity mean values of the free-standing film reference and porous materials described in section II.3. σ_{dense} was calculated for the sulf-aerogel and quenched cryogel as described in section II.4.1.1. *The reference thermal conductivity was extracted from ref* [60]*; **The thermal conductivity of the xerogel was mathematically estimated by the law of mixture (see section II.4.3).*

Material	Density (g/cm^3)	Porosity (%)	PEDOT : PSS ratio (%mol)	σ_{app} (S/cm)	σ_{dense} (S/cm)	S (µV/K)	κ (W/(m.K))	ZT x 10^{-3} (@300K)
Film reference	1.011	0	/	508 ± 70	/	18.5 ± 3	0.300*	**17**
Xerogel	0.6	40	41:59	24 ± 1	/	14.6 ± 0.8	0.190**	**0.8**
Sulf-aerogel	0.06	94	45:55	9 ± 1	~ 340	16.8 ± 0.8	0.054 ± 0.002	**1.4**
Quenched cryogel	0.03	97	41:59	2 ± 0.5	~ 560	19 ± 1	0.042 ± 0.001	**0.5**
Lyophilized dispersion	0.02	98	30:70	0.05	/	19	0.059 ± 0.002	**0.001**

4.2.1. ELECTRICAL CONDUCTIVITY

The free-standing thick film (~ 7µm) has an electrical conductivity of 508 S/cm. This value is lower than for most of the reported PEDOT: PSS films treated with H_2SO_4 that can reach electrical conductivities higher than 2000 S/cm.[13,61] However, this film was not particularly optimized to have high TE properties but to best represent the dense version of the PCPs discussed above.

Xerogels exhibit an apparent electrical conductivity of around 24 S/cm. This low value (as compared to the dense films) shows that xerogels are somehow porous (even if this porosity could not be characterized). As the density decreases (porosity increases), the resistivity increases. Indeed, the mesoporous sulf-aerogels have an apparent electrical conductivity of around 9 S/cm. The very low-density quenched cryogels have an even lower electrical conductivity of around 2 S/cm. The apparent electrical conductivity of PCPs is low compared to the reference free-standing film. It should be noted that σ_{app} takes into account the large volume of (electrically insulating) air present in the material. Using a mathematical model for porous material (as discussed in section II.4.1.1), we calculated σ_{dense} for the sulf-aerogel and the quenched cryogel (340 and 560 S/ cm, respectively). These values are in the same order of magnitude that our reference value for the thick film (508 S/cm). Since the reference film and the PCPs are treated with the same amount of acid, they should have similar electrical conductivity (without taking into account the air content). The calculated σ_{dense} value for the sulf-aerogel deviates more from the electrical conductivity of the reference film. This difference may be due to the mathematical model not accurately representing the mesoporous network of the sulf-aerogel. To explain further the evolution of the electrical conductivity, carrier concentration and mobility could have been measured via Hall effect measurements (although the bulk size and the porosity of our materials might be a limit).[35]

The comparison between the quenched cryogel and the lyophilized dispersion is of particular interest. We observe an increase in electrical conductivity of more than two orders of magnitude for the cryogel (having undergone a gelation step). This increase is attributed to several factors. As seen in section II.2.2, gelation induces major changes in the morphology of the PEDOT: PSS system, its ratio, and the conformation of the PEDOT molecule. The most important factor is probably the lowest content of non-conducting PSS in the hydrogel (59%mol) as compared to the dispersion state (70%mol). However, it was difficult to determine experimentally if the increase in electrical conductivity (after gelation) was due to an increase in the density of charge carriers and/or an increase in their mobility. However, we suggest that both parameters may have been modified by the gelation.

In addition to the reduction of the proportion of PSS, it has been reported in the literature that the acid treatment of PEDOT: PSS films could induce an increase in the density of charge carriers.[13] The change in doping level of PEDOT can be estimated by UV-Vis optical spectroscopy from the polaronic and bipolaronic bands of PEDOT.[62–64] In our case, it was impossible to perform such measurements on our bulk materials. Reflectivity measurements with an integrating sphere were performed but were not successful (strong noise, too much scattering effect). It was also not possible to prepare thin films (measurable in transmission) using the same method as for the gels (the addition of H_2SO_4 in PEDOT: PSS induced too fast gelation, the films were perforated, inhomogeneous and not measurable). No other techniques were readily available to determine the charge carrier density. Only the XPS data provided us some information on the PEDOT:PSS ratio and possible doping state.

With a lower proportion of PSS and slightly higher density, the sulf-aerogels show a higher electrical conductivity than the quenched cryogels. The decrease of the Seebeck coefficient for the sulf-aerogel (as compared with the quenched cryogel) is likely due to an inverse increase in charge carrier concentration. The difference between sulf-aerogel and cryogel could also be attributed to a difference in doping level). Xerogels have the same PEDOT: PSS ratio as the quenched cryogels and yet their electrical conductivity is ten times higher. This is attributed to the higher density and lower air content in the xerogels.

In summary, the removal of PSS, the likely increase in charge carrier density, and the multiscale morphological changes participate in the observed differences in electrical conductivities between xerogel, sulf-aerogel, and quenched cryogel as compared to the lyophilized dispersion. This demonstrates the interest of the gelation step to obtain more conductive porous materials. The porosity also plays a strong role on the charge transport properties and ideally, should not be too high as it the high air content is disadvantageous.

Although electrical conductivity is very low as compared to the film reference, the value measured on the sulf-aerogel stands amongst the highest values reported in the literature for pure PEDOT: PSS porous materials (see section I.2.3).

4.2.2. SEEBECK COEFFICIENT

As shown in Table II.1, the Seebeck coefficients of the PCPs range between 15 and 20 µV/K. The free-standing film reference shows a Seebeck coefficient of 18.5 µV/K which is consistent with other PEDOT: PSS H_2SO_4 treated films.[39] The more porous and less conducting LD and quenched cryogels have the higher Seebeck coefficient of 19 µV/K. For the sulf-aerogel, S is equal to 16.8 µV/K while for the xerogel it is around 14.6 µV/K. Such a low Seebeck coefficient for xerogel would deserve to be verified by another measurement method. Xerogels were highly bent, and it was difficult to guarantee good thermal and electrical contacts of the samples with the probing systems. Therefore, we will not discuss further the Seebeck values of the xerogels.

Surprisingly, the sulf-aerogel exhibit a lower Seebeck coefficient value than the cryogels. Compared with other porous PEDOT: PSS (see Table I.1), we can see that the Seebeck coefficient values are also distributed within 16 and 18 µV/K. No clear porosity effect on the Seebeck coefficient was reported for organic TE. However, some rare examples in porous inorganic TE materials reported energy filtering effects.[65,66] These effects arise from the fact that the low energy charge carriers near the Fermi level are scattered at the material boundaries more efficiently than the higher energy charge carriers. Consequently, the Seebeck coefficient, which transcribes the average energy of the electrons contributing to electrical conduction, increases. Could it be that the porous structure (well-defined pore walls in cryogels, vs. fibrillar network in sulf-aerogel) plays a role on this energy filtering and impact the Seebeck coefficient? Unfortunately, we are unable to answer this question at the moment.

Furthermore, the sulf-aerogels have undergone one supplementary step as compared with the xerogel and the quenched cryogel (a solvent exchange with ethanol). The conduction process in disordered systems such as conducting polymers is governed by the density of state and the Fermi level (not calculated/ measured on our materials in the frame of the PhD work). Doping can modify the distribution of energy carriers and shift the Fermi level, thus inducing modification in the charge transport properties. Thus, the solvent exchange with ethanol might have induced structural modifications at the molecular scale but also some modifications in the DOS of PEDOT: PSS resulting in a lower Seebeck coefficient. The higher σ_{app} combined with an inversely lower Seebeck coefficient of sulf-aerogel suggest that the solvent exchange has slightly increased the charge carrier density (as compared to the cryogel).

4.3. EFFECT OF THE POROUS STRUCTURE ON THE THERMAL CONDUCTIVITY

Only the thermal conductivity of the sulf-aerogels, quenched cryogels and LD could be measured, and their values are reported in Table II.1. The xerogels shape and thickness could not fit the requirements for TPS measurement with the available probe. The free-standing film was also too thin to be measured by this technique. As a reference for the dense material, we chose to use the value of $\kappa_{through\text{-}plane}$ of 0.3 W/(m.K) reported by Liu et al. for micrometer thick free-standing PEDOT: PSS films post treated with DMSO.[60] Although the preparation method was different from ours, the final sample was similar and exhibited an electrical conductivity of around 500 S/cm close to the one we obtained for our reference film. The thermal conductivity of the xerogel was mathematically estimated with the law of mixture (see equation II.6), as reported by Kroon et al.[67]

$$\kappa_{porous} = \kappa_{dense}(1-\Theta) + \kappa_{air} \times \Theta \qquad (II.6)$$

Where κ_{dense}, κ_{air} are the thermal conductivity of the dense PEDOT: PSS (0.3 W/(m.K)) and of air (0.025 W/(m.K)), respectively. Θ is the porosity. Hence, the thermal conductivity of the xerogel is estimated to be ~ 0.19 W/(m.K). Other thermal conductivity measurement techniques such as time-domain thermoreflectance or 3ω method could be used but were not readily available in our case.[68]

Implementing porosity into conducting polymers successfully reduced thermal conductivity far below the $\kappa_{lattice}$ of conducting polymers in thin films (0.2 W/(m.K)). Indeed, the thermal conductivity of the sulf-aerogel and the quenched cryogel were measured to be 0.054

W/(m.K) and 0.042 W/(m.K),respectively, compared to the five times higher thermal conductivity of dense PEDOT: PSS (0.3 W/(m.K)). These low thermal conductivity values are due to the reduction of both $\kappa_{lattice}$ and κ_{elec} (see section I.1.5). The lattice contribution was greatly reduced thanks to the very low density and high porosity of these materials but in all cases $\kappa_{elec} < \kappa_{lattice}$. Considering the Wiedemann-Franz law (assuming a Lorenz factor similar for all PCPs and close to the Sommerfeld value, i.e., 2.4428 10^{-8} W.Ω.K^{-2}), κ_{elec} ranges between 0.04 and 6.4 mW/(m.K) leading to $\kappa_{lattice}$ in the range of 40 to 59 mW/(m.K).

Interestingly, even though its density was the lowest (0.02 g/cm^3), LD sample exhibited a higher thermal conductivity ~ 0.06 W/(m.K) than the quenched cryogel (and the sulf-aerogel). This difference could not be attributed to a higher κ_{elec} for LD as its electrical conductivity is by far the lowest. Hence, we attribute the decrease of thermal conductivity in quenched cryogel (as compared to LD) to the reduction of the lattice component due to a better structuration of the network or better defined solid/gas interfaces (which may play a role in the phonon scattering or thermal resistance).

As discussed in section I.1.5, $\kappa_{lattice}$ depends mainly on conduction heat transfer by gas or solid (convection and radiation phenomenon being neglected for these samples). At ambient pressure, the gaseous contribution to the thermal conductivity varies with the pore size (or nearest solid to solid distance). For it to be minimized, the pore size must be inferior to the mean free path of phonons (i.e., ~ 70 nm). For macroporous materials such as LD or quenched cryogel (pore diameter > 50 nm), κ_{gas}, calculated from equation I.7, is very close to the thermal conductivity of air (~25 mW/(m.K)). Hence, there is almost no scattering of phonons at the solid-gas interface. Conversely, κ_{gas} ~ 4 mW/(m.K) in the sulf-aerogel thanks to its mesoporous structure. Considering that the pore size is inferior to 50 nm, the heat transfer of gas molecules is known as Knudsen diffusion. In this diffusion mode, the phonons are scattered at the boundaries of the solid skeleton and the energy transport by the gas molecules is almost suppressed. Clearly, the conservation of the mesoporous fibrillar network from the native gel is beneficial to the low thermal conductivity as compared to the random macroporous network of the LD sample. On the other hand, the pore size of the quenched cryogels is too big and should not affect the thermal conductivity.

The solid contribution to the thermal conductivity could not be estimated numerically due to the difficulty of obtaining several quantities for calculation such as the sound velocity in dense and porous PEDOT: PSS (see equations I.9 and I.10). However, it is clear that κ_{solid} varies with the density of the porous material. Thus, by considering densities of the PCPs, we were able to assign qualitatively the lowest κ_{solid} to the LD sample and the highest to the sulf-aerogel. Surprisingly, the quenched cryogels that exhibited slightly higher density than the LD have lower thermal conductivity. Theoretically, one should expect the LD to have a lower thermal conductivity than the quenched cryogel (because of a lower κ_{solid}) given that κ_{elec} can be neglected, and κ_{gas} is equivalent in macroporous samples. Again, we suggest that this effect is due to the better structuring of the quenched cryogel. It has been shown that porous closed-cell structures exhibit very good thermal insulation properties.[69] In addition, it is possible that an interface thermal resistance effect takes place in the quenched cryogel. This effect generally exists at interfaces between bound particles in the solid skeleton of the porous material.[70,71] Thus, at the solid-solid interfaces between the nanofibers packed into the walls of the macroporous structure of the cryogel quenched (see section II.3.3.2), we suggest that there is a greater thermal resistance than in the other PCPs discussed previously, reducing κ_{solid}.

Overall, implementing porosity in organic semiconductor materials decreased the thermal conductivity by five times compared to the dense material. Furthermore, we showed that the gelation and drying process have a great importance on the final properties. Indeed, the structuring of the network allowed a better scattering of phonons and thermal insulation effects. Thus, although it is important that the pore size is smaller than the mean free path of air (mesoporous sample), the reduction of thermal conductivity was possible (and even more effective) on macroporous materials. Although some mechanisms of the thermal insulation effects are not fully understood, the effect of the porosity implementation did decrease the thermal conductivity. On the other hand, as discussed in section II.4.2.1, large volumes of air within the material are clearly detrimental to electrical conductivity. In the next section, we discuss more generally the global effect of porosity on the ZT.

4.4. INFLUENCE ON ZT

In the following section, we discuss more generally how the performances of these materials are impacted by the porosity, what material is of best interest, and to what extent porosity can be used in thermoelectricity.

Power factors and ZT have been calculated for all PCPs at 300K according to equations I.2 and I.3. Their values as a function of the density are displayed in Figure II.20. It should be noted that these charts could also have been represented as a function of the porosity Θ ($\Theta = \left[1 - \frac{\rho_{porous}}{\rho_{solid}}\right]$), directly proportional to density, and the TE properties would have had the same trends.

The PCPs designed in this study all exhibit an electrical conductivity above 10^0 S/cm and a Seebeck coefficient close to the reported values for dense films. Their power factors are quite low (between 0.1-0.5 µW/(m.K^2)) compared to the reference film (17 µW/(m.K^2), not represented in the chart). As discussed in section II.4.2, the charge transport properties of these porous materials were negatively impacted by the presence of a large amount of air in the material. It is also clear that the electrical conductivity is directly related to the density (and inversely to the pore size). Although the power factor of such material is quite low as compared to thin film current records,[72] these results are very promising as they show the possibility to produce electrically conducting, mechanically robust, bulk-size PEDOT: PSS with low amounts of material.

With decreasing the density of the PCPs, σ_{app} and κ are decreasing while S slightly increased. κ was reduced five times compared to thin films. Overall, very low thermal conductivity values (in the range of 40-60 mW/(m.K) for the sulf-aerogel and quenched cryogel) were obtained.

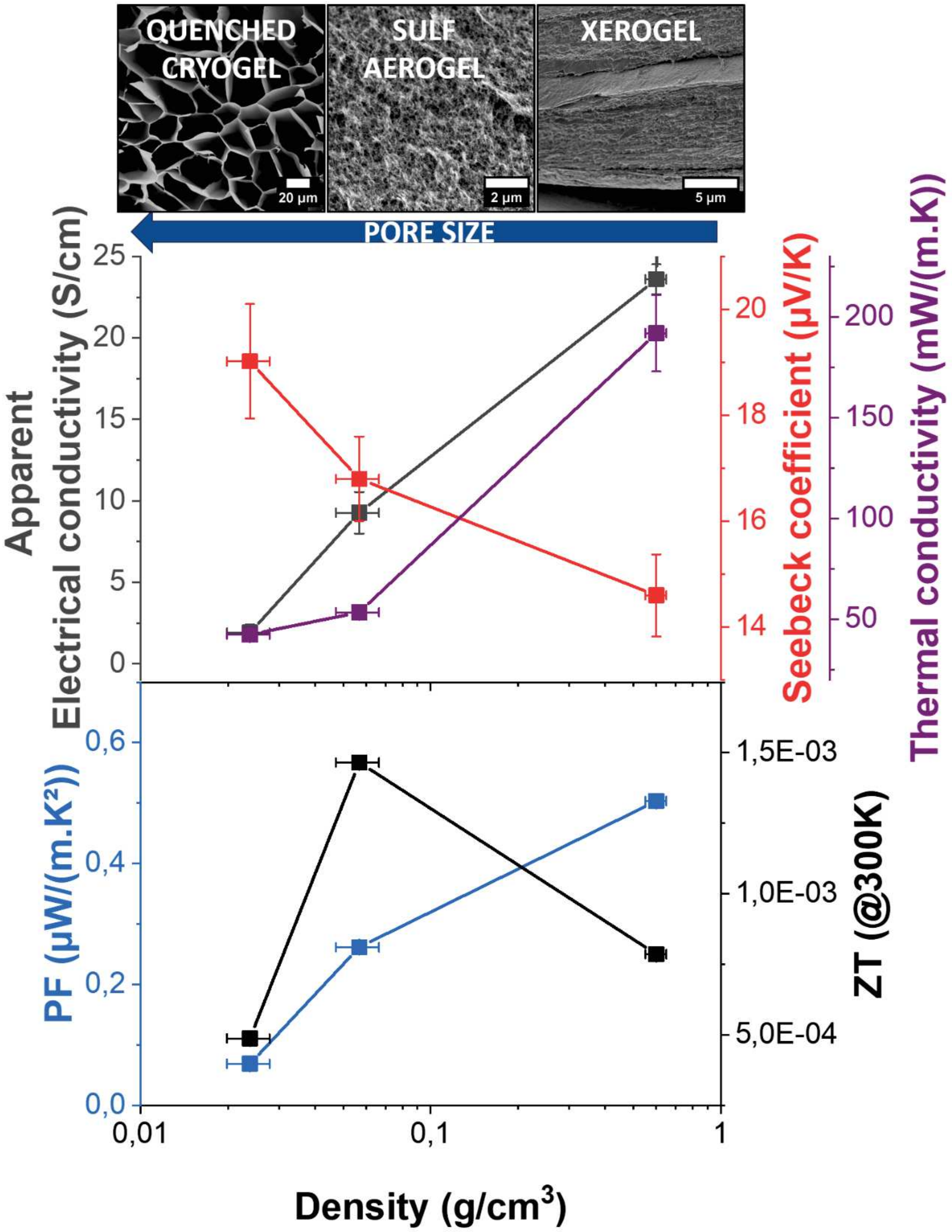

Figure II.20 Evolution of the TE properties of the quenched cryogel, sulf-aerogel, and xerogel as a function of the density. The SEM images at the top of the figure represent the porous structures of the three materials. On the first chart, the apparent electrical conductivity (in gray), the Seebeck coefficient (in red) and the thermal conductivity (in purple) of the three materials are represented vs. the density (it should be noted that the thermal conductivity of the xerogel was estimated according to equation II.5). On the second chart, the power factor PF (in blue) and the ZT (in black) of the three materials are represented vs. the density.

The very low thermal conductivity due to the low density and high porosity of the quenched cryogel and the sulf-aerogel is beneficial to the ZT. The PCPs which underwent the gelation and drying step exhibit a ZT value between 10^{-4} and 10^{-3} which is one hundred to one thousand times higher than for the lyophilized dispersion (ZT ~ 10^{-6}). These results demonstrate the crucial importance of structuration and ordered morphology when designing porous materials. ZT reaches 1.4 x 10^{-3} at 300K for the sulf-aerogel which has the best compromise between σ, κ and S. The sulf-aerogel is the most promising porous material designed in this section and stands amongst the highest reported values for pure PEDOT: PSS porous materials.[73]

The gelation step allowed the PEDOT: PSS to rearrange in a more ordered system, favoring charge transport as compared to the lyophilized dispersion. We were able to reach glass-like thermal insulation properties for mm-thick material by implementing porosity. On the other hand, the apparent electrical conductivity is limited due to the high air content (but the dense electrical conductivity remains high) while the Seebeck coefficient was still comparable to what is obtained in dense materials.

Clearly, the electrical conductivity is directly related to the porosity of the material. This suggests that there is still room for improvement to obtain the best compromise between high porosity (i.e., low thermal conductivity) and electrical conductivity to maximize ZT. One way of improvement would be the fine control of the materials' density. For the sulf-aerogel, it was not possible to control the density of the material, induced by the native gel. Apart from increasing the weight % of the initial dispersion (very challenging because of the low solubility of PEDOT: PSS) modifications of the gelation step could result in even more conducting aerogels. For the quenched cryogels, it may be easier to tune the porous structure considering it is defined by the ice crystals growth during the drying step.

The main goal of chapter II was to elaborate p-type porous materials with various ranges of porosity from PEDOT: PSS. We showed in sections II.2 and II.3 that elaborating these types of materials is feasible, that the process is reproducible and tunable from the same starting material, the hydrogel. The other main goal of this chapter was to demonstrate the interest of porosity for thermoelectric applications. We discussed in section II.4.2, II.4.3 and II.4.4

how the TE properties were influenced by the addition of a large volume of air in the materials and showed the promising properties of the sulf-aerogel. Moreover, even though it is very difficult to calculate the $/W of these materials, it is clear that the elaboration of big, low-density materials using small quantities of PEDOT: PSS is promising for further production of low-cost TE generators.

To go further, one must improve the TE properties of these promising materials. It has been shown that mechanical compression of porous materials (increasing the density) can increase their electrical conductivity.[1] Obviously, this also implies changes in the thermal conductivity as a consequence. Another possibility to improve ZT would be to enhance the charge transport properties by a post-treatment after obtaining the porous structure by analogy with the so-called "secondary doping" of PEDOT: PSS reported in the literature for dense films (see section I.1.4). Moreover, secondary doping by vapor phase is likely to be effective in such materials, Kroon et al. demonstrated that the doping of P3HT foam was more efficient due to the presence of pores, facilitating the infiltration of molecules.[67] In the next section of this chapter, we investigate the effect of vapor-phase solvent treatment on the TE properties of the quenched cryogels and sulf-aerogels to maximize their ZT.

5. DMSO VAPOR PHASE POST-TREATMENT ON PCPS

The following section discusses the effect of dimethyl sulfoxide (DMSO) vapor treatment (VT) on the charge transport properties of sulf-aerogels and quenched cryogels. Xerogels have not been studied here since they suffered from too important shrinkage and were not homogeneous enough. The aim was to optimize further the charge transport properties of our porous samples. DMSO has been chosen for its positive impact on charge transport properties of PEDOT: PSS films (see section I.1.4).

PCPs were exposed to DMSO vapor in a closed vessel at 150 °C for different times. Several samples were used for this study to avoid the effect of the accumulation of the exposure times (a different sample for a specific duration of exposure to the vapor was used). Then, the samples were dried in a vacuum oven at 150 °C to remove any DMSO traces. Further details can be found in the Experimental section. Unfortunately, due to the shrinkage of the sample after exposure, we were unable to follow the evolution of the thermal conductivity. Thus, only the charge transport properties are discussed in this section.

With the goal to enhance the Seebeck coefficient by tuning the oxidation level of PEDOT:PSS,[74] tetrakis(dimethylamino)ethylene (TDAE) vapor exposure was also realized on the cryogels. Unfortunately, the results were inconclusive to be presented here.

5.1. CASE OF THE SULF-AEROGEL

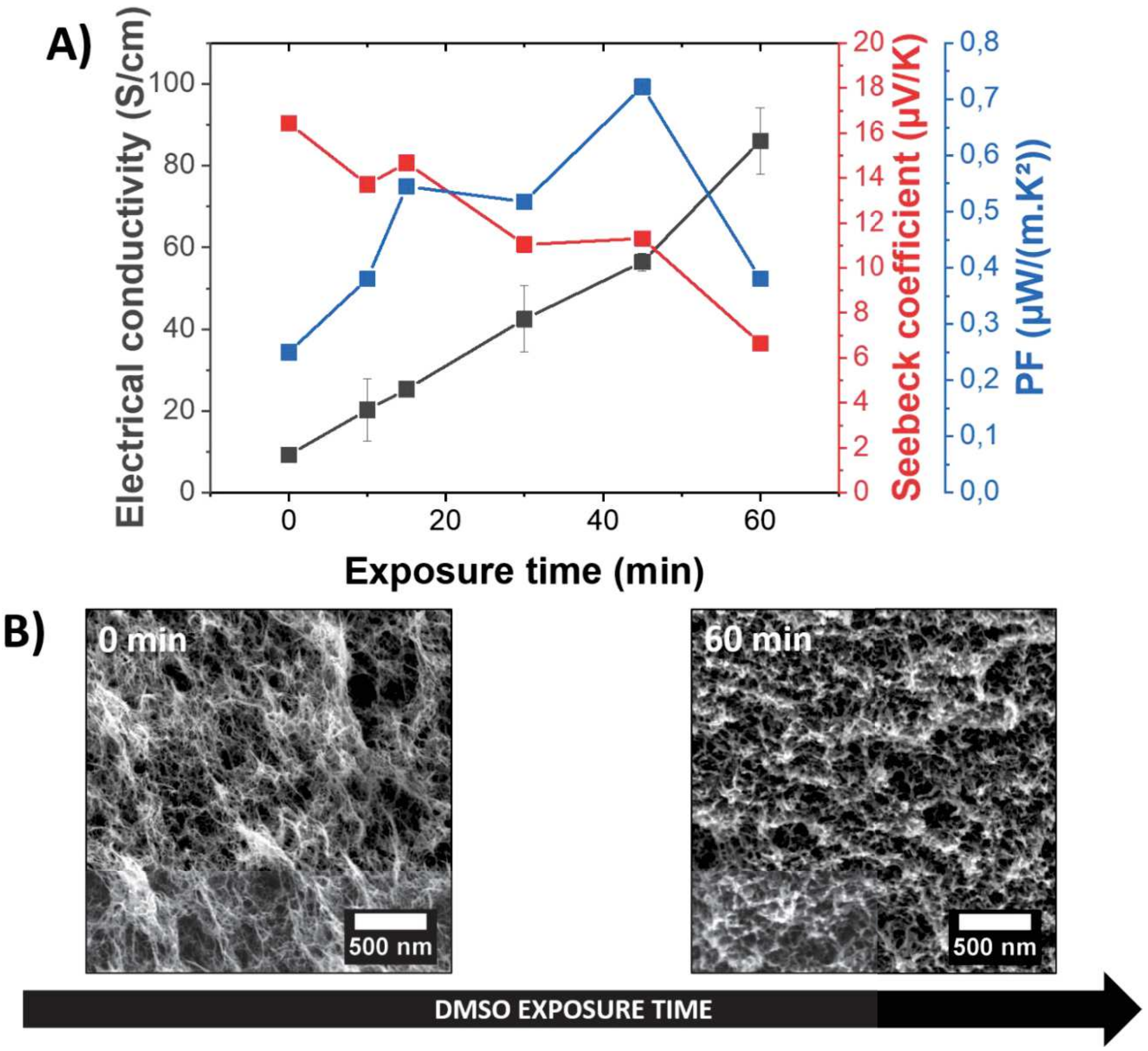

Figure II.21: A) Evolution of the electrical conductivity (in gray), Seebeck coefficient (in red) and PF (in blue) of the sulf-aerogel as a function of DMSO exposure time. B) SEM images of the sulf-aerogel structure before and after 60 min of DMSO VT.

Figure II.21.A illustrates the evolution of the TE properties for different sulf-aerogels upon DMSO exposure. The electrical conductivity increased to about 100 S/cm (ten times its initial value). Conversely, the Seebeck coefficient suffered from the DMSO treatment and decreased from 17 µV/K to ~ 6 µV/K. The inverse evolution of the Seebeck coefficient with electrical conductivity is expected with an increase in charge carrier concentration. The network is much denser (see the SEM image in Figure II.22.B and the graph in Figure II.23.B) after DMSO exposure.

This treatment was rather beneficial for the PF reaching 0.7 µW/(m.K^2) which is roughly twice its initial value at 45 min of exposure. Unfortunately, the sulf-aerogels suffered from a drastic contraction (~ 70% of volume loss) upon long DMSO exposure times. Such shrinkage limits the use of the sample for future applications. This contraction is related to the densification of the network as shown by SEM in Figure II.21.B (sample density increased from 0.057 to 0.9 g/cm^3). This problem occurred during exposure to DMSO vapors and not during the further drying step at 150°C.

A possible way to minimize the contraction while taking the benefit of DMSO treatment could be to add DMSO to the CO_2 in the supercritical phase during the gel drying step. However, this would require much higher pressure and temperature conditions to reach supercritical DMSO conditions.

5.2. CASE OF THE QUENCHED CRYOGEL

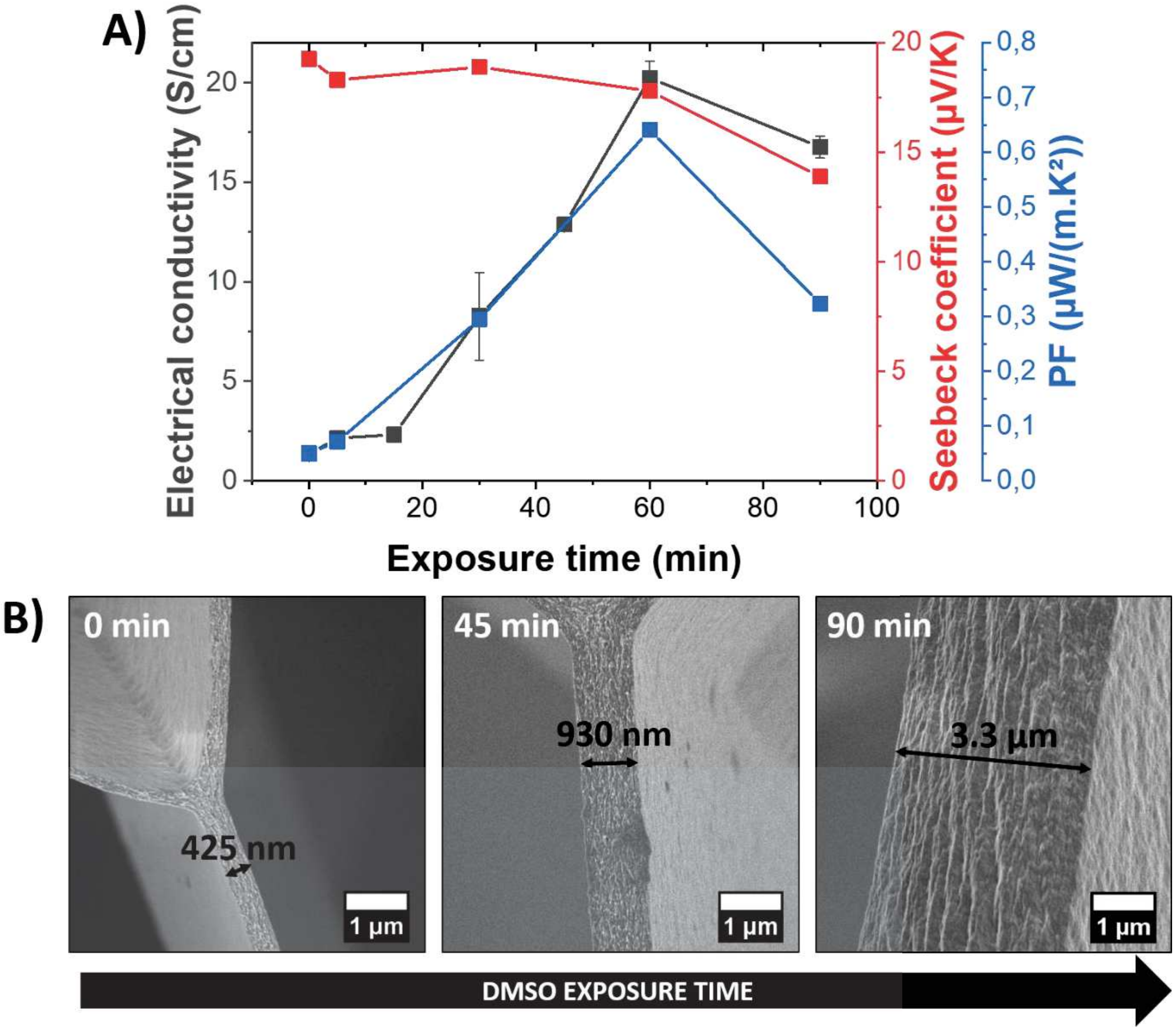

Figure II.22 A) Evolution of the electrical conductivity (in gray), Seebeck coefficient (in red) and PF (in blue) of the quenched cryogel as a function of DMSO exposure time. B) SEM images of the quenched cryogel pore walls before, and after 45 and 90 min of DMSO VT.

The TE properties of the quenched cryogel upon vapor treatment of DMSO are shown in Figure II.22.A. The electrical conductivity gradually increased upon DMSO VT and reached a maximum after 60 min of exposure where a twenty-fold increase was observed (σ_{app} = 20 S/cm). The Seebeck coefficient suffered of a slight decrease from 19 µV/K to 14 µV/K (at 60 min of exposure S = 17.8 µV/K). DMSO VT was beneficial to the charge transport properties of the quenched cryogel. We observed a tenfold increase in the power factor after 60 min of exposure to DMSO vapor. The structure of the quenched cryogel was also altered (see Figure

II.22.B) but less than for the sulf-aerogel. An increase in pore wall thickness, as shown in Figure II.22.B, was observed after exposure to DMSO vapor. The pore walls, initially ~ 400 nm, increased to a thickness of over 3 µm after 90 min of exposure. The honeycomb-like structure was less well-defined after vapor treatment. The sample density increased from 0.03 to 0.1 g/cm^3 after 90 min of DMSO VT (see Figure II.23.A).

5.3. DMSO VT ANALYSIS

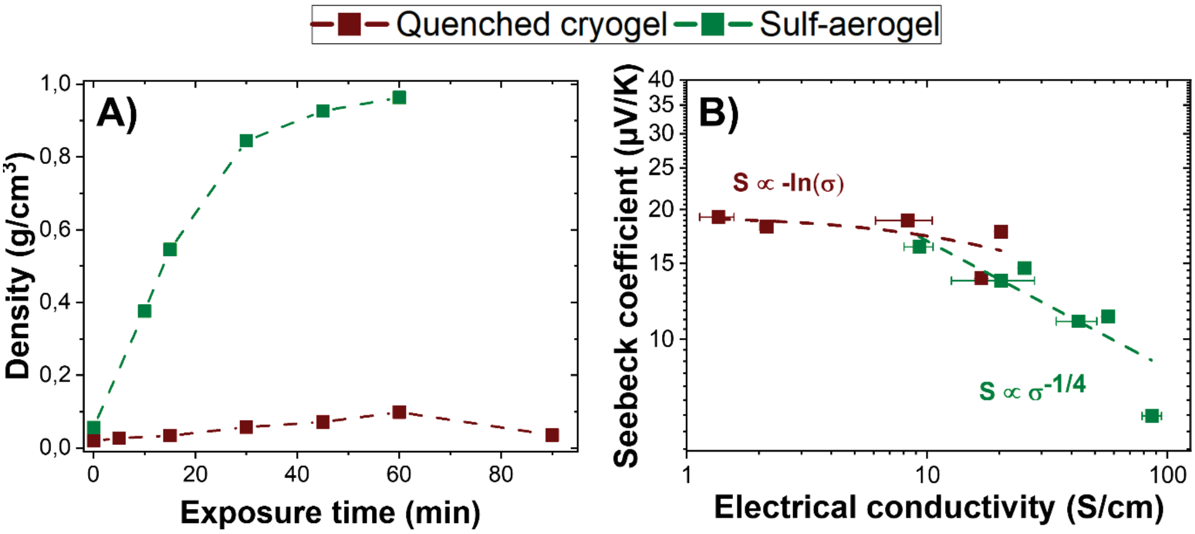

Figure II.23: A) Evolution of the density of the sulf-aerogel and quenched cryogel as a function of exposure time to DMSO vapor; B) Scaling plots of the Seebeck coefficient as a function of the electrical conductivity. The fitting lines have been chosen according to the expressions given in ref [75] *leading to the power law scaling relation* $S \propto \sigma^{-1/4}$ *and the logarithm scaling* $S \propto -\ln \sigma$.

The initial goal of this post-treatment was to increase the charge transport properties. Post-treatments with polar solvents have often been used in the literature to improve the electrical conductivity of thin films. Different mechanisms to attribute this enhancement have been discussed. Firstly, DMSO could induce a screening effect due to the high dielectric constant of the solvent.[76] Thus, DMSO would decrease the coulombic interaction between PEDOT and PSS and thus create a segregation of the polymers. Secondly, a polar solvent treatment could increase the electrical conductivity of a film by reducing the amount of PSS by washing it or by modifying the conformation of PEDOT.[36] Recently, some authors have attempted to rationalize the increase in electrical conductivity by theoretical means of molecular dynamics and density functional theory calculations. For example, Yildirim et al. demonstrated that hydrogen bonding is formed between PSSH and DMSO and is the dominant interaction in DMSO treated PEDOT: PSS.[77] This interaction has two effects on the system. The expansion of the PSS chain causing phase separation between PSSH and PSS interacting with PEDOT, and a screening effect inducing phase separation between PSS and PEDOT. Thus, the partial reduction of the amount of PSS is directly related to the improvement of the electrical conductivity which would be due to an improvement of the morphology of the film by a better connectivity between the PEDOT grains. Cassinelli et al. also studied the effect of DMSO treatment of PEDOT: PSS films by several characterization techniques including X-ray scattering, XPS and ultraviolet photoelectron spectroscopy.[38] Again, they attributed part of the improvement in electrical conductivity to the partial removal of PSS and the rearrangement of the two polymers without an increase in crystallinity.

In our case, it is difficult to attribute the increase in electrical conductivity to a reduction of the amount of PSS. Indeed, since the porous materials were not rinsed after treatment or annealing, if DMSO induced a sufficient screening effect to separate PSSH from PEDOT, it is very unlikely that PSSH was removed. Furthermore, as discussed in section II.2.2.2, excess PSSH has already been washed out during the gelation step. However, it is still possible that a rearrangement occurred, separating the PEDOT and PSS domains, which could partially explain the changes in TE properties. It is evident from the SEM images that DMSO VT induced structural changes: an increase of the density of both materials and a clear increase of the pore walls thicknesses in the quenched cryogel were observed.

In both cases, the increase in electrical conductivity along with a decrease in the Seebeck coefficient was observed upon DMSO VT exposure. Beyond 60 min of exposure for the cryogels, the electrical conductivity tends to decrease. In both cases, no leveling of S or σ was reached, meaning that we did not achieve the end of the process. Considering a similar time of exposure, the changes in S and σ are more important for the sulf-aerogel than for the cryogel. This can be attributed to the strong increase in density (collapse of mesoporous fibrillar structure) in the case of the sulf-aerogel. Moreover, the scaling profiles between the

Seebeck coefficient and the electrical conductivity seem to follow a power law scaling for the sulf-aerogel and a logarithm scaling for the cryogel (see Figure II.23.B). The logarithm scaling has already been observed for less conducting systems.[75,78] These two different profiles highlight that the porous structure plays an important role on the charge transport mechanisms. As compared to their initial values (before vapor treatment), the power factor of cryogel achieved a tenfold improvement while it was only a two-fold improvement for the sulf-aerogel.

These results are quite preliminary, and the evolution of the thermal conductivity should also be monitored for a comprehensive estimation of the DMSO VT influence on the TE properties. But vapor phase post-treatment is promising for porous organic conducting materials. A significant increase of the charge transport properties was observed for both porous structures. The diffusion of the solvent in the material was easily realized and seemed more efficient in the mesoporous structure. Further optimization of the process could even lead to higher charge transport properties. It has been reported in the literature that sequential vapor treatment was more efficient than a long exposure in one shot (see section I.1.3.2). The main issue here is the densification of the network, which will eventually lead to an increase in the thermal conduction properties. One way to optimize this process would be to perform the DMSO exposure either before drying for the quenched cryogel or during supercritical drying for the sulf-aerogel. However, we are unable to predict if the treatment would be as efficient.

6. CONCLUSION

In this chapter, we have demonstrated the possibility of producing porous materials from the commercial dispersion of PEDOT: PSS. For a better understanding of the global process, we first focused on the structural characteristics of the initial dispersion. Contrary to other reports stating that the dispersion consists in spherical particles, we showed by electron microscopy and X-ray scattering techniques the presence of long fibrils of a few nm thicknesses in the dispersion. We suggest that the PEDOT: PSS fibrils tend to arrange themselves in a core-shell system (PEDOT rich core, PSS rich shell). Internally, the fibrils consist of a lamellar structure of π-stacked PEDOT oligomers distributed along the PSS chains. This model is consistent with our observations but also with other reports in the literature. We have demonstrated the possibility to form robust and fibrillar hydrogels of PEDOT: PSS by acidification of the dispersion and we have followed their formation mechanism. Through a combination of spectroscopy and structural analyses, we were able to demonstrate the effect of protonation on the PEDOT: PSS ratio, a change in the PEDOT conformation and in fiber morphology. Overall, we suggested a gelation mechanism involving first the destabilization of the fibrillar dispersion induced by the protonation of the PSS shell. Then, the reconformation of PEDOT molecules facilitates entanglement and π-stacking interactions resulting in a 3D conducting mesoporous fibrillar hydrogel.

From the same hydrogel, we produced three different porous structures with different porosity ranges. Air drying, supercritical drying, and freeze-drying produced xerogels, sulf-aerogels, and quenched cryogels, respectively. The sheet-like structure of the contracted xerogel was difficult to study and its dimensions and shape did not meet the requirements of our material design. Therefore, this material was not further optimized. In contrast, we were able to maintain the native mesoporous fibrillar structure (of the hydrogel) in the highly porous sulf-aerogel through supercritical drying. Clearly, solvent exchange and drying conditions were key parameters in this success. Finally, a third structure was obtained through freeze-drying (for the quenched cryogel). Cryo-SEM revealed how the native fibrillar network of the gel turned into a channel-like structure through ice crystal growth. The templating of a porous structure with ice crystals opened a door to the fine-tuning of the macroporous PEDOT: PSS structure which will be developed in the next chapter. Finally, the TE properties of these PCPs were investigated. We showed a successful reduction of thermal conductivity down to 0.042 W/(m.K) for the quenched cryogel through the implementation of porosity. It was difficult, without additional theoretical modeling and simulation of thermal conduction, to clearly highlight the reason for this reduction. Nevertheless, it is clear that the low density of the material was one of the key factors in the reduction of κ, while the contribution of gas conduction had a smaller impact. Furthermore, compared to the disordered structure of the lyophilized dispersion, the ordered structure of the quenched cryogel exhibited superior thermal insulation properties and apparent electrical conductivity.

Regarding the Seebeck coefficient, it was little affected by the high porosity of the material as compared to thin films. The reason for the low measured S value for xerogel still needs to be investigated. We showed that despite their high porosity, the xerogels, sulf-aerogels, and quenched cryogels exhibited electrical conductivities above 10^0 S/cm, which was not the case for the lyophilized dispersion. Although their electrical conductivities were lower than those of the dense materials, we demonstrated that the backbone composing the sulf-aerogel and quenched cryogel should have similar transport properties (and probably doping state and morphology) as their dense counterpart. In addition, we were able to improve the electrical conductivity and power factor of the sulf-aerogel and quenched cryogels by further solvent treatment. We would like to note that these results are still preliminary, and a full-property study needs to be performed to conclude on the ZT gain. Finally, there is still room for improvement and the finer control of the cryogel porous structure will be developed in chapter III while a PCP with even more promising properties will be discussed in chapter IV.

7. REFERENCES

[1] X. Wang, P. Liu, Q. Jiang, W. Zhou, J. Xu, J. Liu, Y. Jia, X. Duan, Y. Liu, Y. Du, F. Jiang, *ACS Appl. Mater. Interfaces* **2019**, *11*, 2408.

[2] N. Yanagishima, S. Kanehashi, H. Saito, K. Ogino, T. Shimomura, *Polymer (Guildf).* **2020**, *206*, 122912.

[3] M. P. Gordon, E. W. Zaia, P. Zhou, B. Russ, N. E. Coates, A. Sahu, J. J. Urban, *J. Appl. Polym. Sci.* **2017**, *134*, 44070.

[4] X. Zhang, C. Li, Y. Luo, *Langmuir* **2011**, *27*, 1915.

[5] X. Zhang, D. Chang, J. Liu, Y. Luo, *J. Mater. Chem.* **2010**, *20*, 5080.

[6] A. M. D. Wan, S. Inal, T. Williams, K. Wang, P. Leleux, L. Estevez, E. P. Giannelis, C. Fischbach, G. G. Malliaras, D. Gourdon, *J. Mater. Chem. B* **2015**, *3*, 5040.

[7] J. Zhang, X. Fan, X. Meng, J. Zhou, M. Wang, S. Chen, Y. Cao, Y. Chen, C. W. Bielawski, J. Geng, *ACS Nano* **2021**, *15*, 8870.

[8] A. G. Guex, J. L. Puetzer, A. Armgarth, E. Littmann, E. Stavrinidou, E. P. Giannelis, G. G. Malliaras, M. M. Stevens, *Acta Biomater.* **2017**, *62*, 91.

[9] B. Yao, H. Wang, Q. Zhou, M. Wu, M. Zhang, C. Li, G. Shi, *Adv. Mater.* **2017**, *29*, 1700974.

[10] R. Maeda, H. Kawakami, Y. Shinohara, I. Kanazawa, M. Mitsuishi, *Mater. Lett.* **2019**, *251*, 169.

[11] R. Maeda, Y. Shinohara, H. Kawakami, Y. Isoda, I. Kanazawa, M. Mitsuishi, *Nanotechnology*

2020, *32*, 135403.

[12] B. Lu, H. Yuk, S. Lin, N. Jian, K. Qu, J. Xu, X. Zhao, *Nat. Commun.* **2019**, *10*, 1043.

[13] N. Kim, S. Kee, S. H. Lee, B. H. Lee, Y. H. Kahng, Y. R. Jo, B. J. Kim, K. Lee, *Adv. Mater.* **2014**, *26*, 2268.

[14] H. Shi, C. Liu, Q. Jiang, J. Xu, *Adv. Electron. Mater.* **2015**, *1*, 1500017.

[15] Z. Fan, J. Ouyang, *Adv. Electron. Mater.* **2019**, *5*, 1.

[16] M. N. Gueye, A. Carella, J. Faure-Vincent, R. Demadrille, J. P. Simonato, *Prog. Mater. Sci.* **2020**, *108*, 100616.

[17] Y. Xia, J. Ouyang, *ACS Appl. Mater. Interfaces* **2012**, *4*, 4131.

[18] U. Lang, E. Muller, N. Naujoks, J. Dual, *Adv. Funct. Mater.* **2009**, *19*, 1215.

[19] D. Alemu, H. Y. Wei, K. C. Ho, C. W. Chu, *Energy Environ. Sci.* **2012**, *5*, 9662.

[20] J. Rivnay, S. Inal, B. A. Collins, M. Sessolo, E. Stavrinidou, X. Strakosas, C. Tassone, D. M. Delongchamp, G. G. Malliaras, *Nat. Commun.* **2016**, *7*, 7:11287.

[21] T. Takano, H. Masunaga, A. Fujiwara, H. Okuzaki, T. Sasaki, *Macromolecules* **2012**, *45*, 3859.

[22] O. Bubnova, Z. U. Khan, H. Wang, S. Braun, D. R. Evans, M. Fabretto, P. Hojati-Talemi, D. Dagnelund, J. B. Arlin, Y. H. Geerts, S. Desbief, D. W. Breiby, J. W. Andreasen, R. Lazzaroni, W. M. Chen, I. Zozoulenko, M. Fahlman, P. J. Murphy, M. Berggren, X. Crispin, *Nat. Mater.* **2014**, *13*, 190.

[23] C. M. Palumbiny, F. Liu, T. P. Russell, A. Hexemer, C. Wang, P. Müller-Buschbaum, C. Heller, C. J. Schaffer, V. Körstgens, G. Santoro, S. V Roth, P. Müller-Buschbaum, F. Liu, T. P. Russell, A. Hexemer, C. Wang, P. Müller-Buschbaum, *Adv. Mater.* **2015**, *27*, 3391.

[24] A. V. Volkov, K. Wijeratne, E. Mitraka, U. Ail, D. Zhao, K. Tybrandt, J. W. Andreasen, M. Berggren, X. Crispin, I. V. Zozoulenko, *Adv. Funct. Mater.* **2017**, *27*, 1700329.

[25] N. Kim, B. H. Lee, D. Choi, G. Kim, H. Kim, J. R. Kim, J. Lee, Y. H. Kahng, K. Lee, *Phys. Rev. Lett.* **2012**, *109*, 106405.

[26] F. F. Pang, S. Li, W. Q. Sun, G. Z. Han, *Mater. Chem. Phys.* **2017**, *186*, 246.

[27] G. Steger, *IEEE Trans. Pattern Anal. Mach. Intell.* **1998**, *20*, 113.

[28] M. Glaser, J. Schnauß, T. Tschirner, B. U. S. Schmidt, M. Moebius-Winkler, J. A. Käs, D. M. Smith, *New J. Phys.* **2016**, *18*, 055001.

[29] H. Yuk, B. Lu, S. Lin, K. Qu, J. Xu, J. Luo, X. Zhao, *Nat. Commun.* **2020**, *11*, 1.

[30] J. Als-Nielsen, D. McMorrow, *Elements of Modern X-Ray Physics: Second Edition*, John Wiley And Sons, **2011**.

[31] R.-J. Doe, *Methods of X-Ray and Neutron Scattering in Polymer Science*, Oxford University Press, New York, **2000**.

[32] S. R. Kline, *J. Appl. Crystallogr.* **2006**, *39*, 895.

[33] M. A. Leaf, M. Muthukumar, *Macromolecules* **2016**, *49*, 4286.

[34] R. J. Murphy, K. M. Weigandt, D. Uhrig, A. Alsayed, C. Badre, L. Hough, M. Muthukumar, *Macromolecules* **2015**, *48*, 8989.

[35] M. Z. Ali, K. M. K. Ishak, M. A. M. Zawawi, M. Jaafar, Z. Ahmad, *Synth. Met.* **2022**, *286*, 117037.

[36] X. Crispin, S. Marciniak, W. Osikowicz, G. Zotti, A. W. D. V. A. N. D. E. R. Gon, F. Louwet, M. Fahlman, L. Groenendaal, F. D. E. Schryver, W. R. Salaneck, *J. Polym. Sci. Part B Polym. Phys.* **2003**, *41*, 2561.

[37] G. Zotti, S. Zecchin, G. Schiavon, F. Louwet, L. Groenendaal, X. Crispin, W. Osikowicz, W. Salaneck, M. Fahlman, *Macromolecules* **2003**, *36*, 3337.

[38] M. Cassinelli, W. T. Park, Y. Kim, J. H. Kim, Y. Y. Noh, M. Caironi, *Appl. Phys. Lett.* **2021**, *119*, 033301.

[39] S. R. S. Kumar, N. Kurra, H. N. Alshareef, *J. Mater. Chem. C* **2015**, *4*, 215.

[40] N. Su, H. Li, Y. Huang, X. Zhang, *J. Nanomater.* **2015**, *2015*, 1.

[41] E. Hosseini, V. Ozhukil Kollath, K. Karan, *J. Mater. Chem. C* **2020**, *8*, 3982.

[42] Z. U. Khan, O. Bubnova, M. J. Jafari, R. Brooke, X. Liu, R. Gabrielsson, T. Ederth, D. R. Evans, J. W. Andreasen, M. Fahlman, X. Crispin, *J. Mater. Chem. C* **2015**, *3*, 10616.

[43] Q. Zhao, R. Jamal, L. Zhang, M. Wang, T. Abdiryim, *Nanoscale Res. Lett.* **2014**, *9*, 1.

[44] E. Susanti, P. Wulandari, Herman, *J. Phys. Conf. Ser.* **2018**, *1080*, 012010.

[45] J. Ouyang, Q. Xu, C. W. Chu, Y. Yang, G. Li, J. Shinar, *Polymer (Guildf).* **2004**, *45*, 8443.

[46] *IUPAC. Compendium of Chemical Terminology, 2nd Ed. (the "Gold Book"). Compiled by A. D. McNaught and A. Wilkinson. Blackwell Scientific Publications, Oxford*, **1997**.

[47] V. A. Parsegian, *Van Der Waals Forces*, Cambridge University Press, **2005**.

[48] S. Han, F. Jiao, Z. U. Khan, J. Edberg, S. Fabiano, X. Crispin, *Adv. Funct. Mater.* **2017**, *27*, 1703549.

[49] J. C. Kasper, W. Friess, *Eur. J. Pharm. Biopharm.* **2011**, *78*, 248.

[50] S. Deville, *Freezing Colloids: Observations, Principles, Control, and Use*, Springer International Publishing, Cham, **2017**.

[51] J. Dubochet, M. Adrian, J.-J. Chang, J.-C. Homo, J. Lepault, A. McDowall, P. Schultz, *Q. Rev. Biophys.* **1988**, *21*, 129.

[52] C. Efthymiou, M. A. K. Williams, K. M. McGrath, *Food Hydrocoll.* **2017**, *73*, 203.

[53] H. Topsøe, *Geometric Factors in Four Point Resistivity Measurement*, **1968**.

[54] S. Yilmaz, *J. Semicond.* **2015**, *36*, 082001.

[55] M. F. Ashby, A. G. Evans, N. . Fleck, L. J. Gibson, J. . Hutchinson, H. N. G. Wadley, *Metal Foams : A Design Guide*, Butterworth-Heineman, Boston, **2000**.

[56] R. Goodall, L. Weber, A. Mortensen, *J. Appl. Phys.* **2006**, *100*, 44912.

[57] Y. Feng, H. Zheng, Z. Zhu, F. Zu, *Mater. Chem. Phys.* **2003**, *78*, 196.

[58] F. G. Cuevas, J. M. Montes, J. Cintas, P. Urban, *J. Porous Mater.* **2009**, *16*, 675.

[59] K. P. Dharmasena, H. N. G. Wadley, *J. Mater. Res.* **2002**, *17*, 625.

[60] J. Liu, X. Wang, D. Li, N. E. Coates, R. A. Segalman, D. G. Cahill, *Macromolecules* **2015**, *48*, 585.

[61] Y. Xia, K. Sun, J. Ouyang, *Adv. Mater.* **2012**, *24*, 2436.

[62] T. A. Yemata, Y. Zheng, A. K. K. Kyaw, X. Wang, J. Song, W. S. Chin, J. Xu, *RSC Adv.* **2020**, *10*, 1786.

[63] J. C. Gustafsson, B. Liedberg, O. Inganäs, *Solid State Ionics* **1994**, *69*, 145.

[64] X. Chen, O. Inganäs, *J. Phys. Chem.* **1996**, *100*, 15202.

[65] J. H. Lee, G. A. Galli, J. C. Grossman, *Nano Lett.* **2008**, *8*, 3750.

[66] K. Valalaki, P. Benech, A. Galiouna Nassiopoulou, *Nanoscale Res. Lett.* **2016**, *11*, 201.

[67] R. Kroon, J. D. Ryan, D. Kiefer, L. Yu, J. Hynynen, E. Olsson, C. Müller, *Adv. Funct. Mater.* **2017**, *27*, 1704183.

[68] H. Wang, W. Chu, G. Chen, H. Wang, W. Chu, G. Chen, *Adv. Electron. Mater.* **2019**, *5*, 1900167.

[69] M. J. Oh, J. H. Lee, P. J. Yoo, *Adv. Funct. Mater.* **2021**, *31*, 1.

[70] C. W. Nan, R. Birringer, D. R. Clarke, H. Gleiter, *J. Appl. Phys.* **1997**, *81*, 6692.

[71] R. Prasher, *Phys. Rev. B* **2006**, *74*, 165413.

[72] Z. Zhu, C. Liu, F. Jiang, J. Xu, E. Liu, *Synth. Met.* **2017**, *225*, 31.

[73] Q. Weinbach, C. B. Nielsen, L. Biniek, *J. Mater. Chem. C* **2021**, *9*, 10173.

[74] O. Bubnova, Z. U. Khan, A. Malti, S. Braun, M. Fahlman, M. Berggren, X. Crispin, *Nat. Mater.* **2011**, *10*, 429.

[75] M. Lepinoy, P. Limelette, B. Schmaltz, F. T. Van, *Sci. Rep.* **2020**, *10*, 1.

[76] J. Y. Kim, J. H. Jung, D. E. Lee, J. Joo, *Synth. Met.* **2002**, *126*, 311.

[77] E. Yildirim, G. Wu, X. Yong, T. L. Tan, Q. Zhu, J. Xu, J. Ouyang, J. S. Wang, S. W. Yang, *J. Mater. Chem. C* **2018**, *6*, 5122.

[78] V. Vijayakumar, Y. Zhong, V. Untilova, M. Bahri, L. Herrmann, L. Biniek, N. Leclerc, M. Brinkmann, *Adv. Energy Mater.* **2019**, *9*, 1900266.

CHAPTER III IMPACT OF PORE SIZE AND ORIENTATION IN ICE-TEMPLATED MACROPOROUS PEDOT: PSS MATERIALS

III. IMPACT OF PORE SIZE AND ORIENTATION IN ICE-TEMPLATED MACROPOROUS PEDOT: PSS MATERIALS

1. INTRODUCTION

As discussed in chapter II, the freeze-drying technique induces modifications of the porous structure. We demonstrated in section II.3.3.2 by cryo-SEM that the formation of ice crystals in the network allowed the formation of a different porous structure from that of the native hydrogel. With this knowledge, we decided to take advantage of the structural changes induced during drying to control the pore structure of our materials. This interesting strategy to tailor the porous structure of polymers is called the "ice-templating" method, derived from freeze-drying. Ice-templating (also called "freeze-casting" in some reports) is the process of tailoring the porous structure of a material through the controlled growth of ice crystals.[1,2] With this technique, the obtained materials are macroporous and the pores are more or less the invert replica of the ice crystals formed during the freezing step. Although this technique can be applied with many solvents, "ice" is used as a generic term for crystal solvents. In this thesis, we focused only on freezing water.

The quenched cryogels discussed in chapter II exhibited a macroporous honeycomb structure with a rather disordered overall pore organization. Although the pores were oriented in the same direction within micrometer-sized grains, the quenched cryogel can be considered a globally isotropic material. Aligning the whole porous structure could be of great interest. Materials with well-ordered pore morphology and aligned microarchitecture have been shown to exhibit remarkable anisotropic properties, mostly mechanical ones.[3–5] But thermal,[6–9] or electrical[10,11] anisotropic conductivities were also reported for such aligned porous structures. More generally, as discussed in sections I.1.3.3 and I.1.4.3, increasing the order of the micro/macrostructure of conducting polymers is beneficial for charge transport. Moreover, aligning the pores in silicon was shown by Lee et al. to improve the electrical conductivity compared to disordered porosity.[12] Thus, we consider this drying method as a way to better control the properties of our macroporous materials. In addition, we may be able to tune the size of the pores by playing on the freezing rate (as revealed through the cryo-SEM experiment on the hydrogel in section II.3.3.2).

In the literature, the ice-templating method was applied on the PEDOT: PSS dispersion, resulting in poorly defined pores of various shapes and orientations.[13–16] Here, we intend to apply this drying process to our PEDOT: PSS hydrogels to form macroporous materials with ordered pores of tunable size. The influence of pore size and anisotropy on TE properties is investigated. It should be noted that the work discussed in the following chapter was realized with the help of two master students: Naoures Hmili and Emma Gottis.

2. ORIENTATION AND PORE SIZE CONTROL THROUGH ICE CRYSTAL GROWTH CONTROL

2.1. ICE-TEMPLATING THEORY

Before going further in our subject, it is necessary to bring some keys to understand how water crystals grow and modify the porous structure of our material. Figure III.1 illustrates the general process of ice-templating. Generally, it is used on colloidal dispersion (poor cohesion between the polymer particles), in our case we will use this method on our hydrogels (3D fibrillar network).

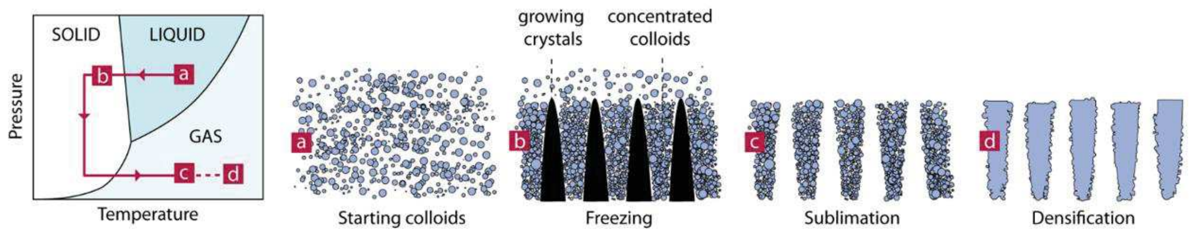

Figure III.1: Schematic diagram of ice-templating; a) starting from a colloidal dispersion at room temperature; b) the dispersion is frozen, ice crystals grow, pushing aside the particles; c) at low temperature and high vacuum, the ice is sublimated leaving cavities in the shape of the ice crystals; d) the final ice-templated solid structure. Reproduced from [17].

2.1.1. FREEZING WATER

Freezing water can be divided into two steps, i) nucleation and ii) ice crystal growth. The very first instants of these two steps are of huge importance as they determine the shape and orientation of the final crystals (and thus of the pores). Matsumoto et al. showed that when water is sufficiently cooled, water molecules tend to form clusters (i.e., nuclei) by hydrogen bonding in an arrangement similar to ice crystals.[18,19] In our non-pure system, nucleation is considered heterogeneous because there are energetically favorable sites for nucleus formation (i.e., impurities, polymer network). Once the critical mass of nuclei is reached (by the diffusion of new atoms or molecules towards the nuclei), ice crystallization occurs throughout the system.

The cooling conditions play a decisive role in the formation of the nuclei (and the crystals). If the cooling is very fast, it is possible to cool water below its freezing point (i.e., supercooled state) before the formation of the first nuclei or crystal. Under these conditions, once the nucleation occurs, the growth of ice crystal is extremely fast as the system is out of equilibrium. Globally, the nucleation temperature (i.e., the supercooling degree) and the freezing rate are the key properties to control the number of nuclei formed, the rate of ice growth, and the size of ice crystals.[20] A high nucleation temperature (i.e., low supercooling degree) implies a low freezing rate leading to a low number of large ice crystals. Conversely, the lower the nucleation temperature (i.e., high supercooling degree), the higher the freezing rate, leading to a greater number of small ice crystals.

2.1.2. CONTROLLING ICE GROWTH TO TUNE THE PORE SIZE AND ORIENTATION

To obtain different sizes of ice crystals, one must play either on the nucleation temperature or on the freezing rate of the solvent. In systems such as gels, it is very difficult to control the nucleation temperature because of the numerous impurities (i.e., the network) being favorable for uncontrolled heterogeneous nucleation. Hence, reaching a low nucleation temperature is not possible in our case. However, it is still possible to control the size of the crystal formed during quench freezing (method used to form the quenched cryogels in chapter II). Indeed, such freezing (i.e., the fast immersion of a vial containing the system into a freezing bath such as liquid nitrogen) results in a low degree of supercooling but a high freezing rate. Hence, by changing the temperature of the freezing bath (and thus the freezing rate), one could be able to tune the size of the ice crystals.

Although quench freezing is advantageous to produce small pores in heterogenous media, we saw in chapter II that the structure of the resulting material is isotropic. This is mainly due to two phenomena. I) Nucleation and ice crystal formation points are not controlled and favored at the interface between the material and the vial, being in direct contact with the freezing solvent. The nucleation and solidification front are very close and moving both in non-nucleated area resulting in grains of different orientations. II) Ice crystals grow anisotropically.[21] As presented in Figure III.2.A, the simplest shape of ice crystals is hexagonal (but various ice crystals shapes exist, see Figure III.2.B-C).[17] The anisotropic growth rate of ice crystals was reported to be faster along their basal plane (a-axis) than perpendicular to it (c-axis), leading to columnar structures.[21] These two growing mechanisms can result in different orientations inside the structure. One can take advantage of both these phenomena to orientate the growth of ice crystals in a whole sample. Indeed, if the temperature gradient is applied unidirectionally along the sample, one can expect the ice crystals to grow in the same direction.

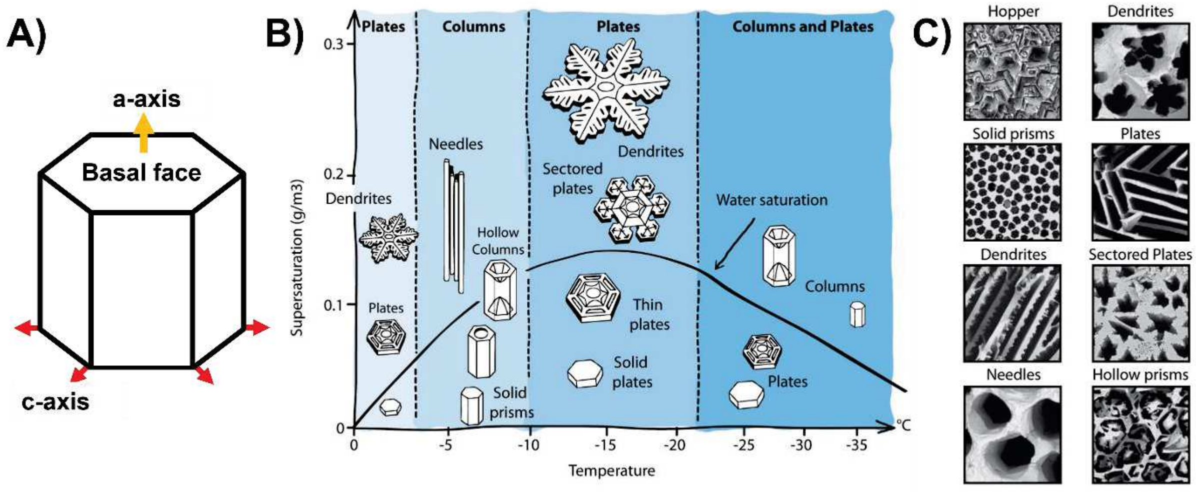

Figure III.2: A) Schematic of simple ice crystal growth along the basal plane (a-axis) and the perpendicular plane (c-axis); B) Schematic of the morphology diagram of the various ice crystals that can be obtained; C) SEM images of ice-templated materials with various shapes of ice crystals. Reproduced from [17]*.*

2.2. APPLYING THE ICE-TEMPLATING METHOD ON THE HYDROGEL

We applied the ice-templating method to control the orientation of the ice crystal growth during the freezing of the hydrogels. Different setups exist to induce directional freezing of a colloidal dispersion.[22] The simplest setup was to freeze the sample from its bottom and induce a vertical temperature gradient. For that, the gels were placed on top of a cooled metal bar immersed in a freezing bath.

Figure III.3.C-D represent two methods used to unidirectionally freeze the hydrogels, more details can be found in the Experimental section. Typically, a hydrogel (whose top and bottom surfaces were cut ~ 0.5 - 1 mm to obtain a smooth surface and get rid of any visible defects) was placed on top of an aluminum rod (chosen for its high thermal conductivity) and then placed in a liquid nitrogen bath (N_{2L}) for 10 min to ensure complete freezing of the gel (method 1, see Figure III.3.C). In method 2 (see Figure III.3.D), the sides of the sample were thermally protected with a Teflon ring (whose diameter was adapted to fit the gel) to ensure that the temperature gradient was vertical. After freezing, the gel was placed in a precooled tank at -15°C and vacuum dried for 48h. To minimize any structure collapsing during the freezing, the Teflon ring surrounding the sample for method 2 was left as a mechanical support. The resulting cryogels will be hereafter called “templated cryogel” to avoid any confusion with the quenched cryogel presented in chapter II.

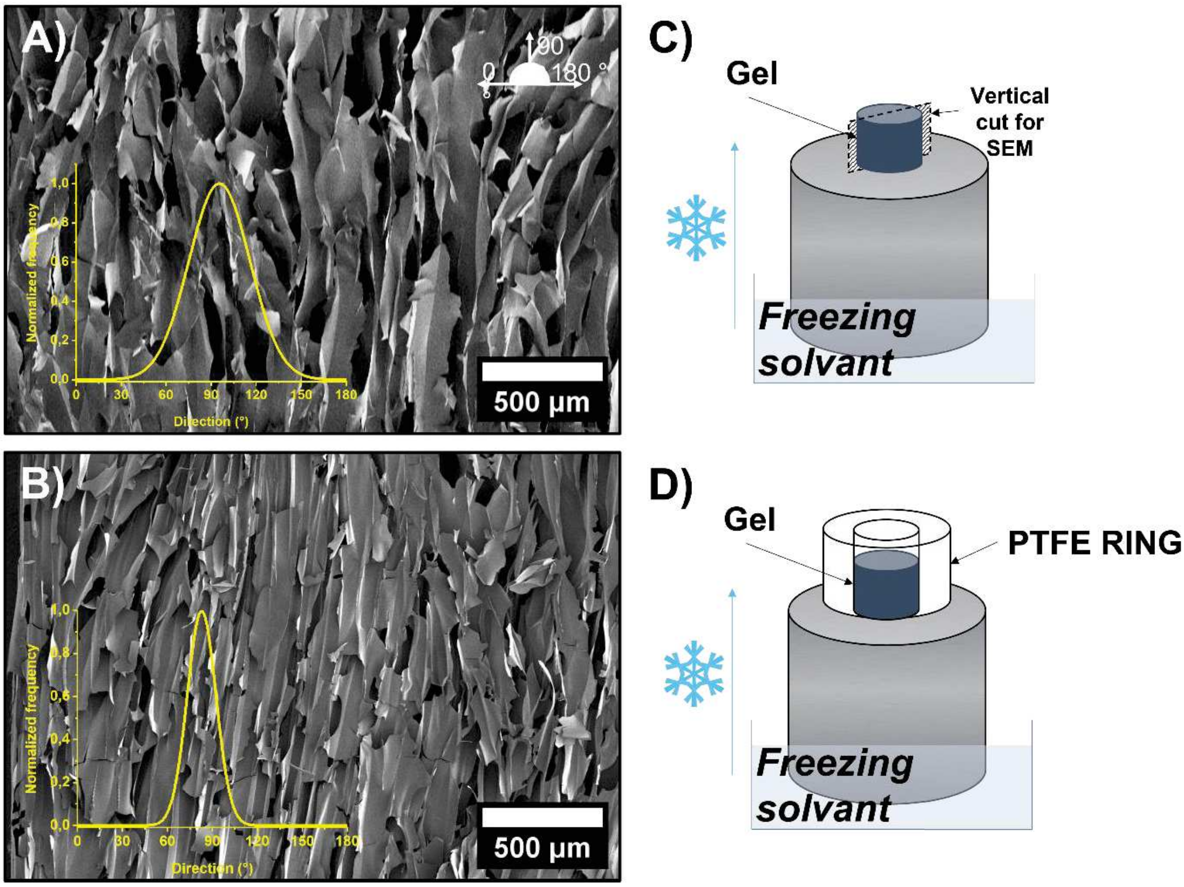

Figure III.3: A-B) Representative SEM images of the vertical cut of a templated cryogel realized with freezing method 1, and method 2, respectively. The insets represent the histogram of pores directionality, measured with the directionality plugin of ImageJ. C-D) Schematic of unidirectional freezing method 1 and 2, respectively.

The porous structure of the templated cryogels was observed by SEM. To monitor the channel-like pore alignment, the samples were cut vertically (plane parallel to the freezing direction, see Figure III.3.C) and observed by SEM as presented in Figure III.3.A-B. To quantitatively determine the degree of orientation, we performed image analysis with ImageJ software. The directionality plugin was used, and a Fourier component analysis was performed (see Experimental section for further details). This analysis allowed us to estimate the orientation of the pores in the templated cryogels by plotting a histogram of the direction of the structures present in the image as shown in the insets in Figure III.3.A-B. As compared to the quenched cryogel (see section II.3.3.2), both ice-templating methods led to globally oriented porosity. The freezing method 1 provided the poorest degree of orientation, the pores were globally aligned towards the freezing direction, but they widely deviated from it (angular distribution ± 30°, see Figure III.3.A). Cold vapors, and projections of boiling N_{2L} might have affected the temperature at the sides of the gel, resulting in a modification of the vertical gradient. As shown in Figure III.3.B, the method 2 yielded to well-aligned pores (angular distribution ± 10°). The thermally insulating Teflon ring placed around the gel probably protected it. The temperature gradient was favored mainly in the vertical direction. This method provided the best alignment of the pores and was used to produce all the templated cryogels mentioned hereafter. We were able to produce samples as thick as a centimeter and with diameter in the range 1.3-1.5 cm.

Thanks to this freezing method, nucleation was better controlled and was favored on the bottom face in contact with the cold aluminum rod. The anisotropy of the ice crystals also favored the overall orientation of the porous structure (see Figure III.2.A). It is difficult to determine with certainty the shape of the ice crystals resulting in such faceted pores. Columnar crystals are the most probable (see Figure III.2.B), but it has been reported that growth of ice crystals in confined environment (such as a polymer network) can be modified. For example, the presence of fibers can prevent dendrites from forming.[23] In our sample, the pores are well aligned with each other but this orientation is not exactly the same as the freezing direction, this slight tilt can be seen in Figure III.4.A. The pores are faceted and shaped as long channels parallel to each other. It is difficult to determine if one single ice crystal grows all along the thickness of the sample (resulting in a single channel-like pore). From SEM images, they are at least 500 µm long (Figure III.4.A). We do not observe significant pore size differences along the thickness of the sample.

The pore morphology was very similar to that observed in section II.3.3.2 for the quenched cryogels, as shown in Figure III.4.B. However, a slight difference in pore size was observed. Since the gels were frozen on an aluminum rod, the cooling rate was slower (-23 °C/min) than when the gel (in a vial) was directly immersed in N_{2L} (> -100 °C/min), which influenced the growth of ice crystals. The templated cryogel was composed of ~ 50 µm channel-like pores aligned along the entire thickness of the sample as shown in Figure III.4.B. The pores are well aligned along the entire sample as shown in Figure III.4.A.

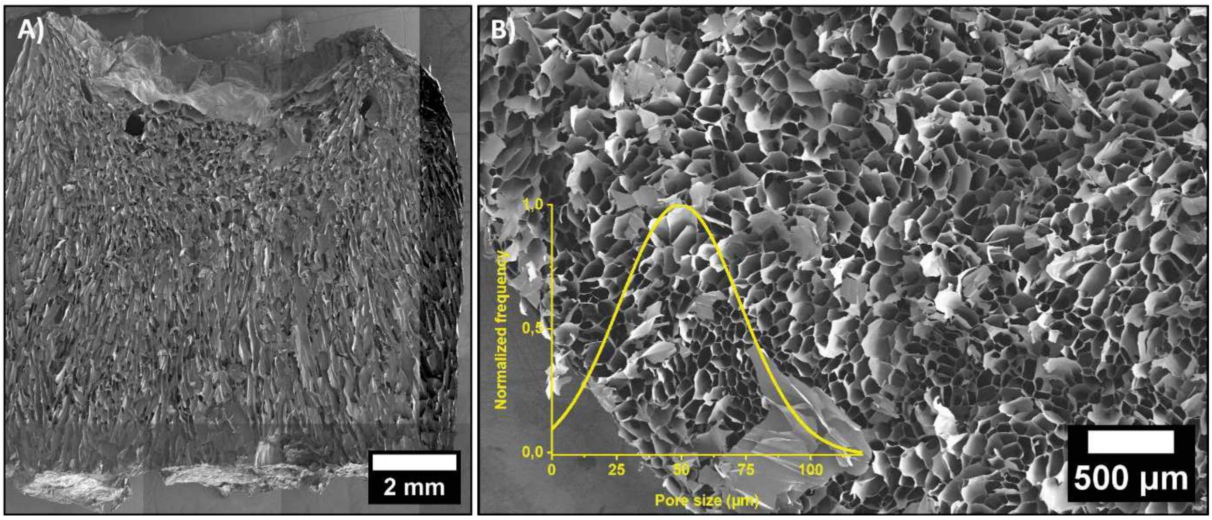

Figure III.4: A) SEM image of the vertical cut of an entire templated N_{2L} cryogel showing an overview of the pore alignment, the top part collapsed slightly; B) SEM image of the horizontal cut of a templated N_{2L} cryogel revealing the honeycomb structure, the inset corresponds to the histogram of measured pore size. The "flakes" lying on top of the pore surfaces are due to the cutting of the sample for SEM analysis and not representative of the real structure.

2.3. IMPACT OF THE FREEZING RATE ON THE PORE SIZE

As discussed in section III.2.1.2, the size of the pores can be tuned by modifying the freezing rate, thus speeding or slowing the ice crystal growth. It was very difficult to increase further the freezing rate while keeping the orientation of the pores. Thus, we were only able to produce bigger pores. The produced cryogels are called "templated -solvent bath- cryogels" hereafter. The global setup was the same as described in section III.2.2 (freezing method 2) as we wanted to keep the orientation of the pores, only the freezing bath was changed. SEM images of the horizontal cut of templated cryogels frozen with N_{2L} (-196°C), liquid nitrogen and ethanol mixture (N_{2L}/EtOH, -115°C), dry ice and isopropanol mixture (CO_{2S}/IPA, -77°C), and cooled isopropanol (IPA, -30°C) baths are shown in Figure III.5.A-D. The freezing rate was measured by monitoring the temperature on top of the gel with a thermocouple placed during the freezing step.

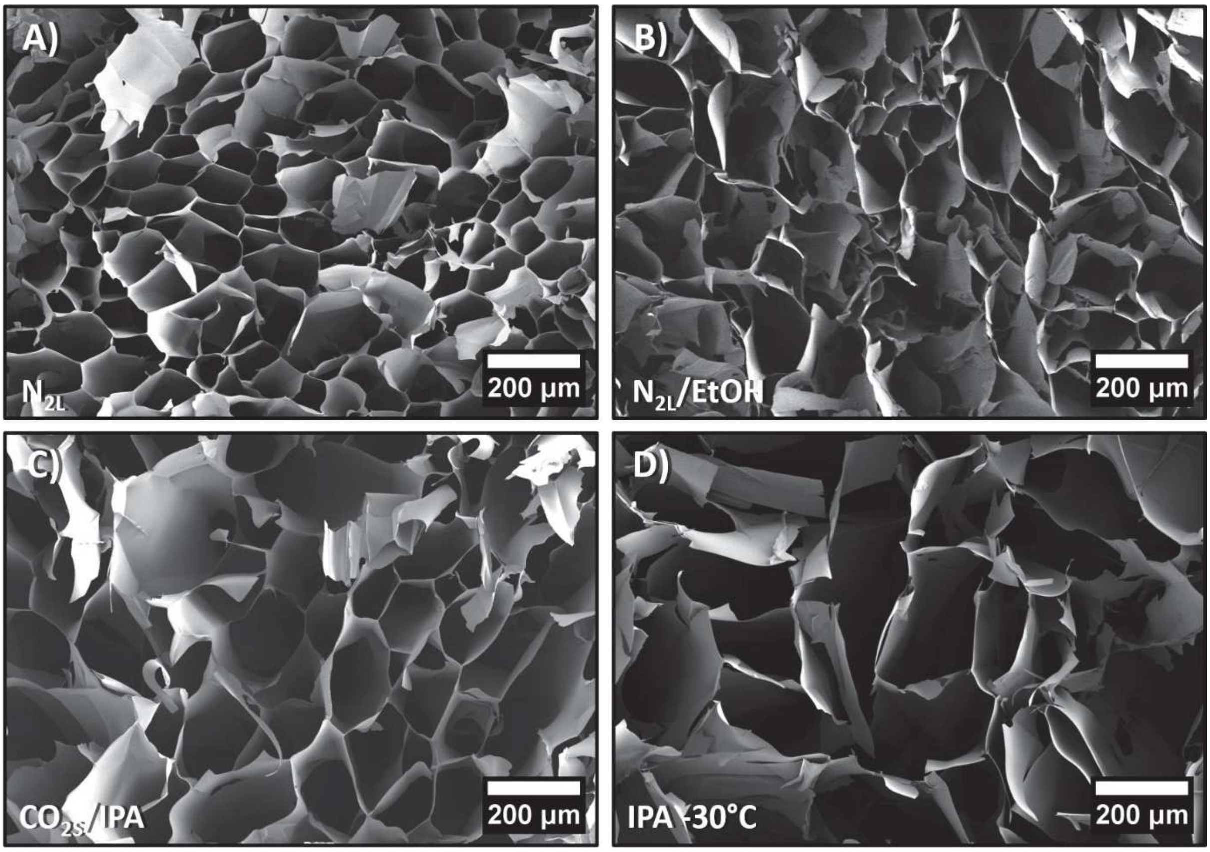

Figure III.5: SEM images of the horizontal cut of templated cryogels templated with A) N_{2L}, B) N_{2L}/EtOH, C) CO_{2S}/IPA, and D) cooled IPA.

The pore structure of the templated cryogels made at different freezing bath temperatures is similar and the density of the different templated cryogels constant (0.02 g/cm^3). The faceted pores form a honeycomb structure composed of channels oriented along the temperature gradient. The higher the temperature of the freezing bath (i.e., the lower absolute value of the freezing rate), the larger the pores. Figure III.6.A shows the evolution of pore size (measured by SEM image analysis, see Experimental section) and freezing rate with the use of different freezing baths. With the highest absolute freezing rate (- 23°C/min), the templated N_{2L} cryogels exhibit the smallest pores of 50 ± 23 µm. As the absolute freezing rate decreases, the ice crystal growth is slower. The templated N_{2L}/EtOH cryogel (freezing rate -8°C/min) has pores in the range 70 ± 40 µm, the templated CO_{2S}/IPA cryogel (freezing rate -4°C/min) has 140 ± 60 µm large pores, and the templated IPA cryogel (freezing rate -1.5°C/min) has pores of 210 ± 95 µm. As the pore size increases, the pores are also less defined (see Figure III.5) and the pore size polydispersity increases (see Figure III.6.A). A constant growth rate of water crystals is required to achieve a homogeneous pore size. At freezing rates below 10°C/min, it is likely that the growth kinetics of ice crystals decrease during freezing, resulting in different pore sizes within the same sample.[22] The pore wall thickness also changed with freezing rates (see Figure III.6.B). This is due to the fact that the pore walls are composed of PEDOT: PSS fibers from the native gel (see section II.3.3.2). Therefore, at constant density, bigger crystals push aside more PEDOT: PSS fibers, forming thicker pore walls (~ 300 nm to 3 µm, depending on the freezing bath).

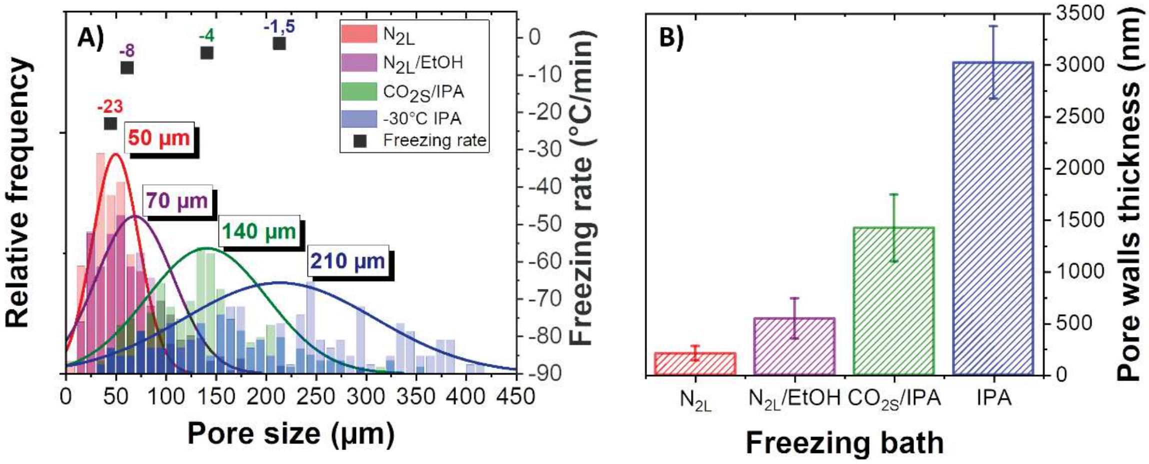

Figure III.6: Evolution of A) the pore size and freezing rate, and B) the pore walls thickness as a function of the freezing baths.

2.4. STRUCTURAL ANISOTROPY

To go further in the structural characterization of the templated cryogels, we performed anisotropic small and wide-angle X-ray scattering (SAXS and WAXS) analyses. The sample was placed either with the incident beam aligned with the channel-like pores (Figure III.7.A) or perpendicular (Figure III.7.B) to them. The analyses were conducted on the most ordered samples (i.e., templated N_{2L} cryogel).

Figure III.7.C shows the SAXS intensity profile of the templated N_{2L} cryogel measured in the parallel (black dots) and perpendicular (red dots) directions. The SAXS intensity profile was not characteristic of the porous channel (pores too large) but rather of the Porod regime. The intensity decays as a q^{-4} power law and reflects a smooth surface and a marked difference between the scattering object and the medium (in our case air). This is a striking difference from the trend observed for the native hydrogel, which follows a q^{-1} law (see section II.2.2.1). This in good agreement with our cryo-SEM observations (see section II.3.3.2). Indeed, we observed that the pore walls are made of densely packed fibers. In the cryogel, we no longer observe the unique fibrils but only their dense packing resulting in the smooth surface of the pore walls. This support the idea that the packing of the fibers is very dense (in agreement with the fact that no microporosity in the pore walls was detected by nitrogen physisorption, see section II.3.3.2).

Overall, we do not see any difference in the SAXS intensity profile between the // and ⊥ measurements. This suggests that in the distance range of the SAXS observation (0.001 $Å^{-1}$ to 0.1 $Å^{-1}$, i.e., ~ 600 nm to ~ 6 nm), we do not see any influence of the pore orientation.

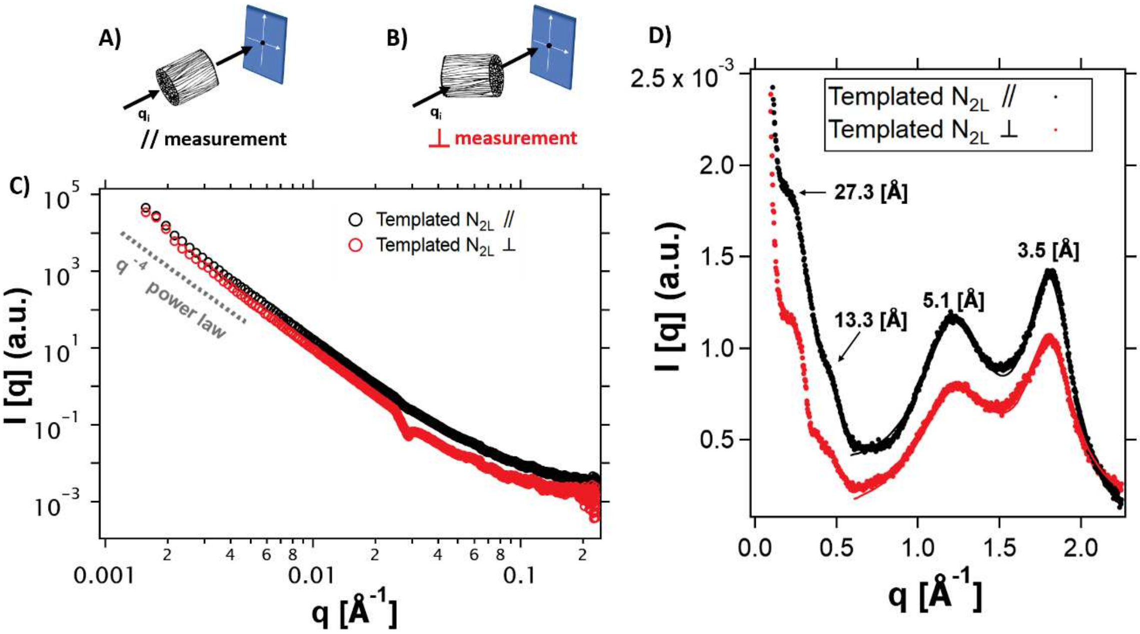

Figure III.7: Schematic of the A) parallel (//), and B) perpendicular (⊥) measurements; B) SAXS, and C) WAXS intensity profile of the templated N_{2L} cryogel in both orientation (// in black, ⊥ in red).

The WAXS intensity profiles measured in both directions are presented in Figure III.7.D. We investigated the peaks at 1.23 $Å^{-1}$ (5.1 Å) and 1.8 $Å^{-1}$ (3.5 Å) corresponding to the PSS and the PEDOT π-stacking distances, respectively.[24] The π-stacking distance value for PEDOT is in the range of distances found for untreated PEDOT: PSS films (3.5 – 3.6 Å).[25,26] This suggests that, despite the addition of sulfuric acid during the gelation step (inducing PEDOT: PSS ratio modifications and PEDOT conformation modifications, see section II.2.2), the molecular packing of PEDOT was not enhanced (although, other measurements showed a slightly smaller π-stacking distance, see Appendix). This behavior was already reported by Kim et al., the PEDOT π-stacking distance of PEDOT: PSS films treated with highly concentrated H_2SO_4 did not change and was measured to be 3.5 Å.[26]

The peaks at 0.23 Å^{-1} (27.3 Å), 0.47 Å^{-1} (13.3 Å) are more ambiguous to interpret due to their weak intensity. In pristine PEDOT: PSS the alternate inter-lamella distance of PEDOT to PEDOT stacks was reported at 22 Å (d_{100}) and 11 Å (d_{200}) for its second order.[24] Upon acid treatment of films (and PSS removal), the d_{100} and d_{200} spacing were reported to shift to lower values, suggesting that the PEDOT stacks got closer due to the partial removal of PSS.[24,26] In our case, considering the PSS quantity decreased during gelation (see section II.2.2.2), it is very unlikely that the spacings at 27.3 Å and 13.3 Å correspond to the d_{100} and d_{200} respectively. As reported by Hosseini et al., we suggest that the distance of 13.3 Å corresponds to the inter-lamella distance of PEDOT to PEDOT stacks, although it is not clear whether it corresponds to d_{100} or d_{200}. Interestingly, the distance of 27.3 Å is very close to the thickness of the fibrils composing the fibers present in the hydrogel (see section II.2.2.1). We observed variations of this distance between samples, although it always ranges in distance close to the fibrils thicknesses (see Appendix). From the information we have, we suggest that this peak may correspond to the fibril-to-fibril characteristic distance of the densely stacked objects within the pore walls.

It has been shown that fiber (or polymer chain) alignment could be induced by geometrical constraints, in particular by the ice-templating method, applied to colloidal solutions. Zhang et al. demonstrated the alignment of PEDOT chains thanks to the ice-templating of a PEDOT: PSS commercial dispersion.[15] Via the study of the azimuthal intensity profiles of X-ray scattering, Munier et al. demonstrated the alignment of cellulose nanofibrils and nanocrystals induced by ice-templating.[27] Figure III.8.C-D shows the 2D detector images of the templated N_{2L} cryogel in the mid-angle range. The ⊥ measurement shows some anisotropy. Interestingly, at wider angles (see Figure III.8.E), there is no anisotropy observed. From this, we extracted the intensity profile in the azimuthal angle along the characteristic distance of the PEDOT: PSS fibers (0.2 Å^{-1}), presented in Figure III.8.F. The intense peaks of the ⊥ profile at 90° and 270° demonstrate the vertical alignment of the fibers perpendicular to the beam (i.e., parallel to the pores and thus, freezing direction). In contrast, the // intensity is almost constant and refers to an isotropic signal. The degree of orientation of the fibers can be quantified with the orientation index f reported by Munier et al.[27] The orientation index is comprised between 0 (random orientation) and 1 (perfect orientation) and can be defined as :

$$f = \frac{180 - FWHM}{180} \qquad (III.1)$$

Where FWHM is the full width at half maximum of the Gaussian fitted peak.

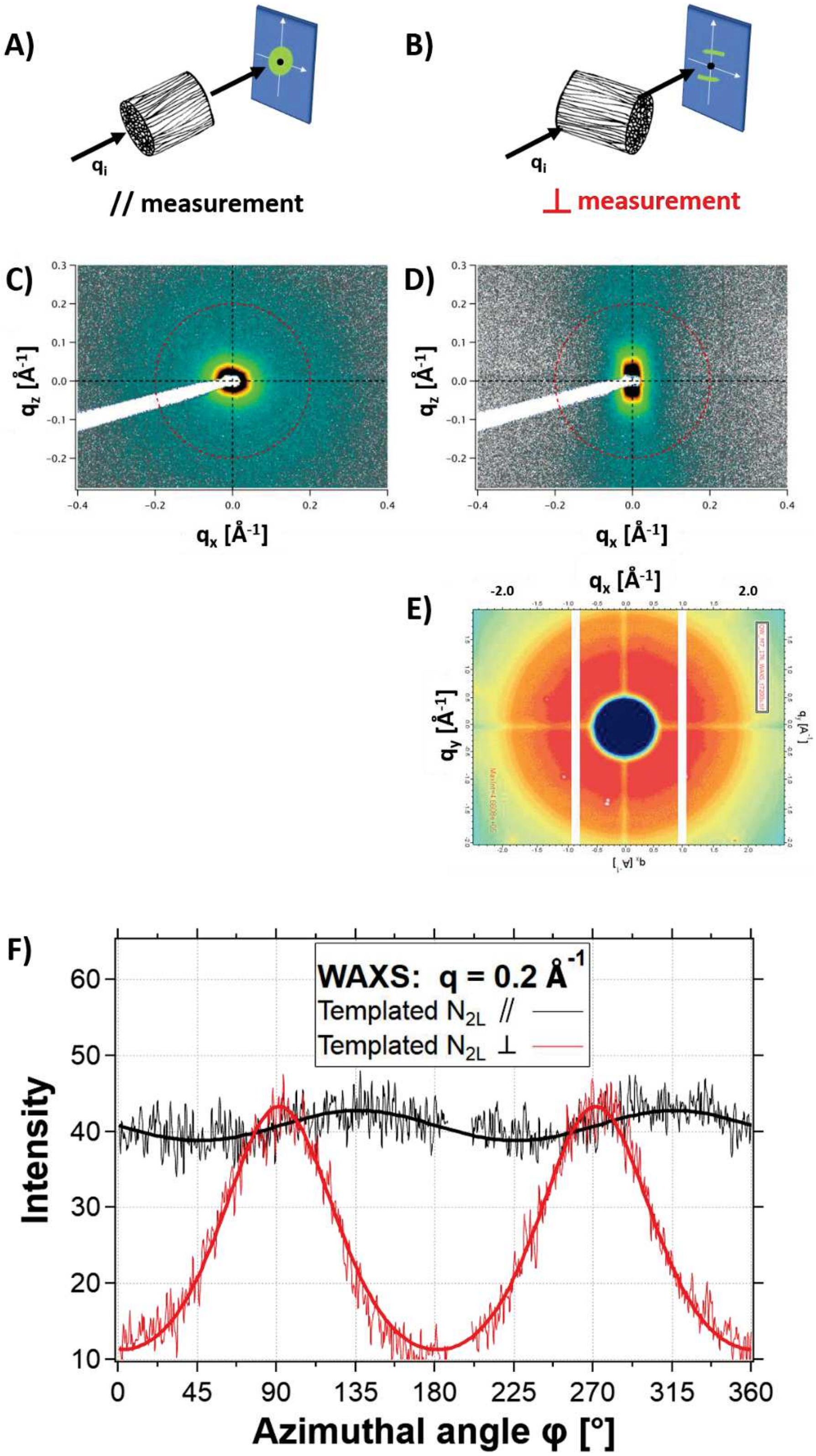

Figure III.8: Schematic of the A) parallel (//), and B) perpendicular (⊥) measurements; 2D detector images of the WAXS profile (~ 0.2 Å^{-1}) of a templated N$_{2L}$ cryogel in the C) //, and D) ⊥ directions; E) 2D detector image of the

WAXS profile at wider angles (> 1 Å^{-1}) showing no anisotropy (measurement realized at ICS); F) azimuthal intensity profile of the templated N$_{2L}$ cryogel measured in the // (black) and ⊥ (red) directions at 0.2 Å^{-1}.

The orientation f = 0.61 reflect the good orientation of the fibers within the pore walls. During the directional freezing, the fibers in the network are subjected to mechanical deformation. It is likely that during ice crystal grow, the fibers undergo an elongation flow field (as depicted in Figure III.9). The fibers are expelled from the growing ice crystals and are compressed in a plane between two moving growth fronts. Thus, we can suppose that a part of the fibers is blocked between two ice crystals while the rest is free. As the crystals grow unidirectionally, the momentum exerted by the ice crystal is applied to the fibers along the same axis. Since one end of the fibers is fixed, the other end undergoes a rotational motion, instead of a translational motion along the growth axis. In the end, a mat of fibers oriented in the plane of the water crystals growth is formed. Interestingly, alignment of fibers was reported on dispersion but not on gels. It is likely that alignment was possible because the physical interactions maintaining the gel are weak.

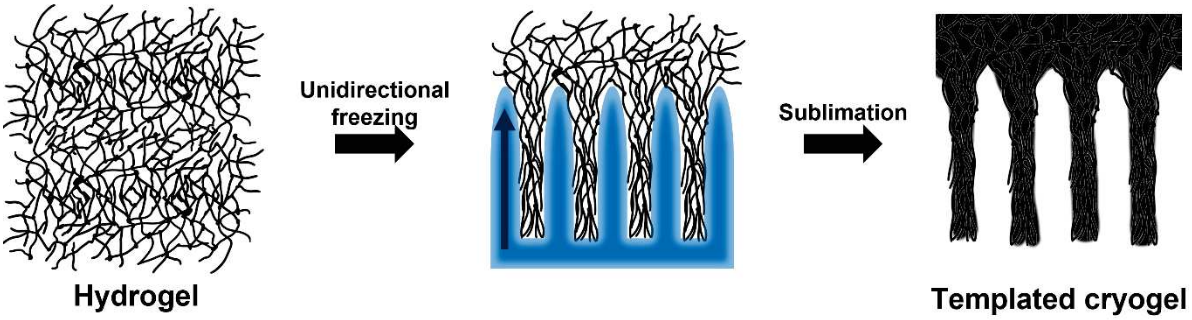

Figure III.9: Schematic of the ice-templating process in our PEDOT: PSS hydrogels. Black lines represent the PEDOT: PSS fibers, blue objects represent the ice crystals.

Herein, we demonstrated the interest of the ice-templating method, applied to PEDOT: PSS gels. We were able to produce cm-thick samples with channel-like macropores oriented in the vertical direction. The size of these pores could be tuned from 50 to 350 µm and the pore walls thickness was modified accordingly. We showed that the templated N$_{2L}$ cryogels exhibit anisotropy within the pore walls due to the orientation of PEDOT: PSS fibers. As discussed in sections I.1.3.3 and I.1.4.3, structural modifications of conducting polymers have an influence on their thermoelectric properties. In particular, as reported in thin films, anisotropy of the material can influence its charge transport properties.[28] In the following section, we investigate the influence of the morphological modifications induced by the ice-templating method (pore size and orientation, anisotropy of pore walls) on the thermoelectric properties.

3. INFLUENCE OF MORPHOLOGICAL MODIFICATIONS ON TE PROPERTIES

3.1. INFLUENCE OF THE PORE AND PORE WALLS SIZE

The thermoelectric properties of the templated cryogels were measured as discussed in section II.4.1, more details can be found in the Experimental section. The electrical conductivity was measured along direction 1 (depicted in Figure III.11). Figure III.10 shows the apparent electrical conductivity, the Seebeck coefficient and the thermal conductivity of the templated cryogels presented in section III.2.3 as a function of the mean pore size. The power factor (PF) and the ZT at 300K were calculated from these values. It should be noted that the density (0.02 ± 0.001 g/cm^3) and the porosity (98%) of all the templated cryogels were equal.

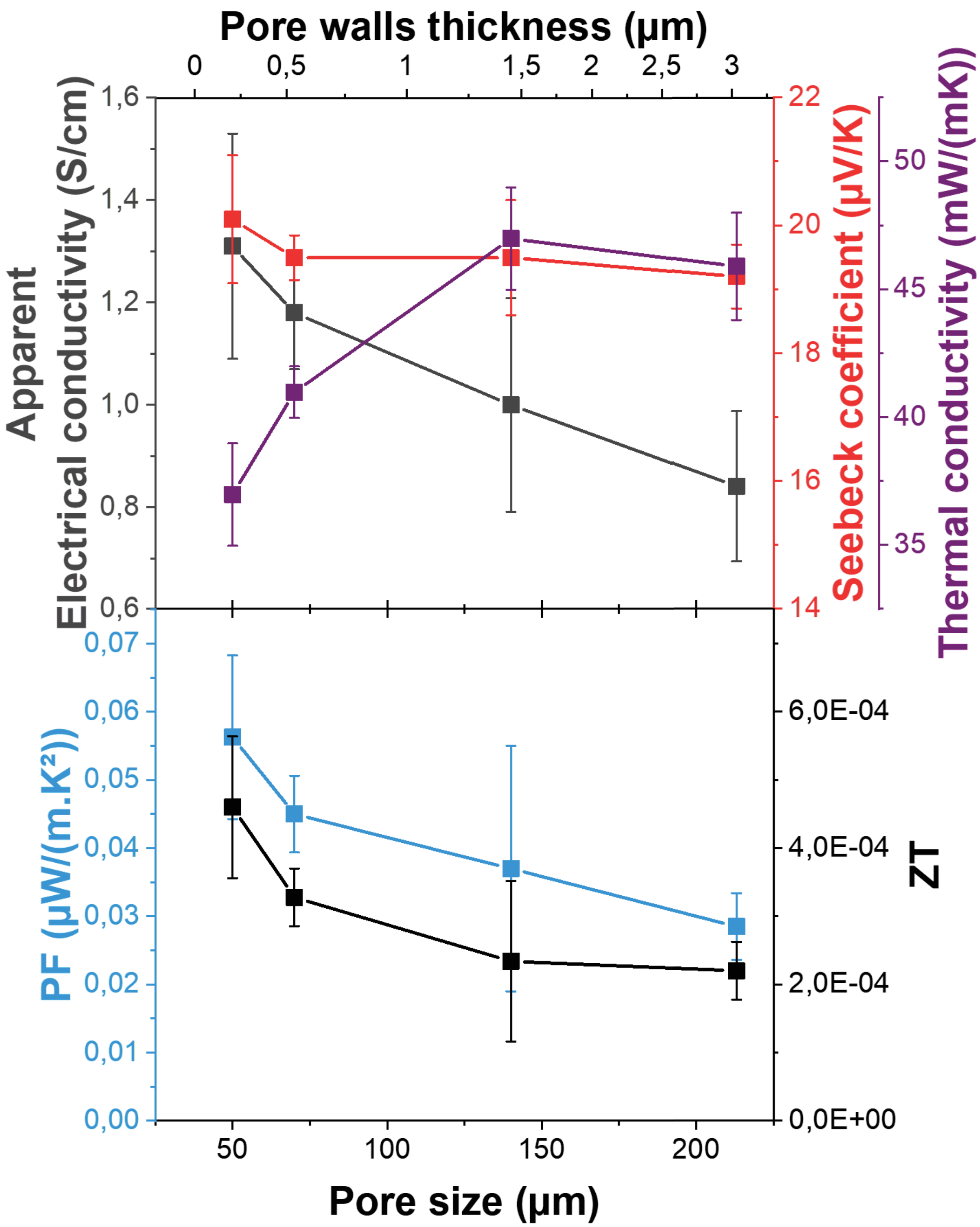

Figure III.10: Thermoelectric properties of the templated cryogels as a function of their mean pore size, the pore walls thickness is given as an indication.

The electrical conductivity of the templated cryogels decreased with increasing pore size. The templated N_{2L} cryogel (with ~50 µm pore size) showed an electrical conductivity of 1.3

S/cm while the electrical conductivity of the templated IPA cryogel (with ~215 µm pore size) was 0.85 S/cm. The Seebeck coefficient of the templated N_{2L} cryogel was about 20 S/cm, which is slightly higher than the H_2SO_4-treated PEDOT: PSS films reported in the literature.[29] Little impact of the pore size on the Seebeck coefficient was observed for the templated cryogels. The low thermal conductivity values of the templated cryogels ranged between 37 and 45 mW/(m.K) depending on the pore size. The thermal conductivity of the templated N_{2L} cryogel was ten times lower than the values reported for dense films and was even lower than that of the quenched cryogel (42 mW/(m.K)). It is interesting to note that the changes in TE properties as a function of pore size are also valid as a function of pore walls size. Since the Seebeck coefficient was not influenced by the evolution of the pore size, the power factor was governed by the electrical conductivity. Hence, the PF decreased with the increasing pore size. Furthermore, as the thermal conductivity even further increased with the pore size, the ZT decreased even faster with the increasing pore size. Despite the fine control of the porous structure, the figure of merit of the templated cryogels are very low ($ZT = 4.6 \times 10^{-4}$ for the templated N_{2L} cryogel) and even lower than that of the quenched cryogel (5×10^{-4}). Considering the structure-properties relationship discussed in sections II.4.2 and II.4.4 (decrease of the electrical conductivity with density), it was expected that the electrical conductivity of the templated N_{2L} cryogel was slightly lower than that of the quenched cryogel (since $\rho_{templated} < \rho_{quenched}$). However, such evolution of the thermal and electrical conductivity with the evolution of the pore size was not expected.

3.1.1. EVOLUTION OF THE ELECTRICAL CONDUCTIVITY

The change in electrical conductivity upon increasing pore size/wall size was difficult to attribute. There is a lack in the description of charge transport mechanisms in porous samples in the literature. Most studies are for inorganic materials and are really dependent on the network architecture.[30–32] In most cases, porosity is the main responsible for the decrease in electrical conductivity. As discussed in section II.4.2.1, it is clear that the very high porosity of the PCPs produced has a detrimental impact on the electrical conductivity. Here, we can clearly see the evolution of the electrical conductivity upon increasing the pore size. In the literature, pore size has been reported to have a very small influence on the electrical conductivity of porous aluminum.[33] Hakamada et al. reported a slight decrease in electrical conductivity when the cross-sectional dimension of the material was similar to the pore size due to local variation in density.[33] In our case, even for the largest pores, the cross-sectional dimension of the templated cryogel is still almost 50 times larger than the pores. We suggest that the evolution of the electrical conductivity cannot be attributed to the evolution of the pore size but to the increase of the pore wall thickness. All templated cryogels were made with the same gelation protocol, so their charge carrier density should be the same. Thus, the decrease in electrical conductivity could be due to a decrease in charge carrier mobility. As discussed in sections I.1.3.3 and I.1.4.3, the microstructure influences the charge transport properties. In our case, we suggest that the organization of the PEDOT:PSS fibers within the fibrils (as demonstrated in section III.2.4) has been somehow modified, resulting in a likely reduction in charge carrier mobility.

3.1.2. EVOLUTION OF THE THERMAL CONDUCTIVITY

As mentioned for the quenched cryogel in section II.4.3, the very low thermal conductivity of these materials is due to their very high porosity. The contribution from solid conduction was greatly reduced due to the low density of the material. Since the density of the templated cryogel (0.02 g/cm^3) is even lower than that of the quenched cryogel (0.03 g/cm^3), the thermal conductivity of the former (37 mW/(m.K)) was expected to be lower than that of the latter (42 mW/(m.K)). However, this cannot be the only mechanism involved in this difference as we observed a higher thermal conductivity as the pore size increased until it exceeded the thermal conductivity of the quenched cryogel. This behavior is quite surprising for macroporous materials. As discussed in section II.4.3, at such a large pore size range, gas conduction is not affected, i.e., κ_{gas} ~ 25 mW/(m.K) and corresponds to the thermal conductivity of air at ambient temperature and pressure conditions. From equations I.6 and I.11 (see section I.1.5), it is difficult to attribute the increase in thermal conductivity upon pore size increase. The radiative and convection contributions are assumed to be negligible at room temperature for samples with pore size lower than 1 mm. The electronic contribution can also be neglected given the low electrical conductivity of templated cryogels (see Appendix). Therefore, we suggest that other mechanisms due to the particular porous structure of templated cryogels are involved in the reduction of thermal conductivity.

Apostolopoulou-Kalkavoura et al. recently published two comprehensive papers on thermal transport in ice-templated cellulose nanomaterials (fibrils and crystals).[9,34] The materials produced have similar structural characteristics to our materials. They are composed of channel-like pores forming an oriented honeycomb structure. The pores are in the range of 50 to 150 µm and the pore walls are several hundred nanometers thick. The pore walls consist of densely stacked fibrils aligned in the direction of freezing. In contrast to our material, they were able to show the presence of micro/mesoporosity inside the pore walls by nitrogen physisorption. It should be noted that in our case, we were only able to perform this analysis once on quenched cryogels without any particular optimization according to the structure of our materials. We were not able to extract a volume of micro-/mesopore, although confirmation with other measurements should be performed. Apostolopoulou-Kalkavoura et al. reported that the very low thermal conductivity obtained for their macroporous materials was mainly due to phonon scattering effects at the solid-solid interface of cellulose fibrils.[9] It is likely that such an effect also occurs for our material. The possibility of phonon scattering effects due to the texturing of the pore walls has already been mentioned in section II.4.3 to explain the low thermal conductivity of quenched cryogels. The effect of phonon scattering at fiber-fiber interface can be expressed by the Kapitza resistance (R_k) and used in a modified expression of the solid conduction contribution $\kappa_{solid,p}$:[9]

$$\kappa_{solid,p} = \phi_{cell} \cdot \frac{\kappa_0}{1 + \kappa_0 \cdot \frac{R_k}{d}} \qquad (III.2)$$

where ϕ_{cell} is the volume fraction of the porous material, κ_0 is thermal conductivity of the solid backbone, and *d* is the average thickness of a PEDOT: PSS fiber. The Kapitza resistance $R_k = \frac{g_i}{\kappa_i}$ with g_i the surface separation distance between two adjacent PEDOT: PSS fibers, and κ_i the interfacial thermal conductivity. Numerical calculation of this contribution to the thermal conductivity would require molecular dynamics simulations to estimate *gi.* In any case, it is clear from equation III.2 that the phonon scattering effect is more important for low interfacial thermal conductivity and high separation distance between two fibers. From the information available to us, we suggest that the increase in thermal conductivity with pore size may be due to the decrease in the phonon scattering effect and probable decrease of interfacial resistance of the pore walls. It has been reported that the packing of anisotropic particles in the frozen structure could be either compact and ordered or randomly arranged.[21] We suggest that, as the pore walls thickness increases, the PEDOT: PSS fibers within the pore walls may be more randomly packed. Thicker pore walls, and random orientation of the fibers would result in a smaller thermal resistance, increasing the thermal conductivity. In addition, a change in the structure within the pore walls would be consistent in explaining the observed differences in electrical conductivity, as mentioned above.

At the moment, the understanding of the influence of pore size in the macroporous range is still incomplete and requires further study. In particular, understanding all the mechanisms involved in the reduction of thermal conductivity down to 37 mW/(m.K) would give keys for the design of highly insulating materials.

3.2. INFLUENCE OF THE ANISOTROPY ON TRANSPORT PROPERTIES

In this section we investigate how the thermoelectric properties are influenced by this anisotropy. It should be noted that the results presented in this section are preliminary and further studies are needed.

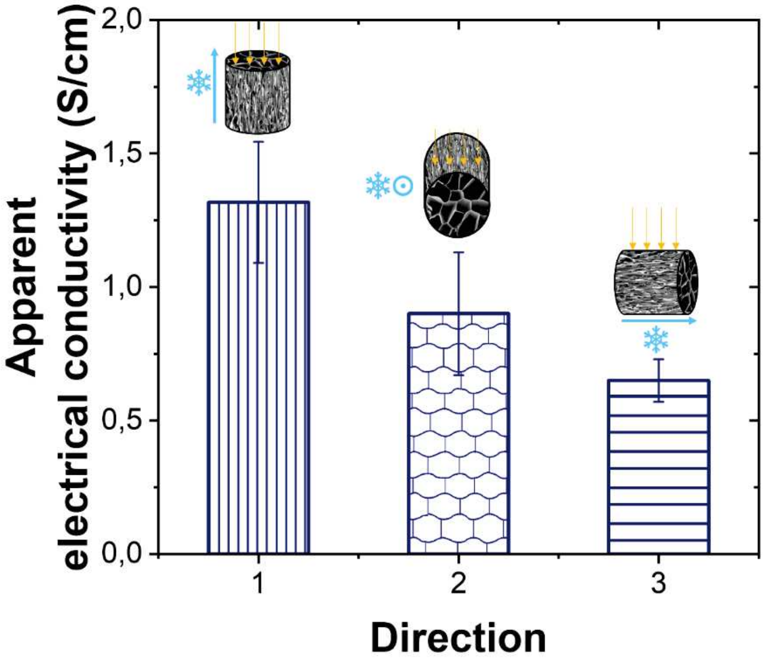

Figure III.11: Apparent electrical conductivity of templated N_{2L} cryogels measured with the probes in the directions 1, 2, and 3. The insets represent schematically how the samples were measured, the yellow arrows represent the probes.

The anisotropic behavior of the electrical conductivity of conductive polymer thin films has already been reported in the literature. Thin films of PEDOT:PSS have shown anisotropic electrical conductivity due to the anisotropic organization of PEDOT.[35,36] Films with conductive polymer chains aligned by high temperature rubbing showed highly anisotropic charge transport properties.[28,37–39] It has also been reported that the orientation of ice-templated macropores in porous metals has an influence on electrical conductivity.[10] Due to the alignment of pores and fibers within the pore walls, we therefore expected to observe anisotropic behavior of the electrical conductivity. We measured the apparent electrical conductivity of templated N_{2L} cryogel with a 4-probe resistivity station in three directions (see insets in Figure III.11). The electrical conductivities measured in the three directions are presented in Figure III.11. It was measured to be higher in the configuration 1 (1.3 ± 0.2 S/cm) than in the configuration 2 (0.9 ± 0.2 S/cm) and configuration 3 (0.65 ± 0.08 S/cm). The error bars are significant because of the difficulty in accurately measuring electrical conductivity in both directions. In particular, in the configurations 2 and 3, the sample tends to deform easily due to the pressure applied by the probes. It is difficult to tell if the measured resistance was affected by this compression. These measurements are preliminary and were difficult to repeat, so care should be taken when interpreting the results. It is really unclear why we observe such trend depending on the direction of measurement.

To go further, we measured the electrical resistance on a single pore wall. This experiment was possible thanks to a nanoprobing station under an SEM (FEG-SEM KLBO, collaboration with L. Simon, IS2M). A templated N_{2L} cryogel was cut in the vertical direction to expose the pore walls towards the beam and probes. It was transferred into the SEM equipped with tungsten tips whose positions could be precisely adjusted by IMINA micro-nanomanipulators (see Figure III.12.C). The probes were connected to a Keithley and the resistance of a single pore wall could be measured along and perpendicular to the freezing direction (see Figure III.12.A-B).

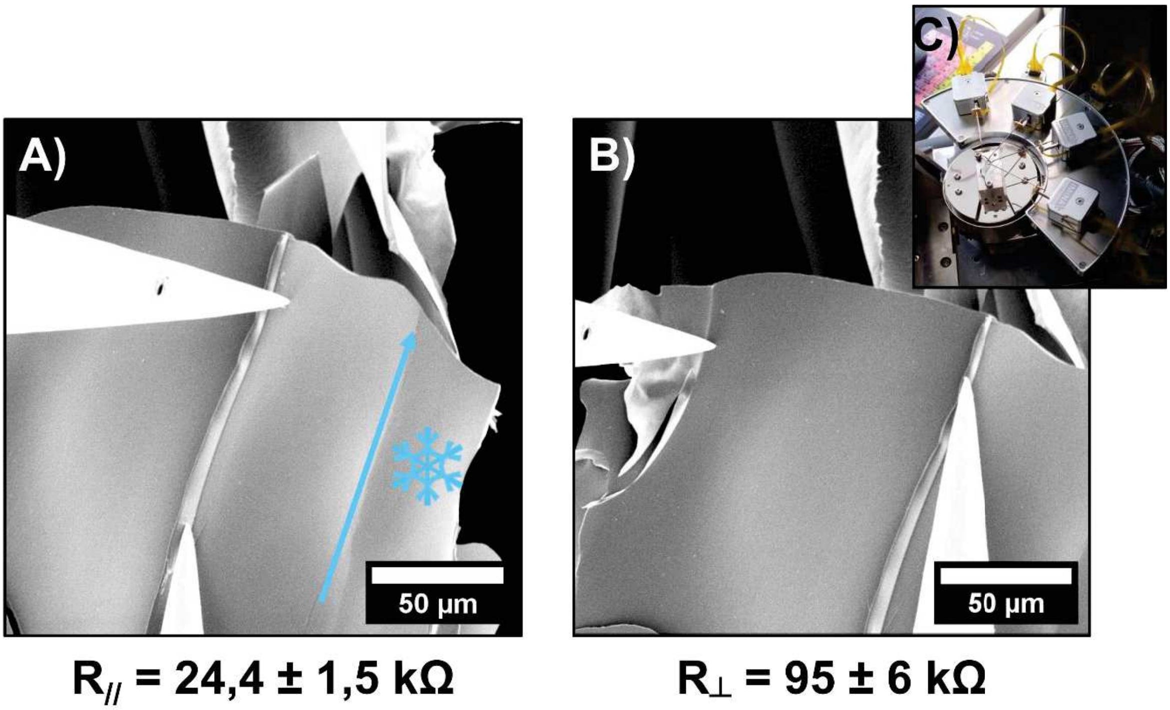

Figure III.12: SEM images of a single pore wall whose electrical resistance was measured A) parallel, and B) perpendicular to the freezing direction (represent by the blue arrow), the probes are 95 µm spaced; C) Photography of the robots holding the probes above the sample holder.

It was difficult to ensure a good contact between the probe and the self-supported pore wall of PEDOT: PSS due to its flexibility. It is very likely that the contact resistance is significant. Therefore, the absolute value of the resistance should not be considered. However, the resistance measured in both directions can be compared. It is interesting to note that the measured resistance is highly anisotropic. The resistance measured parallel to the freezing direction (along the channels) was measured to be 4 times lower than the one measured in the perpendicular direction. PEDOT stacks have been reported to be organized along PSS chains with their backbones in the same direction.[24] It is difficult to determine how the PEDOT and PSS chains organize themselves within the fibrils. However, given their high aspect ratio and the fact that PSS chains are very long, it is likely that they tend to organize in the same direction as the fibrils. Under these conditions, the PEDOT stacks would be oriented in the same direction as the fibrils, and thus aligned in the freezing direction. Considering that intra-chain charge transport along the backbone is the fastest (see section

I.1.2.2), one would expect greater charge mobility along the fibers (i.e., in the freezing direction), and thus a higher electrical conductivity.

We expect the thermal conductivity to be anisotropic, as it has been reported for ice-templated materials.[6,8,9,34] Unfortunately, our setup did not allow us to measure the thermal conductivity in different directions. In the literature, the axial thermal conductivity (measured in the direction parallel to the freezing direction) was always reported to be higher than the radial thermal conductivity (measured in the direction perpendicular to the freezing direction). In particular, for cellulose nanomaterials-based macroporous samples (whose porous structure is very similar to our materials, see discussion in section III.2.4), depending on the solid fraction of cellulose nanocrystals, the axial thermal conductivity was reported to be four to six times higher than the radial one.[9] This difference was mainly attributed to the high intrinsic anisotropic thermal conductivity of the cellulose nanofibrils and their alignment within the pore walls.

In the case of PEDOT: PSS films, the in-plane thermal conductivity was reported to be two to five times higher than in the through-plane direction.[35,40] This behavior was attributed to the higher thermal conductivity along the backbones of the polymer chains. Hence, considering the alignment of the PEDOT: PSS chains along the pore walls, one could expect the axial thermal conductivity to be higher than the radial one.

4. CONCLUSION

We demonstrated in this chapter the fine control of the macroporous structure of PEDOT: PSS cryogels by controlling the freezing process. Via the ice-templating method, the pores were unidirectionally oriented through the control of ice crystals growth. The nucleation was favored at the bottom of the sample, directly in contact with the cooling surface resulting in the unidirectional growth of the ice crystals. While forming in the gel's network, the ice crystals pushed aside the PEDOT: PSS fibers. Due to the unidirectional growth of the crystals, we demonstrated by X-ray scattering analyses that the fibers composing the pore walls were aligned along the freezing direction. Going further in the tuning of the freezing process, the pore size was modified from 50 µm to 350 µm by increasing the freezing rate of the sample through the use of different cooling baths. The resulting templated cryogels exhibited very low thermal conductivity as well as electrical conductivity around 1 S/cm. The thermoelectric properties were modified through these structural changes. The electrical conductivity was shown to decrease with the increase of pore walls size (and pore size) while the thermal conductivity was shown to increase. Moreover, preliminary results tend to show an anisotropic behavior of the electrical conductivity, probably due to the alignment of the fibers within the pore walls. Overall, the understanding of the mechanisms governing the evolution of TE properties as a function of the evolution of the porous structure still requires further investigation. However, these results are promising for the fine control of electrical and thermal transport properties. Although the control of pore orientation and size did not show a buff effect competing the TE properties of sulf-aerogels, these materials are promising, especially for applications other than thermoelectricity, such as scaffolds for tissue engineering.[16,41]

5. REFERENCES

[1] M. A. Shahbazi, M. Ghalkhani, H. Maleki, *Adv. Eng. Mater.* **2020**, *22*, 2000033.

[2] S. Deville, *Freezing Colloids: Observations, Principles, Control, and Use*, Springer International Publishing, Cham, **2017**.

[3] H. L. Gao, Y. B. Zhu, L. B. Mao, F. C. Wang, X. S. Luo, Y. Y. Liu, Y. Lu, Z. Pan, J. Ge, W. Shen, Y. R. Zheng, L. Xu, L. J. Wang, W. H. Xu, H. A. Wu, S. H. Yu, *Nat. Commun.* **2016**, *7*, 1.

[4] A. E. Donius, A. Liu, L. A. Berglund, U. G. K. Wegst, *J. Mech. Behav. Biomed. Mater.* **2014**, *37*, 88.

[5] M. Chen, J. Zhu, G. Qi, C. He, H. Wang, *Mater. Lett.* **2012**, *89*, 104.

[6] L. Hu, C. A. Wang, Y. Huang, C. Sun, S. Lu, Z. Hu, *J. Eur. Ceram. Soc.* **2010**, *30*, 3389.

[7] S. R. Hostler, A. R. Abramson, M. D. Gawryla, S. A. Bandi, D. A. Schiraldi, *Int. J. Heat Mass Transf.* **2009**, *52*, 665.

[8] D. Hautcoeur, Y. Lorgouilloux, A. Leriche, M. Gonon, B. Nait-Ali, D. S. Smith, V. Lardot, F. Cambier, *Ceram. Int.* **2016**, *42*, 14077.

[9] V. Apostolopoulou-Kalkavoura, P. Munier, L. Dlugozima, V. L. Heuthe, L. Bergström, *Sci. Rep.* **2021**, *11*, 1.

[10] D. Driscoll, A. J. Weisenstein, S. W. Sofie, *Mater. Lett.* **2011**, *65*, 3433.

[11] Z. Wang, X. Shen, M. Akbari Garakani, X. Lin, Y. Wu, X. Liu, X. Sun, J. K. Kim, *ACS Appl. Mater.*

Interfaces **2015**, *7*, 5538.

[12] J. H. Lee, G. A. Galli, J. C. Grossman, *Nano Lett.* **2008**, *8*, 3750.

[13] X. Zhang, C. Li, Y. Luo, *Langmuir* **2011**, *27*, 1915.

[14] A. M. D. Wan, S. Inal, T. Williams, K. Wang, P. Leleux, L. Estevez, E. P. Giannelis, C. Fischbach, G. G. Malliaras, D. Gourdon, *J. Mater. Chem. B* **2015**, *3*, 5040.

[15] J. Zhang, X. Fan, X. Meng, J. Zhou, M. Wang, S. Chen, Y. Cao, Y. Chen, C. W. Bielawski, J. Geng, *ACS Nano* **2021**, *15*, 8870.

[16] A. G. Guex, J. L. Puetzer, A. Armgarth, E. Littmann, E. Stavrinidou, E. P. Giannelis, G. G. Malliaras, M. M. Stevens, *Acta Biomater.* **2017**, *62*, 91.

[17] S. Deville, *J. Mater. Res.* **2013**, *28*, 2202.

[18] M. Matsumoto, S. Saito, I. Ohmine, *Nature* **2002**, *416*, 409.

[19] G. Petzold, J. M. Aguilera, *Food Biophys.* **2009**, *4*, 378.

[20] R. Geidobler, G. Winter, *Eur. J. Pharm. Biopharm.* **2013**, *85*, 214.

[21] S. Deville, Springer, Cham, **2017**, pp. 91–170.

[22] S. Deville, Springer, Cham, **2017**, pp. 351–438.

[23] T. Il Mah, K. A. Keller, R. J. Kerans, M. K. Cinibulk, *J. Am. Ceram. Soc.* **2015**, *98*, 1437.

[24] E. Hosseini, V. Ozhukil Kollath, K. Karan, *J. Mater. Chem. C* **2020**, *8*, 3982.

[25] N. Kim, B. H. Lee, D. Choi, G. Kim, H. Kim, J. R. Kim, J. Lee, Y. H. Kahng, K. Lee, *Phys. Rev. Lett.* **2012**, *109*, 106405.

[26] N. Kim, S. Kee, S. H. Lee, B. H. Lee, Y. H. Kahng, Y. R. Jo, B. J. Kim, K. Lee, *Adv. Mater.* **2014**, *26*, 2268.

[27] P. Munier, K. Gordeyeva, L. Bergström, A. B. Fall, *Biomacromolecules* **2016**, *17*, 1875.

[28] L. Biniek, N. Leclerc, T. Heiser, R. Bechara, M. Brinkmann, *Macromolecules* **2013**, *46*, 4014.

[29] S. R. S. Kumar, N. Kurra, H. N. Alshareef, *J. Mater. Chem. C* **2015**, *4*, 215.

[30] M. F. Ashby, A. G. Evans, N. . Fleck, L. J. Gibson, J. . Hutchinson, H. N. G. Wadley, *Metal Foams : A Design Guide*, Butterworth-Heineman, Boston, **2000**.

[31] F. G. Cuevas, J. M. Montes, J. Cintas, P. Urban, *J. Porous Mater.* **2009**, *16*, 675.

[32] K. P. Dharmasena, H. N. G. Wadley, *J. Mater. Res.* **2002**, *17*, 625.

[33] M. Hakamada, T. Kuromura, Y. Chen, H. Kusuda, M. Mabuchi, *Mater. Trans.* **2007**, *48*, 32.

[34] V. Apostolopoulou-Kalkavoura, S. Hu, N. Lavoine, M. Garg, M. Linares, P. Munier, I. Zozoulenko, J. Shiomi, L. Bergström, *Matter* **2021**, *4*, 276.

[35] Q. Wei, M. Mukaida, K. Kirihara, T. Ishida, *ACS Macro Lett.* **2014**, *3*, 948.

[36] A. M. Nardes, M. Kemerink, R. A. J. Janssen, J. A. M. Bastiaansen, N. M. M. Kiggen, B. M. W. Langeveld, A. J. J. M. Van Breemen, M. M. De Kok, *Adv. Mater.* **2007**, *19*, 1196.

[37] L. Biniek, A. Hamidi-Sakr, L. Grodd, S. Escoubas, Y. J. Dappe, S. Grigorian, M. Schmutz, M. Brinkmann, *Adv. Electron. Mater.* **2018**, *4*, 1.

[38] A. Hamidi-Sakr, L. Biniek, J. L. Bantignies, D. Maurin, L. Herrmann, N. Leclerc, P. Lévêque, V. Vijayakumar, N. Zimmermann, M. Brinkmann, *Adv. Funct. Mater.* **2017**, *27*, 1700173.

[39] V. Vijayakumar, Y. Zhong, V. Untilova, M. Bahri, L. Herrmann, L. Biniek, N. Leclerc, M. Brinkmann, *Adv. Energy Mater.* **2019**, *9*, 1900266.

[40] J. Liu, X. Wang, D. Li, N. E. Coates, R. A. Segalman, D. G. Cahill, *Macromolecules* **2015**, *48*, 585.

[41] D. T. Dixon, C. T. Gomillion, *J. Funct. Biomater.* **2022**, *13*, 1.

CHAPTER IV HIGHLY ORDERED MESOPOROUS PEDOT: PSS BY AN ALTERNATIVE GELATION METHOD: PROMISING RESULTS FOR INTEGRATION INTO VERTICAL TEGS

IV. HIGHLY ORDERED MESOPOROUS PEDOT: PSS BY AN ALTERNATIVE GELATION METHOD: PROMISING RESULTS FOR INTEGRATION INTO VERTICAL TEGS

1. INTRODUCTION

We described in chapter II the development of porous PEDOT: PSS with different ranges of porosity by a two-step process: i) gelation, and ii) solvent removal using different drying techniques. Their TE properties were carefully studied and the sulf-aerogel proved to be the most promising material to meet our materials requirements (see section I.1.6). Its mesoporous structure participates both in the reduction of thermal conductivity and in better charge transport properties compared to the other prepared PCPs. However, it was difficult to improve further its TE properties. Although the DMSO vapor treatment of the sulf-aerogel improved its electrical conductivity (see section II.5.2), the structure densification of the material may have negatively impacted its thermal insulation (not experimentally measured).

It was not possible to achieve further modifications of the material through the tuning of the drying step. The main interest of supercritical drying is the conservation of the native network of the gel. Hence, we were not able to achieve drastic structural modifications during the drying step as we did with freeze-drying (see section II.3.3) or ice-templating (see chapter III). Thus, in order to tune the properties of the mesoporous PEDOT: PSS, one must play with the gelation parameters.

Therefore, we focus our attention on the gelation mechanism. Few PEDOT: PSS gels have been reported in the literature, and reports of pure PEDOT: PSS gels without external crosslinking agents are even more scarce (see section I.2.3.2). We deliberately wanted to avoid the use of external crosslinking agents[1] (which may negatively impact the charge transport properties), or the gelation by polymerization of PEDOT: PSS[2] (which could suffer from low electrical conductivity and batch-to-batch variations).

Maeda et al. reported a facile technique to produce a PEDOT: PSS gel/film from commercial PH1000 dispersion.[3,4] Gelation was achieved by interactions between the PEDOT: PSS dispersion and excess of ethanol. The charge transport properties obtained on the air-dried materials were amongst the highest reported for pure (i.e., as obtained from the commercial dispersion) PEDOT: PSS micrometer thick films (σ ~ 300 S/cm and S ~ 20 µV/K for ~ 20 µm thickness) suggesting good organization of the microstructure. Inspired by this method, in this chapter, we focus on the production of thick and pure gels of PEDOT: PSS by interaction with polar solvents. The gel with the best mechanical properties (i.e., manipulability) was then selected for drying by supercritical CO_2 drying.

Herein, we develop a simple and reproducible technique to prepare highly mesoporous, mechanically robust, and handleable aerogels based on entangled PEDOT: PSS fibers using a two-step elaboration process. The 3D fibrillar network is created during gelation of PEDOT: PSS with ethanol interactions and preserved via careful control of supercritical drying. We study the obtained mesoporous gel and alco-aerogel structure and compare its features with the hydrogel and sulf-aerogel discussed in chapter 2. The interconnected fibrillar morphology provides good electrical conductivity and mechanical properties by forming efficient pathways for electron transfer and mechanical strength conservation. In general, the aerogels processed from ethanol, exhibit superior TE performance compared to other porous PEDOT: PSS systems without any additional processing. Hence, they were selected to evaluate the potential use of PEDOT: PSS aerogels in a TE generator by measuring their power output at different temperature gradients. This work led to the publication of an article; this chapter has been adapted from it.[5]

2. FORMATION OF A HIGHLY ORDERED ALCOGEL

2.1. FABRICATION OF THE ALCOGEL

The PEDOT: PSS aqueous dispersion was carefully poured with a syringe (to avoid any mixing) at the bottom of a vial filled with ethanol (EtOH). Due to the density difference between the two liquids, the dispersion remained at the bottom of the vial (as shown in Figure IV.1.A). Upon time and at high temperature, ethanol diffused slowly into the PEDOT: PSS dispersion. A bluish layer appeared at the interface of the two phases (Figure IV.1.B) which highlighted the solvent exchange process. After 20 h, a solid and dark blue alcogel floating in a transparent solution was obtained and the supernatant was replaced with fresh ethanol (Figure IV.1.C). This gelation process resulted in a handleable alcogel whose size and shape could be tuned by using a different mold or cutting it accordingly.

Other polar solvents such as ethylene glycol, dimethyl sulfoxide (DMSO), or methanol were also used to form a gel. Interestingly, with these solvents, a coherent bulk gel was formed but was very mechanically weak compared to the one formed in ethanol. After several attempts to optimize the process, it proved impossible to form a robust gel with these solvents. DMSO is a polar solvent with a high dielectric constant,[6] often used as a post-treatment agent of PEDOT: PSS (see section I.1.4). It has been reported in the literature that the ratio of PEDOT: PSS was drastically altered by DMSO treatments. Indeed, polar solvents with high dielectric constants induce a strong charge screening effect between the dopant and the semiconducting polymer.[7] Thus, the coulombic interactions between the PEDOT cation and the PSS anion are significantly reduced. Overall, the impossibility to form robust gels with DMSO, methanol or ethylene glycol could be explained by their high dielectric constant inducing too strong a screening effect. [6,8] Finally, the gel formed with ethanol was the best candidate.

A mechanism of gelation was suggested by Maeda et al. They considered the PEDOT: PSS system as commonly reported in the literature: a spherical micelle composed of a PEDOT-rich core and a PSS-rich shell.[9–12] It was thought that ethanol washed away the excess PSS present on the surface of the PEDOT: PSS micelles. As the dispersion was destabilized, the spherical PEDOT: PSS micelles moved closer and gradually came into contact with each other, forming a 3D network. Removal of excess PSS along with network formation was hypothesized to occur progressively through the film thickness, resulting in a structure gradient for overly thick films.[3]

Our conclusions on this mechanism, based on the investigation of the native dispersion (see section II.2.1), and XPS, UV-vis, FTIR, cryo-SEM, and SAXS on the alcogel are slightly different and are discussed in the following sections.

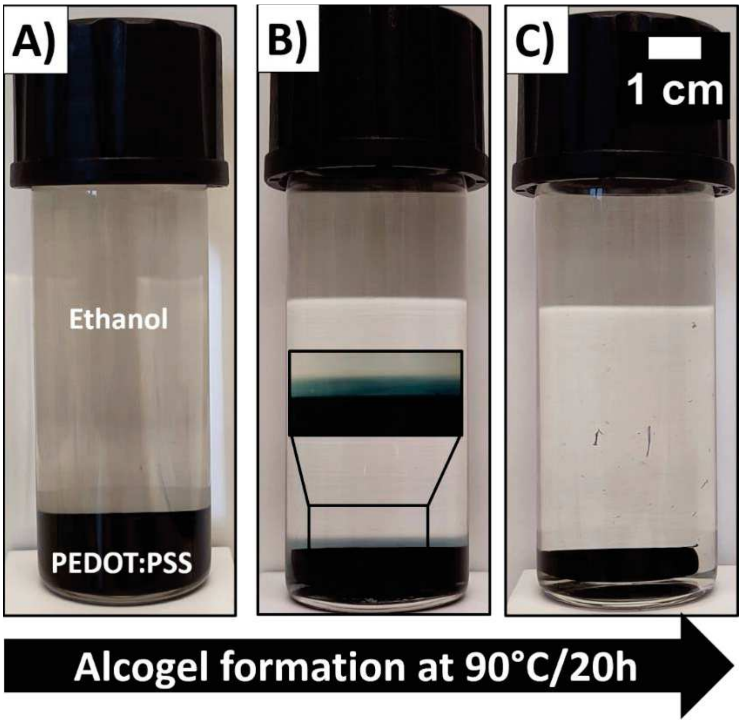

Figure IV.1: PEDOT: PSS alcogel formation process. Photographs were taken during the gelation process at different times: A) t = 0, PEDOT: PSS was deposited at the bottom of ethanol, B) t = 10 h, interaction between ethanol and PEDOT: PSS was visible at the interface of the two phases, C) t = 20 h, the alcogel was formed.

2.2. SPECTROSCOPIC INVESTIGATIONS

As described in chapter II, we demonstrated that the initial dispersion of PEDOT: PSS was not composed of spherical micelles. We showed by cryo-TEM and X-ray scattering measurement the presence of fibrils (of ~ 5 nm thickness and about 100 nm long).

During the gelation it seems that ethanol and PEDOT: PSS aqueous dispersion interact preferentially at their interfaces as shown in Figure IV.1.B. Based on the literature suggesting the removal of PSS in contact with polar solvents and our findings on the gelation of PEDOT: PSS with sulfuric acid (see section II.2.2), we investigated the evolution of the chemical composition of the material after gelation. By analyzing the ethanol supernatant after gelation by UV-Vis spectroscopy, we determined that it contained PSS (as also observed in the supernatant of the gel formed with H_2SO_4). In addition, we performed XPS analysis after drying this alcogel (the drying will be described in section IV.3.1) which is shown in Figure IV.2. We focused on the analysis of the S 2p peaks: the doublet around 164 eV and 165 eV corresponds to the thiophene sulfur of PEDOT while the peak at 169 eV corresponds to the sulfonate of PSS (see section I.2.2.2). It is clear that PSS has been removed during gelation since the molar ratio (calculated from the ratio of the PSS and PEDOT peak areas)[13] of PSS decreases from 70% to 55%. The final ratio contained fewer PSS than for the hydrogel made with H_2SO_4 (59 mol% PSS) discussed in section I.2.2.2. However, this final ratio was similar to that measured on sulf-aerogel (55 mol% of PSS) suggesting a similar doping state in both alco- and sul-aerogels. For reminder, to produce a sulf-aerogel, the hydrogel prepared with H_2SO_4, passed through an intermediate step of solvent exchange in ethanol before supercritical drying (see section II.4.2).

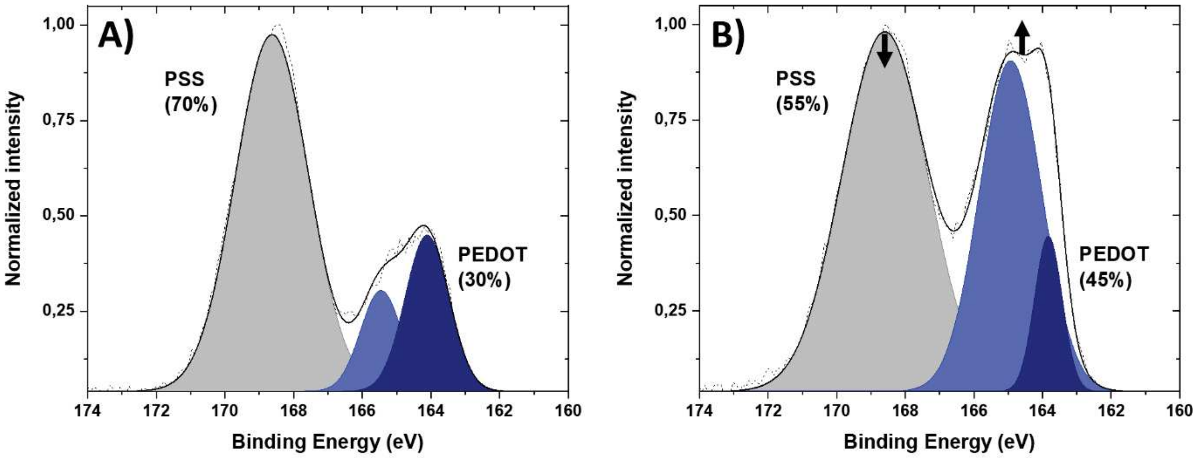

Figure IV.2: S 2p XPS spectra of A) the dried stock PH1000 dispersion and B) the dried alcogel.

As for the gelation with sulfuric acid, the gelation process with ethanol promoted the conformational change of PEDOT from a benzoid to a more quinoid conformation. We demonstrated this change by FTIR analysis on the dried alcogel (see Figure IV.3.A). The interpretation of the spectra is similar to that in section II.2.2.3. It was not possible to quantitatively determine the ratio of the benzoid to the quinoid structure. However, we suggest that, since the shifts of the C_α-$C_{\alpha'}$ stretching (1300 cm^{-1} → large bump around 1340 cm^{-1}), C_β-$C_{\beta'}$ stretching (1365 cm^{-1} → 1371 cm^{-1}), and C_α=C_β asymmetric (1520 cm^{-1} → doublet at 1532 cm^{-1} and 1553 cm^{-1}) vibrational bands were more important than the ones observed on the dried hydrogel (see section II.2.2.3), the proportion of quinoidal structure was more important in this alcogel than in the hydrogel. [14]

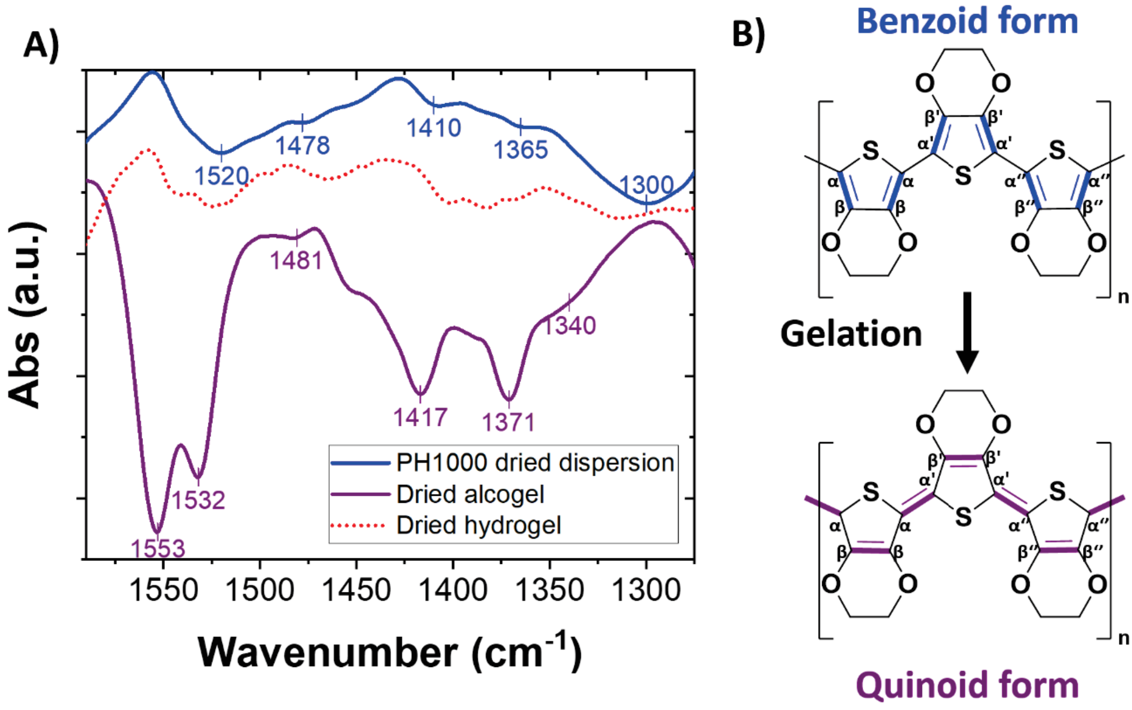

Figure IV.3: A) Infrared spectra of the PH1000 dried dispersion (in blue), dried hydrogel (in red) and the dried alcogel (in purple), B) benzoid and quinoid conformations of PEDOT.

2.3. STRUCTURAL INVESTIGATIONS OF THE FIBRILLAR STRUCTURE OF THE ALCOGEL

We have also investigated the morphology of the gel by cryo-SEM. Because ethanol was difficult to sublimate, we performed a stepwise solvent exchange with deionized water on the alcogel before cryo-SEM analysis. The exchange was performed in several progressive steps to minimize shrinkage and distortion of the gel structure. Typically, the alcogel was left for 24 hours in various ethanol/water mixtures until the solvent was only water. Then, a small piece of gel was cut with a razor blade and quickly immersed in liquid ethane for cryo-SEM observation.[15,16] More information can be found in the Experimental section. The 3D structure of the gel was composed of fibers with a thickness of 13 ± 4 nm (see Figure IV.4.A). The network is homogeneous and the voids are in the range 10 – 50 nm. The SAXS profile of the alcogel is shown in Figure IV.4.C (see section II.2.2.1 and Experimental section for details). In the intermediate regime ($q < 0.01$ Å^{-1}) follows a q^{-1} power law, confirming the presence of 1D objects. The diameter of the unique object (determined by a cylindrical fit) is estimated at 2 – 4 nm. The fibrils tend to entangle (bunches of 3-5 fibrils) to form thicker fibers (as observed by SEM, Figure IV.4.A) composing the 3D network of the gel.

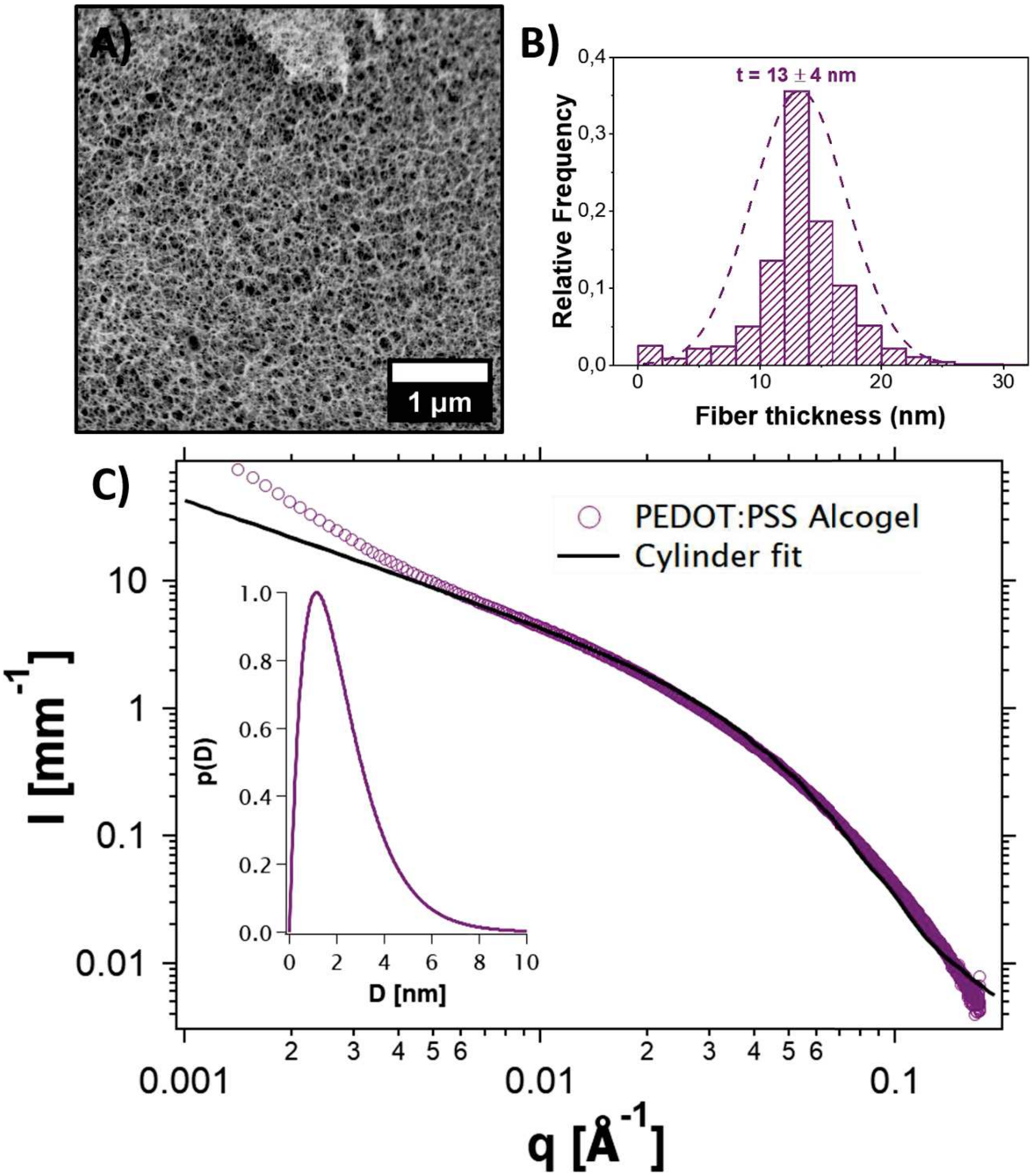

Figure IV.4: A) cryo-SEM image of the fibrillar structure of the alcogel, B) Distribution of the fibers' thickness measured on SEM images by ridge detection, C) SAXS profile of the alcogel, the inset is the Schulz distribution of the fibers' diameter extracted from the cylinder fit.

In the end, our multiscale observations of the formation of this alcogel were very similar to those of the hydrogel formation with sulfuric acid (see section II.2.2). The fibrillar morphology of the gel was equivalent, the few variations detected were more related to the PEDOT: PSS ratio and the conformation of PEDOT. Indeed, it seems that ethanol has the ability to remove more PSS than sulfuric acid during gel formation. Thus, with a final PEDOT:

PSS molar ratio of 45:55 mol%, it is likely from the FTIR observations that more order was induced between the polymer chains by the ethanol gelation process. In order to obtain more details on the order of the chains between them, a WAXS analysis would have been ideal to obtain information on the π-stacking distance or on the global organization of PEDOT and PSS.[17] Despite our efforts, it was not possible to obtain a usable signal in the alcogel state (this is due to the high scattering of the solvent at wide angles). However, it was possible to obtain the WAXS profile of the dried alco-aerogel. The WAXS analysis of the alco-aerogel (discussed more in detail in section IV.4.1.2), as compared with the cryogel, indeed shows a better organization at the molecular level.

We suggest the following gelation mechanism. Upon contact with ethanol, a solvent exchange took place between water and ethanol (highlighted in Figure IV.1.B). Thus, ethanol screened the charges of PSS, decreasing the coulombic interactions between PEDOT and PSS. In the same way as for gelation with sulfuric acid, a part of the PSS (free and/or around a PEDOT-rich core) was then solubilized in ethanol and thus washed out from the PEDOT:PSS complex. The repulsive interactions between the PEDOT: PSS wormlike micelles were drastically decreased and they eventually assembled to form a 3D network. Contrary to Maeda et al., we do not believe that there is a structure or composition gradient (at least for a sample diameter <13 mm and thickness <4 mm) since cryo-SEM, IR, and XPS analyses were performed on several locations of the same gel and no major differences were found.

In the following section, the drying method, mechanical properties and morphology of the final alco-aerogel are discussed.

3. ELABORATION OF A ROBUST ALCO-AEROGEL

3.1. DRYING OF THE ALCOGEL

The PEDOT: PSS alcogels were subjected to supercritical drying, providing alco-aerogels. The conditions of this drying were critical to minimize shrinkage and possible gel distortion. Since the gel produced after the synthesis contained EtOH in its pores, the solvent was directly replaced with liquid CO_2 to facilitate the supercritical drying at mild conditions. The replacement was achieved by a solvent exchange process in the autoclave (Figure IV.5.B, in blue). After the solvent exchange was completed, the autoclave was heated until the conditions reached beyond the supercritical point of the liquid CO_2 (31 °C, 1070 psi, see Figure IV.5.B, in purple). As mentioned in section II.3.2.1, passing through the supercritical state allows the liquid to be transformed into gas in the absence of surface tension and capillary stresses. Hence, extracting the fluid from the sample in this condition resulted in the conservation of the network structure. Therefore, venting (Figure IV.5.B, purple) the autoclave at this condition prevented the collapse of the gel. The resulting alco-aerogel monolith (Figure IV.5.C) was crack-free and retained the same features of the alcogel. However, in our case it suffered from a 40%vol shrinkage which could not be avoided. The shrinkage might be attributed to the interaction of the alcogel with liquid CO_2 during the solvent exchange process, as this behavior was also seen for PEDOT: PSS gels when immersed in other solvents.[18] Nevertheless, the final sample size was still large enough (thickness: 3.5 mm, diameter: 13 mm) considering our material requirements. The alco-aerogels exhibited ultra-low density of 0.07 g.cm^{-3} with porosity of 93%.

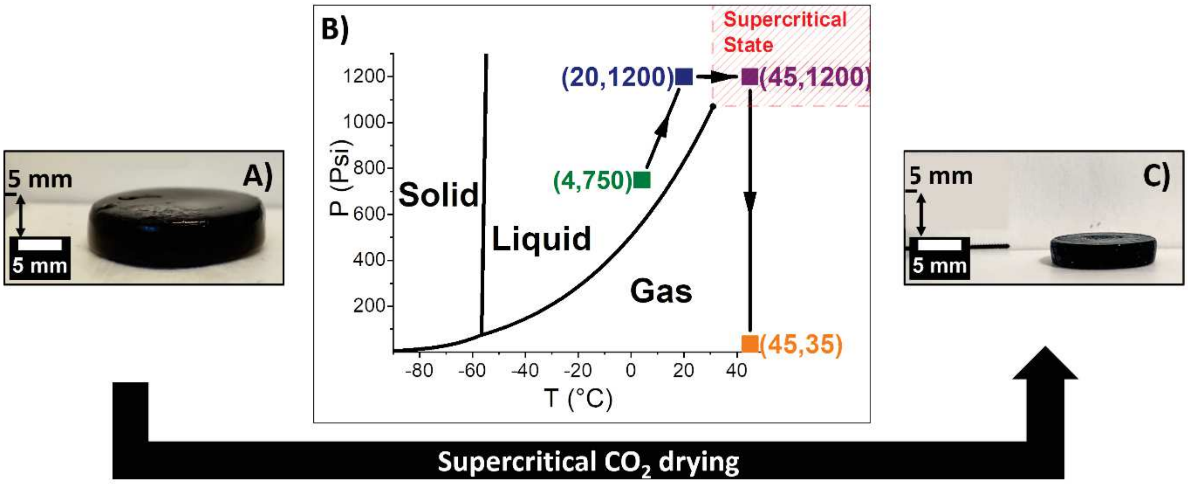

Figure IV.5: Supercritical drying process: A) Photograph of the alcogel before drying, B) Schematic of supercritical drying steps in the (P, T) CO_2 diagram; in green: initial temperature and pressure in the closed autoclave containing the alcogel sample, in blue: ethanol-$CO_{2Liquid}$ exchange, in purple: supercritical state of CO_2 and dynamic drying, in orange: venting step, C) Resulting PEDOT: PSS alco-aerogel.

4. HIGH MECHANICAL PROPERTIES

Complex shear modulus measurements were performed with a stress-imposed rheometer working in oscillatory mode. The parallel plate geometry fixtures (with different diameters) were used to cover the sample area and the fixtures were adjusted according to the height of the sample without causing an excessive compression of the sample.[19] For the alcogel, to avoid drying during measurement, the bottom plate was modified to allow the sample to be immersed in ethanol.

Figure IV.6.A shows the typical response of the alcogels under oscillatory shear. It is characterized by a quasi-constant behavior of the storage modulus (G') and of the loss modulus (G'') with frequency. From the G'-plateau value, an elastic shear modulus of ~10 kPa could be deduced. This value is a hundred times higher than other PEDOT: PSS gel modulus reported in the literature.[18,20] To ensure reproducibility, several alcogels were examined: the measurements led to the same qualitative behavior and values of G' close to 10^4 Pa. In addition, to verify the homogeneity of the alcogels, the mechanical response of three horizontal sections of the same sample (located on the upper, middle, and lower part of the sample, respectively) were examined (Figure IV.6.B). The results obtained show almost identical values with no particular trend. Therefore, from a macroscopic point of view, alcogel samples are homogeneous and do not show any mechanical anisotropy. Thus, the gelation seems to be isotropic and homogeneous in the conditions of preparation (with no gradient of the polymer chain concentration in the sample linked to flocculation/sedimentation effect during gelation).

Furthermore, the G' and G'' behaviors at low- frequency (Figure IV.6.A) were characteristic of the rheological response under shear as expected for a physical gel in the hydrodynamic regime. This behavior is also consistent with the low-frequency response of a chemical gel with a large number of inhomogeneities.[21] To distinguish between chemical and physical bonds constituting the alcogel network, static compression can be applied to the material, followed by an examination of the evolution of the normal reaction force of the sample. Depending on the nature of the nodes forming the network, this normal force is maintained over time in the case of permanent nodes (chemical gel) or relaxed over time if the nodes are transient (physical gel). The inset in Figure IV.6.C focuses on the short times and shows simultaneously the increase in normal force and the progressive decrease in sample thickness (9% in our case over 1 min of contraction time). A rapid increase in normal force during sample compression, followed by a gradual decrease in normal force over time was observed (Figure IV.6.C). This highlights that the alcogel reacted like a physical gel (as also observed for PEDOT: PSS hydrogel [18]) as its force relaxed over time. At the end of the experiment, as the top plate of the cell returned to its pre-compression position, the sample did not return to its initial thickness, indicating that the change in size was irreversible. Figure IV.6.C also shows two regimes of force decay with time: a rapid decay that extends up to ~5 h, followed by a slower decay that extends to the end of the experiment (described by a simple linear decrease with time). Assuming that this linear decrease is maintained over time, this force would vanish after 57 h. In other words, we can identify this time as the lifetime of the longest relaxation mode of the alcogel network (demonstrating that some elasticity endures over time).

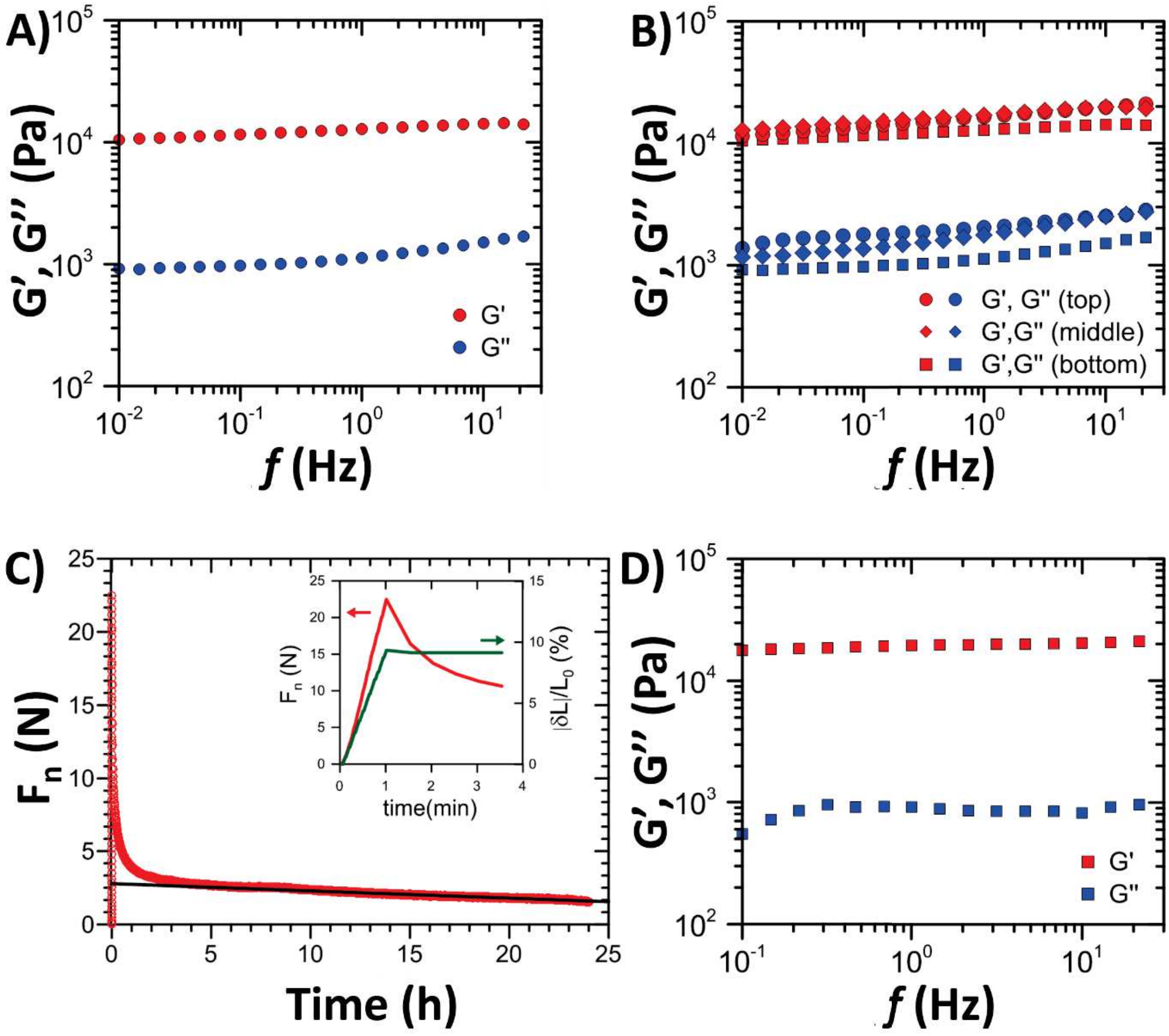

Figure IV.6: A) *Complex shear modulus variation with frequency of the alcogel, B) Shear measurements for three slices cut in the same alcogel sample (top, middle and bottom part of ~ 1.5 mm thickness each), C) Evolution over time of the normal force of an alcogel sample subjected to a reduction in thickness. The time relaxation of this force highlights the physical gel nature of the alcogel, D) complex shear modulus variation with frequency for an alco-aerogel sample.*

To allow a quantitative comparison of the mechanical properties prior to and after drying, the same sample was studied, first in its alcogel state and then in its aerogel state. Figure IV.6.D shows the typical frequency response of the alco-aerogel. This response is qualitatively very similar to that of alcogel, with, in particular, the existence of a low-frequency plateau for *G*' and *G*''. A slight difference was observed for the plateau of *G*'', which persisted at higher frequencies for the alco-aerogel than for alcogel. This frequency extension of the plateau reflects the increase in the lowest relaxation frequency of the internal lattice modes. An increase in the elastic modulus of about a factor of two was observed between the alcogel and the alco-aerogel. As previously mentioned, supercritical drying resulted in a reduction in sample size. Within the accuracy of the measurements, the volume change and the modulus change induced by supercritical drying are comparable ($V_{\text{alco-aerogel}}/V_{\text{alcogel}} = 0.59$ with $V_{\text{alcogel}} = 0.835$ cm^3 and $V_{\text{alco-aerogel}} = 0.489$ cm^3 and $G'_{\text{alcogel}}/G'_{\text{alco-aerogel}} = 0.61$). Since the elastic moduli are proportional to the node density of the network, the number of nodes in the alcogel network remains the same after supercritical drying. The initial network in the alcogel is thus preserved during the alco-aerogel formation.

In summary, the results of the rheology experiments on alcogels show the expected behavior for a physical gel: stress relaxation and frequency response characterized by a low-frequency G'- and G''- plateau. The formulation of alcogels yields samples which are isotropic and homogeneous at the macroscopic scale, and whose elastic modulus is around 10 kPa. The alco-aerogel shows a similar rheological behavior as the alcogel, but with twice the elastic modulus (~20 kPa). A precise analysis of the results carried out on the same sample in the alcogel and alco-aerogel states shows that the increase in the elastic modulus comes from the reduction in the volume of the sample during supercritical drying, while the number of nodes for alcogel and alco-aerogel remains the same. Altogether, the alco-aerogels show interesting structural features that sound promising for TE application.

4.1. FINAL MORPHOLOGY OF THE MESOPOROUS ALCO-AEROGEL

4.1.1. A HIGHLY MESOPOROUS MATERIAL…

The alco-aerogel was observed by SEM and its mesoporous structure is presented in Figure IV.7.A-B. The network is similar to that of the wet gel and is composed of entangled fibers of 9 ± 2 nm mean diameter. The sizes of the voids were estimated within the 10-50 nm range.

The textural properties were also confirmed by nitrogen adsorption/desorption tests (see Figure IV.7.C). Textural characterization was done by determining nitrogen physisorption isotherms at 77 K. Here, the alco-aerogel samples were cut into small pieces and loaded into an analysis tube. Prior to adsorption measurements, the sample was out gassed at 423 K for 6 h under vacuum to remove the moisture from the alco-aerogel. The specific surface area was calculated according to the criteria given in the literature[22,23] and by using the Brunauer−Emmett−Teller (BET) method applied in the $0.02 \leq p/p^0 \leq 0.20$ ranges. A type IVa isotherm with adsorption hysteresis at high relative pressure was obtained and indicates a large number of mesopores formed due to the interconnection of the fibers.[24,25] This type of isotherm is typical of mesoporous adsorbents, in which the initial monolayer-multilayer adsorption on the mesopore walls is followed by pore condensation. Pore condensation is defined as the phenomenon by which a gas condenses into the liquid phase in a pore at a pressure p below the saturation pressure p° of the liquid; in other words, pore condensation reflects a vapor-liquid phase transition in a finite volume system. It is typically observed in such a mesoporous structure. The hysteresis observed in our case resulted from exceeding a certain pore size. When the adsorbate is nitrogen, hysteresis starts to appear for pores larger than about 4 nm.[24] It should be noted that in our case the hysteresis was not complete, this is due to the small amount of material used in the analysis, but does not change the interpretation of the result. Thus, we could confirm that our structure was mainly mesoporous with pore sizes between at least 4 nm and 50 nm. We were not able to analyze the pore size of our material more precisely due to the unconventional pore shape of the structure. The obtained BET surface area of 315 m^2/g was amongst the highest reported in the literature for PEDOT: PSS mesoporous materials[2] and can be correlated to a high apparent external surface due to the fibrillar nature of the objects. The high SAXS intensity in the Porod regime (relative ratio surface/volume, see Appendix) correlates well with the observation of a high specific area. To disprove the presence of macropores, we also performed physisorption measurements of mercury. However, the analysis was inconclusive, because the structure of the alco-aerogel was completely modified by the Hg intrusion.

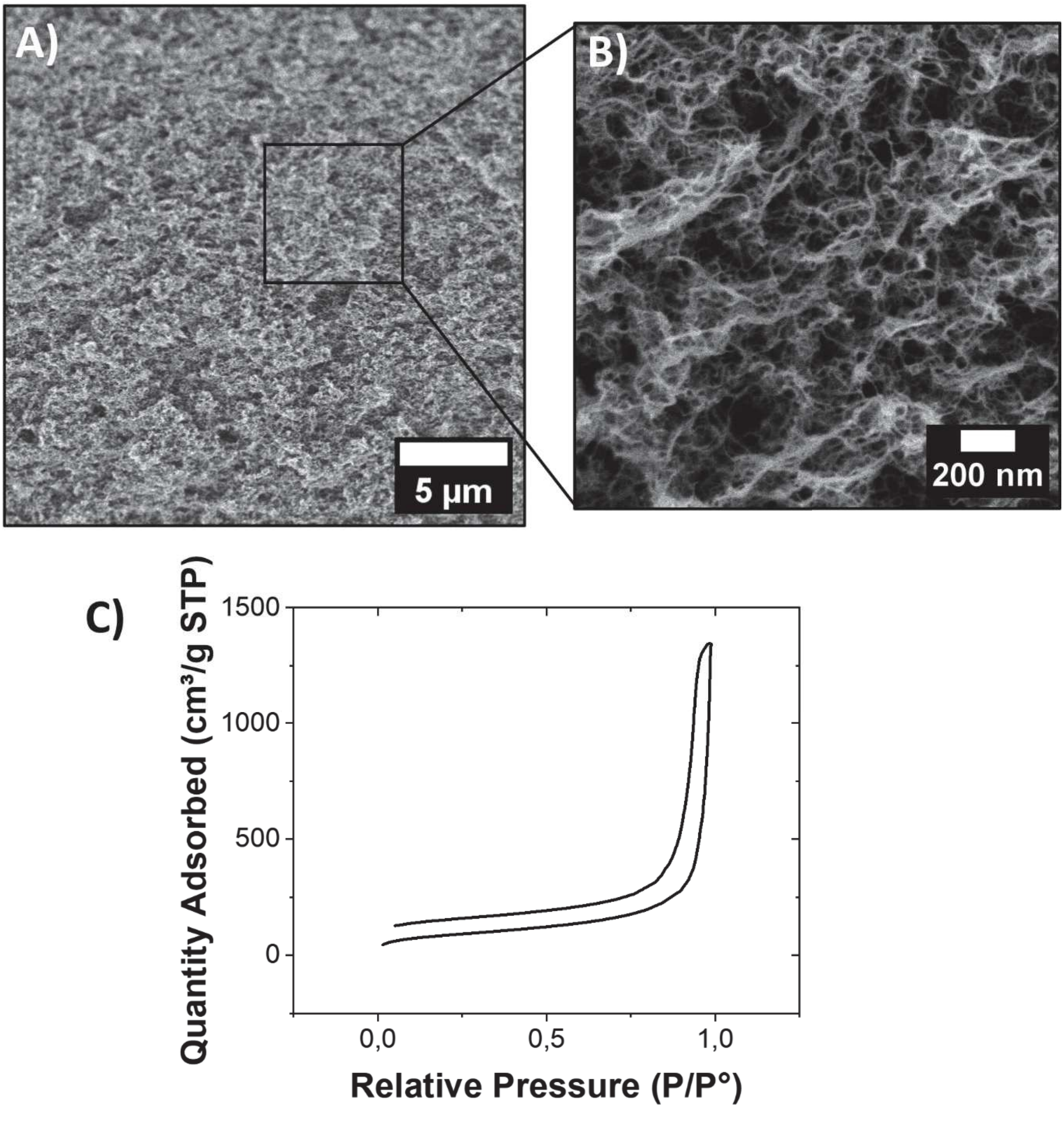

Figure IV.7: A-B) SEM images of the mesoporous fibrillar structure of the alco-aerogel at two different magnifications, C) Typical nitrogen physisorption adsorption and desorption isotherms.

4.1.2. … WITH A HIGH “CRYSTALLINE” ORDER

To further elucidate what composed the fibers and to monitor the impact of drying on them, X-ray scattering experiments were performed at synchrotron Soleil. The scattering of nanostructure constituting the alco-aerogel was studied with the small-angle module (SAXS), whereas the polymer chains packing within the nanostructures was analyzed by wide-angle X-ray scattering experiments (WAXS) (Figure IV.8.A-C). At small angles (0.002 Å^{-1} <q <0.03 Å^{-}

^{1}), the intensity profile decreases and follows a q^{-1} power law (Figure IV.8.A). This dependence highlights the one-dimensionality of the observed nano-objects composing the alco-aerogel. The SAXS domain was fitted with a cylinder model with radius polydispersity (Figure IV.8.A inset), yielding a diameter distribution in the range of 3 to 8 nm. These finding correlates well with the fibrillar structure of the alco-aerogel observed in SEM. At wide angles (0.3 Å^{-1} <q <2.5 Å^{-1}), a series of scattering peaks related to the inner structure of the fibers, can be observed (Figure 2d). Numerous and sharp peaks suggest a high crystalline order of the material (especially compared to the templated N_{2L} cryogel, see Appendix). Five peaks at q values of 0.49, 0.71, 0.98, 1.23 and 1.85 Å^{-1} correspond to lattice spacing of 12.8, 8.8, 6.4, 5.1 and 3.4 Å, respectively, according to Bragg's law. A consensus on the assignment of PEDOT: PSS X-ray diffraction peaks has not yet been reached in the literature (see section I.1.4.3). Hosseini et al.[17] attributed the peak at 12.8 Å to the second order of interlamellar spacing between two side-by-side PEDOT lamellae. The attribution of the two other peaks (8.8 and 6.4 Å) is not yet clearly understood. [12,26,27] In all cases, the well-defined peak at small distance (3.4 Å) is known to be the characteristic of the π-π stacking distance of the PEDOT aromatic rings. Interestingly, the π-π stacking spacing measured in the alco-aerogel was slightly lower than the one measured on non-treated PEDOT: PSS films (3.5-3.6 Å) suggesting some increase in molecular packing degree.[26] The structural order of PEDOT within the fibers was investigated by fitting the peak at 1.85 Å^{-1} with a Lorentzian model: $I(q) = \frac{I_{\max}}{1+\left(\frac{q-q_0}{\gamma}\right)^2}$. The half-width at half maximum (HWHM) of the peak, γ, is related to the domain size D by the Scherrer equation: $D \cong \frac{2\pi}{\gamma}$. This relation is equivalent to the more common form $\cong \frac{K\lambda}{B\cos\theta}$, where we assume the Scherrer constant $K = 1$ for coherence with the existing literature.[12] Fitting directly the $I(q)$ data yielded D = 5.5 nm, but the fit was not optimum, since the experimental peak is asymmetric. A better fit was obtained by using the Kratky plot $q^2I(q)$ as a function of q and yields D = 6.8 nm (red line in Figure IV.8.C). Therefore, the size of the PEDOT crystallite domains along the π-π stacking direction (along the b-axis) reached 6.8 nm, corresponding to ~19-20 stacks of PEDOT oligomers. As a comparison, pristine PEDOT: PSS films or films treated with ethylene glycol present lower crystallite size of D~1.2 nm and D~4.5 nm, respectively.[12] Although we cannot conclude on the orientation of the stacks within the fiber, it is worth noticing that the domain size along the π-π stacking direction of PEDOT is comparable to the diameter of the fiber. Altogether, the multiscale analysis of the alco-aerogels' morphology demonstrated the possibility to produce robust mesoporous alco-aerogels with a high degree of order of the PEDOT chains induced by the slow gelation process with ethanol.

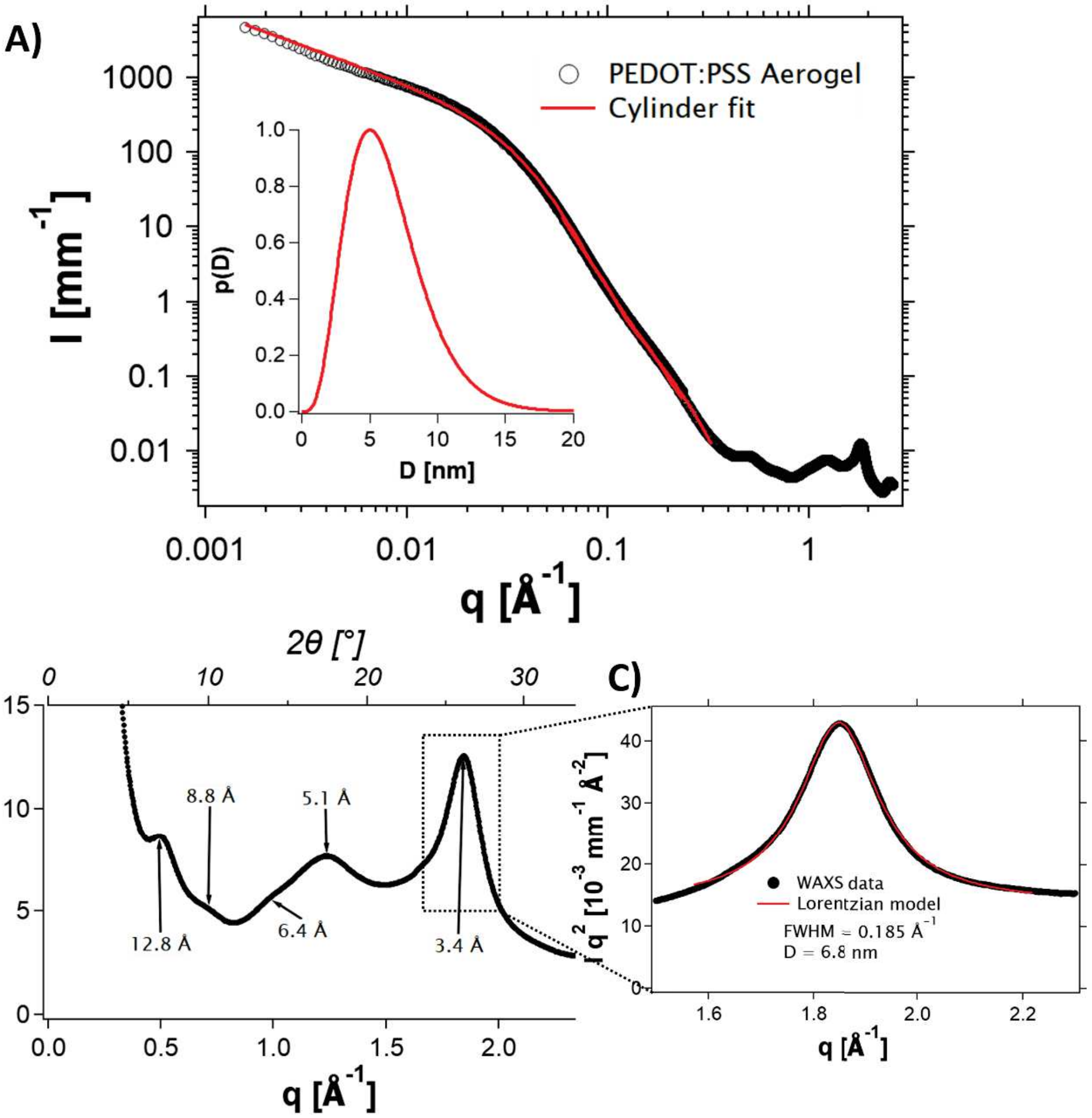

Figure IV.8:A) Scattered intensity as a function of the scattering vector, I(q), for the SAXS and WAXS configurations (black dots) fitted with a cylinder model in red (the diameter polydispersity is described by a Schulz distribution p(D), displayed in the inset). B) WAXS signal I(q) (solid dots). The abscissa is also given as 2 ϑ for Cu Kα radiation along the top axis. The peaks are identified by arrows and labeled with the corresponding distances. C) The Lorentzian fit of the 3.4 Å peak is shown as a red solid line.

5. INVESTIGATION OF THE THERMOELECTRIC PROPERTIES

Electrical conductivity, Seebeck coefficient and thermal conductivity mean values of the alco-aerogel are reported in Table IV.1.

5.1. A MATERIAL WITH HIGH CHARGE TRANSPORT PROPERTIES…

5.1.1. ELECTRICAL CONDUCTIVITY

Electrical resistance was measured on the alco-aerogels with a four-probe collinear resistivity setup. The resistance was isotropic (measured on both sides of the samples, on different spots). The alco-aerogels displayed a mean electrical conductivity value of 21 ± 2 S/cm which is amongst the highest values reported for pure and porous PEDOT: PSS materials with such high thickness and low density (see Table I.1 for comparison) and the highest amongst the other PCPs we produced (see chapters II and III). We suggest that such high charge transport property in a highly porous material is due to the best internal structural order of the polymer chains within the fibers induced during the gelation step (see the WAXS discussion above on the coherence length of the PEDOT domains along the π-π stacking direction). Furthermore, the interconnected fibrillar morphology provides good electrical conductivity by forming effective pathways for electron transfer.

To evaluate the electrical conductivity of our highly porous PEDOT: PSS alco-aerogels (93% porosity) as compared with solid PEDOT: PSS films (no porosity), we can follow different approaches. Experimentally, we have dried the PEDOT: PSS alcogels in air which afforded inhomogeneous but self-supported thick films (~10 µm) displaying an electrical conductivity of 403 ± 53 S/cm. This value is close to the ones reported by Maeda and co-workers.[3] As discussed in section II.4.1.1, we can also consider mathematical models taking into account the pore geometry and the volume fraction of the pores to determine the electrical conductivity of the solid without pores (i.e., σ_{dense}). However, these models have been mostly developed for closed-cell metallic foams, which are far from the structure reported in this work.[28–31] Interestingly, the model developed by Ashby et al. describes a general equation for open-cell porous materials.[32] In this model, the cell edges form a 3D network in which one third of the cell edges are aligned with the potential gradient. This model also takes into account the contribution of nodes in the electrical path. Although this model is only strictly applicable in an ideal system, we chose to use it here because the alco-aerogel shows an open cell structure with a large number of nodes. Accordingly, σ_{dense} of the solid PEDOT: PSS material can be estimated at 500-600 S/cm using the following equation [32]:

$$\sigma_{dense} = \frac{\sigma_{app}}{\frac{1}{3}[(1-\Theta)+2(1-\Theta)^{\frac{3}{2}}]} \qquad (II.5)$$

where σ_{app} is the apparent electrical conductivity measured on the porous material, and Θ the porosity of the material. The value obtained here is in fair agreement with the experimental data (403 ± 53 S/cm). Optimizing the theoretical model is out of the scope of this thesis but Ashby's model could be considered for fibrillar porous structure.

5.1.2. SEEBECK COEFFICIENT

The Seebeck coefficient S was measured in-plane via the differential method (see Experimental section). This p-type material exhibited a positive Seebeck coefficient of 18 ± 1 µV/K. Additionally, the Seebeck coefficient was also measured in a cross-plane configuration (see Experimental section) with a $\Delta T_{\max} = 6$ K, centered around 293 K. Both in-plane and cross-plane values are consistent, which confirms the structural isotropy of the sample and the appropriate metrology used to characterize bulk samples. These results also correlate with values reported in the literature for PEDOT: PSS dense films swollen in ethanol (S = 18 µV/K).[3] It is worth mentioning that the Seebeck coefficient was not impacted by the high porosity of alco-aerogels (high air content), as also observed in the case of P3HT foams[33] in the literature or on the PCPs described in chapter II.

5.2. … AND LOW THERMAL CONDUCTIVITY

The measurements were performed on different pairs of alco-aerogels and repeated consecutively with an interval of 30 min between each trial (see Experimental section). The average thermal conductivity of the alco-aerogels was measured to be 0.065 W/(m.K) (thermal diffusivity = 0.55 mm²/s). Again, this low value accounts for the high porosity of the alco-aerogels and their mesoporous structure. Phonon scattering at the interface between air and the polymer network was favored thanks to the small size of the pores. Their low density participated in reducing the thermal conductivity contribution to the solid conduction. As demonstrated for the other PCPs developed in this thesis introducing porosity and phonon engineering of conducting polymers is an efficient strategy to decrease κ_{lat} below 0.2 W/(m.K) (see section I.1.5).

Although the thermal conductivity of this material is low, it is the highest amongst the PCPs in this thesis. Especially when compared to sulf-aerogel which had a very similar mesoporous structure. A difference of ~ 0.01 W/(m.K) was observed and was attributed to the higher electrical conductivity of the alco-aerogel compared to the sulf-aerogel. κ_{elec} can be estimated by the Wiedemann-Franz law. It was shown that the Lorentz number, usually taken at the Sommerfeld value, could deviate largely according to the energy disorder in organic conducting materials.[34] It is difficult to numerically estimate κ_{elec} without more information. However, if one calculates κ_{elec} for the sulf-aerogel and alco-aerogel with the same Lorentz number the obtained values are $\kappa_{elec\text{-}sulf}$ ~ 0.006 W/(m.K) and $\kappa_{elec\text{-}alco}$ ~ 0.015 W/(m.K) (see Appendix II), corresponding to a difference of ~ 0.01 W/(m.K) as observed for κ_{total}. This suggests that: i) the difference of thermal conductivity may arise only from the difference of electrical conductivity between the two samples, and ii) that both materials may have a similar energetic disorder.

5.3. ZT AND COMPARISON WITH THE SULF-AEROGEL

Finally, from the thermoelectric properties obtained above, a *zT* of 3.1 x 10^{-3} at 300 K was calculated for mesoporous PEDOT: PSS alco-aerogels. This value is amongst the highest reported in the literature for such thick and light-weight samples (see Table I.1). An exact comparison with other reported values is difficult as porous PEDOT: PSS materials are processed differently which impacts their structural and functional properties. As discussed earlier, most of the reports either omit the gelation aspect of the synthesis or utilize different drying techniques to obtain porous solids (comprised of macropores). To compensate for the resulting poor TE features, they utilize post-processing steps such as solution/vapor treatment with organic solvents [35–37] or compression [37]. However, this comes at the cost of sample shrinkage (pore collapse) or of decrease in sample size (increase in density) as seen in section II.5.

Although it is difficult to compare their thermoelectric properties with other reports in the literature, we can definitely compare these alco-aerogels with the sulf-aerogels described in chapter II. A summary of the measured properties of both alco-aerogel and sulf-aerogel are reported in Table IV.1. Even though they both have a very low density (and high porosity), and a fibrillar mesoporous structure composed of PEDOT: PSS fibers with the same molar ratio (45:55 mol%) with PEDOT favored in the quinoid conformation, a twofold difference in the electrical conductivity was observed. Surprisingly, even a difference of Seebeck coefficient was observed, the alco-aerogel presenting the higher one. A study of the doping state of both materials could have been useful to discuss these differences. However, it was very difficult to measure the optical properties of these bulk, dark blue, porous samples. For instance, polaronic bands could not be observed by UV-Vis NIR spectroscopy (in reflection mode, using an integration sphere) because of the important signal noise.

*Table IV.1: Mean values of the measured properties of the sulf-aerogel and alco-aerogel. **σ_{dense} *was calculated by equation II.5.*

Material	Density (g/cm^3)	Porosity (%)	PEDOT : PSS ratio (%mol)	σ_{app} (S/cm)	σ_{dense}* (S/cm)	S (µV/K)	κ (mW/(m.K))	ZT x10^{-3} (@300K)
Sulf-aerogel	0.06	94	45:55	9 ± 1	~ 340	16.8 ± 0.8	54 ± 2	**1.4**
Alco-aerogel	0.07	93	45:55	21 ± 2	~ 550	18 ± 1	65 ± 1	**3.1**

It is likely that the high degree of chain organization in PEDOT:PSS fibers obtained by gelation with ethanol results in good charge mobility in the system. We were not able to measure it, but it has been well reported in the literature that increasing the structural order in conjugated polymers induced an improvement in their electrical conductivity (see section

I.1.3.3 and I.1.4.3). In addition, low π-stacking distance and high crystal order promote interchain transport and thus enhance charge transport. The increase in electrical conductivity with decreasing π-stacking distance of PEDOT has been well reported in the literature.[17] The sulf-aerogel exhibits a similar molecular order (see Appendix I), and similar PEDOT: PSS ratio. Hence, the higher charge transport properties of the alco-aerogel compared to the sulf-aerogel cannot be attributed to a better organization of the chains or a higher charge carrier density. It was not possible to demonstrate it, but it is likely that the fibrils/fibers connectivity of the alco-aerogel might be better than in the sulf-aerogel, correlating with a higher electrical conductivity.

The difference in S between sulf-aerogel and alco-aerogel is not significant and is difficult to attribute. One possibility is that this difference comes from a difference in charge carrier concentration between the two materials. It has been reported that post-treatment of PEDOT: PSS films with H_2SO_4 induced a higher concentration of charge carriers leading to a reduction in S with sulfuric acid treatment.[38] Therefore, we suggest that a similar behavior was observed here, explaining the smaller Seebeck coefficient of sulf-aerogel compared to alco-aerogel.

Finally, it is clear that this alco-aerogel is the best PCP produced in this thesis work. Its high molecular organization and mesoporous structure result in very promising TE properties. Given its size, its implementation in TEGs is facilitated compared to thin films. In the next section, we discuss its potential implementation in vertical TEGs.

6. A PROMISING MATERIAL TO IMPLEMENT INTO VERTICAL TEGS?

6.1. PEDOT: PSS ALCO-AEROGEL AS A BODY HEAT HARVESTER?

One of the applications for which such material could be interesting is the generation of electricity by harvesting body heat. It is possible to calculate a theoretical maximum efficiency (neglecting any contact resistance) from the ZT of the material from equation I.4.[39] To simulate body heat power generation, the hot side (i.e., the skin) and the cold side (i.e., the ambient air) were chosen according to the results from Leonov.[40] Hence, T_H = 306

K and T_c = 293 K. Considering the ZT of the material to be 3.1 x 10^{-3}. With such temperature difference, the Carnot efficiency ($\eta_C = \frac{T_h - T_c}{T_h}$) is ~ 4%, limiting the maximum efficiency η_{max} of the material which can be estimated ~ 0.003%. Such low efficiency is not surprising considering this low temperature gradient and ZT.[39] From this value, we can estimate the theoretical maximum power output from:

$$\eta_{max} = \frac{P_{out\ max}}{Q_{in}} \qquad (IV.1)$$

Where Q_{in} is the heat flow entering the generator and $P_{out\ max}$ the maximum theoretical power generated by the generator. The heat flow on the wrist of a human skin was estimated between 18 mW/cm² for a standing subject to 80 mW/cm² for a moving subject.[41] Thus, from equation IV.1, the theoretical maximum power output of our alco-aerogel would be 0.55 – 2.5 µW/cm² (for standing – moving body, respectively). Such power is already sufficient to power low-consumption devices such as quartz watches. The Seiko Thermic, which was developed with built-in TEG could produce up to 22 µW in 1999.[42] Today, the Seiko Kinetic movement requires only 0.7 µW to work but still need a lithium battery.[43] One could imagine that one day, this kind of watch could work with a small TEG harvesting body heat instead.

6.2. DEMONSTRATION OF ACTUAL POWER GENERATION

To demonstrate the potential of PEDOT: PSS alco-aerogels in a TE generator, the power output was measured as a function of an adjustable external load circuit in air (at ambient temperature). This measurement was possible thanks to the collaboration with Nicolas Stein from Institut Jean Lamour, Metz. Here, an alco-aerogel was sandwiched between two copper discs and several temperature gradients were applied through two Peltier elements (One hot and one cold Peltier, the average temperature was set at 20°C). The maximum power output was determined when the load resistance was equal to the internal resistance of the sample. The alco-aerogel exhibits a maximum power output of 0.102 µW and a small internal resistance of 0.044 Ω for a small temperature gradient of 7 K (with the average temperature fixed at 20°C). Interestingly, the maximum power output was increased twenty times to 2 µW for a temperature gradient of 36.5 K (maximum temperature difference achievable with the setup). The evolution of the power output per area (the measurement area was 1 cm^2) as a function of temperature gradient is presented in Figure IV.9.A. At 36.5K of temperature difference between the two copper discs, the power output per area of a single alco-aerogel can be as high as 2.54 µW/cm^2. To our knowledge, it is the highest power output reported for pure organic porous thermoelectric material. As a comparison, Wang et al.[37] developed a TE generator consisting of six pairs of p-type PEDOT: PSS-based cryogel (with heterogeneous macroporosity) and n-type CNT fibers as legs and the maximum power output of 0.62 µW was generated at a temperature gradient of 60 K.

The actual power output of the pure material might be slightly underestimated due contact resistances at the interface between the alco-aerogel and the copper discs. To limit even more such contact resistance, the surfaces of the alco-aerogel would require to be perfectly smooth and planar. Although the existence of contact resistances should not be neglected, this measurement gives a very good estimation of the power that can deliver the mesoporous PEDOT: PSS alco-aerogels.

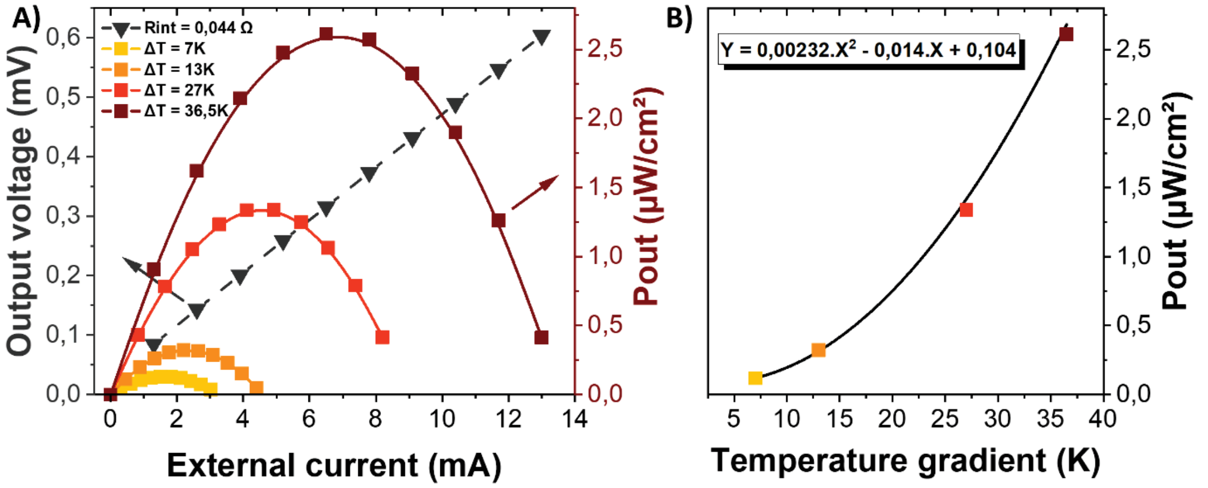

Figure IV.9: A) Output voltage and output power per area as a function of current for a typical alco-aerogel for temperature gradients from 7 K to 36.5 K, B) Quadratic evolution of the power output per area as a function of the temperature gradient applied.

Interestingly, the power output per area as a function of temperature gradient follows a 2nd order polynomial function (Figure IV.9.B). This type of behavior was expected for power generation with a thermoelectric material.[44]

This measurement demonstrates the power output of a "virtual" one-leg thermoelectric generator. Increasing the number of legs and coupling with n-type alco-aerogel counterparts (with balanced properties) can lead to promising next-generation TE generators. For instance, Thielen et al. estimated the theoretical optimal number of n-p legs pairs to be around 100 for efficient body heat harvesting.[41]

Although the actual measurement of the power generated by the alco-aerogel was a very interesting way to demonstrate the interest of such material in real TEGs, it lacked realism. Indeed, major issues in the community to develop efficient TEGs are due to the important contact resistances arising from the combination of ceramic, metallic contact and TE material. Moreover, the question of dissipating heat with efficient and cheap heat exchangers is very important. Overall, for a better demonstration of its promising properties, a prototype TE generator should be realized with the alco-aerogel as the p-type material. Unfortunately, in the given time of this thesis it was not possible to develop it.

6.3. STABILITY OF THE PCPS

For effective use of porous conductive polymers in TEGs, it is necessary to ensure their reliability over time. The stability of conjugated polymers such as PEDOT: PSS is one of the major challenges currently discussed in the literature. In this section, the evolution of electrical and thermal transport properties over time are discussed. These results are preliminary and have only been performed on a set of samples for 25 days, but they already show the trend of the PCPs' stability over time. In order to effectively discuss the evolution of the properties over time, the four most studied sample types in this thesis were followed: quenched cryogel, templated N_{2L} cryogel, sulf-aerogel and alco-aerogel.

The measurements were realized for 25 days, in the period of May to June (relative humidity > 60 %) The samples were left in closed vials (snap cap type) in the lab. We realized quickly that the mass of the sample increased with time, suggesting absorption of ambient moisture. The evolution of the density was followed by measuring the samples' dimensions and weights. The Seebeck coefficient could not be followed due to the brittleness of the copper legs attached to the sample for measurement. Hence, only the electrical and thermal conductivity were followed. Figure IV.10 illustrates the evolution of the density, moisture content, electrical and thermal conductivities upon time of the quenched and templated N_{2L} cryogels as well as the sulf- and alco-aerogels. The density, electrical conductivity, and thermal conductivity were represented relatively to their initial value (signified by the exponent "0"). From Figure IV.10, one can observe two different behaviors between the quenched and templated N_{2L} cryogels (macroporous samples) and the alco- and sulf-aerogels (mesoporous samples).

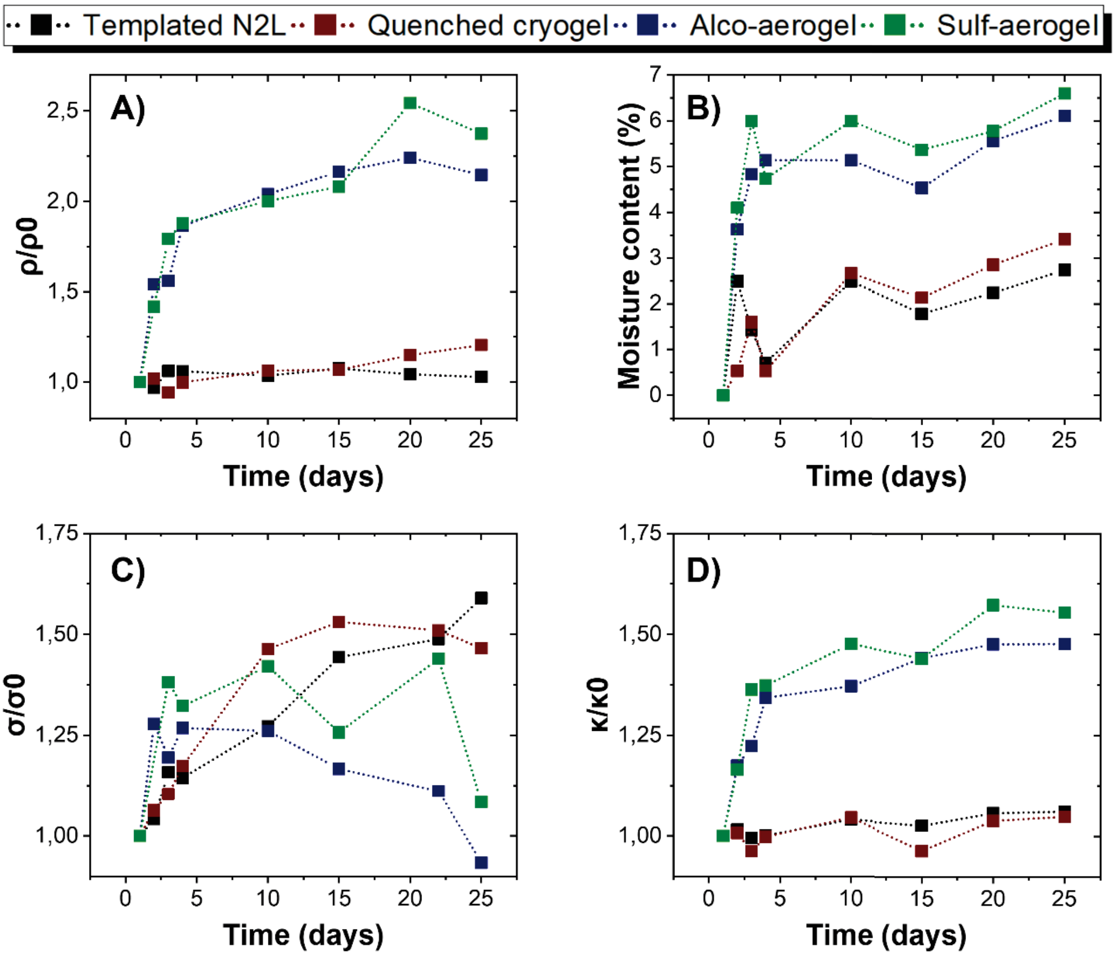

Figure IV.10: Evolution of physical and transport properties as a function of time for the most representative PCPs: A) Relative density, B) Moisture content, C) relative electrical conductivity and D) relative thermal conductivity.

The relative density evolved quite differently with time (see Figure IV.10.A) depending on the porous structure of the PCPs. Indeed, the density of the macroporous samples only slightly changed (up to 1.2 times for the quenched cryogel and only 1.03 times for the templated N_{2L} after 25 days of storage in air), while that of the two mesoporous samples increased more than twofold (up to 2.15 times for the alco-aerogel and 2.3 times for the sulf-aerogel). The density follows a one-phase exponential decay function with a time constant parameter (i.e., a fast increased followed by a plateau) for the mesoporous samples while it hardly changes for the macroporous ones. This can be explained by the difference of moisture adsorption for the macroporous samples and the mesoporous ones (see Figure IV.10.B). Interestingly, all the PCPs quickly adsorbed some moisture before reaching a saturation point, around 3% for the macroporous samples and 6% for the mesoporous ones (similar exponential decay observed for the density evolution of the mesoporous samples). The mesoporous samples (fibrillar network) have a higher specific surface area than the macroporous ones (channel-like structure), favoring water absorption. Moreover, as they adsorbed water, the mesoporous samples tend to shrink which was not the case for the macroporous samples. It looks like the porous structure of quenched and templated N_{2L} cryogels could handle adsorption of water with no modification. It is quite difficult to explain this behavior, but we suggest that it may be due to the different texture of the pore walls (dense stacking of fibers for the macroporous samples, fibrillar network for the mesoporous samples) and the fact that the pores are closed cells (for the macroporous samples). The different mechanical properties of the two types of structure are also probably at stake.

The charge transport properties also evolved with time but with no clear trend (see Figure IV.10.C). Interestingly, after 25 days, the electrical conductivity of the macroporous samples increased by 1.5 times while the one of the mesoporous samples slightly decreased. These two behaviors are quite contradictory. As discussed in sections II.4.2 and II.4.4, the electrical conductivity of porous materials is directly related to their density. Hence, with such an increase in density for the mesoporous materials, we were expecting an increase of the electrical conductivity. Conversely, as the density of the macroporous materials nearly changed, the electrical conductivity was not expected to increase upon time. For now, we are not able to explain such evolution. Overall, the electrical conductivity of the PCPs was not negatively impacted over time.

The evolution of the thermal conductivity is clearer, and the trend is similar to that of the density (see Figure IV.10.D). While the thermal conductivity of the macroporous samples hardly changed, the one of the mesoporous samples increased up to 1.5 times after 25 days of storage in air. As discussed in section II.4.3, κ_{solid}, is the predominant contribution to the thermal conductivity of our materials (depending on their density). Thus, it was expected that an increase in the density of the mesoporous samples would be accompanied by an increase in the thermal conductivity. This is also confirmed by the fact that the thermal conductivity of the macroporous samples almost did not change.

Overall, two different behaviors are to be noted regarding the stability of these PCPs. On the one hand, the mesoporous samples are very hygroscopic, and their thermal conductivity was highly impacted. After 25 days of storage at ambient temperature, pressure and humidity, the mesoporous materials were still electrically conducting but their initially interesting low thermal conductivity (54-65 mW/(m.K)), provided by their structure, was increased (to 90-100 mW/(m.K). On the other hand, water adsorption had a positive effect on the electrical conductivity of the macroporous materials while the density and thermal conductivity were hardly affected. This raises questions about the stability of alco-aerogels for actual use in TEGs. Even though their thermal conductivity increased, they remain the best candidates for use in TEGs. These are preliminary results but demonstrate important topics that should be studied if one wants to use PCPs in TEGs. Although it was not investigated in this thesis, the variation of electrical/thermal conductivity with moisture content could be used as an advantage to use PCPs as light-weight, low-cost humidity sensors.

7. CONCLUSION

In this chapter, we have developed a facile process to prepare alco-aerogels that exhibit competitive values compared to the literature. The improved charge transport properties of the alco-aerogels compared to sulf-aerogel were still not fully understood. A hypothesis would be a that the fibers (or fibrils) are better interconnected in the alco-aerogel network, resulting in a higher charge mobility. We demonstrated the production of homogeneous physical gels of PEDOT: PSS up to a few mm thickness with high reproducibility. Their 3D fibrillar network was highlighted by SEM images and confirmed by X-ray scattering measurements. Moreover, as shown by rheological studies, the solid network is robust and homogeneous throughout the sample. It was demonstrated by SEM images and modulus measurements that the 3D fibrillar mesoporous network is preserved in the dry state, despite a volume loss of 40% after drying. The high crystallinity of PEDOT: PSS alco-aerogels along the π-stacking direction was demonstrated by WAXS. The final alco-aerogels are ultralight, handleable and mechanically robust. Regarding the functional properties, the electrical conductivity and Seebeck coefficient were studied extensively. They exhibit the best charge transport properties amongst the PCPs produced in this PhD work thanks to nanostructuring. Moreover, implementing porosity successfully reduced their thermal conductivity down to 0.065 W/(m.K) resulting in the promising ZT of 3.1 x 10^{-3} at 300K. After 25 days of stability study, the alco-aerogels' thermal conductivity slightly increased but they still show great promise for energy harvesting applications. The high power output of the p-type material was demonstrated, the next step would be the development of its n-type counterpart and the production of a real TEG.

8. REFERENCES

[1] S. Han, F. Jiao, Z. U. Khan, J. Edberg, S. Fabiano, X. Crispin, *Adv. Funct. Mater.* **2017**, *27*, 1703549.

[2] X. Zhang, D. Chang, J. Liu, Y. Luo, *J. Mater. Chem.* **2010**, *20*, 5080.

[3] R. Maeda, H. Kawakami, Y. Shinohara, I. Kanazawa, M. Mitsuishi, *Mater. Lett.* **2019**, *251*, 169.

[4] R. Maeda, Y. Shinohara, H. Kawakami, Y. Isoda, I. Kanazawa, M. Mitsuishi, *Nanotechnology* **2020**, *32*, 135403.

[5] Q. Weinbach, S. V. Thakkar, A. Carvalho, G. Chaplais, J. Combet, D. Constantin, N. Stein, D. Collin, L. Biniek, *Front. Electron. Mater.* **2022**, *2*, 875856.

[6] "Dielectric Constant – Flowline Liquid & Solid Level Sensors, Switches & Controllers," can be found under https://www.flowline.com/dielectric-constant/, **n.d.**

[7] J. Y. Kim, J. H. Jung, D. E. Lee, J. Joo, *Synth. Met.* **2002**, *126*, 311.

[8] D. Alemu, H. Y. Wei, K. C. Ho, C. W. Chu, *Energy Environ. Sci.* **2012**, *5*, 9662.

[9] U. Lang, E. Muller, N. Naujoks, J. Dual, *Adv. Funct. Mater.* **2009**, *19*, 1215.

[10] D. Alemu, H. Y. Wei, K. C. Ho, C. W. Chu, *Energy Environ. Sci.* **2012**, *5*, 9662.

[11] J. Rivnay, S. Inal, B. A. Collins, M. Sessolo, E. Stavrinidou, X. Strakosas, C. Tassone, D. M. Delongchamp, G. G. Malliaras, *Nat. Commun.* **2016**, *7*, DOI 10.1038/ncomms11287.

[12] T. Takano, H. Masunaga, A. Fujiwara, H. Okuzaki, T. Sasaki, *Macromolecules* **2012**, *45*, 3859.

[13] G. Zotti, S. Zecchin, G. Schiavon, F. Louwet, L. Groenendaal, X. Crispin, W. Osikowicz, W. Salaneck, M. Fahlman, *Macromolecules* **2003**, *36*, 3337.

[14] Z. U. Khan, O. Bubnova, M. J. Jafari, R. Brooke, X. Liu, R. Gabrielsson, T. Ederth, D. R. Evans, J. W. Andreasen, M. Fahlman, X. Crispin, *J. Mater. Chem. C* **2015**, *3*, 10616.

[15] J. Dubochet, M. Adrian, J.-J. Chang, J.-C. Homo, J. Lepault, A. McDowall, P. Schultz, *Q. Rev. Biophys.* **1988**, *21*, 129.

[16] C. Efthymiou, M. A. K. Williams, K. M. McGrath, *Food Hydrocoll.* **2017**, *73*, 203.

[17] E. Hosseini, V. Ozhukil Kollath, K. Karan, *J. Mater. Chem. C* **2020**, *8*, 3982.

[18] B. Yao, H. Wang, Q. Zhou, M. Wu, M. Zhang, C. Li, G. Shi, *Adv. Mater.* **2017**, *29*, 1700974.

[19] D. Collin, P. Lavalle, J. M. Garza, J. C. Voegel, P. Schaaf, P. Martinoty, *Macromolecules* **2004**, *37*, 10195.

[20] V. R. Feig, H. Tran, M. Lee, Z. Bao, *Nat. Commun.* **2018**, *9*, 1.

[21] M. Rubinstein, R. H. Colby, *Thermodynamics of Mixing*, Oxford University Press, Oxford, **2003**.

[22] J. Rouquerol, P. Llewellyn, F. Rouquerol, *Stud. Surf. Sci. Catal.* **2007**, *160*, 49.

[23] K. S. Walton, R. Q. Snurr, *J. Am. Chem. Soc.* **2007**, *129*, 8552.

[24] M. Thommes, K. Kaneko, A. V. Neimark, J. P. Olivier, F. Rodriguez-Reinoso, J. Rouquerol, K. S. W. Sing, *Pure Appl. Chem.* **2015**, *87*, 1051.

[25] K. A. Cychosz, M. Thommes, *Engineering* **2018**, *4*, 559.

[26] N. Kim, B. H. Lee, D. Choi, G. Kim, H. Kim, J. R. Kim, J. Lee, Y. H. Kahng, K. Lee, *Phys. Rev. Lett.* **2012**, *109*, DOI 10.1103/PhysRevLett.109.106405.

[27] N. Massonnet, A. Carella, A. De Geyer, J. Faure-Vincent, J. P. Simonato, *Chem. Sci.* **2014**, *6*, 412.

[28] F. G. Cuevas, J. M. Montes, J. Cintas, P. Urban, *J. Porous Mater.* **2009**, *16*, 675.

[29] P. S. Liu, T. F. Li, C. Fu, *Mater. Sci. Eng. A* **1999**, *268*, 208.

[30] K. P. Dharmasena, H. N. G. Wadley, *J. Mater. Res.* **2002**, *17*, 625.

[31] R. Goodall, L. Weber, A. Mortensen, *J. Appl. Phys.* **2006**, *100*, 44912.

[32] M. F. Ashby, A. G. Evans, N. . Fleck, L. J. Gibson, J. . Hutchinson, H. N. G. Wadley, *Metal Foams : A Design Guide*, Butterworth-Heineman, Boston, **2000**.

[33] R. Kroon, J. D. Ryan, D. Kiefer, L. Yu, J. Hynynen, E. Olsson, C. Müller, *Adv. Funct. Mater.* **2017**, *27*, 1704183.

[34] D. Scheunemann, M. Kemerink, *Phys. Rev. B* **2020**, *101*, 75206.

[35] M. P. Gordon, E. W. Zaia, P. Zhou, B. Russ, N. E. Coates, A. Sahu, J. J. Urban, *J. Appl. Polym. Sci.* **2017**, *134*, 44070.

[36] N. Yanagishima, S. Kanehashi, H. Saito, K. Ogino, T. Shimomura, *Polymer (Guildf).* **2020**, *206*, 122912.

[37] X. Wang, P. Liu, Q. Jiang, W. Zhou, J. Xu, J. Liu, Y. Jia, X. Duan, Y. Liu, Y. Du, F. Jiang, *ACS Appl. Mater. Interfaces* **2019**, *11*, 2408.

[38] E. Jin Bae, Y. Hun Kang, K. S. Jang, S. Yun Cho, *Nat. Sci. Reports* **2016**, *6*, DOI 10.1038/srep18805.

[39] M. Culebras, C. M. Gómez, A. Cantarero, *Materials (Basel).* **2014**, *6*, 6701.

[40] V. Leonov, *IEEE Sens. J.* **2013**, *13*, 2284.

[41] M. Thielen, L. Sigrist, M. Magno, C. Hierold, L. Benini, *Energy Convers. Manag.* **2017**, *131*, 44.

[42] G. J. Snyder, in *Energy Harvest. Technol.*, **2009**, pp. 325–335.

[43] “Seiko - La montre Kinetic - - WorldTempus,” can be found under https://fr.worldtempus.com/article/seiko-la-montre-kinetic-14518.html, **n.d.**

[44] D. M. Rowe, in *CRC Handb. Thermoelectr.* (Ed.: D.M. Rowe), CRC Press, **1995**.

CONCLUSION AND PERSPECTIVES

CONCLUSION AND PERSPECTIVES

Organic conducting materials show promising properties for energy harvesting applications. Indeed, their low operating temperature range, as well as their abundance and ease of implementation make them good complements to their inorganic counterparts. Considering the recent work of Scheunemann et al., one of the leitmotifs of our work was to decrease $\kappa_{lattice}$ below 0.2 W/(m.K). In this PhD work, we focused on developing bulk-size materials with low lattice thermal conductivity ($\kappa_{lattice}$) by implementing porosity in organic TE materials. Designing large, low-cost materials to facilitate their integration into vertical TEGs was also an objective of this PhD work. Given the material specifications, we focused on designing porous conducting polymers (PCPs). Since this particular architecture is quite different from the majority of conducting polymers developed for TEGs, we also focused on understanding the structure-property relationships of these new materials. As a starting point, we chose to use the commercial dispersion of PEDOT: PSS, PH1000 to produce p-type PCPs. Amongst the different ways to design porous organic materials, we chose to first, form a polymer gel. Then, its solvent was removed by several drying techniques, resulting in various porous structures.

Since it is our starting point, we studied the structural characteristics of the PEDOT: PSS commercial dispersion. Contrary to other reports stating that the dispersion consists of spherical particles, we revealed the presence of long fibrils a few nm thick. The structural features of the fibrils were studied by transmission electron microscopy and X-ray scattering techniques. We suggest that PEDOT: PSS fibrils tend to arrange themselves in a core-shell system (PEDOT-rich core, PSS-rich shell). Within the fibrils, at a molecular scale, it is difficult to determine precisely how the molecules assemble. Despite the numerous publications using PEDOT: PSS, this work is one of the first to challenge the initial structure of the PEDOT: PSS system in its commercial dispersion state through a combination of cryo-electron microscopy and X-ray scattering.

Next, we successfully developed two gelation processes via the addition of H_2SO_4 or ethanol. The two gels produced (hydrogel for the H_2SO_4 process and alcogel for the ethanol process) were tunable in shape and size. We followed the gelation mechanism by several structural and spectroscopic techniques. We demonstrated by UV-vis and XPS spectroscopy, the partial removal of excess PSS chains during gelation. Interestingly, the final amount of PSS was lower in the alcogel than in the hydrogel. In addition, FTIR spectroscopy showed that the gelation step favored the quinoid conformation of PEDOT molecules more in the alcogel than in the hydrogel. The spectroscopic study of the gels gave indications of the likely different doping state between the hydrogel and the alcogel. Although they appear to be slightly different on a molecular scale, the structural characteristics of the two gels are quite similar. They both exhibit a fibrillar mesoporous structure with fibers ~ 10 nm thick. We were able to demonstrate by TEM that the addition of sulfuric acid to the initial dispersion tends to modify the fibril structure (reduced thickness and increased length). The reduction in their size correlates well with the partial loss of excess PSS chains. We were able to confirm the structural characteristics of the fibrils in the hydrogel and alcogel states by SAXS. Although it is difficult to state with certainty the mechanism of gel formation, we suggest the following. I) First, the initial fibrillar dispersion interacts with either sulfuric acid or ethanol. In both cases, the coulombic interactions between PEDOT and some PSS (weakly bound to PEDOT molecules and/or free in the dispersion) are somehow reduced. As a result, there is a partial removal of some PSS chains. II) As the electrostatic repulsions of the dispersion are reduced, the fibrils tend to move closer to each other. III) Three to five fibrils become entangled to form thicker fibers. Finally, a robust network is formed by VdW and π-stacking interactions. We could even demonstrate the physical nature of the nodes of the alcogel networks by rheological studies.

Then we applied three different drying techniques to the hydrogel and one to the alcogel. Figure C.1 illustrates the different routes used to produce the (air-dried) xerogels, the (supercritical dried) sulf-aerogels and alco-aerogels, and the (freeze-dried) quenched and templated cryogels. From the same gel, we successfully achieved to produce three different structures with various ranges of porosities.

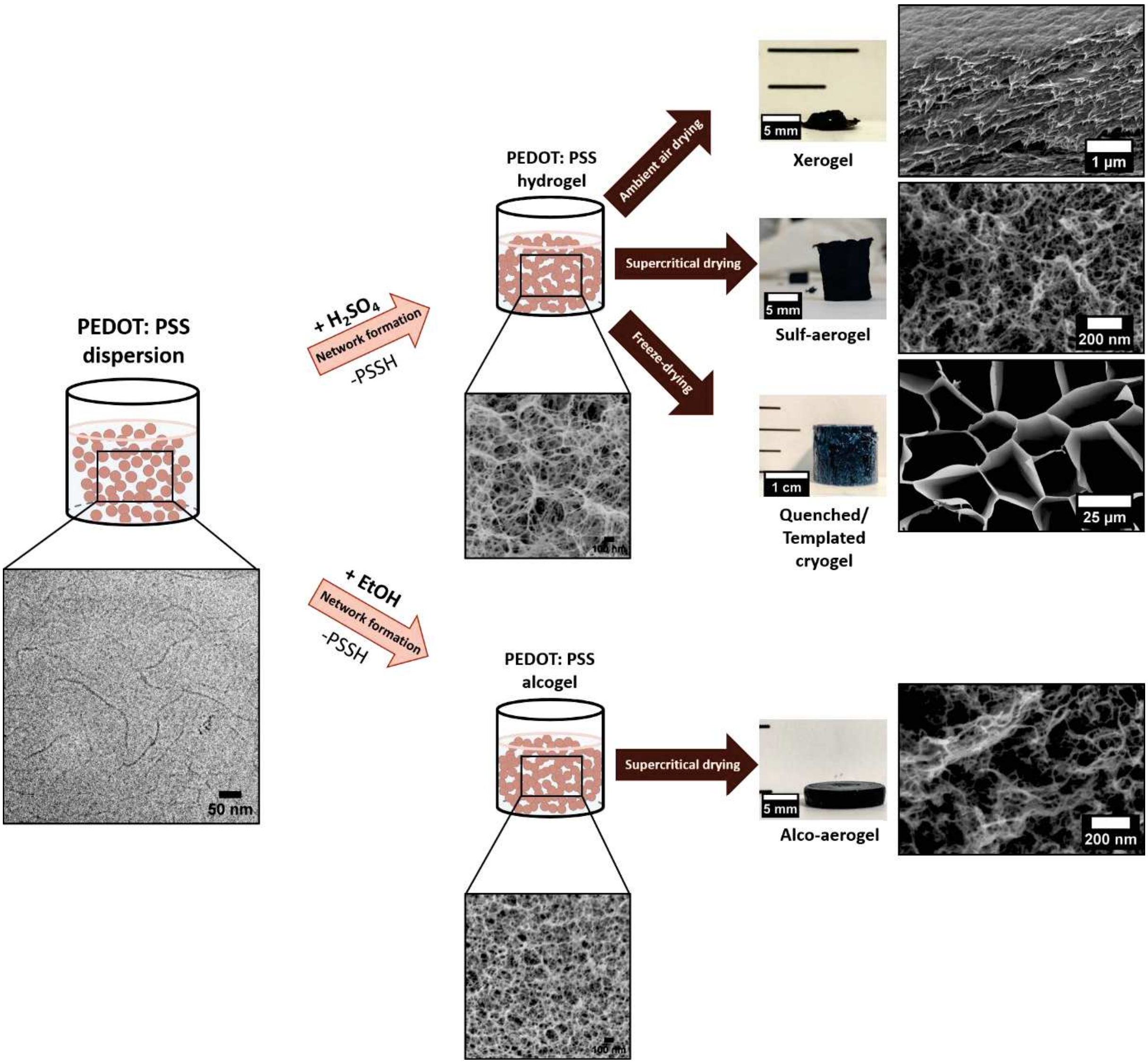

Figure C.1: Schematic overview of the elaboration routes of the hydro- and alcogel followed by their drying steps. Ambient air drying gave rise to the shrunk xerogels, supercritical drying resulted in either sulf-aerogel or alco-aerogel depending on the initial gel, freeze-drying the hydrogel resulted in either quenched (for the quench freezing method) or templated (for the unidirectional freezing method) cryogels.

Air drying of the hydrogel under ambient pressure and temperature conditions resulted in important shrinkage of the sample. The sheet-like structure of the xerogel does not resemble that of the original hydrogel. Although its density is lower than that of pure PEDOT: PSS (suggesting some porosity), it has not been studied further. Conversely, we developed a supercritical drying method, in which the solvent in the gel was replaced by CO_2 which could go from the liquid to the gas phase without phase transition. Thus, by finely optimizing the drying parameters, we were able to produce sulf- and alco-aerogels (depending on the dried gel) whose mesoporous fibrillar structure was identical to that of the native gel. Their structural characteristics were studied by electron microscopy and X-ray scattering. We could confirm the presence of small 1D objects by SAXS intensity profile analysis. As discussed above, during network formation, the fibrils entangle to form thicker fibers composing the coherent and robust gel. Interestingly, we were able to finely analyze the intensity profile of the sulf- and alco-aerogels at a mid- and wide-angle. They show fine and numerous peaks, suggesting some crystalline order. Based on the reported DFT calculations, molecular dynamics simulation, and X-ray models, we expect that within the fibrils, the PEDOT: PSS system tends to arrange itself into a lamellar structure. The π-π stacks of PEDOT oligomers are expected to be distributed along the PSS chains and separated by PSS chains, resulting in alternating PEDOT and PSS molecules. Based on the structural analyses of hydrogels, alcogels, sulf-aerogels, and alco-aerogels, we propose the possible structural arrangement of PEDOT and PSS in a fibril (in the case of the material showing more crystalline order, i.e., in sulf-aerogel or alco-aerogel) shown in Figure C.2.

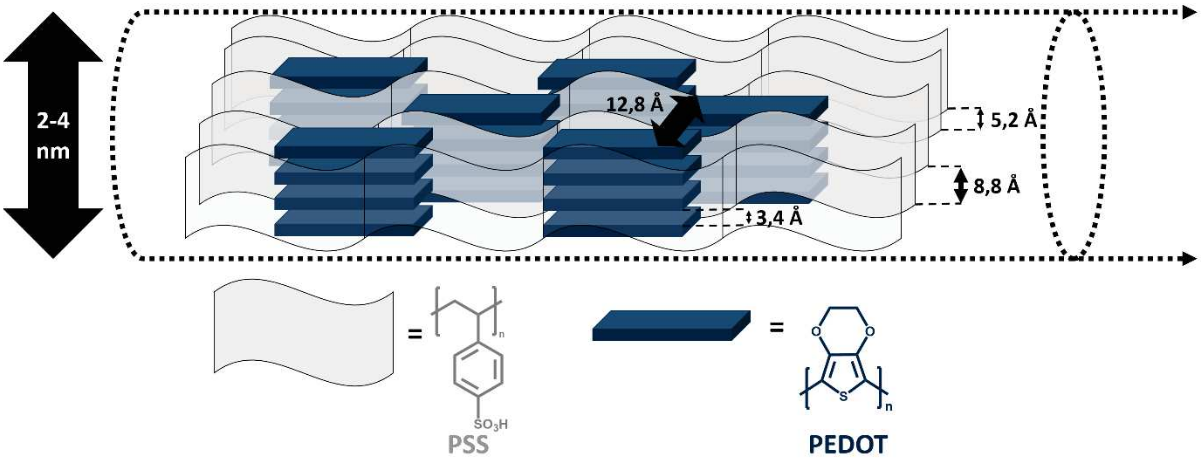

Figure C.2: Proposition of a structural arrangement of PEDOT and PSS within the fibrils. PSS molecules (in gray) arrange in a lamellar morphology, alternating with PEDOT (in blue) stacked along the π-stacking direction. We measured on the WAXS profile (see Annex I) the typical PEDOT and PSS π-stacking distances to be 3.4 Å and 5.2 Å, respectively. We suggest that the distances at 8.8 Å and 12.8 Å to be the typical PSS to PSS and PEDOT to PEDOT lamella distances, respectively. Based on the anisotropy of the diffusion in the mid-angle range (discussed in chapter III) we suggest that the peak around 27-30 Å (which correlates well with the thickness of a fibril, measured either by TEM or SAXS analysis) corresponds to the typical thickness of a fibril.

Thanks to their high crystalline order, the sulf- and alco-aerogel exhibit the best charge transport properties amongst the PCPs produced in this PhD work. Interestingly (and despite their very similar structural and molecular features), the alco-aerogel (σ = 21 S/cm, S = 18 µV/K) exhibited higher charge transport properties than the sulf-aerogel (σ = 9 S/cm, S = 16.8 µV/K). Further studies must be performed to conclude on these differences but it probably arises during the gelation step.

The cryogels exhibited the lowest charge transport properties but also the lower thermal conductivity (quenched cryogel: σ = 2 S/cm, S = 19 µV/K, κ = 0.042 W/(m.K); templated N_{2L} cryogel: σ = 1.3 S/cm, S = 20 µV/K, κ = 0.037 W/(m.K)). This is due to their very low density and particular macroporous structure. We investigated in detail the formation of these pores, very different from the initial hydrogel structure.

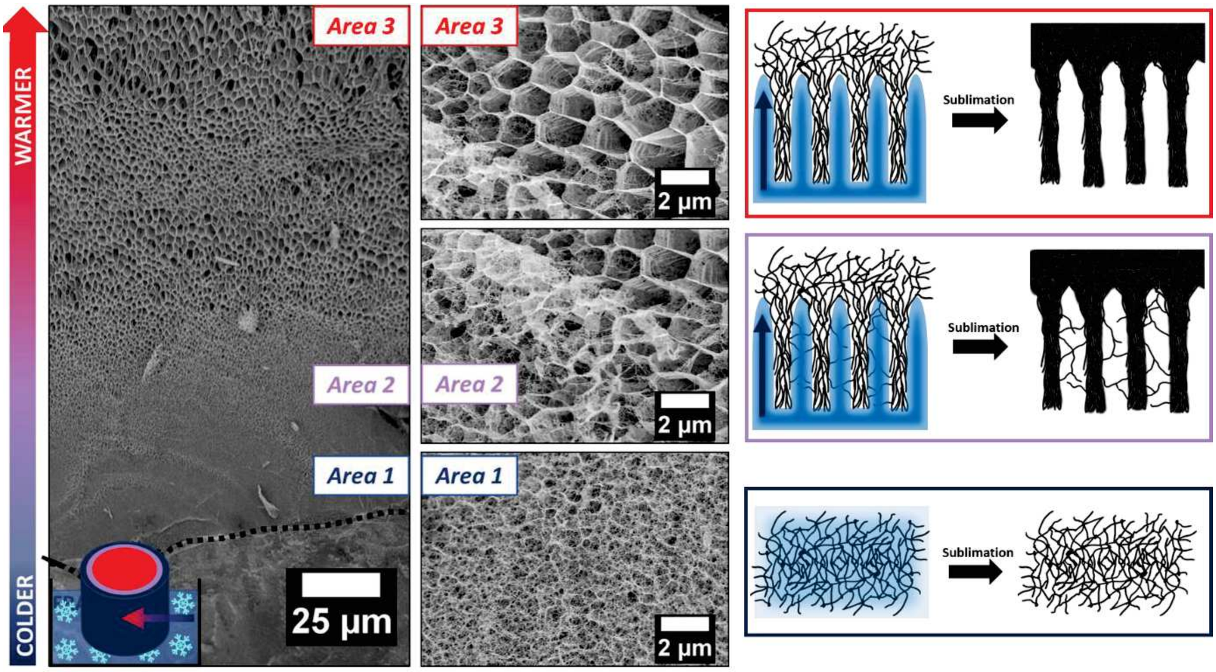

Figure C.3: Schematic of the mechanism of formation of the honeycomb-like microporous structure. In area 1, the gel's structure was frozen very fast, hence the ice retaining the structure is amorphous and well conserve the original fibrillar structure. In area 2, the freezing rate was slightly higher and some ice crystals begin to form, destroying the mesoporous network of the gel. After sublimating the sample, we can observe pores that are the inverse replica of the ice crystals. In area 3, the ice crystals could completely grow, pushing aside the fibers into compact segregated areas (i.e., the pore walls), leaving faceted cavities after the sublimation of ice.

Investigation of the formation of these pores through ice crystal formation (see Figure C.3) demonstrated that control of the freezing step (and thus ice crystal growth) could be of interest in tuning the pore structure of cryogels. We developed a unidirectional freezing method and demonstrated that we were able to completely orient the channel-liked pores along the thickness of cm-sized gels. Using X-ray scattering analysis, we were even able to demonstrate that the orientation of the pores, also induced the orientation of objects (fibers of the initial gel network) within the pore walls. Only preliminary studies have been performed, but it is very likely that the transport properties (electrical and thermal) of this material may be anisotropic. Finally, by controlling the freezing rate, we were able to tune the size of the ice crystals that grow in the gel network. We were able to adjust the pore size from 50 to 250 µm while maintaining their orientation in the freezing direction. Overall, the templated cryogels exhibited very low thermal (and electrical) conductivities. Interestingly, we were able to control these transport properties by adjusting the pore size. With smaller pores, the highest electrical conductivity (1.3 S/cm) and lowest thermal conductivity (0.037 W/(m.K)) were obtained for the templated N_{2L} cryogel. We suggest that the low thermal conductivity is due to phonon scattering effects inside the pore walls due to the orientation of the fibers inside them. The evolution of electrical conductivity was more difficult to attribute but we suggested that it was due to increased morphological disorder in the pore walls as the pore (and pore wall) size increases.

Overall, we observed a change in TE properties between the different PCPs. At low densities, both electrical and thermal conductivities were low. Interestingly, even for the most conducting material (alco-aerogel), the implementation of porosity in the TE materials reduced drastically the thermal conductivity of the PCPs. To further demonstrate the impact of porosity, we can estimate the contribution of the lattice on the thermal conductivity. Although it has been reported that the Lorentz number can take different values depending on the energetic disorder of a material, we assume that all of our PCPs are broadly similar (with respect to charge transport). We therefore calculated κ_{elec} with the Wiedemann-Franz law (taking L at the Sommerfeld value) to deduce $\kappa_{lattice}$. Figure C.4 shows the evolution of the lattice and electronic contributions to the thermal conductivity as a function of density. As expected, κ_{elec} is almost negligible for all samples, it only increases slightly for the most conductive PCP (i.e., alco-aerogel). More interestingly, the implementation of porosity reduced the lattice contribution to thermal conductivity well below 0.2 W/(m.K) for all PCPs produced.

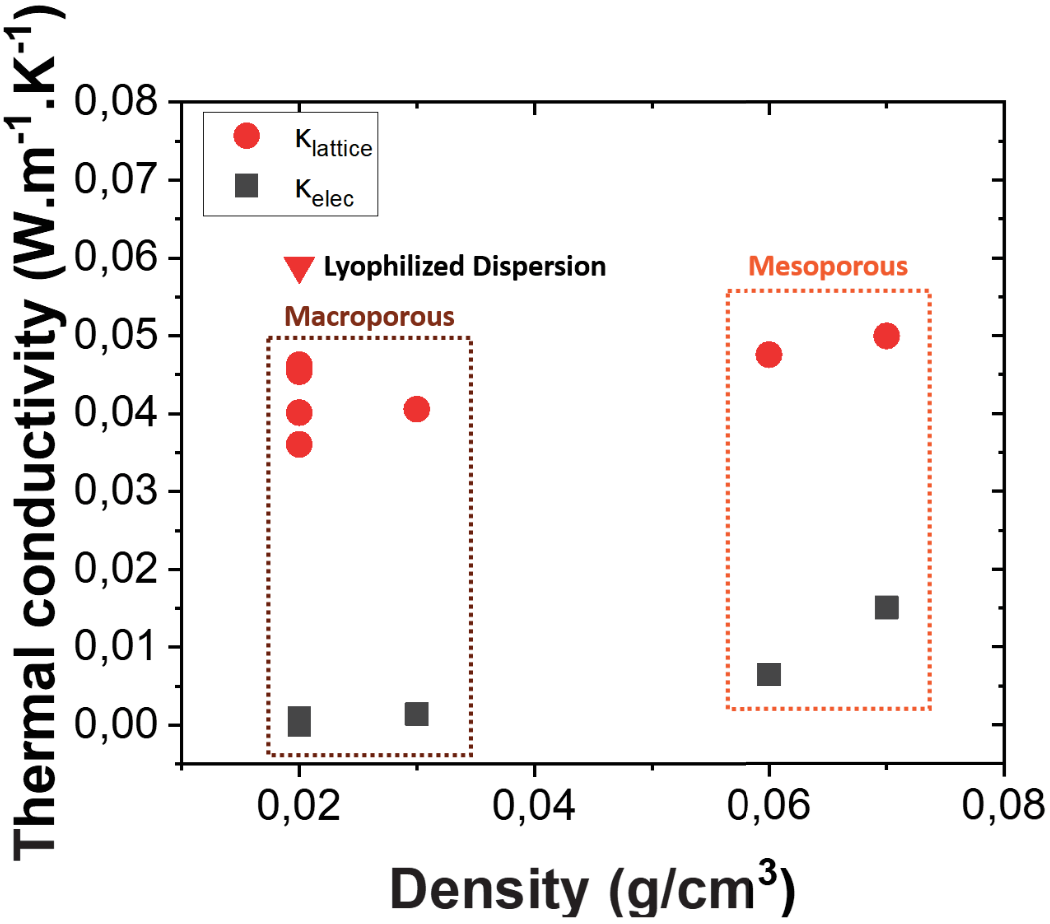

Figure C.4: Evolution of the lattice and electronic contributions to the thermal conductivity as a function of the density.

In this PhD work, we demonstrated the interest of implementing porosity in organic TE materials. Their lattice thermal conductivity was reduced below 0.2 W/(m.K) and their electrical conductivity remained above 1 S/cm. The gelation and solvent removal route enabled the design and development of large porous materials at a fairly low cost (~ 2€ raw material for cm-sized PCPs). Although these are only preliminary results, we have begun to investigate the air stability of these materials. Over twenty-five days, the sulf- and alco-aerogels suffered from a slight increase in thermal conductivity. Conversely, the templated and quenched N_{2L} cryogels showed better stability. Finally, we even demonstrated the potential use of porous organic materials in actual vertical TEGs by measuring their power output. The alco-aerogel exhibited a power output of 2.5 µW/cm² for a temperature gradient of 36.5 K. Such heat-to-electricity conversion holds great promise for powering low-power devices in the future.

For now, the main drawback of these porous materials is their poor charge transport properties. Although DMSO vapor treatment was used and successfully increased the electrical conductivity of sulf-aerogel and quenched cryogel to ~ 90 S/cm and ~ 20 S/cm, these were only preliminary studies. In addition, we do not currently know the effect of such treatment on the thermal conductivity. Therefore, in the future, attention should be focused on developing and improving techniques to increase the charge transport properties of these PCPs while maintaining a low lattice thermal conductivity. One strategy could be the use of reducing agents such as TDAE to increase the Seebeck coefficient of porous PEDOT: PSS materials. Tuning (and slightly increasing) the density (and thus reducing the porosity) of PCPs, could also be a solution to increase the charge transport properties. However, as demonstrated in this work, attention must be paid to the thermal conductivity which might increase as well.

To further confirm the interest of PCPs in vertical TEGs, developing prototypes of generators should be the next step. One must pay attention to the dimension of the material, the generator in itself, and the contact electrical resistance. Air stability studies should also be pursued if one wants to use this material in body heat harvesters in the future. The fact that we observed moisture absorption (and the evolution of the electrical and thermal conductivities accordingly) on PCPs could also be leveraged. Indeed, one could imagine another application for these materials as moisture sensors.

Finally, now that the method and mechanisms of formation of porous organic materials from gels have been studied on PEDOT: PSS, other conducting polymers should be used. For instance, poly(3-hexylthiophene) (P3HT) already showed promising results. Our team successfully developed process to form robust P3HT gels. First trials on their drying by the supercritical drying technique are encouraging. Developing porous materials from such undoped organic semiconductors opens new doors on the fine-tune of their charge transport properties via doping. To go further, n-type porous materials should also be developed in order to produce “all porous” TEGs. Usually, n-type organic materials suffer a lot from poor air stability. Our team already performed some trials on the development of n-type materials mixed in a porous matrix. Poly(Ni-ett) (n-type metal coordination polymers) particles were dispersed in porous organic aerogels and exhibited interesting charge transport properties as well as low thermal conductivity. During this thesis, a similar method was tried using fullerene derivatives. Although the first trials were promising, the development of such material requires a lot of optimization on the percolation of the fullerenes as well as their doping.

Overall, thanks to their low thermal conductivity, PCPs demonstrated that they are very promising materials for the future of organic thermoelectric but there is still plenty of room for the improvement of their charge transport properties.

EXPERIMENTAL SECTION

1. MATERIALS.

All materials were obtained from commercial suppliers and used as received, unless otherwise stated.

PEDOT:PSS (Clevios^{TM} PH1000, 1.0-1.2 wt.%) was purchased from Heraeus.

Absolute ethanol and isopropanol were obtained from Carlo ERBA, sulfuric acid (≥ 95%) from Fisher Scientific.

Silver paste was purchased from Agar Scientific (AGG3691), liquid CO_2 and liquid ethane from Air Liquide.

Potassium bromide and poly(sodium 4-styrenesulfonate) (NaPSS, Mw = 1000 000) were purchased from Sigma-Aldrich

2. SAMPLE PREPARATION

2.1. HYDROGEL FABRICATION

The exact weight percentage of PH1000 dispersion was measured by evaporating 10 mL of the dispersion on a hot plate (100°C) for 2H and weighting the remaining solid. For both batches used in this work, the weight percentage of PEDOT:PSS in water was 1.08%. PEDOT:PSS gelation process was adapted from Yao et al. work.[1] The method is based on acidification of the dispersion with H_2SO_4 and can be described as follows. First, the PEDOT:PSS dispersion was vortexed for a few minutes and filtered through a PVDF 0.45µm membrane to insure homogeneous dispersion. A given volume was then introduced in a flat bottom Pyrex tube (SVL screwcap) and treated with 0.1 mol/L of sulfuric acid. (e.g., 66µL of 3 mol/L H_2SO_4 for 2 mL of filtered PH1000). The mixture was immediately placed in a 90 °C oil bath for 3 to 30 hours depending on the total volume of the dispersion (2 to 10 mL, respectively). The hydrogel, while forming, kept the shape of the mold (in our case flat bottom cylindrical tube of 22 mm inner diameter gives rise to cylindrical gel of ~16 mm diameter). The resulting sample was shrunk and floated in a transparent supernatant. The supernatant was removed after gelation, and the gel was washed with fresh deionized water with a volume equal to the volume of PEDOT:PSS used to form the gel. The water was replaced again after 24 h (RW2) and left for another 24 h before replacement (RW3).

2.2. ALCOGEL FABRICATION

Based on the work of Maeda et al.,[2,3] the alcogels were formed by slow diffusion of ethanol into the PEDOT:PSS. Typically, the PH1000 dispersion was vortexed for a few minutes and then filtered through a 0.45 µm PVDF membrane to ensure homogeneous dispersion prior to use. Next, 41.5 mL of ethanol were introduced in a flat bottom Pyrex tube with an SVL screwcap. Then 5 mL of the filtered PEDOT:PSS dispersion were slowly deposited at the bottom of the vial with a syringe. Then, the mixture was immediately placed in a 90°C oil bath for 20 hours. The alcogel, while forming, took the shape of the mold (in this case, a flat bottom cylindrical tube of 25 mm inner diameter gave rise to a gel in the shape of a disc of ~15 mm diameter). The resulting sample was shrunk and floated in a transparent supernatant. The supernatant was removed after gelation, and the gel was washed twice with 50 mL of fresh ethanol (i.e., placed in fresh ethanol, let sit and change after 24 H).

3. XEROGEL FORMATION

Xerogels were obtained by letting the wet hydrogel or alcogel on a dish plate for a certain amount of time. The drying was done at ambient pressure and temperature or at higher temperatures by placing the dish plate on a hot plate. The obtained xerogel was very shrunk and a razor blade was necessary to unstick it from the dish plate.

4. CRYOGEL FORMATION

In both methods, prior to freeze, the samples were cut at bottom and top interfaces (~0.5 mm thickness removal at both interfaces) with a razor blade to flatten both surfaces.

4.1. QUENCHED FREEZING METHOD (QUENCHED CRYOGEL).

To obtain a quenched cryogel, a wet hydrogel was placed in a flat bottom SVL Pyrex tube. The tube was quickly dived into liquid nitrogen (N_{2L}) bath and let for 10 min to allow complete freezing of the sample. Then, the tube was placed inside a homemade airtight stainless-steel container precooled down at -15°C in an open cooling bath circulator (18226 Bioblock Scientific cryostat). The sublimation of water took place under vacuum (10^{-2} mbar) at -15 °C for 48h. After complete drying, the container was left to stabilize at ambient temperature and filled with Argon to avoid the obtained cryogel absorbing moisture.

4.2. ICE-TEMPLATING METHOD (TEMPLATED CRYOGEL).

To obtain a templated cryogel, a wet hydrogel was placed inside a homemade PTFE cylinder (4 mm wall thickness, inner diameter just equal to the diameter of the wet gel). The top and bottom surfaces of the gel were left uncovered. The PTFE cylinder plays the dual role of thermal insulator from the sample's sides and of mechanical reinforcement of the gel minimizing collapse. The gel surrounded by the PTFE ring was placed on top of a 6 cm height aluminum rod and quickly dived into a cold bath. Different freezing baths were used. We used liquid nitrogen (-196 °C), a mixture of ethanol and liquid nitrogen (-114°C), isopropanol and dry ice (-77 °C), and cooled isopropanol thanks to a chiller (-30°C). Temperature decrease over time was followed by placing a thermocouple on top of the gel, providing a freezing rate. After a determined amount of time depending on the bath temperature and the height of the gel, the gel was completely frozen (e.g., ~ 10 min for a 10 mm sample using N_{2L} bath). The frozen gel, still surrounded with the PTFE cylinder was placed in the stainless-steel container under 10^{-2} mbar vacuum at -15°C for 48h. After complete water sublimation, the container was left to stabilize at ambient temperature and filled with argon.

5. AEROGEL FORMATION

Sulf-aerogel and alco-aerogel are defined as aerogels obtained from a gel formed with H_2SO_4 or ethanol, respectively. For the sulf-aerogel, a solvent exchange was needed before drying as the water in the gel is not soluble with liquid CO_2. Every 24H, the gel was placed in 50 mL of water/ethanol mixture with increasing ethanol concentration (75/25, 50/50, 25/75, 0/100).

Prior to drying, the upper surface of the sample was cut off (~0.5 mm thickness removal) with a razor blade to obtain a flat surface. The gel was loaded with a splash of EtOH into a 100 mL capacity autoclave (manufactured by SFT-110 supercritical fluid extractor) which was then sealed. To ensure that CO_2 was first in the liquid phase (4°C, 750 psi in the bottle), the temperature in the autoclave was maintained at 20°C and the pressure raised to 1200 psi. The gel in the autoclave was stored in liquid CO_2 for 30 minutes and then the liquid CO_2 inside the autoclave was half-drained and flushed in with a fresh one. This solvent exchange was repeated five times in 30-minute intervals to completely replace EtOH with liquid CO_2 in the gel. After the solvent exchange was complete, the autoclave at 1200 psi was heated up to 45°C for 2 h, to induce the transition of the CO_2 from the liquid to the supercritical phase. Then, the outlet valve was slightly opened to create a dynamic flow inside the autoclave, allowing supercritical CO_2 to flow through the gel. The sample was kept under these conditions (45°C and 1200 psi) for 1 h, followed by a slow release of the pressure while keeping the temperature constant. After complete venting (approx. 30 min), the sample was transferred to a vial and degassed for a few minutes, after which the vacuum was switched to argon atmosphere for storage.

6. LYOPHILIZED DISPERSION

Prior to drying, the stock PH1000 dispersion was vortexed and filtered through a 0.45µm PTFE filter. Then, the PEDOT: PSS dispersion was placed in a flat bottom SVL Pyrex tube. The tube was quickly dived into liquid nitrogen (N_{2L}) bath and let for 10 min to allow complete freezing of the sample. Then, the tube was placed inside a homemade airtight stainless-steel container precooled down at -15°C in an open cooling bath circulator (18226 Bioblock Scientific cryostat). The sublimation of water took place under vacuum (10^{-2} mbar) at -15 °C for 48h.

6.1. FREE-STANDING REFERENCE FILMS

6.1.1. REFERENCE FILM FOR H_2SO_4 GELATION

Prior to use, the stock PH1000 dispersion was vortexed and filtered through a 0.45µm PTFE filter. Two milliliters of PEDOT: PSS dispersion were mixed with 66µL of 3 mol/L H_2SO_4 and instantly poured in a crystallizing dish. The drop-casted solution was then left to dry on a hot plate at 100 °C for 30 min. Once dried, the film was removed from the dish with the use of a razor blade. The free-standing films were rinsed with distilled water and left in 100 mL of distilled water for 2h. Finally, the rinsed films were dried on a hot plate at 100 °C. The thickness of ~ 7 µm was determined by SEM.

6.1.2. REFERENCE FILM FOR ETHANOL GELATION

Prior to use, the stock PH1000 dispersion was vortexed and filtered through a 0.45µm PTFE filter. 2 mL of ethanol were introduced in a flat bottom Pyrex tube with an SVL screwcap and 250 µL of the filtered PEDOT:PSS dispersion were slowly deposited at the bottom of the vial with a syringe. The mixture was placed at 90°C for 1 h. The supernatant was removed after gelation, and the thin gel was washed twice with 50 mL of fresh ethanol (i.e., placed in fresh ethanol, let sit and change after 24 H). The gel was left to dry at ambient T,P conditions for 1 H. The thickness of ~ 10 µm was determined by SEM.

7. DMSO VAPOR TREATMENT

As shown in Figure Exp.1, a closed vessel was filled with glass beads and DMSO. The closed system was preheated on a hot plate at 150°C. PCPs were placed on a glass slide put on the glass beads to avoid direct contact of DMSO with PCPs. Each DMSO vapor exposure time was performed at 150°C, on a single sample. Then, the samples were dried in a vacuum oven at 150 °C to remove any DMSO present in the material.

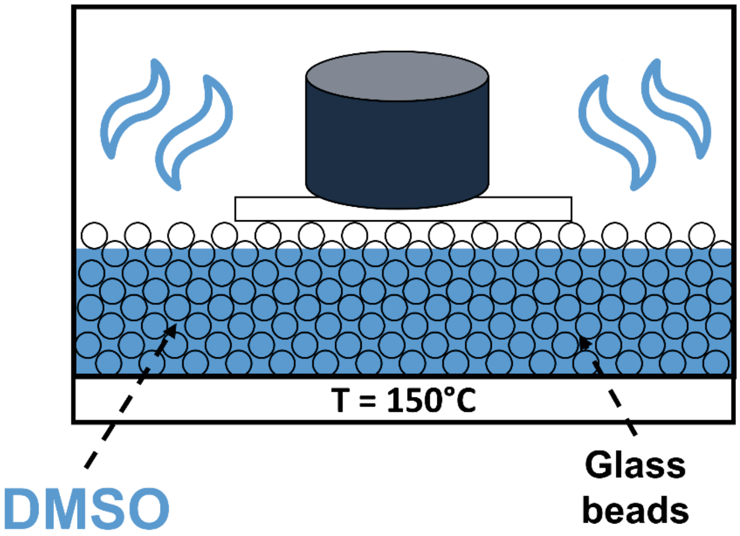

Figure Exp.1: Schematic of DMSO vapor treatment. PCPs were exposed to DMSO vapor in a closed vessel at 150°C.

8. CHARACTERIZATION METHODS

8.1. DIMENSION AND DENSITY MEASUREMENT

The dimensions and weight of cryogels were measured respectively with an OTMT caliper and an analytical balance right after drying. Their porosity Θ was estimated with the following equation:

$$\Theta = \left[1 - \frac{\rho_{porous}}{\rho_{solid}}\right] \times 100 \qquad (V.1)$$

Where $\rho_{porous}, \rho_{solid}$ are the density of the porous material and solid PEDOT:PSS density ($\rho_{solid} = 1.011\ g.cm^{-3}$) given by Heraeus.

8.2. SCANNING ELECTRON MICROSCOPY (SEM)

8.2.1. CRYO-SEM

Cryo-SEM experiment were realized by Alain Carvalho at Institut Charles Sadron. For the alcogels, as ethanol was difficult to sublimate, a gradual solvent exchange with deionized water was applied in the gel phase, prior to cryo-SEM analysis. The exchange was done in several incremental steps to minimize shrinkage and gel structure distortion. Typically, the alcogel (100%vol ethanol) was left for 24h in different ethanol/water (%vol) solutions (75/25, 50/50, 25/75, and finally in 100% water). For hydrogels, no solvent exchange was required.

A small piece of gel was sliced off with a razor blade and quickly dipped into liquid ethane (used as an efficient coolant to avoid crystalline ice formation[4,5] and then transferred under high vacuum (10^{-6} mbar) and low temperature (-150°C) into the Quorum PT 3010 chamber attached to the microscope. There, the frozen sample was fractured with an adapted razor blade. After a slight sublimation of water at −90 °C to reveal the details of the morphology, the sample was eventually transferred to the FEG-cryo-SEM (Hitachi SU8010) and observed at 1 kV at −150°C (under 10^{-6} mbar).

8.2.2. SEM

The materials were cut with a razor blade to reveal the surface of interest. The samples were observed at 1 kV at room temperature with the FEG-cry-SEM (Hitachi SU8010).

8.3. CRYO-TRANSMISSION ELECTRON MICROSCOPY (TEM)

Cryo-TEM experiment were performed by Marc Schmutz at Institut Charles Sadron.

The diluted PEDOT: PSS dispersion was observed prior to and after acid treatment.

The PH1000 dispersion was vortexed for a few minutes, filtered through a PVDF 0.45µm membrane, and then diluted with deionized water 8 times.

For the acidified sample, the PH1000 dispersion was vortexed for a few minutes, filtered through a PVDF 0.45 µm membrane, and then diluted 2 times with deionized water. Eight microliters of H_2SO_4 (3 M) were added to the diluted dispersion and then vortexed for 30 s. This acidified solution was further diluted 50 times. A high dilution rate was applied for the acidified sample to observe the unique fibers and minimize the gelation process.

Five microliters of the samples (as described above) were applied onto a 400-mesh Cu grid covered with a lacey carbon film that was freshly glow discharged to render it hydrophilic (Elmo, Cordouan Technologies). The grid was rapidly plunged into a liquid ethane slush by using a homemade freezing machine with a controlled temperature chamber. The grid was then mounted onto a Gatan 626 cryoholder and observed under low dose conditions on a Tecnai G2 microscope (FEI) operating at 200 kV. The images were recorded with a slow-scan CCD camera (Eagle 2k2k FEI).

8.4. ELECTRON MICROSCOPY IMAGES ANALYSES

8.4.1. PORE SIZE MEASUREMENT

The pore size of cryogels was estimated from SEM images with ImageJ software. As shown in Figure Exp.2, brightness and contrast are adjusted to obtain a black and white image. Then, ellipses were fitted on the pores and their dimensions were displayed. The mean value between the great and small axes of each ellipse was taken for an accurate estimation. Several images in different areas of the sample were observed to estimate the pore size all over the material. Pore size was then determined by plotting at least 200 values and fitting a Gaussian curve.

For materials with less defined porosity (i.e., aerogels and xerogels), the size of the voids was estimated manually with the measuring tool of ImageJ software.

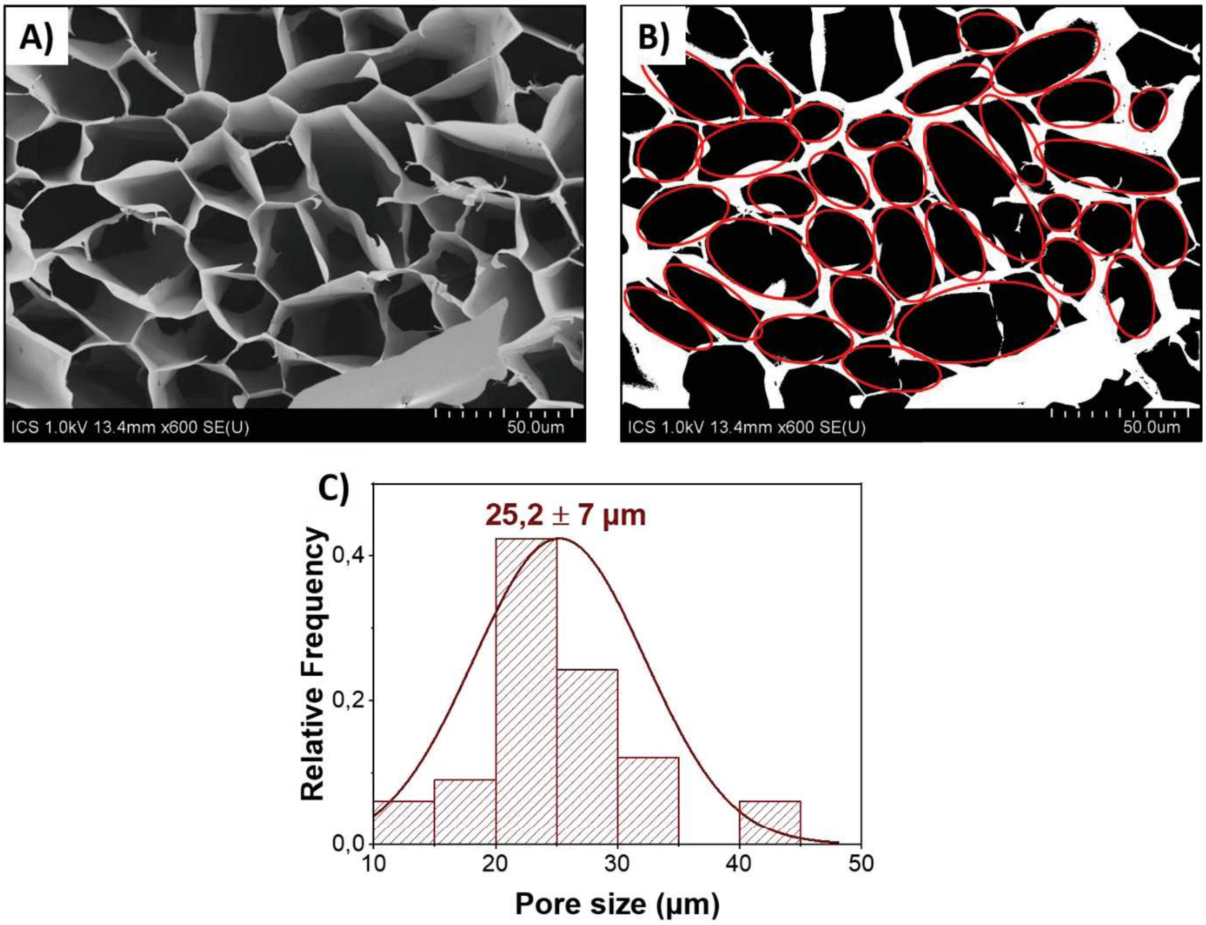

Figure Exp.2 A) SEM image of a cryogel vertically cut B) Transformed black and white image and fitted ellipses, C) Resulting histogram and Gaussian fit of the mean ellipses sizes.

8.4.2. FIBER THICKNESS MEASUREMENT

To accurately estimate the thickness of fibers observed either by cryo-TEM, cryo-SEM, or SEM, image analyses were performed with ImageJ software.

First, a Difference of Gaussian filter with sigma1 (local contrast) of five and sigma2 (local noise) of one was applied. A difference of Gaussian filter improves the contrast of image features. Basically, this algorithm involves the subtraction of a blurred Gaussian version of an image from another, less blurred version. Overall, this filter improves the edge detection of an image. The result of the use of this filter on a cryo-SEM image is shown in Figure Exp.3.B.

Then, the ridge detection plugin of ImageJ was applied on the filtered image. This plugin is based on Steger's algorithm for lines and ridges detection[6] and was successfully used to analyze grayscale images in the literature.[7] Typically, it is possible to detect lines on an image and measure their wideness and length. In our case, the length was not considered. The optimum parameters to accurately measure the thickness of the fibers were reached by trials and error. The result of the use of this plugin on a cryo-SEM image of the PEDOT: PSS hydrogel described in section II.2.2 is presented in Figure Exp.3.C.

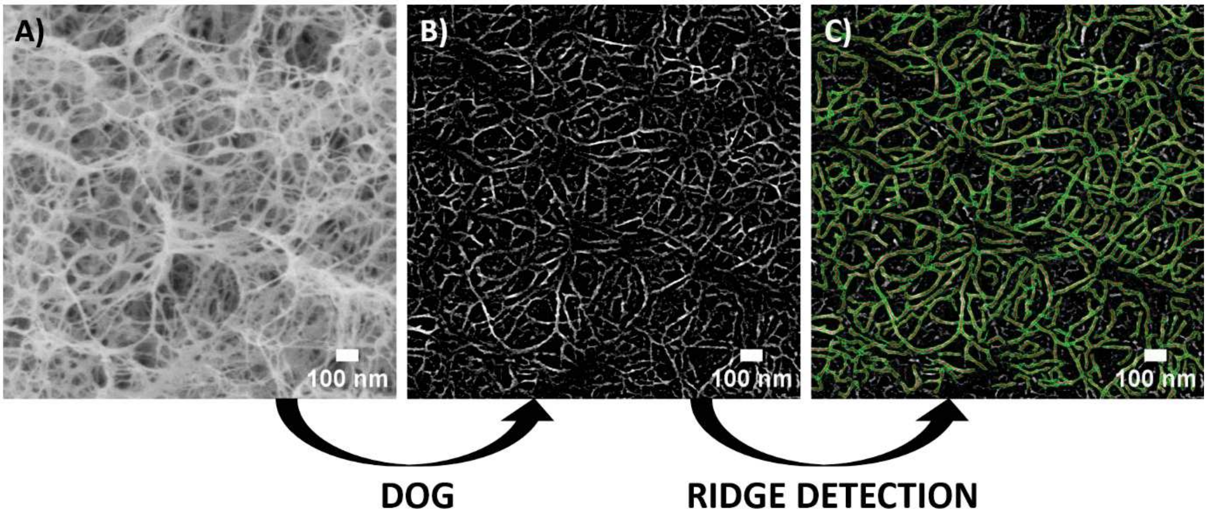

Figure Exp.3 A) Original cryo-SEM image of a PEDOT: PSS hydrogel, B) same cryo-SEM image of a PEDOT: PSS hydrogel with applied difference of Gaussian filter, C) Ridge detection of the fibers forming a PEDOT: PSS hydrogel network.

8.4.3. DIRECTIONALITY PLUGIN

To estimate the alignment of pores, the directionality plugin was used.

The plugin computes a histogram showing the amount of structures in a given direction. For example, an image with a preferred orientation should result in a histogram with peaks in that direction, while an isotropic image should result in a flat histogram. Finally, the resulting histogram can be normalized to obtain the relative intensity in a given direction.

This method is based on Fourier spectral analysis. In the case of a square image, the structure with the preferred direction produces a periodic pattern in the +90° direction in the Fourier transform of the image relative to the direction of the object in the input image. The image is then sliced into squares whose Fourier power spectra are calculated. Finally, the Fourier transforms are analyzed using the spatial filters of Liu et al.[8]

8.5. X-RAY SCATTERING

X-ray scattering measurements were performed by Doru Constantin and beam manager on the SOLEIL synchrotron (data presented in the thesis). Jérôme Combet and Guillaume Fleith performed X-ray scattering measurement at Institut Charles Sadron (data presented in Appendix).

8.5.1. MEASUREMENTS AT ICS

X-ray scattering experiments were performed with a diffractometer developed by the DiffériX facility at the ICS. The instrument works with a pinhole collimator and a hybrid photon counting detector (HPC - Dectrics Pilatus®3 R 300K). The monochromatic beam (λ = 0.154 nm Cu Kα1, with a resolution = 0.03 nm-1) was obtained by projecting the primary beam from an X-ray generator (Rigaku, MicroMax 007HF) onto a confocal mirror with a multilayer coating (Confocal Max-FluxTM Optic, Rigaku). The size of the beam incident on the sample is about 800 µm. The distance between the sample and the detector was 68 cm for SAXS, 25.8 cm for MAXS, 7.7 cm for WAXS configurations.

8.5.2. MEASUREMENT AT SYNCHROTRON SOLEIL

SAXS and WAXS (small- and wide-angle X-ray scattering) measurements were performed on the SWING beamline of the SOLEIL synchrotron (Saint-Aubin, France) at a beam energy E = 16 keV. The sample-to-detector distance was 6.22 m and 0.52 m, respectively, covering a total scattering vector range of $0.0016<q<2.5$ Å^{-1} (for the sulf-alcogel and sulf-aerogel the total scattering vector range was $0.0016<q<1.42$ Å^{-1}). The beam size was approximately 500 × 200 µm^2 (H × V). All measurements were performed at room temperature (22°C).

The scattered signal was recorded by an Eiger 4 M detector (Dectris Ltd., Switzerland) with a pixel size of 75 µm. Preliminary data treatment (angular averaging and normalization) was done using the software Foxtrot developed at the beamline, which yielded the intensity as a function of the scattering vector $I(q)$ in absolute units. Subsequent data modeling was done in Igor Pro 7.0 using functions available in the NCNR SANS package.[9]

For the serial dilution analysis in section II.2.1, several concentrations of the PEDOT: PSS were prepared. First, the stock dispersion was vortexed for a few minutes and filtered through a PVDF 0.45 µm membrane. To prepare the more concentrated sample (i.e., c x 1.75), a vial containing 1 g of the PEDOT: PSS dispersion was left open under a constant argon flow to favor partial evaporation of the water. Then, the final mass was weighted and the final concentration of 1.75 times the initial dispersion was calculated. To produce the less concentrated samples c/2, c/4, and c/8, a corresponding mass of water was added to dilute the initial PEDOT: PSS dispersion by a factor of two, four, and eight respectively.

8.5.3. DESCRIPTION OF THE TECHNIQUE AND ANALYSIS

In systems consisting of identical particles, the shape of a single particle can be analyzed by analytically or numerically evaluating the form and structure factors.[10,11]

Very generally, the form factor of a particle can be defined as follows:

$$F(\boldsymbol{q}) = \frac{1}{V_p}\int_{V_p} e^{iq.r} dV_p \qquad (V.2)$$

where V_p is the volume of the object and $\boldsymbol{q}$ is the wave vector. Thus, in the absence of interparticle interactions, the scattered intensity can be written as:

$$I(\boldsymbol{q}) = \Delta\rho^2 V_p^2 |F(\boldsymbol{q})|^2 \qquad (V.3)$$

where $\Delta\rho = (\rho_{si,p} - \rho_{si,0})$ and $\rho_{si,p}$ and $\rho_{si,0}$ are the scattering length densities of the particles and of the solvent, respectively.

In solution, the particles assume all possible orientations, so that equation V.3 must be averaged over these configurations or, equivalently, over all directions (θ, φ) of the scattering vector $\boldsymbol{q} = (q, \theta, \varphi)$, in order to obtain the experimentally relevant quantity:

$$I(q = |\boldsymbol{q}|) = \Delta\rho^2 V_p^2 \; |F(q)|^2 = \Delta\rho^2 V_p^2 \; \langle |F(\boldsymbol{q})|^2 \rangle_{(\theta,\varphi)} \qquad (V.4)$$

The form factor depends on the morphology of the particle. In most cases, it cannot be computed by analytical means and must be evaluated numerically. Closed-form expressions exist for simple shapes such as the sphere, whose form factor is:

$$F(q) = \frac{3 j_1(qR)}{qR} \;, \qquad (V.5)$$

where R is the sphere radius and $j_1(x)$ is the spherical Bessel function of the first kind.

A general measure of the object extension is the radius of gyration R_g, defined as the root-mean-squared distance from the particle's center of mass. For spheres $R_g = \sqrt{\frac{3}{5}} R$.

In the case of the PH1000 dispersion, the measurement is not done in the diluted regime. Thus, inter-particle interactions must be considered. These interactions can be accounted for by introducing a structure factor $S(q)$. Hence, equation V.3 becomes:

$$I(q) = \Delta\rho^2 V_p^2 |F(q)|^2 S(q) \qquad (V.6)$$

In our case, the objects composing the PEDOT: PSS dispersion are not spherical but rather fiber-like, as observed by cryo-TEM and cryo-SEM. Hence, we describe the SAXS data by the model of a right circular cylinder with uniform scattering length density and polydisperse radius, available in the NIST SANS package in Igor Pro 7. The form factor is normalized by the particle volume and averaged over the normalized size distribution. Hence, the size-averaged form factor is defined as:

$$\overline{F(q)} = \frac{scale}{V_{poly}} \Delta\rho^2 \int_0^x V_p^2(r) f(r) dr \int_0^{\frac{\pi}{2}} |F^2(q,\theta)| \sin(\theta)\, d\theta \ , \qquad (V.7)$$

where θ is the angle between the cylinder axis and the scattering vector $\boldsymbol{q}$, V_{poly} is the polydisperse volume, f(r) is the normalized Schulz distribution of the radius and *F* is the form factor defined above.

8.6. X-RAY PHOTOELECTRON SPECTROSCOPY

X-ray photoelectron spectroscopy (XPS) measurements were conducted by Vasiliki Papaefthymiou, ICPEES, Strasbourg. The measurements were performed in an ultrahigh vacuum spectrometer equipped with a RESOLVE 120 MCD5 hemispherical electron analyzer. The Al Kα line (Al Kα, hv=1486.6 eV) of a dual anode X-ray source was used as incident radiation. The constant pass energy mode with pass energies 100 and 20 eV, was used to record survey and high-resolution spectra respectively. In all samples surface there is oxygen, carbon, nitrogen and sulfur. The XPS peaks of all elements exist in the survey scan of each sample. Several scans were performed on dried gels at different locations (surface and bulk) to ensure representative spectra.

8.7. NITROGEN PHYSISORPTION

Nitrogen physisorption measurements were performed by Gerald Chaplais and Habiba Nouali at IS2M, Mulhouse.

Textural characterization was done using a Micromeritics ASAP 2420 apparatus by determining nitrogen physisorption isotherms at 77 K. Here, the porous samples were cut into small pieces and loaded into an analysis tube. Prior to adsorption measurements, the sample was out gassed at 423 K for 6 h under vacuum to remove the moisture from the material. The specific surface area (S_{BET}) was calculated according to the criteria given in the literature[12,13] and by using the Brunauer−Emmett−Teller (BET) method applied in the $0.02 \leq p/p^0 \leq 0.20$ ranges.

8.8. RHEOLOGY

Rheology measurements were performed by Dominique Collin at Institut Charles Sadron.

Complex shear modulus measurements were performed with a stress-imposed rheometer (Mars III, Haake) working in oscillatory mode. For alcogel and alco-aerogel samples, the parallel plate geometry fixtures (with different diameters) were used to cover the sample area. In the case of alcogels, the bottom plate was modified to allow the sample to be immersed in ethanol (to avoid drying during measurement). To ensure measurements in the linear response domain, the stress applied did not exceed 5 Pa. All measurements were performed at 20°C. The fixtures were adjusted according to the height of the sample without causing an excessive compression of the sample.[14] Normal force was measured simultaneously during the shear experiments.

8.9. TRANSPORT PROPERTIES MEASUREMENTS

A Keithley 2634B sourcemeter and a Lab Assistant Semiprobe station inside a Jacomex glovebox under N_2 atmosphere (≈ 1 ppm O_2, ≈ 1 ppm H_2O) were used to measure the electrical conductivity and the in-plane Seebeck coefficient. The cross-plane Seebeck coefficient and thermal conductivity were measured in ambient pressure and temperature. Figure Exp.4 illustrates the experimental setups used to measure the transport properties of the PCPs.

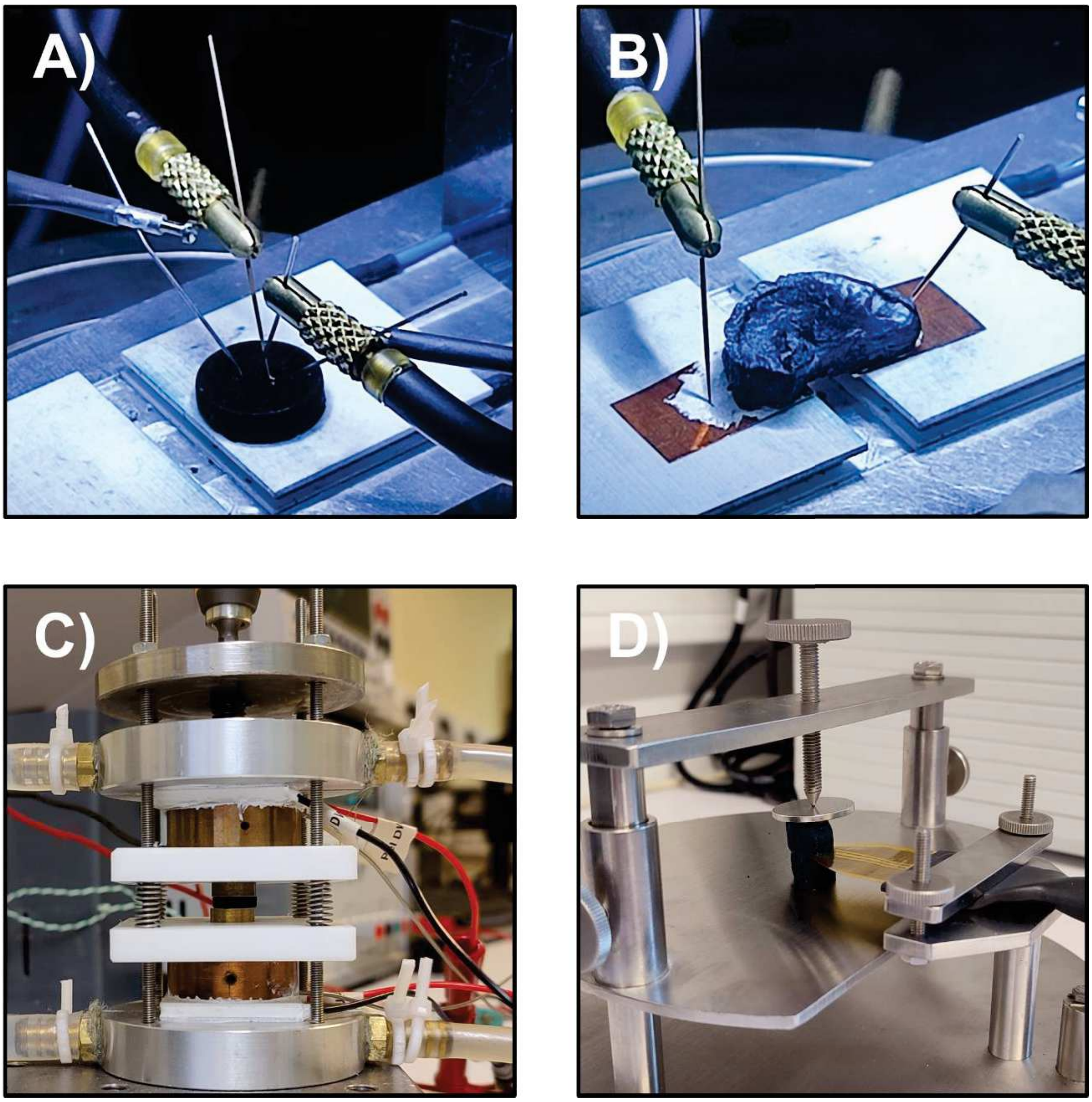

Figure Exp.4 Photos of the experimental setups to measure the transport properties. A) 4-probe resistivity; B) In-plane Seebeck coefficient; C) Cross-plane Seebeck coefficient; D) Thermal conductivity.

8.9.1. ELECTRICAL CONDUCTIVITY

The electrical resistance was measured using a standard collinear four-probe method with a probe space of 1.6 mm. It was measured on two similar setups, one with fixed probes and the other with adjustable probes. The space probe for the second measurement was done using a patterned mask.

The electrical resistivity and conductivity in the vertical direction were calculated with the following equation extracted from Yilmaz et al. work[15]

$$\rho = \frac{1}{\sigma} = G.\frac{V}{I} \quad \text{and} \tag{V.8}$$

$$G = 2\pi s. F_0(s). F_1\left(\frac{t}{s}\right). F_2\left(\frac{d}{s}\right) \tag{V.9}$$

With:

$$F_0(s) = 2\pi s \tag{V.10}$$

$$F_1\left(\frac{t}{s}\right) = \frac{\frac{t}{s}}{2\ln\left[\frac{\sinh\left(\frac{t}{s}\right)}{\sinh\left(\frac{t}{2s}\right)}\right]} \tag{V.11}$$

$$F_2\left(\frac{d}{s}\right) = \left[1 + \frac{1}{\ln 2}\, ln\frac{\left(\frac{d}{s}\right)^2 + 3}{\left(\frac{d}{s}\right)^2 - 3}\right] \tag{V.12}$$

where ρ is the electrical resistivity, σ the electrical conductivity, *V* the voltage, *I* the current intensity, *s* the probe space, t the thickness of the sample and d the diameter. F_0, F_1 and F_2 are geometric correctional factors used when the sample is circular and t > s/2. For measurement in the horizontal direction (see section III.3.2), the semi-infinite thick model from Topsoe report was used.[16]

$$\rho = \frac{1}{\sigma} = G.\frac{V}{I} \quad \text{and} \qquad (V.8)$$

$$G = 2\pi s.T_1(s) \qquad (V.13)$$

where ρ is the electrical resistivity, σ the electrical conductivity, V the voltage, I the current intensity, s the probe space and $T_1(\frac{t}{s})$ a correctional factor for an infinite plane sample of finite thickness (t > 2s).[16]

The 4-probe measurements were repeated 4 times on each sample at different locations for accurate measurement of the electrical conductivity.

8.9.2. IN-PLANE MEASUREMENTS (SEEBECK COEFFICIENT)

To measure the Seebeck coefficient, a differential temperature method was used. A homemade setup made of one heating and one cooling Peltier cells allows an in-plane controllable temperature gradient. Measurements were performed by gradually increasing the temperature difference between the two Peltier cells up to 12.8 K (starting from 293 K, the midpoint temperature). For each temperature step, the tension was measured five times with a 20 s interval.[17] To allow good thermal contact between the Peltier cells and the aerogels, copper legs (1 x 1 x 0.2 mm) were bonded on the bottom of the sample with conducting silver paste. The tension was measured directly on the silver paste. Calibration of the measurement was made with a constantan.[18]

8.9.3. CROSS-PLANE MEASUREMENTS (SEEBECK COEFFICIENT AND POWER OUTPUT)

Cross plane Seebeck coefficients and output power were measured with a homemade setup from Nicolas Stein, IJL. The samples were sandwiched between hot and cold copper discs of 1 cm diameter.[19,20] The applied pressure to the samples was below 0.3 Nm (through the use of a torque screwdriver). Using Peltier modules as heating-cooling sources and embedded thermocouples inside each copper disc, a temperature gradient was then imposed and measured across the two sides of the samples. An external cooling flow system, with the help of a cryostat, was used to keep the thermal gradient across the sample thickness. The operating temperature was defined as 293 K, whereas the thermal gradient was set between 3 K and 36.5 K. The system allows measuring the potential difference ΔU and the temperature difference ΔT, giving the Seebeck coefficient S from the slope $\Delta U/\Delta T$ of the voltage-temperature curve. Considering the sample as a thermoelectric generator, the output power was determined as a function of an adjustable external load circuit. When the output power is at its maximum, the load resistance is then equal to the internal resistance of the sample.

8.9.4. THERMAL CONDUCTIVITY

The thermal conductivity of the porous materials was measured by the transient planar source (TPS) technique using a commercial device (Hot Disc®, TPS 1000). Here, the sensor with radius 3.189 mm (consisting of a double nickel spiral protected by a thin layer of Kapton insulation) was sandwiched between two porous PEDOT:PSS materials. Only samples with appropriate dimensions relative to the sensor radius can be considered to satisfy the thermal conductivity equation in a thermally infinite medium. The distance from the edge of the sensor to the nearest free boundary of the sample must be at least equal to the radius of the sensor (i.e., with this sensor, only samples at least 12.8 mm in diameter and 3.2 mm thick can be processed).

The setup was placed under a metallic bell to avoid any temperature fluctuations arising from air currents. Before each measurement, the sample was degassed for 30 minutes to remove the adsorbed moisture and stabilized at room temperature for 10 min to avoid thermal drift of the sample. The thermal equilibrium of the sample was also checked for 40 s before each measurement. The room temperature (in general 19-21 °C) was recorded using a thermocouple, and the value was incorporated in the software before starting the measurement.

During the measurement, an electrical current of known power and duration was passed through the sensor which also recorded the increase in temperature of the sensor as a function of time. The temperature increase ($\overline{\Delta T}$) across the sensor area was measured by monitoring the total resistance of the sensor according to the following equation:

$$R(t) = R_0 + [1 + \alpha\overline{\Delta T}(\tau)] \qquad (V.14)$$

where R is the total electrical resistance at time t, R_0 is the initial resistance at $t = 0$, $\alpha = 6.41 \times 10^{-3}\ 1/°C$ is the temperature coefficient of resistivity of nickel. Therefore, equation V.14

allowed the accurate determination of $\overline{\Delta T}$ as a function of time, which was actually recorded by the TPS1000 analyzer. In general, 200 experimental points are obtained and the first 15 data points were eliminated prior to calculation - as they are also affected by the resistance of the air layer between sensor and sample. The optimal time window (i.e., the data point interval to consider) was selected to meet the best conditions to be within the limits of total characteristic time.[21] We plotted the temperature increase on a $t^{-1/2}$ scale and located the more linear part of the curve corresponding to the plot $\overline{\Delta T}$ as a function of $D(\tau)$. A straight line should be obtained. According to equation V.15, the thermal conductivity κ, can be calculated from the slope of that line:

$$\overline{\Delta T}\ (\tau) = \frac{P_0}{\sqrt{\pi^3} r\kappa} D(\tau) \qquad (V.15)$$

With P_0, the input power, r, the radius of the largest ring of the sensor, $D(\tau)$ a complex dimensionless time dependent function (with $\tau = \sqrt{\frac{t}{TCR}}$) t the time measured from the start of the transient recording and TCR, the total characteristic time).[21]

The input power and duration time required for a reliable measurement depend strongly on the characteristics of the sample. We first used the reported conditions for polyurethane foams (a thermally isolating lightweight sample with a known κ = 0.042 W/(m.K)) measurements and then a trial-and-error approach to reach the best conditions to be within the limits of total characteristic time (between 0.33 and 1),[21] temperature increase ($2 < \Delta T < 5$K) and penetration depth (larger than $\sqrt{4\alpha t}$ with α, the thermal diffusivity of the sample and t the measurement time). [22] Evaluation of the results was also done by assessing the residual curve, which represents the temperature difference between the theoretical Hot Disc model and the experimental data. In the ideal case, the residuals should be randomly scattered around a horizontal line. The experiments were performed in ambient conditions and the input power and time duration were set at 10 mW and 10 s, respectively for measuring aerogels. For the cryogels, the input power was only of 5 mW while the duration time was 10 s.

9. REFERENCES

[1] B. Yao, H. Wang, Q. Zhou, M. Wu, M. Zhang, C. Li, G. Shi, *Adv. Mater.* **2017**, *29*, 1700974.

[2] R. Maeda, H. Kawakami, Y. Shinohara, I. Kanazawa, M. Mitsuishi, *Mater. Lett.* **2019**, *251*, 169.

[3] R. Maeda, Y. Shinohara, H. Kawakami, Y. Isoda, I. Kanazawa, M. Mitsuishi, *Nanotechnology* **2020**, *32*, 135403.

[4] J. Dubochet, M. Adrian, J.-J. Chang, J.-C. Homo, J. Lepault, A. McDowall, P. Schultz, *Q. Rev. Biophys.* **1988**, *21*, 129.

[5] C. Efthymiou, M. A. K. Williams, K. M. McGrath, *Food Hydrocoll.* **2017**, *73*, 203.

[6] G. Steger, *IEEE Trans. Pattern Anal. Mach. Intell.* **1998**, *20*, 113.

[7] M. Glaser, J. Schnauß, T. Tschirner, B. U. S. Schmidt, M. Moebius-Winkler, J. A. Käs, D. M. Smith, *New J. Phys.* **2016**, *18*, 055001.

[8] Z.-Q. Liu, *Appl. Opt.* **1991**, *30*, 1369.

[9] S. R. Kline, *J. Appl. Crystallogr.* **2006**, *39*, 895.

[10] J. Als-Nielsen, D. McMorrow, *Elements of Modern X-Ray Physics: Second Edition*, John Wiley And Sons, **2011**.

[11] R.-J. Doe, *Methods of X-Ray and Neutron Scattering in Polymer Science*, Oxford University Press, New York, **2000**.

[12] J. Rouquerol, P. Llewellyn, F. Rouquerol, *Stud. Surf. Sci. Catal.* **2007**, *160*, 49.

[13] K. S. Walton, R. Q. Snurr, *J. Am. Chem. Soc.* **2007**, *129*, 8552.

[14] D. Collin, P. Lavalle, J. M. Garza, J. C. Voegel, P. Schaaf, P. Martinoty, *Macromolecules* **2004**, *37*, 10195.

[15] S. Yilmaz, *J. Semicond.* **2015**, *36*, 082001.

[16] H. Topsøe, *Geometric Factors in Four Point Resistivity Measurement*, **1968**.

[17] A. Hamidi-Sakr, L. Biniek, J. L. Bantignies, D. Maurin, L. Herrmann, N. Leclerc, P. Lévêque, V. Vijayakumar, N. Zimmermann, M. Brinkmann, *Adv. Funct. Mater.* **2017**, *27*, 1700173.

[18] R. E. Bentley, *Handbook of Temperature Measurement Vol. 3: The Theory and Practice of Thermoelectric Thermometry*, Springer Science & Business Media, Singapore, **1998**.

[19] A. Danine, J. Schoenleber, J. Ghanbaja, F. Montaigne, C. Boulanger, N. Stein, *Electrochim. Acta* **2018**, *279*, 258.

[20] C. Frantz, N. Stein, L. Gravier, S. Granville, C. Boulanger, *J. Electron. Mater.* **2010**, *39*, 2043.

[21] V. Bohac, M. K. Gustavsson, L. Kubicar, S. E. Gustafsson, *Rev. Sci. Instrum.* **2000**, *71*, 2452.

[22] Y. He, *Thermochim. Acta* **2005**, *436*, 122.

APPENDIX

APPENDIX I : PCPS STRUCTURAL FEATURES COMPARISON BY X-RAY SCATTERING

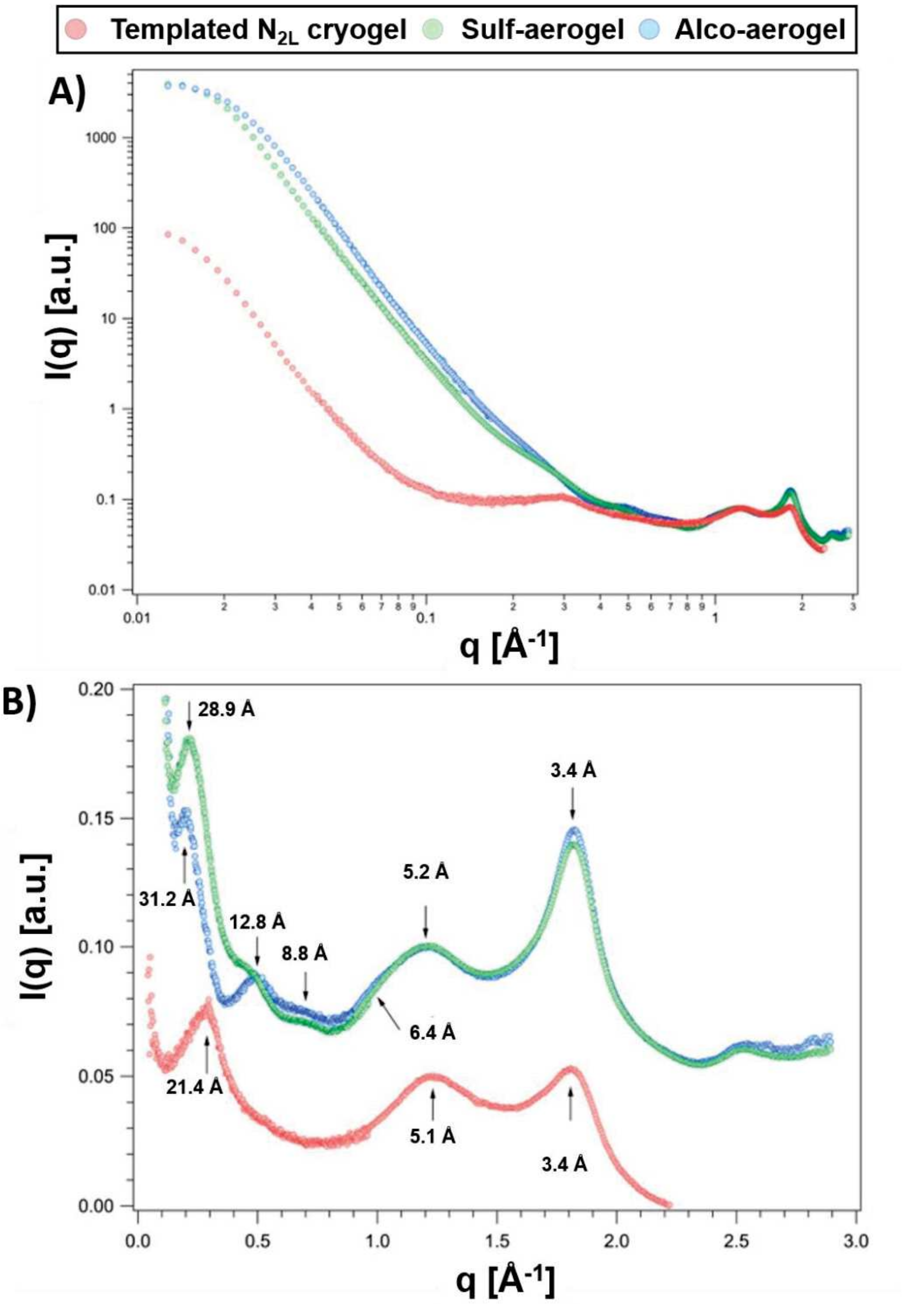

Appendix 1 : A) SAXS and WAXS intensity profile of the templated N_{2L} cryogel (in red), sulf-aerogel (in green), alco-aerogel (in blue); B) WAXS data subtracted from the q^{-4} contribution in the Porod regime. Experiments made at ICS on the DIFERRIX platform.

In the WAXS range, the peaks between 0.4 and 2.5 $Å^{-1}$ are related to the internal structure of the fibrils (i.e., molecular arrangement between PEDOT and PSS). The sulf- and alco-aerogels exhibit numerous and sharp peaks suggesting higher crystalline order than in the cryogel.

The peaks at 3.4 Å and 5.1-5.2 Å correspond to the characteristic π-stacking distances of PEDOT and PSS, respectively. The π -stacking of the PEDOT is at the same position but is less intense for the cryogels than for both aerogel samples. The peaks at 8.8 Å and 12.8 Å correspond to the characteristic interlamellar distance of PSS and PEDOT, respectively. We cannot clearly attribute the peak at 6.4 Å, clearly seen in sulf- and alco-aerogels but not in the cryogel. The difference of crystalline order within the fibrils constituting the aerogels and the cryogel is quite surprising. We would expect the internal organization within the fibrils to happen during the gelation step (which are fairly similar in the case of the cryogel and the sulf-aerogel). The solvent exchange step of the sulf-aerogel in ethanol and/or the supercritical conditions impact the inner structure of the fibrils.

Comparing the sulf- and alco-aerogels, their inner structures are relatively similar and this cannot explain their difference in properties (electrical and thermal conductivities).

In the mid-angle range, a diffusion peak is observed at 28.9 Å and 31.2 Å for the sulf- and alco-aerogels. We suggest that it corresponds to a fibril-to fibril distance (closed to the thickness determined by Cryo-SEM).

For the cryogel, this peak is shifted at 21.4 Å (measurement on the DIFFERIX platform at ICS). On the synchrotron measurement, discussed in chapter III, this peak was detected around 27 Å. At the moment, we cannot explain why we observed such difference in peak position. But in both cases, it is this peak that shows some anisotropic behaviour (depending on the orientation of the templated cryogels towards the beam). Therefore, we propose to attribute this peak to a fibril-to fibril distance within the pore walls.

In the SAXS range, the intensity of diffusion is much higher for the aerogels than for the cryogel. This is characteristic of a higher specific area in the fibrillar mesoporous samples as compared to the channel-like macroporous structure.

Further studies are needed to fully elaborate a clear structural model of PEDOT: PSS arrangement within the fibrils and to gain a better comprehension of the impacts of the drying processes on the final structures.

APPENDIX II : ESTIMATION OF THE DIFFERENT CONTRIBUTION TO THE THERMAL CONDUCTIVITY OF ALL SAMPLES

Material	κ_{gas} [W/(m.K)]	κ_{solid} [W/(m.K)]	κ_{elec} [W/(m.K)]	$\kappa_{lattice}$ [W/(m.K)]	$\kappa_{measured}$ [W/(m.K)]
Lyophilized dispersion	0,025	0,034	0,000036	0,059	0,059
Quenched cryogel	0,025	0,016	0,001	0,041	0,042
Templated N_{2L} cryogel	0,025	0,011	0,001	0,036	0,037
Templated N_{2L}/EtOH cryogel	0,025	0,015	0,001	0,040	0,041
Templated CO_{2S}/IPA cryogel	0,025	0,021	0,001	0,046	0,047
Templated IPA cryogel	0,025	0,020	0,001	0,045	0,046
Sulf-aerogel	0,004	0,044	0,006	0,048	0,05
Alco-aerogel	0,004	0,046	0,015	0,050	0,07

Appendix 2 : Sum-up table of the gas, solid, electronic and lattice contributions to the thermal conductivity.

κ_{gas} was calculated from equation I.7, κ_{elec} was calculated from Wiedemann-Franz law (see equation I.12) by taking the Lorentz number at Sommerfeld value ($L = 2.4428\ 10^{-8}$ W.Ω.K^{-2}=. Then, $\kappa_{lattice}$ and κ_{solid} were deduced from the other values. Two groups can be clearly seen : the macroporous sample have a high κ_{gas} and very low κ_{solid} while the mesoporous samples (i.e., the sulf- and alco-aerogel) have a very low κ_{gas} (due to their pore size inferior to the mean free path of air molecules) and higher κ_{solid}.

RÉSUMÉ EN FRANÇAIS

1. INTRODUCTION

La consommation d'énergie de la population mondiale a considérablement augmenté au cours des dernières décennies et devrait atteindre 26 TW en 2050.[1,2] Dans le contexte alarmant du réchauffement climatique, il est impératif de développer des moyens de produire suffisamment d'énergie tout en diminuant nos émissions de carbone. Les sources d'énergie renouvelables présentent un grand intérêt pour un tel objectif. Aujourd'hui, ces sources d'énergie sont principalement solaires, éoliennes et hydrauliques. Bien que la conversion de la chaleur en électricité soit bien connue et utilisée depuis des décennies (moteurs à combustion), son utilisation en tant que source d'énergie renouvelable est relativement faible. En effet, la chaleur est l'une des sources d'énergie les plus présentes sur terre. Elle provient principalement du soleil, de la géothermie, des activités humaines et de la chaleur corporelle. Par exemple, le soleil fournit à lui seul (par ondes infrarouges) plus que suffisamment d'énergie pour répondre à la demande mondiale. Bien que cette source d'énergie soit abondante, elle est présente sur terre de manière très diffuse, entraînant des différences de température de quelques dizaines de degrés seulement. Il en va de même pour la chaleur géothermique. D'autre part, environ 60 % de la consommation mondiale d'énergie est transformée en chaleur. Récupérer et convertir une partie de cette chaleur en électricité semble être une voie intéressante pour augmenter l'efficacité énergétique globale. Le dernier rapport du GIEC montre en particulier que la limitation des pertes d'énergie est d'une grande importance pour répondre aux futurs besoins énergétiques mondiaux tout en réduisant notre impact sur l'environnement. La chaleur perdue peut provenir à la fois des ménages (chaleur perdue à basse température) et des déchets/processus industriels (chaleur perdue à moyenne ou haute température). Cette chaleur est généralement assez localisée, ce qui la rend plus facile à convertir que la chaleur du soleil ou l'énergie géothermique. Enfin, la chaleur dégagée par le corps humain (jusqu'à 80 mW/cm² pour un individu en mouvement)[3,4] est une source facilement accessible de chaleur résiduelle. C'est dans ce contexte que les générateurs thermoélectriques (qui peuvent convertir la chaleur en électricité) présentent un intérêt. A partir d'un gradient de température, ce type de générateur peut produire jusqu'à quelques W d'électricité (en fonction du gradient de température et du rendement du générateur). Par exemple, les générateur thermoélectriques (TEG) pourraient être utilisés dans le secteur automobile (ou pour tout équipement contenant un moteur thermique) pour convertir la chaleur dégagée en énergie électrique en plaçant un TEG sur les tuyaux d'échappement.

Il existe de nombreux matériaux thermoélectriques (TE) différents, principalement divisés en deux catégories : les matériaux inorganiques et les matériaux organiques. Pour convertir la chaleur à des gradients supérieurs à 800 K, il existe plusieurs types de technologies prometteuses, utilisant des matériaux inorganiques non toxiques et abondants.[5] Pour les gradients de température inférieurs, la situation est différente. Il existe également des technologies inorganiques prometteuses, mais utilisant des matériaux plus rares et plus toxiques tels que Pb, Bi ou Te. À l'inverse, les matériaux organiques sont généralement moins toxiques, plus abondants, légers et mécaniquement flexibles. Ces avantages sont tout de même à nuancer car leur origine généralement pétro-sourcée risque, à terme, d'être problématique. Les performances de ces matériaux sont inférieures à celles de leurs homologues inorganiques, mais les avantages mentionnés, ainsi que leur faible température de fonctionnement (300-500 K) en font de bons compléments aux matériaux inorganiques. Dans cette thèse, nous nous concentrons sur les matériaux organiques pour des applications en thermoélectricité. Compte tenu de leur performance relativement faible, leur utilisation optimale est la récupération de la chaleur corporelle pour alimenter de petits capteurs ou des appareils électroniques portables de faible puissance pour une utilisation sportive/médicale.

Une attention considérable a été portée sur le domaine de le thermoélectricité organiques après le travail pionnier de Bubnova et al. en 2011.[6] En contrôlant le niveau d'oxydation du poly(3,4-éthylènedioxythiophène) (PEDOT), ils ont obtenu des valeurs de ZT (c’est-à-dire, la figure de mérite, un nombre adimensionnel reflétant la qualité d'un matériau thermoélectrique) de 0,25 à température ambiante. A la suite de ces travaux, la communauté s'est principalement concentrée sur l'augmentation des propriétés de transport de charge[7] (c'est-à-dire le coefficient Seebeck et la conductivité électrique) jusqu'à atteindre des conductivités électriques allant jusqu'à 10^5 S/cm et des facteurs de puissance (PF = σS^2) de plusieurs mW/(m.K^2) pour les dérivés de polythiophène dopés type p.[8] Globalement, la recherche dans le domaine de la thermoélectricité organique est principalement axée sur le développement de films minces avec des facteurs de puissance élevés (principalement des matériaux de type p, les matériaux de type n étant plus difficiles à produire).

Cela soulève plusieurs problèmes. Bien que la recherche en laboratoire soit axée sur le développement de films minces, leur intégration finale dans des générateurs thermoélectriques est un véritable défi. En outre, de bonnes propriétés de transport de charge sont évidemment nécessaires pour des matériaux TE efficaces, mais leur conductivité thermique ne doit pas non plus être négligée. Enfin, la stabilité à l'air et le coût de ces matériaux sont des paramètres importants si l'on souhaite les utiliser dans le futur. Dans ce travail de thèse, nous avons décidé d'adopter une approche différente pour tenter de trouver des solutions à ces problèmes. Pour mieux comprendre cette approche, nous devons définir ZT:

$$ZT = \frac{\sigma S^2}{\kappa_{elec} + \kappa_{lattice}}.T,$$

Où σ est la conductivité électrique, S est le coefficient Seebeck, T est la température, et κ_{elec} et $\kappa_{lattice}$ sont respectivement la contribution électronique et de réseau à la conductivité thermique. La conductivité électrique, le coefficient Seebeck et la conductivité thermique électronique sont des paramètres interdépendants. Le seul paramètre isolé est $\kappa_{lattice}$, qui est un véritable levier pour réduire la conductivité thermique globale sans perturber les autres propriétés de transport. De plus, il a été montré par Scheunemann et al. que pour que des matériaux TE organiques non désordonnés énergétiquement puissent atteindre un ZT supérieur ou égal à l'unité, $\kappa_{lattice}$ doit être inférieur à 0,2 W/(m.K) (ce qui n'est pas le cas actuellement pour les matériaux TE organiques dopés).[9] Ainsi, l'ingénierie phononique est une piste intéressante pour réduire $\kappa_{lattice}$. Inspirés par les aérogels (hautement isolants thermiquement), nous démontrons dans cette thèse l'intérêt d'ajouter de la porosité dans des matériaux TE organiques de type p. En plus de réduire $\kappa_{lattice}$, la production de matériaux poreux permet d'augmenter significativement leur taille facilement, permettant une intégration simple dans des TEGs verticaux.

Notre objectif principal est de mettre en évidence les relations structure-propriété du PEDOT:PSS poreux et d'étudier leur pertinence pour leur application en thermoélectricité. À cette fin, nous développons dans cette thèse des gels de PEDOT:PSS, puis par des techniques de séchage par solvant, nous obtenons un matériau poreux. Les polymères conducteurs poreux (PCPs) rapportés dans la littérature présentent un mauvais contrôle du processus de séchage et de la structure poreuse finale.[10–13] Il y a également un clair manque de compréhension et de caractérisation de la formation des pores (et du mécanisme de gélification, lorsque cette étape est présente dans la production des PCPs). Dans cette thèse, nous nous efforçons de développer et d'adapter des méthodes expérimentales complètes pour mesurer toutes les propriétés d'intérêt dans les matériaux conducteurs poreux. L'intérêt principal de la mise en œuvre de la porosité dans les matériaux TE est de réduire la conductivité thermique. Cependant, l'impact de la structure poreuse sur la conductivité thermique du matériau est souvent difficile à contrôler. Ici, nous avons l'intention i) d'établir une méthode robuste pour mesurer les propriétés de conduction thermique des PCP, ii) d'évaluer les trois paramètres thermoélectriques (σ, S et κ). En plus de leur ZT, la puissance de sortie des matériaux les plus prometteurs sera étudiée afin de quantifier leur intérêt potentiel dans les générateurs TE. Enfin, l'objectif ultime serait de réaliser un prototype de générateur avec le matériau présentant les meilleures propriétés TE.

2. ELABORATION DE GELS ET MATERIAUX POREUX TE DE TYPE P A PARTIR DE PEDOT:PSS

Nous proposons de développer un processus en deux étapes pour produire du PEDOT:PSS poreux par gélification suivie d'un séchage contrôlé. Nous visons à développer des matériaux poreux de structures diverses à partir du même gel de polymère. Tout d'abord, nous nous efforçons de comprendre la composition et la structure de la dispersion commerciale de PEDOT :PSS. Ensuite, un hydrogel de PEDOT:PSS est formé, et le mécanisme de gélification est discuté. En parallèle, un alcogel de PEDOT : PSS est formé par ajout d’éthanol. Trois méthodes de séchage conduisant à différentes structures poreuses sont utilisées pour produire des xérogels, des aérogels et des cryogels. Enfin, les propriétés thermoélectriques des différents matériaux poreux sont étudiées, et les relations structure-propriété sont discutées. Pour comparaison, la dispersion (avant gélification) est également lyophilisée.

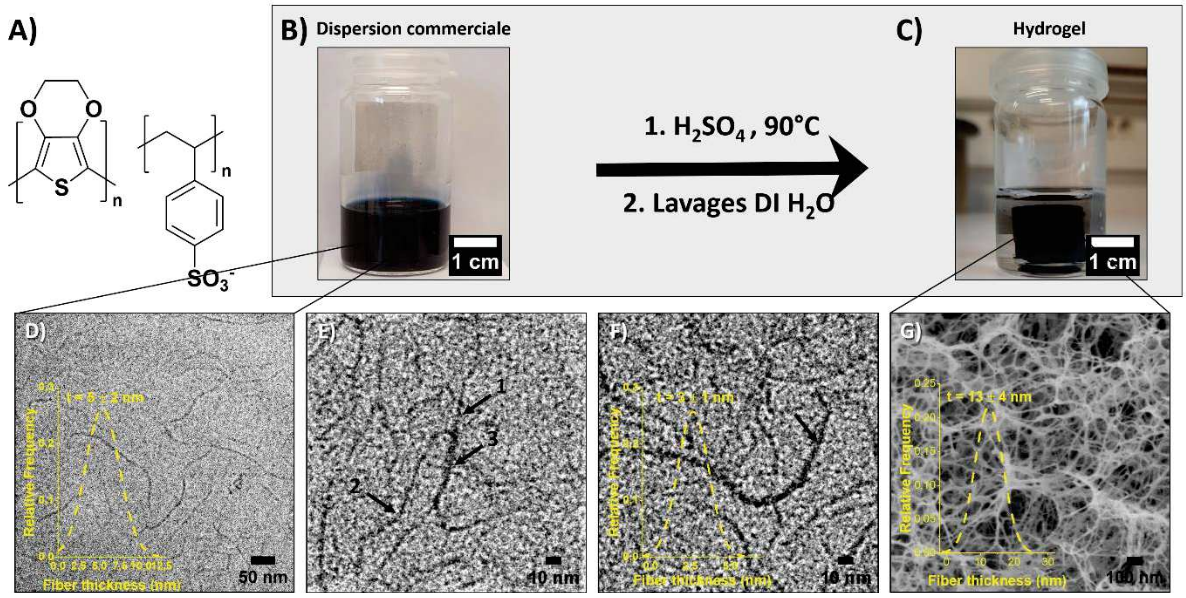

Figure 5 : A) Structure chimique du PEDOT:PSS ; Photos de B) la dispersion commercial et C) l'hydrogel de PEDOT:PSS. D-F) Images cryo-MET de la dispersion à différentes étapes de gélification : D) Dispersion initiale, diamètre des fibres est t = 5 ± 2 nm ; E-F) Dispersion acidifiée, on peut voir deux fibrilles (flèches 1 et 2, t = 3 ± 1 nm) s'entremêler pour donner une plus grosse fibre. G) Images cryo-MEB de l'hydrogel, le diamètre des fibres et de t = 13 ± 4 nm.

Afin de faire la lumière sur le mécanisme de gélification, nous avons d'abord étudié la dispersion du PEDOT : PSS. Jusqu'à présent, la structure du PEDOT : PSS à l'état de dispersion était toujours considérée comme des microgels de polyélectrolytes[14] ou des structures micellaires[15,16]. Nous avons montré par cryo-MET que la dispersion est principalement composée de fibrilles d'un diamètre moyen de 5 ± 2 nm et d'une longueur de 110 ± 35 nm (voir Figure 5.A). Les caractéristiques structurelles de l'objet composant de la dispersion ont été confirmées par des techniques de diffusion des rayons X, en étudiant à la fois le facteur de forme et de structure des objets. Nous suggérons que les fibrilles de PEDOT:PSS ont tendance à s'organiser en un système cœur-coquille (cœur riche en PEDOT, coquille riche en PSS). À l'intérieur, les fibrilles sont constituées d'une structure lamellaire d'oligomères de PEDOT π-empilés distribués le long des chaînes de PSS. Ce modèle est cohérent avec nos observations mais aussi avec d'autres rapports de la littérature.

Ensuite, nous avons développé avec succès deux processus de gélification via l'ajout de H_2SO_4 (voir Figure 5.B-C) ou d'éthanol. La forme et la taille des deux gels produits (hydrogel pour le procédé H_2SO_4 et alcogel pour le procédé éthanol) peuvent être ajustées en fonction des paramètres de synthèse. Nous avons suivi le mécanisme de gélification par plusieurs techniques structurelles et spectroscopiques. Nous avons démontré par spectroscopie UV-vis et XPS, l'élimination partielle des chaînes PSS en excès pendant la gélification. Il est intéressant de noter que la quantité finale de PSS était plus faible dans l'alcogel que dans l'hydrogel. De plus, la spectroscopie FTIR a montré que l'étape de gélification favorise la conformation quinoïdale des molécules de PEDOT plus dans l'alcogel que dans l'hydrogel. L'étude spectroscopique des gels donne des indications sur l'état de dopage probablement différent entre l'hydrogel et l'alcogel. Bien qu'ils semblent être légèrement différents à l'échelle moléculaire, les caractéristiques structurelles des deux gels sont assez similaires. Ils présentent tous deux une structure mésoporeuse fibrillaire avec des fibres d'une épaisseur de ~ 10 nm. Nous avons pu démontrer par cryo-MET que l'ajout d'acide sulfurique à la dispersion initiale tend à modifier la structure des fibrilles (réduction de leur épaisseur et augmentation de leur longueur, voir Figure 5.E-F). La réduction de leur taille est bien corrélée à la perte partielle des chaînes PSS en excès. Nous avons pu confirmer les caractéristiques structurelles des fibrilles à l'état d'hydrogel et d'alcogel par SAXS. Bien qu'il soit difficile d'affirmer avec certitude le mécanisme de formation du gel, nous suggérons ce qui suit (voir Figure 6). I) Tout d'abord, la dispersion fibrillaire initiale interagit avec de l'acide sulfurique ou de l'éthanol. Dans les deux cas, les interactions coulombiennes entre le PEDOT et certaines chaines de PSS (faiblement liés aux molécules de PEDOT et/ou libres dans la dispersion) sont réduites. Par conséquent, il y a une élimination partielle de certaines chaînes de PSS. II) Comme les répulsions électrostatiques de la dispersion sont réduites, les fibrilles ont tendance à se rapprocher les unes des autres. III) Trois à cinq fibrilles s'enchevêtrent pour former des fibres plus épaisses. Enfin, un réseau robuste est formé par les interactions VdW et π-stacking. Nous avons même pu démontrer la nature physique des nœuds du réseau des alcogels par des études rhéologiques.

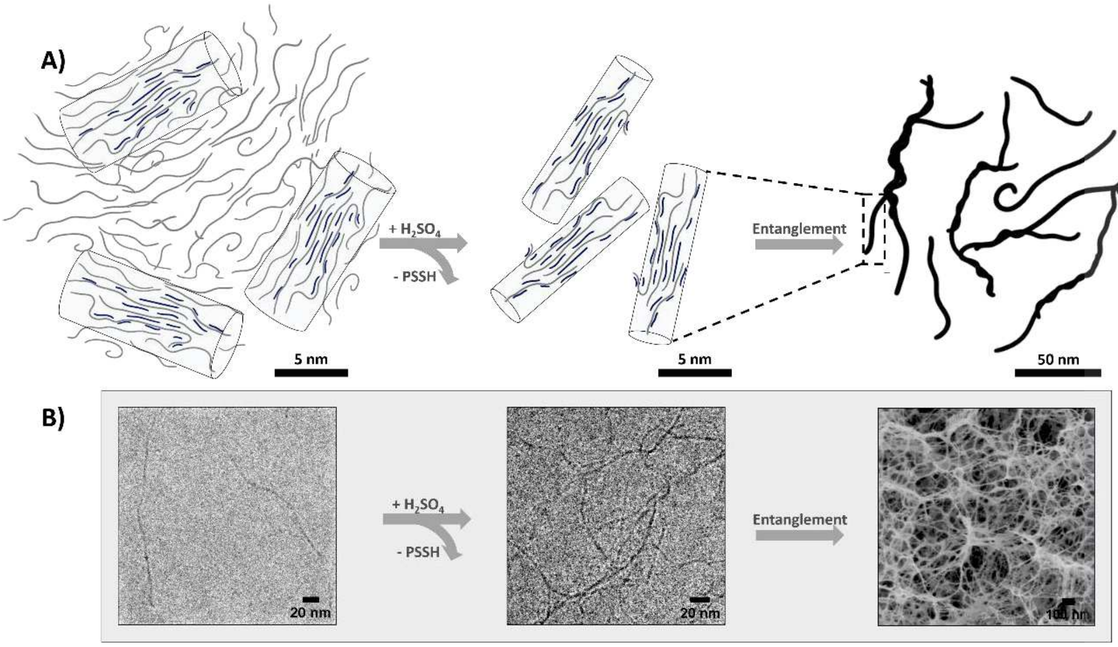

Figure 6 : A) Schéma du mécanisme de gélification proposé avec les empilements d'oligomères PEDOT en bleu et les chaînes PSS en gris ; B) Images cryo-MET et MEB associées aux différentes étapes de la gélification. La dispersion initiale est composée de fibrilles de noyau riche en PEDOT et de coquille riche en PSS d'environ 5 nm d'épaisseur, il est probable qu'une partie du PSS libre soit présente dans la dispersion ; après acidification, certaines chaînes de PSS sont protonées et éliminées pendant le lavage du gel. Par conséquent, la dispersion est déstabilisée et les fibrilles d'environ 3 nm d'épaisseur ont tendance à s'assembler via des interactions VdW et de π-stacking. Enfin, une fois les fibres enchevêtrées, le réseau 3D mésoporeux est formé.

Nous avons ensuite appliqué trois techniques de séchage à l'hydrogel et une à l'alcogel. La Figure 7 illustre les différentes voies utilisées pour produire les « xérogels » (séchés à l'air), les « sulf-aérogels » et « alco-aérogels » (séchage supercritique), et les « quenched » et « templated cryogels » (lyophilisés). À partir d'un même gel, nous avons réussi à produire trois structures différentes avec des gammes de porosités variées.

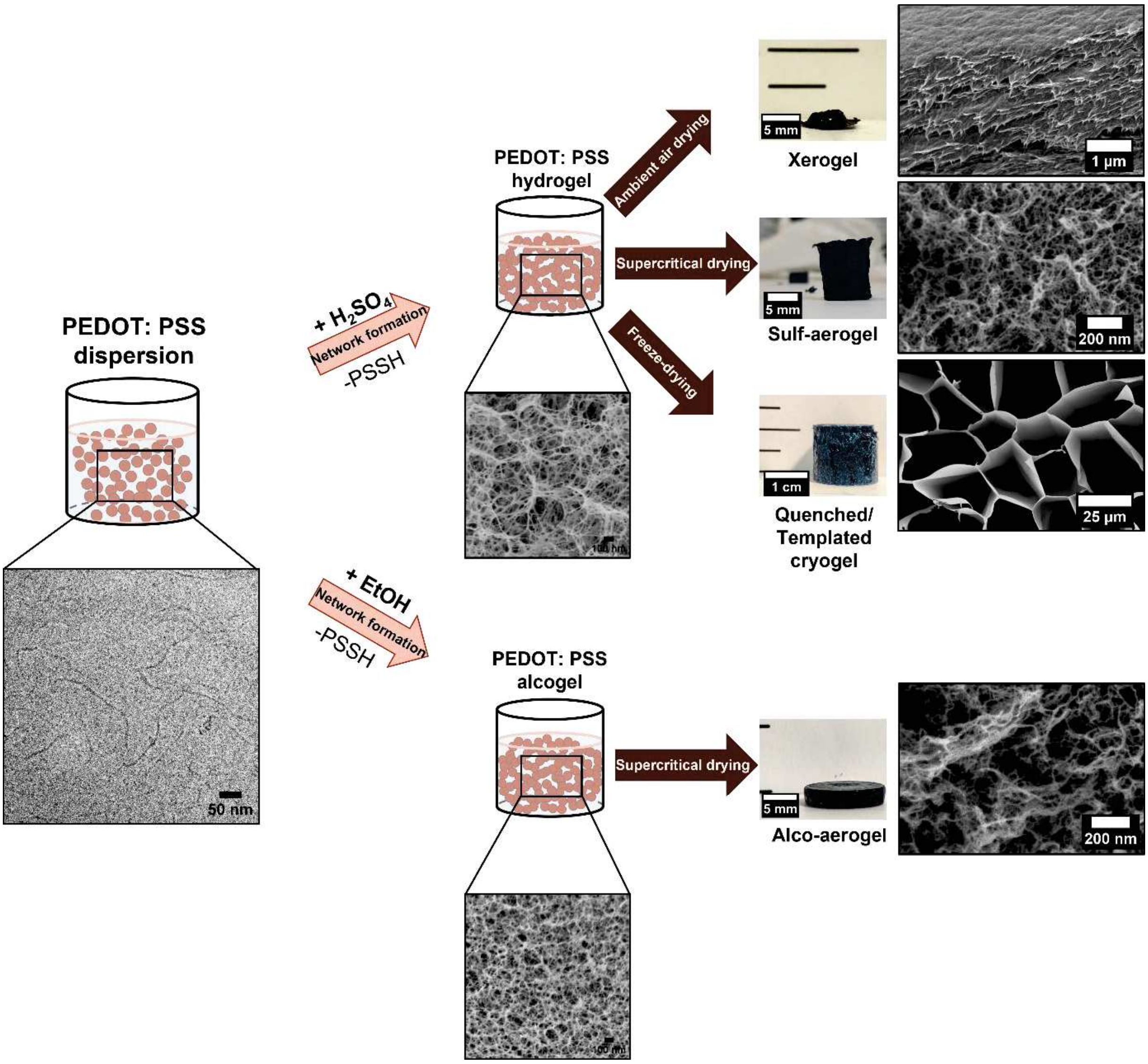

Figure 7 : Schéma des différentes voies d'élaboration de l'hydro- et de l'alcogel suivies de leurs étapes de séchage. Le séchage à l'air ambiant donne lieu aux xérogels, le séchage supercritique donne lieu à un sulf-aérogel ou à un alco-aérogel en fonction du gel initial, la lyophilisation de l'hydrogel donne lieu à des quenched cryogels (pour la méthode de congélation par trempe) ou templated cryogels (pour la méthode de congélation unidirectionnelle).

Le séchage à l'air (dans des conditions de pression et de température ambiantes) de l'hydrogel entraîne une contraction importante de l'échantillon. La structure en feuillet du xérogel est très différente de celle de l'hydrogel. Bien que sa densité soit inférieure à celle du PEDOT : PSS pur (ce qui suggère une certaine porosité), il n'a pas été étudié plus avant. A l'inverse, nous avons développé une méthode de séchage supercritique, dans laquelle le solvant du gel est remplacé par du CO_2 qui peut passer de la phase liquide à la phase gazeuse sans transition de phase. Ainsi, en optimisant finement les paramètres de séchage, nous avons pu produire des sulfo- et alco-aérogels (selon le gel séché) dont la structure fibrillaire mésoporeuse était identique à celle du gel natif. Leurs caractéristiques structurales ont été étudiées par microscopie électronique et par diffusion des rayons X. Nous avons pu confirmer la présence de petits objets 1D par l'analyse du profil d'intensité SAXS. Comme discuté ci-dessus, pendant la formation du réseau, les fibrilles s'enchevêtrent pour former des fibres plus épaisses composant un gel cohérent et robuste. De plus, nous avons pu analyser en détail le profil d'intensité des rayons X des sulfo- et alco-aérogels aux moyen et grands. Ils présentent des pics fins et nombreux, suggérant un certain ordre cristallin.

Les cryogels présentent les propriétés de transport de charge les plus faibles, mais aussi la conductivité thermique la plus faible. Ceci est dû à leur très faible densité et à leur structure macroporeuse particulière. Nous avons étudié en détail la formation de ces pores, très différents de la structure initiale de l'hydrogel.

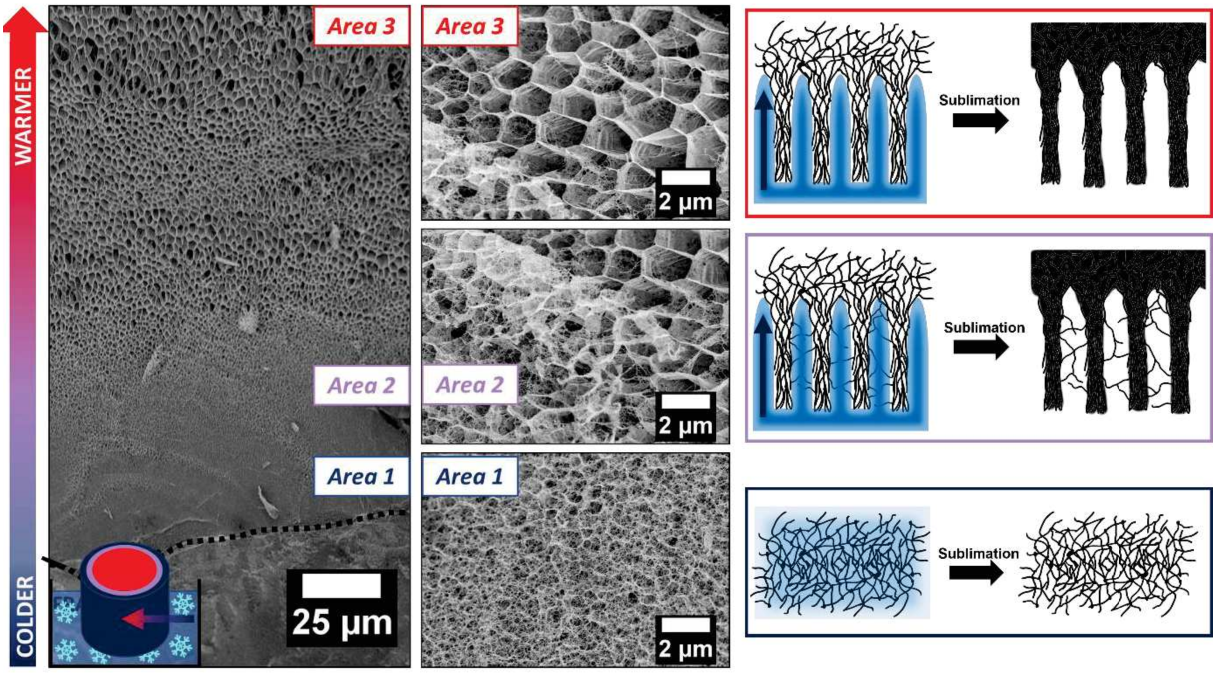

Figure 8 : Schéma du mécanisme de formation de la structure macroporeuse en nid d'abeille. Le gel (représenté schématiquement en bas à gauche de l'image) a été plongé dans l'éthane liquide afin de congeler son solvant (de l'eau). Différentes vitesses de congélation peuvent être observées au sein du même échantillon. Ainsi on peut observer sur les images cryo-MEB différentes états de formation des cristaux d'eau. On peut faire une analogie de l'état de chacune de ces zones au mécanisme de formation des pores lors d'une lyophilisation classique des gels. A droite, la formation de la glace (amorphe ou cristalline) dans le réseau du gel est schématiquement représentée.

La Figure 8 illustre la formation des cristaux de glace au sein de la structure du gel, mettant ainsi en évidence la formation des pores dans le cryogel final. Dans la zone 1, la structure du gel a été gelée très rapidement, donc la glace retenant la structure est amorphe et conserve bien la structure fibrillaire native. Dans la zone 2, le taux de congélation était légèrement plus élevé et certains cristaux de glace commencent à se former, détruisant le réseau mésoporeux du gel. Après avoir sublimé l'échantillon, nous pouvons observer des pores qui sont la réplique inverse des cristaux de glace. Dans la zone 3, les cristaux de glace ont pu se développer complètement, repoussant les fibres dans des zones ségrégées compactes (c'est-à-dire les parois des pores), laissant des cavités à facettes après la sublimation de la glace. L'étude de la formation de ces pores par la formation de cristaux de glace (voir Figure 8) a démontré que le contrôle de l'étape de congélation (et donc de la croissance des cristaux de glace) pourrait être intéressant pour modifier la structure des pores des cryogels.

3. MODIFICATION DE LA STRUCTURE MACROPOREUSE PAR ICE-TEMPLATING ET ETUDE DE SON INFLUENCE SUR LES PROPRIETES TE

Dans cette thèse, nous avons démontré la possibilité de contrôler la structure macroporeuse des cryogels par la méthode d’ice-templating (donnant lieu aux templated cryogels). Nous avons développé une méthode de congélation unidirectionnelle et démontré que nous étions en mesure d'orienter complètement les pores le long de l'épaisseur de gels de taille centimétrique (voir Figure 9.B-C). La congélation unidirectionnelle a été possible en plaçant le gel au sommet d'un barreau d'aluminium refroidi et en protégeant les côtés de l’échantillon avec un anneau de téflon (voir Figure 9.A). La nucléation des cristaux d’eau a été favorisée au fond de l'échantillon, directement en contact avec la surface de refroidissement, entraînant la croissance unidirectionnelle des cristaux de glace. En se formant dans le réseau du gel, les cristaux de glace ont repoussé les fibres de PEDOT : PSS. En analysant ces matériaux par diffusion des rayons X (profil d’intensité anisotrope, voir Figure 9.D-G), nous avons même pu démontrer que l'orientation des pores, induisait également l'orientation d'objets (fibres du réseau initial de gel) à l'intérieur des parois des pores. Seules des études préliminaires ont été réalisées, mais il est très probable que les propriétés de transport (électriques et thermiques) de ce matériau puissent être anisotropes.

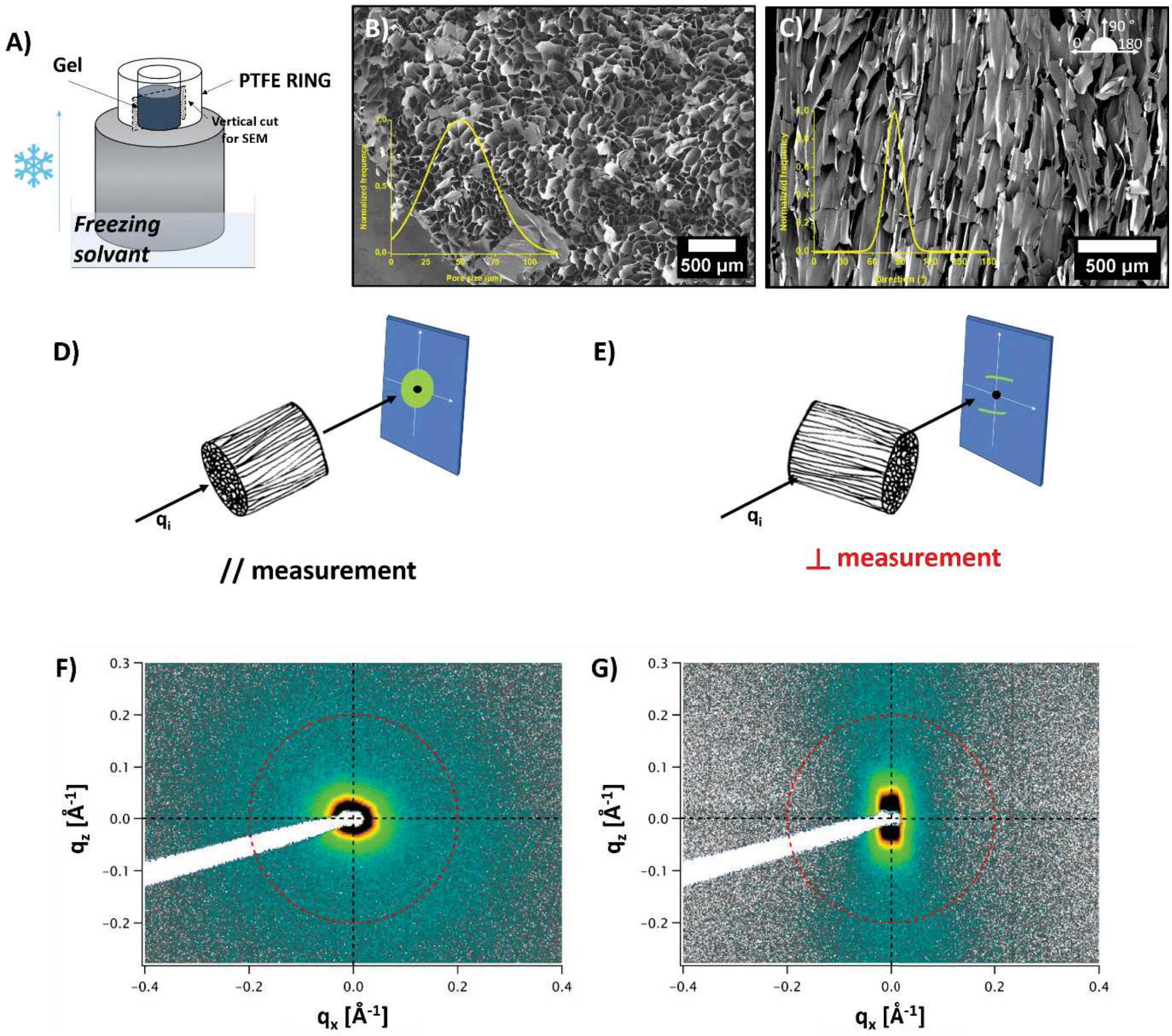

Figure 9 : A) Schéma de la méthode de congélation unidirectionnelle ; B-C) Images MEB représentatives de la coupe horizontale et verticale d'un cryogel modelé. Les encarts représentent l'histogramme de la directionnalité et de la taille des pores. D-E) Schéma des mesures de diffusion parallèle et perpendiculaire des rayons X du cryogel modelé ; F-G) Images de détecteur 2D du profil WAXS (~ 0,2 Å-1) d'un cryogel modelé dans les directions F) //, et G) ⊥.

Pour aller plus loin dans le contrôle fin de la structure poreuse, nous avons étudié la possibilité de modifier la taille des macropores. En augmentant la vitesse de congélation de l'échantillon par l'utilisation de différents bains de refroidissement (N_{2L} -196°C, N_{2L}/EtOH -115°C, CO_{2S}/IPA -77°C, IPA refroidi -30°C), la taille des pores a été modifiée de 50 µm à 350 µm. La structure des pores des templated cryogels fabriqués à différentes températures de bain de congélation est similaire et leur densités constante (0,02 g/cm^3). Les pores facettés forment une structure en nid d'abeille composée de canaux orientés le long du gradient de température. Plus la température du bain de congélation est élevée (c'est-à-dire plus la valeur absolue du taux de congélation est faible), plus les pores sont grands. La Figure 10.A-B montre l'évolution de la taille des pores et des parois (mesurée par analyse d'image MEB) et du taux de congélation avec l'utilisation de différents bains de congélation. Avec le taux de congélation absolu le plus élevé (- 23°C/min), les templated N_{2L} cryogels présentent les plus petits pores de 50 ± 23 µm. Lorsque la valeur absolue de la vitesse de congélation diminue, la croissance des cristaux de glace est plus lente. De plus, lorsque la taille des pores augmente, les pores sont également moins définis (voir Figure 10.C-F) et la polydispersité de la taille des pores augmente (voir Figure 10.A). L'épaisseur de la paroi des pores a également changé avec les taux de congélation (voir Figure 10.B). Ceci est dû au fait que les parois des pores sont composées de fibres de PEDOT : PSS provenant du gel natif. Par conséquent, à densité constante, de plus gros cristaux repoussent davantage de fibres PEDOT : PSS, formant ainsi des parois de pores plus épaisses (~ 300 nm à 3 µm, selon le bain de congélation). Dans l'ensemble, nous avons été en mesure de produire des cryogels macroporeux hautement anisotropes avec une taille de pore ajustable.

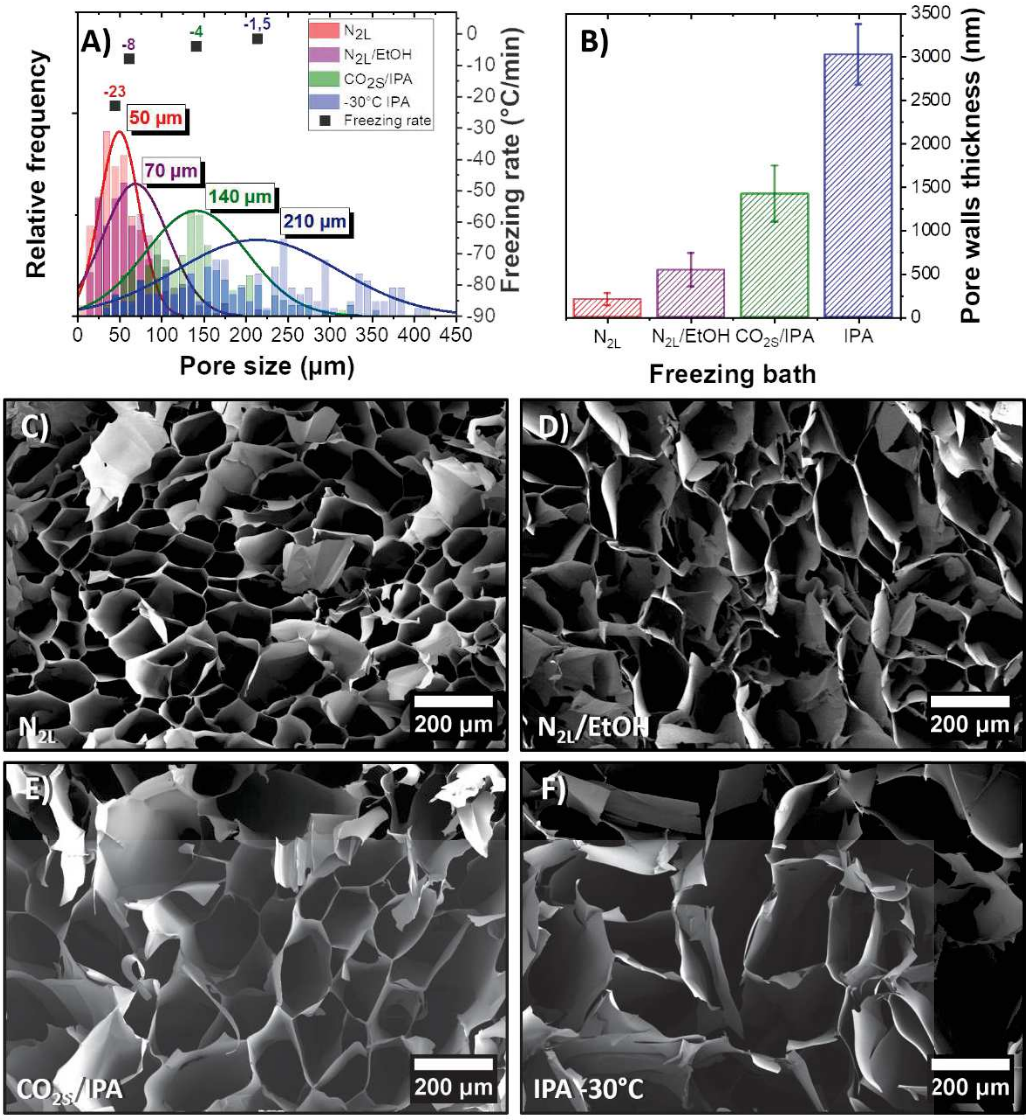

Figure 10 : Evolution de A) la taille des pores et de la vitesse de congélation, et B) l'épaisseur des parois des pores en fonction des bains de congélation ; C-F) Images MEB de la coupe horizontale de C) N_{2L}, D) N_{2L}/EtOH, E) CO_{2S}/IPA, et F) IPA templated cryogels.

Il est intéressant de noter que nous avons pu contrôler ces propriétés de transport en ajustant la taille des pores. Avec des pores plus petits, la conductivité électrique la plus élevée (1,3 S/cm) et la conductivité thermique la plus faible (0,037 W/(m.K)) ont été obtenues pour le cryogel N2L modelé. Nous suggérons que la faible conductivité thermique est due aux effets de diffusion des phonons à l'intérieur des parois des pores en raison de l'orientation des fibres à l'intérieur de ceux-ci. L'évolution de la conductivité électrique était plus difficile à attribuer mais nous avons suggéré qu'elle était due à l'augmentation du désordre morphologique dans les parois des pores lorsque la taille des pores (et des parois des pores) augmente.

4. COMPARAISON DES CARACTERISTIQUES STRUCTURELLES DES PCPS PAR DIFFUSION DES RAYONS X

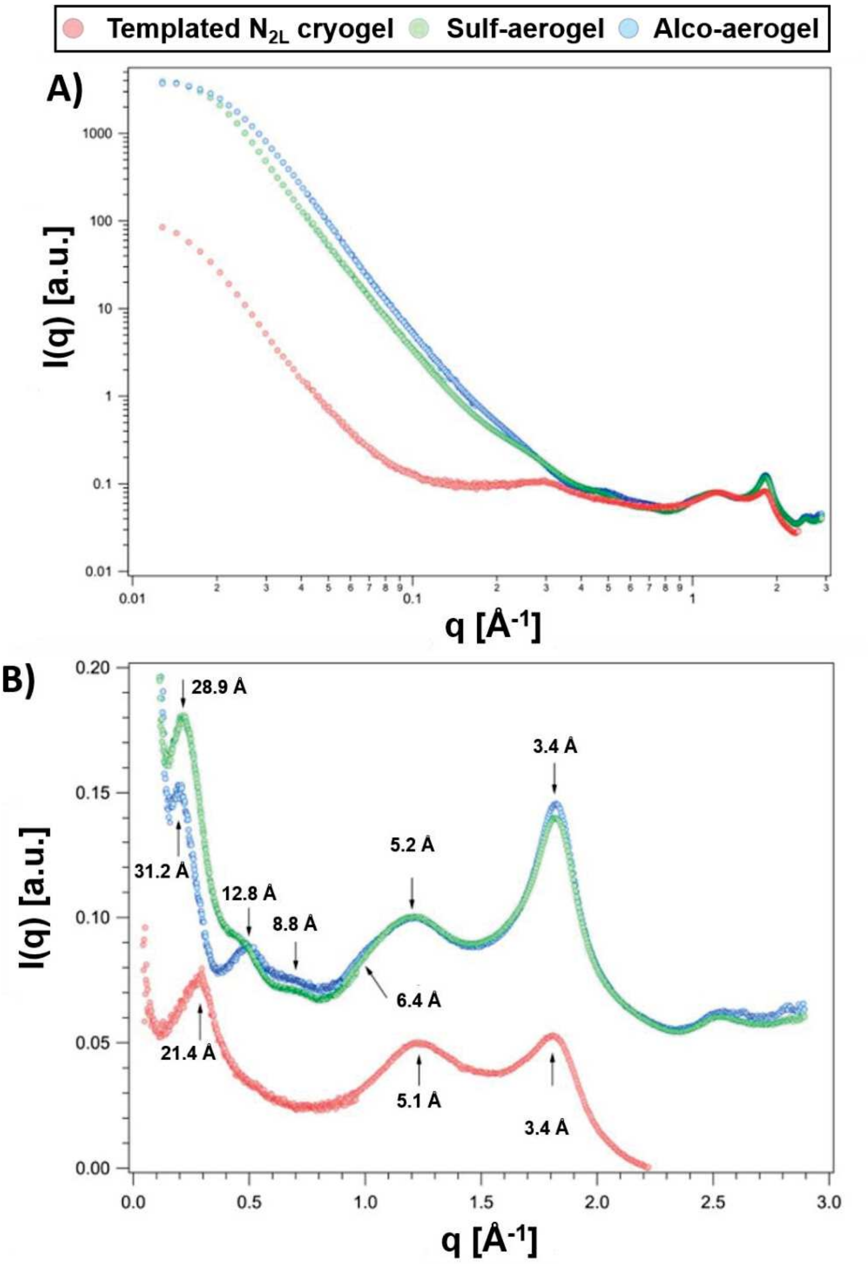

Figure 11 : A) Profil d'intensité SAXS et WAXS du templated N_{2L} cryogel (en rouge), du sulf-aérogel (en vert), de l'alco-aérogel (en bleu) ; B) données WAXS soustraites de la contribution q^{-4} dans le régime de Porod.

Dans le domaine WAXS, les pics entre 0,4 et 2,5 Å^{-1} sont liés à la structure interne des fibrilles (c'est-à-dire l'arrangement moléculaire entre le PEDOT et le PSS). Les sulfo- et alco-aérogels présentent des pics nombreux et fins suggérant un ordre cristallin plus élevé que dans le cryogel. Les pics à 3,4 Å et 5,1-5,2 Å correspondent respectivement aux distances de π-stacking caractéristiques du PEDOT et du PSS. Le pic du π-stacking du PEDOT est à la même position mais est moins intense pour les cryogels que pour les deux échantillons d'aérogel. Les pics à 8.8 Å et 12.8 Å correspondent à la distance interlamellaire caractéristique du PSS et du PEDOT, respectivement. Nous ne pouvons pas attribuer clairement le pic à 6.4 Å, clairement vu dans les sulf- et alco-aérogels mais pas dans le cryogel. La différence d'ordre cristallin au sein des fibrilles constituant les aérogels et le cryogel est assez surprenante. On s'attendrait à ce que l'organisation interne des fibrilles se produise pendant l'étape de gélification (qui est assez similaire dans le cas du cryogel et du sulf-aérogel). L'étape d'échange de solvant du sulf-aérogel dans l'éthanol et/ou les conditions supercritiques ont un impact sur la structure interne des fibrilles.

Dans le domaine des angles moyens, un pic de diffusion est observé à 28,9 Å et 31,2 Å pour les sulf- et alco-aérogels. Nous suggérons qu'il correspond à une distance fibrille à fibrille (proche de l'épaisseur déterminée par cryo-MEB). Pour le cryogel, ce pic est décalé à 21.4 Å (mesure sur la plateforme DIFFERIX à l'ICS) ou 27 Å (mesure synchrotron). Pour l'instant, nous ne pouvons pas expliquer pourquoi nous avons observé une telle différence dans la position du pic. Mais dans les deux cas, c'est ce pic qui présente un certain comportement anisotrope (dépendant de l'orientation des templated cryogels vers le faisceau). Par conséquent, nous proposons d'attribuer ce pic à une distance de fibrille à fibrille dans les parois des pores.

Grâce à ces résultats et sur la base des calculs DFT, de la simulation de dynamique moléculaire et des modèles de rayons X reportés dans la littérature, nous pensons qu'à l'intérieur des fibrilles, le système PEDOT : PSS a tendance à s'organiser en une structure lamellaire. Les empilements π-π des oligomères de PEDOT sont certainement distribués le long des chaînes de PSS et séparés par des chaînes de PSS, ce qui entraîne une alternance de molécules de PEDOT et de PSS. Sur la base des analyses structurelles des hydrogels, des cryogels, des alcogels, des sulf-aérogels et des alco-aérogels, nous proposons l'arrangement structurel possible du PEDOT et du PSS dans une fibrille (dans le cas du matériau présentant un ordre plus cristallin, c'est-à-dire dans le sulf-aérogel ou l'alco-aérogel) illustrée dans la Figure 12 : Proposition d'un arrangement structurel de PEDOT et PSS dans les fibrilles. Les molécules de PSS (en gris) sont disposées selon une morphologie lamellaire, en alternance avec le PEDOT (en bleu) empilé le long de la direction de π-stacking. Nous avons mesuré sur le profil WAXS les distances typiques de π-stacking du PEDOT et du PSS à 3.4 Å et 5.2 Å, respectivement. Nous suggérons que les distances à 8.8 Å et 12.8 Å sont respectivement les distances typiques des lamelles PSS à PSS et PEDOT à PEDOT. Sur la base de l'anisotropie de la diffusion dans la gamme des angles moyens, nous suggérons que le pic autour de 27-30 Å correspond à l'épaisseur typique d'une fibrille.

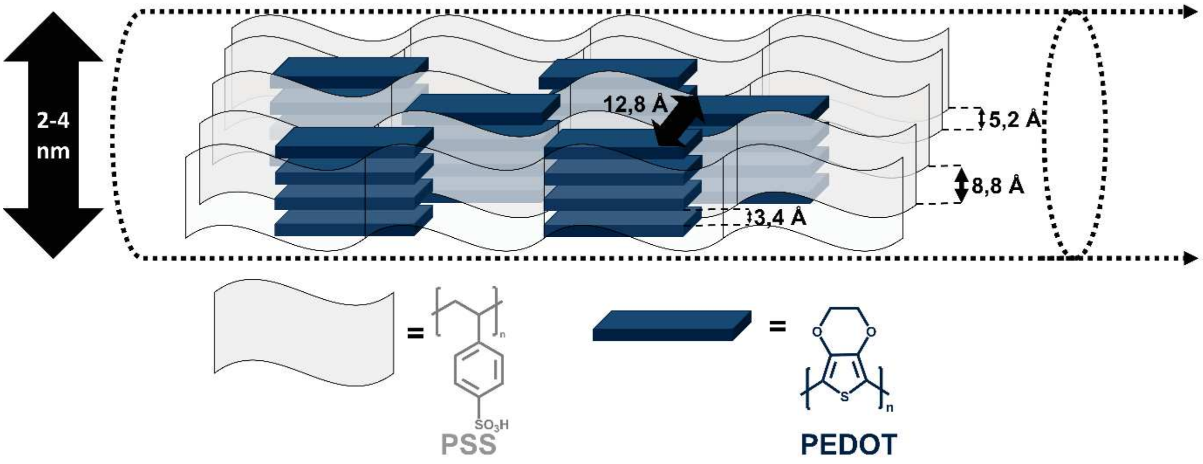

Figure 12 : Proposition d'un arrangement structurel de PEDOT et PSS dans les fibrilles. Les molécules de PSS (en gris) sont disposées selon une morphologie lamellaire, en alternance avec le PEDOT (en bleu) empilé le long de la direction de π-stacking. Nous avons mesuré sur le profil WAXS les distances typiques de π-stacking du PEDOT et du PSS à 3.4 Å et 5.2 Å, respectivement. Nous suggérons que les distances à 8.8 Å et 12.8 Å sont respectivement les distances typiques des lamelles PSS à PSS et PEDOT à PEDOT. Sur la base de l'anisotropie de la diffusion dans la gamme des angles moyens, nous suggérons que le pic autour de 27-30 Å correspond à l'épaisseur typique d'une fibrille.

5. INFLUENCE DE LA POROSITE SUR LES PROPRIETES TE

Nous avons réussi à obtenir différents types de porosité et différentes structures poreuses à partir du même gel PEDOT : PSS. Nous avons étudié la relation structure-propriétés des matériaux présentés ci-dessus. Dans ce travail de thèse, nous avons d'abord dû développer des techniques de caractérisation appropriées pour nos échantillons massifs, légers et poreux. Notre laboratoire disposait de l'infrastructure nécessaire pour mesurer la conductivité électrique et le coefficient Seebeck des matériaux TE organiques. Cependant, les montages existants étaient conçus pour des mesures sur des films minces déposés sur des substrats. Nous avons dû adapter les mesures à nos échantillons (et vice versa) tout en assurant la fiabilité de nos mesures. Pour les mesures de conductivité thermique, une machine spécifique a été achetée après comparaison et test de plusieurs méthodes différentes. Finalement, il a fallu prendre en main cette technique. Le schéma et la réponse typique pour la mesure des propriétés TE de nos PCPs sont illustrés dans la Figure 13.

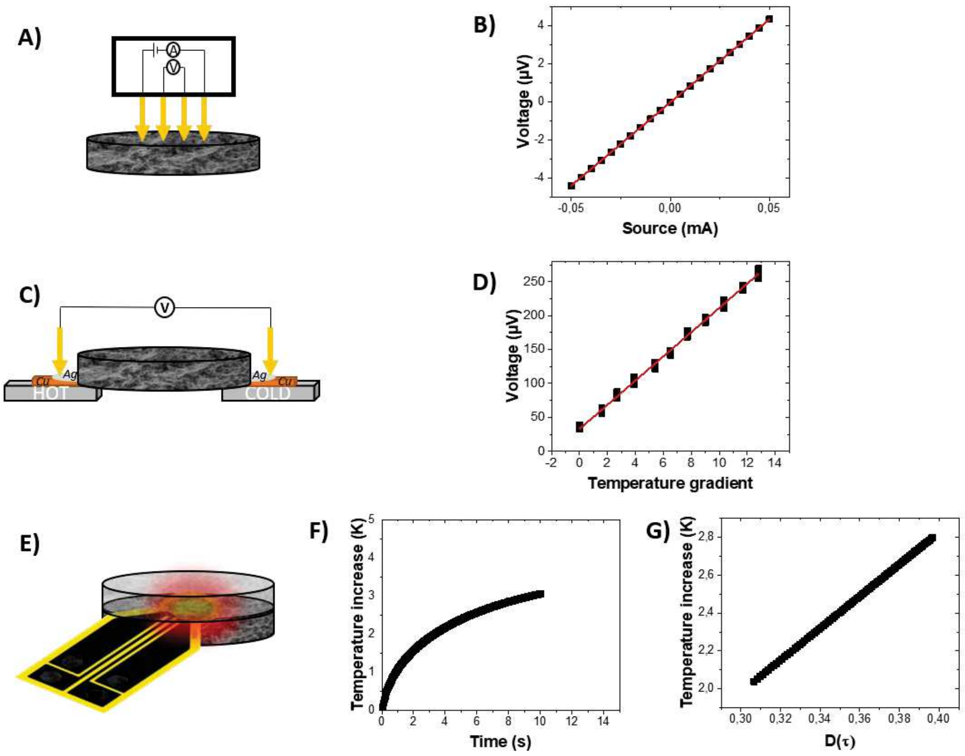

Figure 13 : Schéma et courbes typiques obtenues lors de la mesure des propriétés TE. A) Schéma de la mesure de la résistance électrique par la méthode de résistivité 4 pointes; B) courbe I/V typique de la mesure de la résistance électrique ; C) schéma de la mesure du coefficient Seebeck dans le plan. Pour assurer un bon contact

électrique avec les sondes et un bon contact thermique avec les éléments Peltier, les échantillons ont été collés sur une patte de cuivre (Cu) avec de la pâte d'argent (Ag) ; D) courbe typique de la mesure du coefficient Seebeck ; E) configuration de l'échantillon pour la mesure de la conductivité thermique isotrope, le capteur est pris en sandwich entre deux PCPs de taille relativement identique. Les échantillons ont été maintenus en place à l'aide d'une pastille d'aluminium légère au sommet de l'échantillon supérieur, assurant un bon contact entre le capteur et la surface des échantillons, F) courbe transitoire typique des mesures de conductivité thermique, G) graphique typique calculé (ΔT) en fonction de D(τ).

Les propriétés TE du xérogel, du sulf- et alco-aérogel, et du quenched cryogel ont été mesurées par les méthodes décrites plus haut et sont présentées Figure 14. Un film autosupporté de quelques µm d'épaisseur a été réalisé comme référence dense (σ = 508 ± 70 S/cm, S = 18,5 ± 3 µV/K, κ = 0,3 W/(m.K)), la dispersion brute a été lyophilisée afin d'avoir une référence poreuse (σ ~ 0.05 S/cm, S ~ 19 µV/K, κ ~ 0,059 W/(m.K).

Les PCPs conçus dans ce travail de thèse présentent tous une conductivité électrique supérieure à 10^0 S/cm (supérieure à la dispersion lyophilisée) et un coefficient Seebeck proche des valeurs rapportées pour les films denses. Leurs facteurs de puissance sont assez faibles (entre 0,1-0,5 µW/(m.K²)) par rapport au film de référence (17 µW/(m.K²), non représenté dans le graphique Figure 14). Les propriétés de transport de charge de ces matériaux poreux ont été négativement impactées par la présence d'une grande quantité d'air dans le matériau. Il est également clair que la conductivité électrique est directement liée à la densité (et inversement à la taille des pores). Bien que le facteur de puissance de ce matériau soit assez faible par rapport aux valeurs reportées dans la littérature en couche mince,[17] ces résultats sont très prometteurs car ils montrent la possibilité de produire des matériaux massifs, poreux, électriquement conducteurs et mécaniquement robustes avec de faibles quantités de PEDOT:PSS.

Avec la diminution de la densité des PCPs, σ et κ diminuent tandis que S augment légèrement. κ a été réduit cinq fois par rapport aux films minces. Dans l'ensemble, des valeurs de conductivité thermique très faibles (de l'ordre de 40-60 mW/(m.K) pour le sulf-aérogel et le quenched cryogel) ont été obtenues.

Grâce à leur ordre cristallin élevé, le sulf- et l'alco-aérogel présentent les meilleures propriétés de transport de charge parmi les PCPs produits dans ce travail de thèse. De manière intéressante (et malgré leurs caractéristiques structurelles et moléculaires très similaires), l'alco-aérogel (σ = 21 S/cm, S = 18 µV/K) présente des propriétés de transport de charge plus élevées que le sulf-aérogel (σ = 9 S/cm, S = 16,8 µV/K). D'autres études doivent être réalisées pour conclure sur ces différences, mais il est probable qu'elles surviennent lors de l'étape de gélification. Inversement, les cryogels présentent les propriétés de transport de charge les plus faibles, mais aussi la conductivité thermique la plus basse (quenched cryogel : σ = 2 S/cm, S = 19 µV/K, κ = 0,042 W/(m.K) ; templated N_{2L} cryogel : σ = 1,3 S/cm, S = 20 µV/K, κ = 0,037 W/(m.K)). Ceci est dû à leur très faible densité et à leur structure macroporeuse particulière.

La très faible conductivité thermique due à la faible densité et à la porosité élevée du cryogel trempé, du sulf- et de l'alco-aérogel est bénéfique pour le ZT. Les PCPs qui ont subi l'étape de gélification et de séchage présentent une valeur ZT comprise entre 10^{-4} et 10^{-3}, ce qui est cent à mille fois plus élevé que pour la dispersion lyophilisée (ZT ~ 10^{-6}). Ces résultats démontrent l'importance cruciale de la structuration et de la morphologie ordonnée lors de la conception de matériaux poreux. Le ZT atteint même 3.1 x 10^{-3} à 300K pour l'alco-aérogel qui présente le meilleur compromis entre σ, κ et S. L'alco-aérogel est le matériau poreux le plus prometteur conçu dans ce travail de thèse et se situe parmi les valeurs les plus élevées rapportées pour les matériaux poreux en PEDOT : PSS pur.[18]

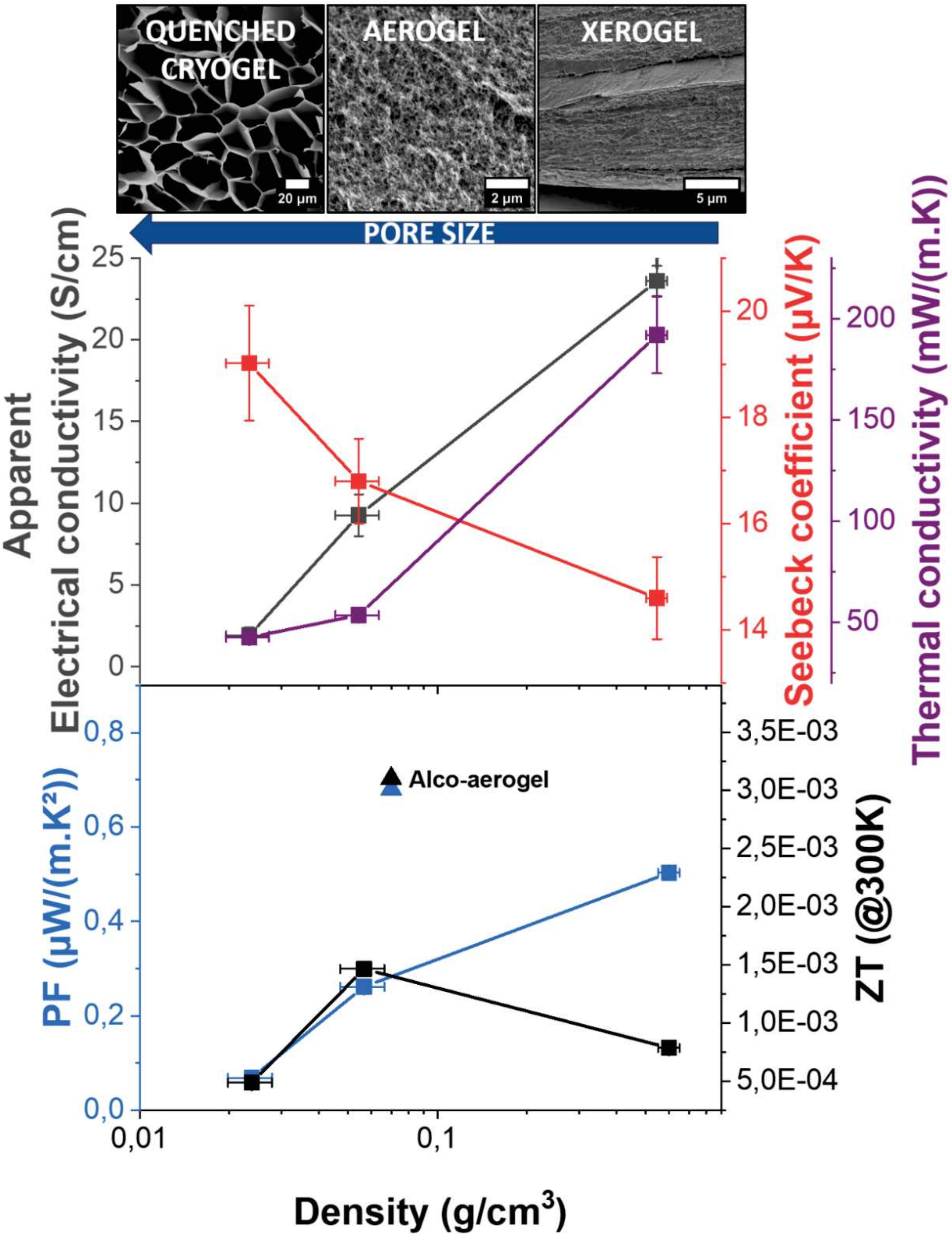

Figure 14 : Évolution des propriétés TE du quenched cryogel, du sulf-aérogel, et du xérogel en fonction de la densité, l'alco-aérogel est également représenté par des triangles. Les images MEB en haut de la figure représentent les structures poreuses des trois matériaux. Sur le premier graphique, la conductivité électrique apparente (en gris), le coefficient Seebeck (en rouge) et la conductivité thermique (en violet) des trois matériaux sont représentés en fonction de la densité (il est à noter que la conductivité thermique du xérogel a été estimée). Sur le second graphique, le facteur de puissance PF (en bleu) et le ZT (en noir) des quatre matériaux sont représentés en fonction de la densité.

L'étape de gélification a permis au PEDOT : PSS de se réarranger en un système plus ordonné, favorisant le transport de charges par rapport à la dispersion lyophilisée. Nous avons pu atteindre des propriétés d'isolation thermique semblables à celles du verre pour un matériau de plusieurs mm d'épaisseur grâce à la porosité. En revanche, la conductivité électrique apparente est limitée en raison de la forte teneur en air tandis que le coefficient Seebeck est comparable à celui obtenu dans les matériaux denses.

Globalement, nous avons observé un changement des propriétés TE entre les différents PCPs. Aux faibles densités, les conductivités électrique et thermique sont toutes deux faibles. Il est intéressant de noter que même pour le matériau le plus conducteur (alco-aérogel), l'implantation de la porosité dans les matériaux TE a réduit considérablement la conductivité thermique des PCPs. Pour mieux démontrer l'impact de la porosité, nous pouvons estimer la contribution du réseau sur la conductivité thermique. Bien qu'il ait été rapporté que le nombre de Lorentz peut prendre différentes valeurs en fonction du désordre énergétique d'un matériau,[9] nous supposons que tous nos PCP sont globalement similaires (en ce qui concerne le transport de charges). Nous avons donc calculé κ_{elec} avec la loi de Wiedemann-Franz (en prenant L à la valeur de Sommerfeld) pour en déduire $\kappa_{lattice}$. La Figure 15 montre l'évolution des contributions du réseau et électronique à la conductivité thermique en fonction de la densité. Comme prévu, κ_{elec} est presque négligeable pour tous les échantillons, elle n'augmente que légèrement pour le PCP le plus conducteur (c'est-à-dire l'alco-aérogel). De manière plus intéressante, l'implantation de la porosité a réduit la contribution du réseau à la conductivité thermique bien en dessous de 0,2 W/(m.K) pour tous les PCPs produits.

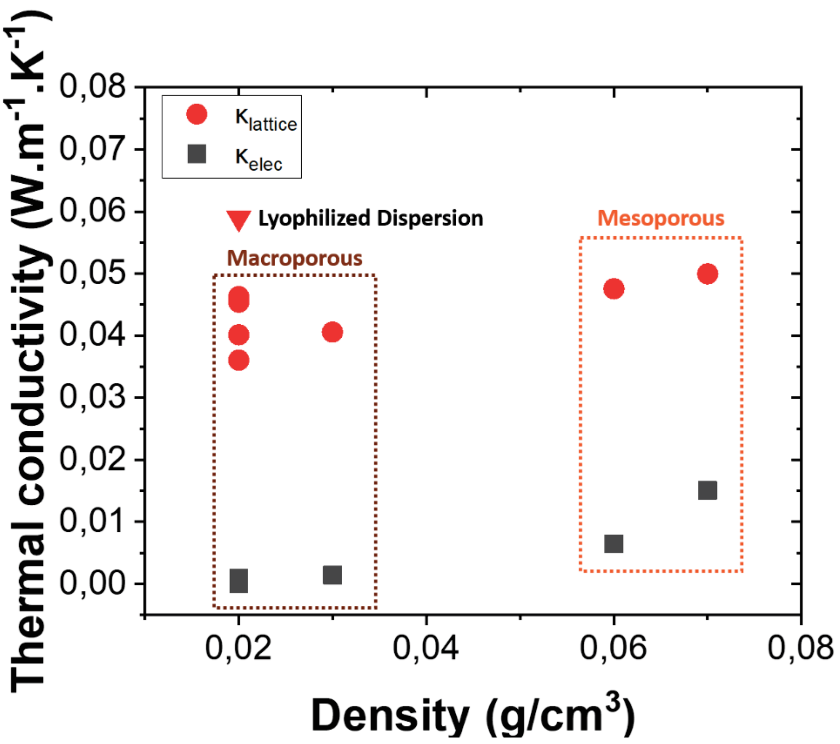

Figure 15 : Évolution des contributions du réseau et électronique à la conductivité thermique en fonction de la densité.

6. LES PCPS COMME MATERIAUX PROMETTEURS A IMPLEMENTER DANS LES GENERATEURS TE

Une des applications pour lesquelles un tel matériau pourrait être intéressant est la génération d'électricité par la récolte de la chaleur corporelle. Il est possible de calculer un rendement théorique maximal (en négligeant toute résistance de contact) à partir du ZT du matériau.[19] Pour simuler la production d'électricité par la chaleur corporelle, le côté chaud (c'est-à-dire la peau) et le côté froid (c'est-à-dire, l'air) ont été choisi selon les valeurs rapportées dans la littérature.[3] Par conséquent, T_H = 306 K et T_C = 293 K. Si l'on considère que le ZT du matériau est de 3,1 x 10^{-3}, avec une telle différence de température, l'efficacité maximale η_{max} du matériau peut être estimée à ~ 0,003 %. Une efficacité aussi faible n'est pas surprenante compte tenu de ce faible gradient de température et du ZT.[19] A partir de cette valeur, nous pouvons estimer la puissance maximale théorique de notre alco-aérogel (en considérant le flux de chaleur sur le poignet d'une peau humaine entre 18 mW/cm² pour un sujet debout et 80 mW/cm² pour un sujet en mouvement) à 0,55 - 2,5 µW/cm² (pour un corps debout - en mouvement, respectivement). Une telle puissance est déjà suffisante pour alimenter des appareils à faible consommation tels que les montres à quartz.[20,21] On pourrait imaginer qu'un jour, ce type de montre pourrait fonctionner avec un petit TEG récoltant la chaleur corporelle.

Pour démontrer le potentiel réel des alco-aérogels de PEDOT : PSS dans un générateur TE, la puissance de sortie a été mesurée en fonction d'un circuit de charge externe réglable (à température et pression ambiante). L'alco-aérogel présente une puissance de sortie maximale de 0,102 µW et une faible résistance interne de 0,044 Ω pour un petit gradient de température de 7 K (avec la température moyenne fixée à 20°C). Il est intéressant de noter que la puissance maximale de sortie a été multipliée par vingt pour atteindre 2 µW pour un gradient de température de 36,5 K. L'évolution de la puissance de sortie surfacique (la surface de mesure était de 1 cm²) en fonction du gradient de température est présentée dans la Figure 16. A 36,5 K de différence de température entre les deux disques de cuivre, la puissance surfacique d'un seul alco-aérogel peut atteindre 2,54 µW/cm². À notre connaissance, il s'agit de la puissance de sortie la plus élevée rapportée pour un matériau thermoélectrique poreux organique pur.[10]

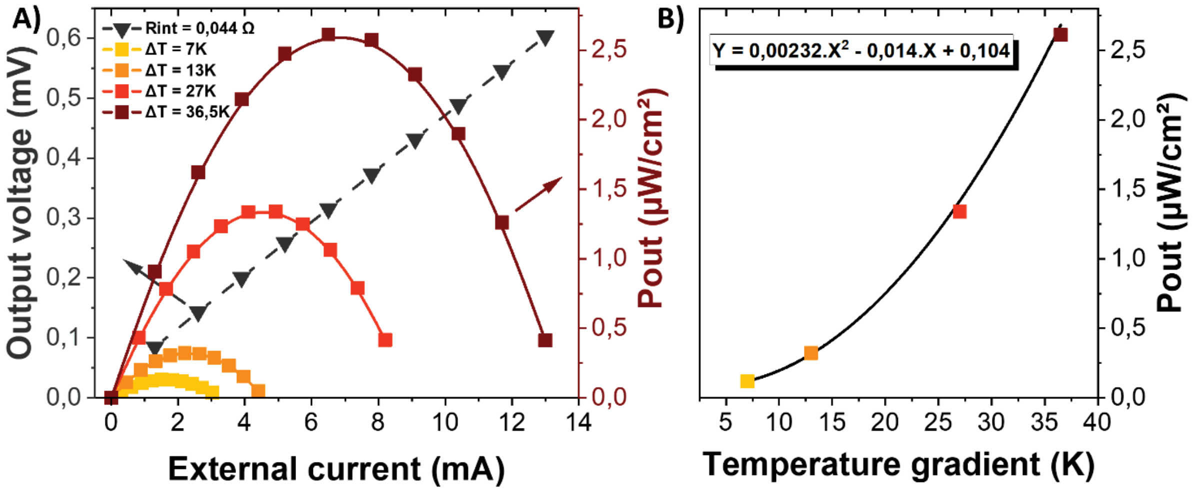

Figure 16 : A) Tension et puissance de sortie surfacique en fonction du courant pour un alco-aérogel pour des gradients de température de 7 K à 36,5 K ; B) Évolution quadratique de la puissance de sortie surfacique en fonction du gradient de température appliqué.

7. CONCLUSION

Dans ce travail de thèse, nous avons démontré l'intérêt de mettre en œuvre la porosité dans des matériaux TE organiques. Leur conductivité thermique de réseau a été réduite en dessous de 0,2 W/(m.K) et leur conductivité électrique est restée supérieure à 1 S/cm. L'élaboration de ces matériaux par gélification et d'élimination du solvant a permis la conception et le développement de matériaux poreux de grande taille à un coût assez faible (~ 2€ de matière première pour des PCPs de taille centimétrique). Bien qu'il ne s'agisse que de résultats préliminaires, nous avons commencé à étudier la stabilité à l'air de ces matériaux. Sur vingt-cinq jours, les sulf- et alco-aérogels ont souffert d'une légère augmentation de la conductivité thermique. À l'inverse, les quenched et templated N_{2L} cryogels ont montré une meilleure stabilité. Enfin, nous avons même démontré l'utilisation potentielle de matériaux organiques poreux dans des TEG verticaux réels en mesurant leur puissance de sortie. L'alco-aérogel a présenté une puissance de sortie de 2,5 µW/cm² pour un gradient de température de 36,5 K. Cette conversion de chaleur en électricité est très prometteuse pour l'alimentation de dispositifs de faible puissance à l'avenir.

Pour l'instant, le principal inconvénient de ces matériaux poreux est leur faible capacité de transport de charges. Par conséquent, à l'avenir, l'attention devrait être portée sur le développement et l'amélioration des techniques permettant d'augmenter les propriétés de transport de charge de ces PCPs tout en maintenant une faible conductivité thermique du réseau. Une stratégie pourrait être l'utilisation d'agents réducteurs tels que le TDAE pour augmenter le coefficient Seebeck des matériaux poreux PEDOT : PSS poreux.

Pour confirmer l'intérêt des PCP dans les TEGs verticaux, le développement de prototypes de générateurs devrait être la prochaine étape. Une attention particulière devrait être portée sur la dimension du matériau, au générateur en lui-même et aux résistances électriques de contact. Des études sur la stabilité de l'air doivent également être menées si l'on souhaite utiliser ce matériau dans les capteurs de chaleur corporelle à l'avenir.

REFERENCES

[1] O. Bubnova, X. Crispin, *Energy Environ. Sci.* **2012**, *5*, 9345.

[2] M. Campoy-Quiles, *Philos. Trans. R. Soc. A* **2019**, *377*, 20180352.

[3] V. Leonov, *IEEE Sens. J.* **2013**, *13*, 2284.

[4] M. Thielen, L. Sigrist, M. Magno, C. Hierold, L. Benini, *Energy Convers. Manag.* **2017**, *131*, 44.

[5] D. Beretta, N. Neophytou, J. M. Hodges, M. G. Kanatzidis, D. Narducci, M. Martin-Gonzalez, M. Beekman, B. Balke, G. Cerretti, W. Tremel, A. Zevalkink, A. I. Hofmann, C. Müller, B. Dörling, M. Campoy-Quiles, M. Caironi, *Mater. Sci. Eng. R Reports* **2019**, *138*, 100501.

[6] O. Bubnova, Z. U. Khan, A. Malti, S. Braun, M. Fahlman, M. Berggren, X. Crispin, *Nat. Mater.* **2011**, *10*, 429.

[7] A. D. Scaccabarozzi, A. Basu, F. Aniés, J. Liu, O. Zapata-Arteaga, R. Warren, Y. Firdaus, M. I. Nugraha, Y. Lin, M. Campoy-Quiles, N. Koch, C. Müller, L. Tsetseris, M. Heeney, T. D. Anthopoulos, *Chem. Rev.* **2022**, *122*, 4420.

[8] V. Vijayakumar, Y. Zhong, V. Untilova, M. Bahri, L. Herrmann, L. Biniek, N. Leclerc, M. Brinkmann, *Adv. Energy Mater.* **2019**, *9*, 1900266.

[9] D. Scheunemann, M. Kemerink, *Phys. Rev. B* **2020**, *101*, 75206.

[10] X. Wang, P. Liu, Q. Jiang, W. Zhou, J. Xu, J. Liu, Y. Jia, X. Duan, Y. Liu, Y. Du, F. Jiang, *ACS Appl. Mater. Interfaces* **2019**, *11*, 2408.

[11] M. P. Gordon, E. W. Zaia, P. Zhou, B. Russ, N. E. Coates, A. Sahu, J. J. Urban, *J. Appl. Polym. Sci.* **2017**, *134*, 44070.

[12] S. Han, F. Jiao, Z. U. Khan, J. Edberg, S. Fabiano, X. Crispin, *Adv. Funct. Mater.* **2017**, *27*, 1703549.

[13] N. Yanagishima, S. Kanehashi, H. Saito, K. Ogino, T. Shimomura, *Polymer (Guildf).* **2020**, *206*, 122912.

[14] M. A. Leaf, M. Muthukumar, *Macromolecules* **2016**, *49*, 4286.

[15] T. Takano, H. Masunaga, A. Fujiwara, H. Okuzaki, T. Sasaki, *Macromolecules* **2012**, *45*, 3859.

[16] N. Kim, S. Kee, S. H. Lee, B. H. Lee, Y. H. Kahng, Y. R. Jo, B. J. Kim, K. Lee, *Adv. Mater.* **2014**, *26*, 2268.

[17] Z. Zhu, C. Liu, F. Jiang, J. Xu, E. Liu, *Synth. Met.* **2017**, *225*, 31.

[18] Q. Weinbach, C. B. Nielsen, L. Biniek, *J. Mater. Chem. C* **2021**, *9*, 10173.

[19] M. Culebras, C. M. Gómez, A. Cantarero, *Materials (Basel).* **2014**, *6*, 6701.

[20] G. J. Snyder, in *Energy Harvest. Technol.*, **2009**, pp. 325–335.

[21] “Seiko - La montre Kinetic - - WorldTempus,” can be found under https://fr.worldtempus.com/article/seiko-la-montre-kinetic-14518.html, **n.d.**

Quentin WEINBACH

Elaboration and Characterization of Porous Conducting Polymers: Application to Thermoelectricity

Résumé

Les polymères conducteurs sont des matériaux très prometteurs pour des applications en thermoélectricité visant à transformer la chaleur résiduelle ou perdue dans la gamme de l'ambiant (0 – 100°C) en énergie électrique. Nous proposons une architecture innovante de polymère conducteur nous permettant de produire des matériaux poreux très isolants thermiquement grâce à une technique de gélification suivie d'un séchage du solvant. Trois architectures différentes basées sur le polymère conducteur poly(3,4-ethylenedioxy thiophène):poly(styrène sulfonate) (PEDOT:PSS) ont été conçues. Leur structure a été caractérisée par Microscope Electronique à Balayage (MEB et cryo-MEB), ainsi que par des techniques de spectroscopies telles que la diffusion des rayons X aux grands et petits angles (WAXS/SAXS). Des gels fibrillaires mésoporeux de PEDOT:PSS peuvent être formés par l'ajout d'acide sulfurique ou d'éthanol. Les gels peuvent ensuite être séchés par différentes techniques : séchage supercritique (aérogel), freeze-drying (cryogel) ou à pression et température ambiante (xerogel). La structure poreuse du xerogel est incontrôlée et hétérogène alors que l'aérogel conserve la structure fibrillaire 3D du gel conduisant à un réseau mésoporeux. Enfin, la technique de freeze-drying permet de produire une structure macroporeuse en « nid d'abeille ». La structure peut être ajustée par le contrôle de la cristallisation du solvant du gel pendant l'étape de congélation. Les propriétés thermoélectriques (conductivités électrique et thermique et coefficient Seebeck) ont été mesurées et l'influence de la porosité étudiée. Nous démontrons ainsi la production et la caractérisation de matériaux thermoélectriques organiques très isolants thermiquement (36-52 mW.m^{-1}.K^{-1}) tout en maintenant une conductivité électrique jusqu'à 20 S/cm. Lorsqu'il est soumis à un gradient de 36,5K, un aérogel de PEDOT:PSS peut produire plus de 2,5 µW/cm².

Mots clés : Thermoélectrique organique, PEDOT :PSS, Matériaux poreux, Collecte d'Energie

Summary

Conducting polymers are promising materials for thermoelectric application for energy harvesting of residual heat in the ambient range (0-100°C). Here, we propose an innovative architecture of conductive polymers allowing us to produce highly thermally insulating porous materials through a gelation technique followed by solvent drying. Three different architectures based on the conducting polymer poly(3,4-ethylenedioxy thiophene):poly(styrene sulfonate) (PEDOT:PSS) have been designed. Their structures were characterized by Scanning Electron Microscope (SEM) and cryo-SEM, as well as by spectroscopic techniques such as wide and small angle X-ray scattering (WAXS/SAXS). Mesoporous fibrillar PEDOT: PSS gels can be formed via the addition of sulfuric acid or ethanol. Gels can then be dried by different techniques: supercritical drying (aerogel), freeze-drying (cryogel) or at pressure and room temperature (xerogel). The porous structure of the xerogel is uncontrolled and heterogeneous whereas the aerogel retains the 3D fibrillar structure of the gel leading to a mesoporous network. Finally, the freeze-drying technique produces a macroporous honeycomb structure. The structure can be adjusted by controlling the crystallization of the gel solvent during the freezing step. The thermoelectric properties (electrical and thermal conductivities and Seebeck coefficient) were measured and the influence of the porosity was studied. We demonstrate the production and characterization of highly thermally insulating organic thermoelectric materials (36-52 mW.m^{-1}.K^{-1}) while maintaining electrical conductivity up to 20 S/cm. When subjected to a gradient of 36.5K a PEDOT:PSS aerogel can produce more than 2,5 µW/cm².

Keywords: Organic thermoelectrics, PEDOT:PSS, Porous materials, Energy harvesting